

Characterization and Control of a Strongly-Coupled Atom-Cavity System

Thesis by
Russell L. Miller

In Partial Fulfillment of the Requirements
for the Degree of
Doctor of Philosophy



California Institute of Technology
Pasadena, California

2009

(Defended May 4, 2009)

© 2009

Russell L. Miller

All rights Reserved

This dissertation is dedicated to the memory of N. Barr and Virginia S. Miller.

Acknowledgements

*sa evāyam mayā te 'dya yogah proktaḥ purātanah
bhakto 'si me sakhā ceti rahasyam hy etad uttamam*

Baghavad Gitā

Verse 4.3

Thanks especially to Prof. Jeff Kimble for his support, guidance and for sharing his immense enthusiasm for scientific discovery.

Thanks to Andreea Boca, Dal Wilson, David Boozer, Kevin Birnbaum, Jason McKeever, Joe Buck and Tracy Northup for their direct involvement in the work described herein. You've been fantastic friends, colleagues and collaborators through good times ("Wow, sideband suppression!") and bad ("Wow, I think I saw a spark shoot from my forehead!"). After all the time we spent in Lab 11, whenever I find something isn't working I'm sure I'll always instinctively suspect its because, somewhere, the 4 – 4' beam isn't switching.

Thanks to the members of the Caltech Quantum Optics Group over the years: Barack, Cindy, Chin-wen, Daniel A., Daniel F., Hugues, Julien, Liz, Takao, Sergey, Scott K., Scott P., Scott C., Warwick, and Win.

Also to the members of the TIQC Group at Michigan - Boris, David, Patty, Louis, Martin, Winnie, Paul, Kathy-Anne and Dan - from whom I learned the basics of rigorous experimental science. Special thanks go to Prof. Chris Monroe whose enthusiasm and encouragement sparked my interest in atomic physics. This dissertation may be about neutral atoms, but I've still got an "ion my hand."

Thanks to Orville Yenoir, Seyhan Ege, Jianming Qian, David Gerdes, and to my other teachers over the years to whom I owe a debt of gratitude for sparking my intellectual curiosity and inspiring me to always look deeper.

Finally, very special thanks to my parents, Douglas and Marguerite Miller, for their love, unfaltering support, and for demonstrating to me the importance of an active intellectual life.

Characterization and Control of a Strongly-Coupled Atom-Cavity System

by

Russell L. Miller

In Partial Fulfillment of the
Requirements for the Degree of
Doctor of Philosophy

Abstract

In recent years, remarkable advances in the science of laser cooling and trapping of atomic samples have led to breakthroughs in quantum optics and, in particular, in cavity quantum electrodynamics (QED). The ability to optically trap an atom within the mode of a ultra-high finesse cavity of small mode volume for experimentally significant periods of time now allows for the continuous observation of fundamental quantum optical effects. This dissertation will focus on experiments conducted to fully characterize and exert quantum control over a strongly-coupled atom-cavity system consisting of single cesium atoms isolated by a dipole trapping in the mode of a Fabry-Perot optical resonator.

In particular, we describe techniques developed and implemented for exerting coherent control over the internal and quantum motional state of these atoms using stimulated Raman processes. We also focus on the applications of this system to quantum networking and quantum information science, particularly within the context of coherently transferring quantum states from atom to quantum optical fields and back. Finally, we describe a series of measurements carried out to explore the characteristic dynamics of the Jaynes-Cummings Hamiltonian which governs the system. This includes spectroscopic measurement of the signature vacuum Rabi splitting for strongly-coupled cavity QED as well as evidence in the time domain for coherent Rabi nutation of excitation between atom and field on resonance.

Contents

1	Introduction	1
1.1	Motivations	1
1.2	Overview of My Involvement in the Group	3
1.3	Overview	5
2	Theory and Formalism	7
2.1	The Jaynes-Cummings Hamiltonian	7
2.1.1	The Hamiltonian	7
2.1.2	Eigenvalues and Eigenvectors	9
2.2	Dissipation and the Quantum Master Equation	14
2.2.1	Why Cavity QED?	14
2.2.2	The Master Equation Approach	17
2.3	Practical Considerations	25
2.3.1	Multi-State Atom: Cesium	25
2.3.2	Fabry-Perot Resonators	35
2.3.3	A Note on Numerical Simulations	47
3	Experimental Apparatus	48
3.1	The Physics Cavity	48
3.1.1	The Mirrors	49
3.1.2	The Cavity Assembly	50
3.1.3	Cavity Parameters	51
3.1.4	Summary of Cavity Parameters	63

3.2	The Vacuum Chamber and MOTs	63
3.2.1	Vacuum Chamber	65
3.2.2	A Source of Cold Atoms	67
3.3	Intracavity Optical Dipole Trapping	73
3.3.1	The Optical Dipole Force	74
3.3.2	Cesium’s “Magic” Wavelength	77
3.3.3	A State-Insensitive Trap	80
3.4	Lasers and Frequency Servos	90
3.4.1	Cesium Lasers	90
3.4.2	Physics Cavity Stabilization	96
3.5	Beam Paths	98
3.5.1	Cavity Input and Output Paths	98
3.5.2	Cavity “Side” Beams	104
3.6	Experimental Timing	107
4	Raman Transitions in an Optical Cavity	111
4.1	Atomic Hyperfine State Detection	111
4.1.1	“Down-goer” Detection	112
4.1.2	“Up-goer” Detection	116
4.1.3	Photon Generation-Based Techniques	117
4.2	Stimulated Raman Transitions in an Optical Cavity	118
4.2.1	Theoretical Model	119
4.2.2	Cavity Modes and Raman Configurations	122
4.2.3	Generalization to Cesium	125
4.2.4	Experimental Implementation	126
4.3	Raman as a Diagnostic Tool	131
4.3.1	Raman Spectroscopy	133
4.3.2	Raman Magnetometry and Field Nulling	140
4.4	Rabi Nutation and Decoherence	143
4.4.1	Decoherence Theory	143

4.4.2	Measurements	151
4.5	Incoherent Raman Optical Pumping	155
4.5.1	Overview	155
4.5.2	Experimental Configuration	156
4.5.3	Coherent vs. Incoherent Raman transitions	156
4.5.4	Population Measurement via Raman Spectroscopy	157
4.5.5	Optical Pumping Scheme	158
4.5.6	Transition Rate for Incoherent Raman Transitions	161
4.5.7	Summary	165
4.6	Motional Effects and Cooling	166
4.6.1	Ground State Cooling on the First Order Sideband	169
4.6.2	Cooling on the Second Order Sideband	176
4.7	Sisyphus Cooling with Raman Repumper	179
5	Reversible Atom-Field State Transfer	183
5.1	Quantum Networking	184
5.2	Stimulated Raman Adiabatic Passage (STIRAP)	185
5.2.1	Theoretical Description	185
5.2.2	Physical Implementation in Cesium	191
5.3	A Deterministic Source of Single Photons	192
5.3.1	Overview and Results	193
5.3.2	Attenuation and R	197
5.4	Demonstration of Reversibility	204
6	Experimental Atom-Cavity Dynamics	213
6.1	Time-Domain Measurements	214
6.1.1	Resonant Vacuum Rabi Oscillation	215
6.1.2	Numerical Simulation	220
6.1.3	Results and Correspondence with Theory	237
6.1.4	Atom-Photon Correlation Measurements	244
6.2	Frequency-Domain Measurements	253

6.2.1	Review of Early Work	253
6.2.2	Vacuum Rabi Spectra for One and Two Atoms	256
A	Cesium D2 Dipole Matrix Elements	262
B	ADWIN Gold Timing Code	266
B.1	Syntax	266
B.2	Header and Preamble	268
B.3	External Device Programming	271
B.4	MOT and FORT Loading	271
B.5	Individual Experiment Code Blocks	273
B.5.1	STIRAP-Based Single Photon Generation	273
B.5.2	Reversible State Transfer Measurements	274
B.5.3	Raman Spectroscopy	279
B.5.4	Fast Atomic Excitation	280
C	Quantum Optics Toolbox Simulation	282
C.1	Introduction	282
C.2	Preamble and User-Specified Parameters	283
C.3	Generate System Operators	286
C.3.1	Atomic Operators	286
C.3.2	Cavity Operators	294
C.4	Generate Decay Superoperators	294
C.5	Prepare Initial Density Matrix	297
C.6	State-Dependent Detuning Effects	299
C.6.1	Magnetic Fields	299
C.6.2	FORT Shifts	300
C.6.3	Cavity Effects	302
C.7	Interaction Hamiltonians	303
C.7.1	Jaynes-Cummings Hamiltonian	303
C.7.2	User-Controlled Interactions	304

C.8 Construct Integrate Liouvillian	305
C.9 Calculate Observables	306
C.10 Subroutines	308
C.10.1 Integrating the Master Equation	308
C.10.2 Calculating Indices for Atomic States	309

List of Figures

2.1	Eigenenergy Spectrum for the Jaynes-Cummings Hamiltonian	12
2.2	The Vacuum Rabi Splitting	22
2.3	Vacuum Rabi Splitting as a Function of g and Δ	24
2.4	Time Domain Vacuum Rabi Nutation	25
2.5	Cesium 133 D_2 Spectroscopic Structure	27
2.6	Fabry-Perot Optical Cavity and Fundamental Mode Shape	35
2.7	Electric Field Diagram for a Fabry-Perot Resonator	39
3.1	Geometry of the Physics Cavity Mirrors	49
3.2	Photograph and Diagram of the Physics Cavity	50
3.3	Physics Cavity Mount and Vibration Isolation	52
3.4	Physics Cavity Linewidth Measurement	57
3.5	Theoretical Cavity Response to Circularly Polarized Probe Beam	60
3.6	Measured Birefringent Splitting of a Circularly Polarized Probe	62
3.7	Lab 11 Vacuum Chamber Layout	66
3.8	Magneto-Optical Trap in 1D	68
3.9	MOT Beams and Coils	70
3.10	The “Magic” Wavelength for a Three-State Atom	77
3.11	Cesium ($6S_{1/2}, F = 4$) and ($6P_{3/2}, F' = 5$) Light Shifts	79
3.12	($6P_{3/2}$) Zeeman Shifts in the FORT	82
3.13	FORT Anharmonicity	84
3.14	Lattice Beam Configuration	86
3.15	FORT-QED Field Registration	89

3.16	Master Laser Configuration	91
3.17	Slave Laser Configuration	93
3.18	Repumper Laser Configuration	95
3.19	Physics Cavity Input and Output Paths	101
3.20	Physics Cavity Side Beam Diffraction Patter	105
3.21	Block Timing Diagram for Loading the FORT	110
4.1	Histogram Representation of a “Down-Goer”-type Measurement	115
4.2	The Raman Λ -Scheme	120
4.3	Electronic Phase Lock for Raman Pair Generation	128
4.4	Raman Laser Beatnote Signals	129
4.5	Injection Lock for Raman Pair Generation	132
4.6	Example Raman Spectrum	135
4.7	Raman Spectrum for $(3, 0\rangle \leftrightarrow 4, 0\rangle)$ Transition	137
4.8	Raman Spectrum with Transverse Magnetic Field	138
4.9	Raman Field Nulling Measurements	142
4.10	Rabi Nutation on the Bloch Sphere	146
4.11	Decoherence on the Bloch Sphere	148
4.12	Experimental Rabi Oscillations	151
4.13	Detuned Rabi Oscillation Measurements	153
4.14	Initial Population Distribution Raman Scan	158
4.15	Power Spectrum Data For the Incoherent Raman Pair	160
4.16	Raman Spectra Demonstrating Incoherent Raman Optical Pumping	162
4.17	Higher-Frequency Raman-Raman Beam Switching Configuration	170
4.18	Raman Spectra Demonstrating First Order Sideband Ground State Cooling	173
4.19	First Order Sideband Cooling Survival Probabilities	174
4.20	Response of Sideband Cooling to Variations in Parameters	176
4.21	Second Order Sideband Raman Cooling Measurements	177
5.1	Quantum Networking with Cavity QED	186
5.2	Atomic Level Diagram for STIRAP	192

5.3	Characteristics of STIRAP-Generated Cavity Emission	196
5.4	Simple Model for Attenuation of Emitted Light	199
5.5	Timing Diagram for Reversible Atom-Field State Transfer	208
5.6	Coherent versus Incoherent Absorption Probability	210
5.7	Interference Between Reversibly Generated Field and Reference State	211
6.1	Photodetector Measurement of Ω_T Pulse Shape	217
6.2	Schematic Diagram of Impulsively Excited Atom-Cavity System	218
6.3	Model Hamiltonian Impulse Envelope	221
6.4	Intracavity Photon Number Following Impulsive Excitation (Theory)	223
6.5	Effects of Ensemble Averaging Over Ω'_0	226
6.6	Impulsively-Generated Photon Wave Packet Versus Rabi Frequency	230
6.7	Thermal Averaging Effects	235
6.8	Data in the Absence of Atoms	236
6.9	Impulsively-Generated Photon Wave Packet	238
6.10	wave packet Shape Versus Impulse Intensity	240
6.11	Photodetection Probability P_1 Versus Rabi Frequency	241
6.12	Comparison of Theory and Experiment	243
6.13	State Readout Experiment Protocol	244
6.14	Raman Spectra Demonstrating Distribution of Atomic Population Following Excitation	248
6.15	Vacuum Rabi Spectra for One-and-the-Same Atom	254
6.16	Atom Number Discrimination Results	258
6.17	Vacuum Rabi Spectra for One and Two Atoms	261

List of Tables

2.1	Landé g-factors for the Cesium D -lines	31
3.1	Distribution of Longitudinal Modes for the Lab 11 Physics Cavity	54
3.2	Summary of Lab 11 Physics Cavity Parameters	64
3.3	Lower Chamber Magnetic Bias Coil Information	72
3.4	Physics Cavity Input Fields	99
3.5	Accounting of Detection Path Losses	103
4.1	Loading Efficiencies for Lattice-Lattice versus Raman-Lattice Configurations	181
5.1	Table of Reversibility Verification Measurements	206
6.1	Atom-Photon Correlation Data	252
A.1	$(6S_{1/2}, F = 3, m_F), \pi$ -Polarization Dipole Matrix Elements	262
A.2	$(6S_{1/2}, F = 3, m_F), \sigma^+$ -Polarization Dipole Matrix Elements	263
A.3	$(6S_{1/2}, F = 3, m_F), \sigma^-$ -Polarization Dipole Matrix Elements	263
A.4	$(6S_{1/2}, F = 4, m_F), \pi$ -Polarization Dipole Matrix Elements	264
A.5	$(6S_{1/2}, F = 4, m_F), \sigma^+$ -Polarization Dipole Matrix Elements	264
A.6	$(6S_{1/2}, F = 4, m_F), \sigma^-$ -Polarization Dipole Matrix Elements	265

Chapter 1

Introduction

This chapter is intended to offer a brief introduction to cavity electrodynamics as well as to broadly describe and to offer motivation for the research in which I've been involved over the preceding six years. This work, which is the continuation of a project which was begun just over ten years ago, is the aggregate result of the efforts of a number of generations of graduate students and postdoctoral fellows. In order to delineate my particular involvement in and contributions to this work, I will also attempt to provide a short, "historical" overview of the experimental progress which we have made (the details of which will be discussed in subsequent chapters).

1.1 Motivations

In very general terms, the subject of this thesis is the study of the coherent interaction between a quantized electromagnetic field and a single atom. It is useful to quantify of this type of interaction in terms of a rate $g \sim \langle \hat{H}_{int} \rangle / \hbar$, where \hat{H}_{int} is the Hamiltonian describing the energy associated with the coupling between field and atom. For the case of a single, stationary atom which is resonantly coupled to a freely propagating single photon, this quantity is governed by the size of the intrinsic atomic moment for dipole transitions and by magnitude of the electric field associated with the photon. Unfortunately from an experimental viewpoint, the electric field associated with one, freely-propagating, resonant photon is generally so small as to result in a rate of coherent coupling, g , which is insignificant on the scale of the rates at which that quanta of excitation is irreversibly lost

into the environment. It follows that in order to study this interaction while its coherence persists, we are required to tailor the strength of coupling experimentally.

So as to increase the rate, g , of coherent evolution between matter and field, we are presented two routes. First, we can seek out atoms or atom-like systems which exhibit large intrinsic transition strengths and thereby couple more strongly to the field. This approach is of limited usefulness - particularly when dealing with atoms because nature offers us only a finite variety of systems from which to choose. A second, more practical approach would be to ensure that the atom sees as large as possible an electromagnetic field per quanta of excitation. In order to do this, we can, for example, tightly focus the field onto the atom using a lens (an option which suffers from the diffraction limitations of real lenses among other problems). Another, more promising possibility would be to establish a set of boundary conditions - a cavity - that would constrain the field to exist within only a very small volume of space, V . Governed by these boundary conditions, a simple calculation based on the classical energy density for an electromagnetic field shows that the intracavity electric field associated with a fixed-magnitude input field should then be proportional to $V^{-\frac{1}{2}}$. By sufficiently decreasing this physical volume we are thereby able to generate an electric field associated with the presence of just one photon which is of sufficient magnitude to appreciably and coherently alter the dynamics of an atomic system on timescales shorter than the relevant incoherent decay channels in the system. This approach to the study of atom-field interactions is known as cavity quantum electrodynamics.

The motivations for this type of research are diverse. In broad terms, the system is appealing to a physicist from the standpoint of its inherent simplicity and fundamental importance - the controlled study of coupled quantum systems, one excitation at a time, offers deep insight into the dynamics of both systems as well as the quantum nature of their coupling. From the perspective of a quantum optician, the cavity QED interaction offers a controllable source of non-classical light which is emitted cleanly into the spatial output mode of the cavity. Furthermore, as will be demonstrated in subsequent chapters, the study of atomic physics at the level of single-atoms is greatly facilitated by the strong coupling of those atoms to an optical cavity. Finally, within the context of engineering atom-cavity systems as functional nodes in a “quantum network,” this work has been strongly motivated

by an interplay with the nascent quantum information science community. It is my intention that this thesis will draw from each of these diverse fields to present a context for the work in which I've been engaged.

1.2 Overview of My Involvement in the Group

I joined the Caltech Quantum Optics Group during late Summer, 2003. Upon my arrival in the group, I began work, temporarily, on a project in Lab 11a involving the generation of an optical supercontinuum from a mode-locked Ti:Sapphire laser coupled into a photonic crystal fiber. Continuing from where the previous student on the project, James Chou, had left the apparatus, over the next 3 months I was able to achieve mode-locking of the laser and generation of a broadband frequency comb spanning ~ 900 nm. This project, which was originally intended to provide a distributed frequency standard for integration into each of the individual experiments being carried out within our research group, was continued under my supervision in the Summer of 2004 by visiting undergraduate Thomas Pickles and was subsequently adapted by the personnel in Lab 2 to interferometrically stabilize a set of optical paths in their laboratory. This thesis includes no further discussion of this work, however, but will instead focus on my involvement in the cavity QED experiments in Lab 11 conducted from October, 2003 to the present.

The Fabry-Perot cavity experiment in Lab 11 first came on line in 1999 as the result of work by post-doctoral fellow Jun Ye and graduate student David Vernooy. By way of tremendous foresight and experimental skill in its construction, as well as meticulous stewardship by subsequent generations of students and a bit of serendipity, this cavity (still under original vacuum) has been in continuous use now for just under a decade with no measurable degradation or deterioration of any integral component of the system.

The original goal of this project was to provide an experiment in which a single atom could be trapped and strongly coupled to a high-finesse optical cavity for experimentally significant periods of time (in contrast with all prior experiments in strong-coupling cQED, in which a weak flux of atoms transited the cavity). The design of the vacuum chamber and cavity [1] was done with this purpose in mind, and the first few years of research

on the project (1999-2002) were dedicated to studying the physical properties of optical dipole trapping potentials generated within the mode of the cavity by driving fundamental longitudinal modes a few free spectral ranges away from the cQED resonance.[1].

Just prior to my joining the group, in early 2003, the Lab 11 subgroup (at the time comprised of Jason McKeever, Joseph Buck, Alex Kuzmich, Hanns-Christoph Nägerl, David Boozer and Andreea Boca) had just made a significant breakthrough in their experiment with the demonstration of “state-insensitive” trapping and cooling of a single atom within the mode of their optical cavity for greatly extended periods of time (~ 3 s) [2]. Using this technique, Jason and colleagues were able to create what they dubbed a “single-atom laser in the regime of strong coupling.” By driving a trapped atom with light propagating transverse to the axis of the cavity (in analogy to pumping a traditional laser wherein the gain medium of the laser has been reduced to its conceptual limit: one-and-the-same atom), they were able to measure manifestly non-classical photon statistics for light gathered in the cavity output mode.

Immediately following publication of this work, in October, 2003, I joined Jason in the laboratory and began helping him to adapt the “single-atom laser” technique to demonstrate efficient generation of single photons from the atom-cavity system. It was with this experiment, the details of which will be discussed much more thoroughly in Chapter 5, that I first began working on the cavity QED project.

Throughout the subsequent five years I have been involved in a variety of projects involving the same experimental apparatus and a group of fantastic collaborators. Following Jason’s graduation from Caltech, Andreea Boca and I began to work together in the lab and subsequently produced a measurement of the vacuum-Rabi spectrum for one-and-the-same atom trapped within our cavity, and an observation of what we dubbed the “Photon Blockade” effect. We also invested considerable time towards the implementation of a novel scheme for driving Raman processes inside of our optical cavity which had been developed theoretically by David Boozer. Using David’s scheme, Andreea and I were able to demonstrate motional ground state cooling of an atom trapped within our cavity.

In 2006, following the ground state cooling result, Andreea and I were joined in the laboratory by Tracy Northup, who had previously been working on the Lab 1 cavity project

(by then discontinued due to technical problems). Together, we were able to explicitly demonstrate the reversible nature of the single photon generation process that Jason and I had worked on in late 2003. After Andreea's graduation and departure for SpectroLab, Inc., Tracy and I began work on a series of projects to greatly refine our control over the degrees of freedom in our system. The motivation for these improvements was to work towards a measurement of atom-photon entanglement which ultimately proved to be extremely challenging and experimental infeasible with our current apparatus. However, this work resulted in a number of interesting new techniques and measurements which will be discussed herein.

My particular involvement in each of these projects, particularly those following the 2004 single photon generation measurements, is difficult to delineate from those of my colleagues in the lab. As a group, we tended to not subdivide the experiment into domains with which only one of us would have familiarity or control. In aiming for completeness, some of the content of this thesis overlaps in the margins with the theses of former group members. However, where relevant in each chapter, I will emphasize those innovations and improvements in the laboratory that came largely at my suggestion or as a result of my work.

1.3 Overview

This thesis will attempt to provide a complete summary of most of the work I've participated in during my time in Lab 11, with an emphasis on the more recent projects.

In Chapter 2, I will lay out a basic theoretical framework for the discussion of the cavity QED interaction, both for a two-state atom as well as for the more complicated (and applicable) case of atomic cesium. I will also present a basic description of some of the atomic physics necessary to discuss the trapping and coherent control of individual atoms within the context of our experiment and also provide an overview of the geometry, mode structure and QED parameters for Fabry-Perot optical resonators.

Chapter 3 provides a working description of the experimental apparatus, both as it currently exists in Lab 11 and during its gradual evolution as we have steadily refined our

control over the system. Here, I will describe the set of techniques we use for laser and cavity frequency stabilization, for measurement and detection of light emitted from the cavity, and for optical confinement of single atoms within the cavity mode.

Continuing from the discussion in the previous chapter, in Chapter 4, I will detail a broad set of commonly used experimental methods in our lab which have facilitated the experiments described in each of the subsequent chapters. This chapter will focus principally on a pair of techniques which we have developed for driving coherent Raman transitions between the $6S_{1/2}, F = 3, 4$ hyperfine ground states of cesium. Applications of this technique include demonstration of a novel technique for Zeeman state-specific optical pumping and cooling to the quantum ground state of motion along the cavity axis of an atom trapped inside of that cavity.

Chapter 5 contains a discussion of experiments carried out in our lab involving the generation, detection, characterization and coherent mapping of atomic quantum states onto and from photonic quantum states.

Finally, in Chapter 6 I will describe a series of measurements which characterize the atom-cavity coupling in our system. This discussion will include measurement of the signature one-atom vacuum Rabi spectrum for a single, continuously trapped atom as well as for ensemble averages over exclusively one and exclusively two atoms present in the cavity. I will also describe time-domain measurements of the vacuum Rabi nutation for a single excitation in the system.

In the accompanying appendices, I will include a variety of tables and computer code relevant to the operation of and predictive modeling of phenomena in our atom-cavity system. Appendix A provides a complete tabular listing of the dimensionless dipole matrix elements for atomic transitions within the cesium D2 line. In Appendix B, I will describe the syntax and structure of the proprietary front end programming language which David Boozer has developed and is used by us to control experimental timing with an ADWin Gold digital I/O interface. Finally, in Appendix C, I will discuss my contributions to a set of .m-file scripts commonly used in our group for modeling atom-cavity physics in the MATLAB “Quantum Optics Toolbox” suite.

Chapter 2

Theory and Formalism

The goal of this Chapter is to provide a basic theoretical understanding of the experimental results which will follow in later Chapters. We will begin by describing the rudimentary Jaynes-Cummings Hamiltonian for atom-field interactions and the types of dynamical behavior which this simple model predicts. Using these results as a foundation, we will continue by exploring the quantum dynamics of open atom-field systems in the context of the quantum mechanical master equation. In particular we will focus on how dissipation necessitates the use of an optical resonator to study the atom-field interaction. Finally, we will consider refinements to our model necessary to accommodate some of the complexities of cavity QED with real atoms and cavities. In this context, we will describe the internal energy level structure of the cesium $D2$ line so as to provide a starting point for discussions of laser cooling and trapping, state manipulation and the internal quantum dynamics of individual atoms which will follow in subsequent Chapters.

2.1 The Jaynes-Cummings Hamiltonian

2.1.1 The Hamiltonian

We begin by considering a model of the closed (i.e., non-dissipative), dipole interaction between a two-state atom and a single mode of the electromagnetic field. The atom will be assumed to exhibit two internal states, a ground state, $|g\rangle$, and excited state, $|e\rangle$, split by energy $E_A = \hbar\omega_A$ and between which dipole transitions are allowed. The field with which

we will concern ourselves is a single spatio-temporal mode with corresponding single photon energy $E_F = \hbar\omega_F$ and, in general, arbitrary photon occupation number.

The Hamiltonian operator for this system can be expressed as the sum of three terms,

$$\hat{H}_0 = \hat{H}_{atom} + \hat{H}_{field} + \hat{H}_{dipole}. \quad (2.1)$$

Here, \hat{H}_{atom} , \hat{H}_{field} are the free-atom and free-field Hamiltonians respectively, and \hat{H}_{dipole} is the interaction Hamiltonian resulting from the dipole coupling between field and atom. Substituting the well-known forms of \hat{H}_{atom} , \hat{H}_{field} and a functional expression for the dipole term, we have

$$\hat{H}_0 = \frac{1}{2}\hbar\omega_A\hat{\sigma}_z + \hbar\omega_F\left(\hat{a}^\dagger\hat{a} + \frac{1}{2}\right) - \hat{d} \cdot \hat{E}. \quad (2.2)$$

Here we have introduced the inversion Pauli operator

$$\hat{\sigma}_z = (|e\rangle\langle e| - |g\rangle\langle g|), \quad (2.3)$$

and the field raising and lowering operators

$$\hat{a}|n\rangle = \sqrt{n}|n-1\rangle \quad (2.4)$$

$$\hat{a}^\dagger|n\rangle = \sqrt{n+1}|n+1\rangle. \quad (2.5)$$

Next, we write the atomic dipole operator, \hat{d} , as the product of the scalar dipole matrix element, d , and the atomic raising and lowering operators, $\hat{\sigma}^\pm$:

$$\begin{aligned} \hat{d} &= d(|g\rangle\langle e| + |e\rangle\langle g|) \\ &= d(\hat{\sigma}_+ + \hat{\sigma}_-). \end{aligned} \quad (2.6)$$

Similarly, we can express the electric field operator, \hat{E} , using the standard formalism from second quantization theory:

$$\hat{E} = \sqrt{\frac{\hbar\omega_F}{2\epsilon_0 V_m}}\psi(\vec{r})\left(\hat{a} + \hat{a}^\dagger\right) \quad (2.7)$$

where V_m is the physical volume of the mode as defined by the boundary conditions imposed on the problem and $\psi(\vec{r})$ is a dimensionless expression which describes the variations in electric field strength as a function of atomic position, \vec{r} . Returning to Equation (2.2), we can write the dipole interaction Hamiltonian:

$$\hat{H}_{dipole} = \sqrt{\frac{\hbar d^2 \omega_F}{2\epsilon_0 V_m}} \psi(\vec{r}) (\hat{\sigma}_+ + \hat{\sigma}_-) (\hat{a} + \hat{a}^\dagger). \quad (2.8)$$

Finally, by moving into the interaction picture and making the rotating-wave approximation (*i.e.*, dropping terms which oscillate at frequency $\Delta' = (\omega_A + \omega_f)$ in favor of terms which oscillate at $\Delta = (\omega_A - \omega_F)$), we can very closely approximate the dipole Hamiltonian, again in the Schrödinger picture, as

$$\begin{aligned} \hat{H}_{dipole} &= \sqrt{\frac{\hbar d^2 \omega_F}{2\epsilon_0 V_m}} \psi(\vec{r}) (\hat{\sigma}_+ \hat{a} + \hat{\sigma}_- \hat{a}^\dagger), \\ &= \hbar g(\vec{r}) (\hat{\sigma}_+ \hat{a} + \hat{\sigma}_- \hat{a}^\dagger). \end{aligned} \quad (2.9)$$

Here, we have defined a new quantity with units of frequency,

$$\begin{aligned} g(\vec{r}) &= \sqrt{\frac{d^2 \omega_F}{2\hbar \epsilon_0 V_m}} \psi(\vec{r}) \\ &= g_0 \psi(\vec{r}). \end{aligned} \quad (2.10)$$

The total Hamiltonian is therefore:

$$\hat{H}_0 = \frac{1}{2} \hbar \omega_A \hat{\sigma}_z + \hbar \omega_F \left(\hat{a}^\dagger \hat{a} + \frac{1}{2} \right) + \hbar g(\vec{r}) (\hat{\sigma}_+ \hat{a} + \hat{\sigma}_- \hat{a}^\dagger). \quad (2.11)$$

This is the well-known Jaynes-Cummings Hamiltonian for describing atom-field interactions [3].

2.1.2 Eigenvalues and Eigenvectors

In order to solve for the eigenvectors and eigenvalues of the system, we will express \hat{H}_0 in matrix form over a set of basis states \mathbb{B}_0 composed of the tensor products between vectors

spanning the atomic ($|g\rangle, |e\rangle$) and field bases (*i.e.*, Fock states):

$$\begin{aligned}
\mathbb{B}_0 &= \mathbb{B}_{atom} \otimes \mathbb{B}_{field} \\
&= \{|g\rangle, |e\rangle\} \otimes \{|0\rangle, |1\rangle, |2\rangle, |3\rangle, \dots\} \\
&= \{|g, 0\rangle, |e, 0\rangle, |g, 1\rangle, |e, 1\rangle, |g, 2\rangle, |e, 2\rangle, \dots\}.
\end{aligned} \tag{2.12}$$

Here we have adopted the notation $|x, y\rangle \equiv |x\rangle \otimes |y\rangle$. In this basis, we can express \hat{H}_0 as partitioned matrix of the form

$$\hat{H}_0 = \begin{pmatrix} \frac{1}{2}\hbar(\omega_F - \omega_A) & 0 & 0 & \cdots & 0 \\ 0 & \hat{H}_1 & 0 & \cdots & 0 \\ 0 & 0 & \hat{H}_2 & \cdots & 0 \\ \vdots & \vdots & \vdots & \ddots & 0 \\ 0 & 0 & 0 & 0 & \hat{H}_n \end{pmatrix}. \tag{2.13}$$

The matrix element $\langle g, 0 | \hat{H}_0 | g, 0 \rangle$ is the sum of the vacuum energy of the field and the (arbitrarily-defined) energy of the atomic ground state. Each of the remaining block-diagonal elements of \hat{H}_0 are 2×2 matrices of the form:

$$\hat{H}_n = \begin{pmatrix} \hbar(n\omega_F + \frac{1}{2}(\omega_F - \omega_A)) & \hbar g(\vec{r})\sqrt{n} \\ \hbar g(\vec{r})\sqrt{n} & \hbar(n\omega_F - \frac{1}{2}(\omega_F - \omega_A)) \end{pmatrix} \tag{2.14}$$

over the basis $\{|g, n\rangle, |e, n-1\rangle\}$.

We can diagonalize these matrices to find the eigenenergies and normalized eigenstates of the system,

$$\begin{aligned}
|\pm\rangle_n &= \frac{\hbar(-\Delta \pm \sqrt{4ng(\vec{r})^2 + \Delta^2})}{\sqrt{\left|(-\hbar\Delta \pm \hbar\sqrt{4ng(\vec{r})^2 + \Delta^2})^2 + 4n\hbar^2g(\vec{r})^2\right|}} |g, n\rangle \\
&+ \frac{2\sqrt{n}\hbar g(\vec{r})}{\sqrt{\left|(-\hbar\Delta \pm \hbar\sqrt{4ng(\vec{r})^2 + \Delta^2})^2 + 4n\hbar^2g(\vec{r})^2\right|}} |e, n-1\rangle
\end{aligned} \tag{2.15}$$

with associated eigenenergies:

$$E_{n,\pm} = \hbar \left(n\omega_F \pm \frac{1}{2} \sqrt{4ng(\vec{r})^2 + \Delta^2} \right). \quad (2.16)$$

Here we have defined the atom-field detuning, $\Delta = (\omega_A - \omega_F)$.

Before moving on, it is instructive to consider the resonant case, $\omega \equiv \omega_F = \omega_A$, ($\Delta = 0$), and explore the eigenvalue spectrum and temporal dynamics of the system. Equations (2.16),(2.15) generalize to

$$E_{n,\pm} = \hbar(n\omega \pm \sqrt{n}g(\vec{r})) \quad (2.17)$$

$$|\pm\rangle_n = \frac{1}{\sqrt{2}} (|e, n-1\rangle \pm |g, n\rangle). \quad (2.18)$$

The spectrum of eigenenergies is shown in Figure 2.1 for both the coupled ($g(\vec{r}) > 0$) and uncoupled ($g(\vec{r}) = 0$) cases in order to emphasize the normal mode splitting. The states $|\pm\rangle_n$ are commonly referred to as atom-field “dressed” states.

The characteristic property of this system is the manner in which the n -th cavity Fock energy eigenstate is split into two energy eigenstates spaced by energy $E_{n,\delta} = 2\hbar\sqrt{n}g(\vec{r})$. Note that the magnitude of this normal-mode splitting is anharmonic as a function of the number of quanta of excitation in the system. For the special case $n = 1$ (i.e., for a weakly driven system where we constrain our field basis to $\{|0\rangle, |1\rangle\}$), we have $E_{1,\delta} = 2\hbar g(\vec{r})$. This particular feature, the direct result of the interaction of exactly one atom and one photon, is known as the vacuum-Rabi splitting and will be discussed in an experimental context in Chapter 6. It is also interesting to note that the eigenstates of the weakly driven system are Bell states in the basis $\{|g, 1\rangle, |e, 0\rangle\}$ - the Jaynes-Cummings interaction maximally entangles field and atom, though in our experiment practice this entanglement has proven to be inaccessible.

Finally, we will explore the temporal dynamics of the system by applying the time evolution operator,

$$\widehat{\mathcal{U}}(t, t_0 = 0) = \widehat{\mathcal{U}}_0(t) = e^{-\frac{i}{\hbar}\widehat{H}_0 t}, \quad (2.19)$$

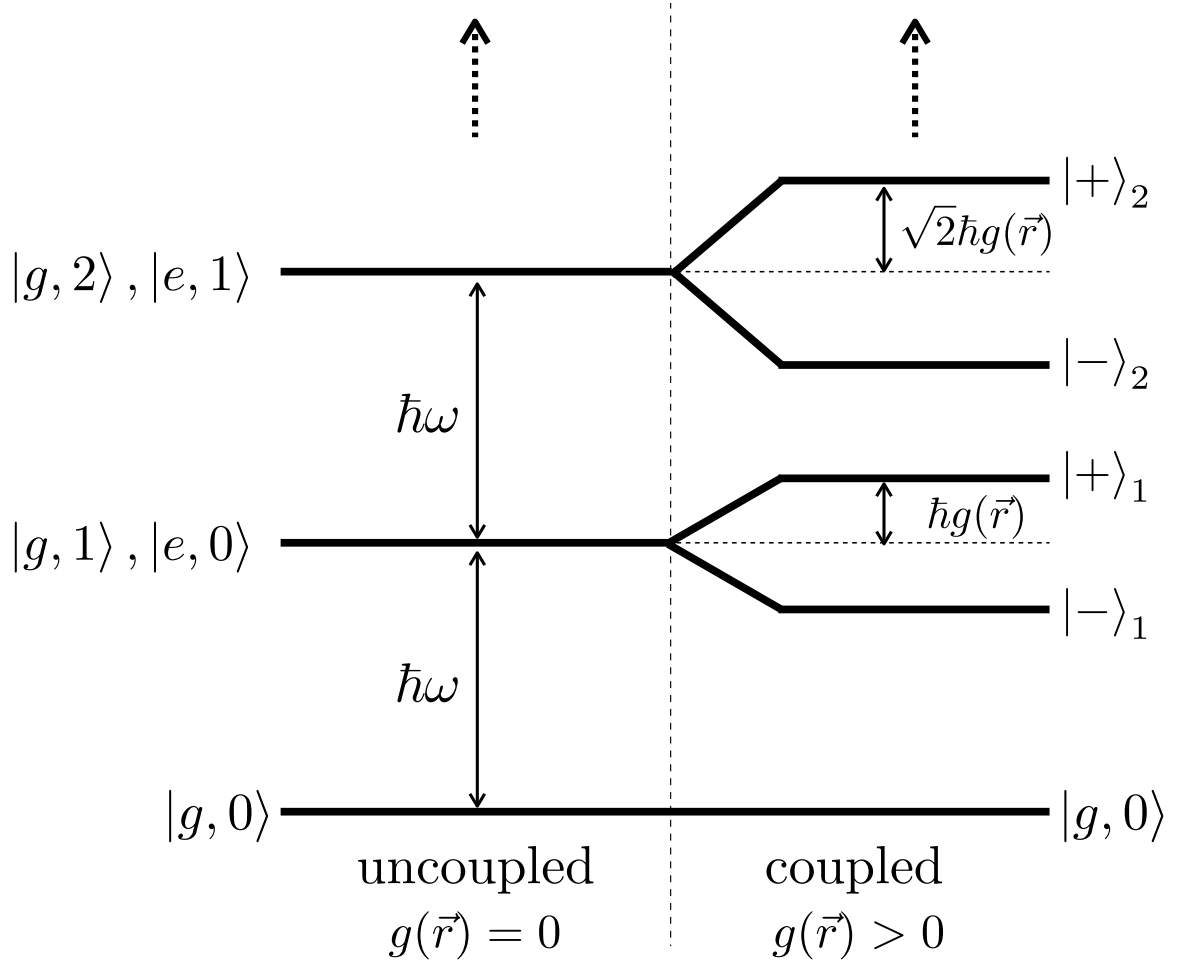


Figure 2.1: The eigenvalue spectrum for the Jaynes-Cummings Hamiltonian for both the coupled ($g(\vec{r}) > 0$) and uncoupled ($g(\vec{r}) = 0$) cases. Note the characteristic normal-mode splitting of each uncoupled state by an energy $E_{n,\delta} = 2\hbar\sqrt{n}g(\vec{r})$ in the presence of atom-field coupling.

to an arbitrary initial state of the system, $|\psi(t=0)\rangle$. We will also move into an interaction picture where the atom and field components of the total Hamiltonian are stationary and therefore do not contribute. In this frame, we can write:

$$\begin{aligned}\widehat{\mathcal{U}}_0(t) &= \exp\left[-\frac{i}{\hbar}\widehat{H}_{dipole}t\right] \\ &= \exp\left[-ig(\vec{r})t\left(\hat{\sigma}_+\hat{a} + \hat{\sigma}_-\hat{a}^\dagger\right)\right].\end{aligned}\quad (2.20)$$

It can be shown [4] by power series expansion and by grouping terms of even and odd parity that $\widehat{\mathcal{U}}_0(t)$ can be expressed as a sum over Pauli matrices in the atomic basis:

$$\begin{aligned}\widehat{\mathcal{U}}_0(t) &= \left[\cos(g(\vec{r})t\sqrt{\hat{a}^\dagger\hat{a}+1}) + \cos(g(\vec{r})t\sqrt{\hat{a}^\dagger\hat{a}})\right]\hat{I} \\ &+ \left[\cos(g(\vec{r})t\sqrt{\hat{a}^\dagger\hat{a}+1}) - \cos(g(\vec{r})t\sqrt{\hat{a}^\dagger\hat{a}})\right]\hat{\sigma}_z \\ &- i\left[\frac{\sin(g(\vec{r})t\sqrt{\hat{a}^\dagger\hat{a}+1})}{\sqrt{\hat{a}^\dagger\hat{a}+1}}\hat{a}\right]\hat{\sigma}_+ \\ &- i\left[\frac{\sin(g(\vec{r})t\sqrt{\hat{a}^\dagger\hat{a}})}{\sqrt{\hat{a}^\dagger\hat{a}}}\hat{a}^\dagger\right]\hat{\sigma}_-\end{aligned}\quad (2.21)$$

Next, we formally define an arbitrary initial state for n quanta of excitation in the system:

$$|\psi(t=0)\rangle = (\alpha|e, n-1\rangle + \beta|g, n\rangle), \quad (2.22)$$

and apply (2.21):

$$\begin{aligned}|\psi(t)\rangle &= \widehat{\mathcal{U}}_0(t)|\psi(t=0)\rangle \\ &= \left[\alpha\cos(g(\vec{r})t\sqrt{n}) - i\beta\sin(g(\vec{r})t\sqrt{n})\right]|e, n-1\rangle \\ &+ \left[-i\alpha\sin(g(\vec{r})t\sqrt{n}) + \beta\cos(g(\vec{r})t\sqrt{n})\right]|g, n\rangle.\end{aligned}\quad (2.23)$$

Not surprisingly, we find the frequency-domain normal-mode splitting, which was calculated above, corresponds to a time-domain Rabi oscillation of population between states $|e, n-1\rangle$ and $|g, n\rangle$ with the characteristic frequency $\Omega = E_{n,\delta}/\hbar = 2\sqrt{n}g(\vec{r})$.

2.2 Dissipation and the Quantum Master Equation

Evaluating the behavior of a coupled atom-field system using only the Jaynes-Cummings Hamiltonian is valuable in the sense that, although this is a very simple model, it still manages to capture the basic quantum dynamics that we are interested in studying. That said, from an experimental point of view it is not sufficient to treat the atom-field system as closed - in general, both atom and field can couple to a very large, external reservoir of states and any excitation present in the system will be dissipated over some characteristic timescales. Understanding these dissipative mechanisms will ultimately underly the importance of studying the atom-field interaction in the presence of an electromagnetic resonator and lead this discussion naturally into cavity quantum electrodynamics. This will be the topic of discussion in Subsection 2.2.1.

In Subsection 2.2.2 we will construct a formal model that treats dissipation in the particular case of an atom coupled to the mode of an electromagnetic resonator. This discussion won't rely heavily on the geometry or mode structure of the particular resonator, but rather on some simple assumptions about how the resonator dissipatively couples to its environment. There are a variety of approaches to modeling dissipation in a coupled atom-cavity system. These include the use of Wigner-Weisskopf formalism [5] and application of Fermi's golden rule [6]. However our discussion will focus on what is the most general and arguably the most useful of these methods - the quantum master equation approach. The presentation in this Section will follow the formalism presented in the excellent two-volume series by Howard Carmichael on statistical methods on quantum optics [7].

2.2.1 Why Cavity QED?

In this Subsection we will make some very simple assumptions about how dissipation manifests itself in a coupled atom-cavity system. These assumptions will be made rigorous in the next Subsection. For now we will assume that population in the atomic excited state decays exponentially and irreversibly at a rate γ from the atom into modes of the field other than that which was chosen when we constructed the Jaynes-Cummings Hamiltonian. We will also assume that the number of photons in the field to which the atom is coupled undergoes

a similar exponential and irreversible decay at characteristic rate κ . From our discussion of the Jaynes-Cummings model, and because the coherent dynamics of the atom-field interaction are the phenomena in which we are interested, it is important that we require of our experiment that g_0 should dominate all dissipative rates, *i.e.*,

$$g_0 \gg (\gamma, \kappa, T^{-1}). \quad (2.24)$$

Here, in addition to the two previously discussed rates, (γ, κ) , at which information escapes irreversibly into the environment, we have also included T , the the mean lifetime of the atom in the field (*i.e.*, the average length of time for which $g(\vec{r}) > 0$). In the limit described by (2.24), the system is said to be in the regime of strong coupling.

In order to enter this regime, we need to appropriately parameterize our system. The two most significant degrees of freedom we have are choice of atom (which determines γ and the atomic dipole moment, d) and choice of electromagnetic boundary conditions (which determine κ and the mode volume, V_m). Both choices affect $g_0(d, V_m) \propto \sqrt{d/V_m}$. In practice, novel techniques from the world of laser cooling and trapping grant us coupling lifetimes, T , which are more than eight orders of magnitude larger than g_0^{-1} . We therefore won't devote any discussion to the importance of T for the moment, but will instead return to this topic in an experimental context in Chapter 3.

Nature presents us with a finite selection of atomic systems from which to choose (man-made atom-like systems such as quantum dots [8] and Cooper-pair boxes [9, 10] offer a less scalable alternative). The work in this dissertation involves the $D2$ line in atomic cesium at 852.4 nm which provides a favorably large atomic dipole moment along with an associated transition linewidth which is proportional to the Einstein A coefficient:

$$\gamma = \frac{d^2 \omega^3}{6\pi \hbar \epsilon_0 c^3} \quad (2.25)$$

$$\gamma_{D2} = (2\pi)(2.6 \text{ MHz}). \quad (2.26)$$

A detailed discussion of the energy level structure and calculation of the dipole matrix elements for cesium follows in Subsection 2.3.1.

For purpose of discussion, we begin by considering a thought experiment in “free space QED.” We will make some very modest experimental assumptions: our electromagnetic field is comprised of a single, freely propagating photon in the form of a traveling wave with a planar wavefront, a TEM₀₀ spatial mode, collimated to a spot size $w_0 = 25 \mu\text{m}$ and exhibiting a Lorentzian temporal profile with halfwidth,

$$\Gamma \equiv \gamma_{D2}^{-1} \simeq 30 \text{ ns.} \quad (2.27)$$

This spatial wavepacket of this photon is made to intersect a two-state atom located at $(x, y, z) = 0$ and which is otherwise isolated from its environment. It is straightforward to calculate the instantaneous effective mode volume for such a photon:

$$V_m = \int_V |\psi^2(\vec{r})| d\vec{r} \quad (2.28)$$

$$= \int_{-\infty}^{\infty} \int_{-\infty}^{\infty} \int_{-\infty}^{\infty} \cos^2(2\pi z/\lambda) \frac{(c\Gamma)^4}{(z^2 + (c\Gamma)^2)^2} e^{-2\frac{x^2+y^2}{w_0}} dx dy dz, \quad (2.29)$$

Taking this integral for the relevant experimental parameters, it follows that $V_m \approx 2.8 \times 10^9 \mu\text{m}^3$ and $\kappa \approx \gamma$. Solving (2.10) using the largest atomic dipole moment, $d = 3.16ea_0$, allowed within in the cesium $D2$ manifold of transitions (see Subsection 2.3.1), we calculate the maximum single photon Rabi frequency:

$$g_0 \approx (2\pi)(87.0 \text{ kHz}), \quad (2.30)$$

which lies well outside the regime of strong coupling.

How, then, can we tailor the parameters of our free-space QED system to observe strong coupling? Temporally shortening the pulse by an amount $\Delta\Gamma$ increases g_0 by $\Delta g_0 \propto g_0(\Delta\Gamma/2\Gamma + O(\Delta\Gamma^2))$, but also increases the effective field decay rate $\Delta\kappa = (\Delta\Gamma)^{-1}$. Regardless of how short we make the pulse, we are guaranteed to approach the undesirable limit $\kappa \gg g_0$. Another avenue would be to collimate the beam to an increasingly small spot size. However, even if we assume a diffraction-limited waist, in free space we can expect at best $g_0 \sim \gamma$. It follows that for an experimentally reasonable set of assumptions about a freely propagating field, g_0 is insufficiently large to observe strong coupling between one

atom and one photon.

Studying this type of interaction in free space simply won't suffice. It is clear that we need to introduce some sort of electromagnetic boundary conditions which constrain the field to a much smaller volume of space. The experimental solution to this problem comes in the form of optical cavities - objects which define modes via a set of resonance conditions and which can be designed such that the volume subsumed by these modes is a function of the geometry of the object. What we have arrived at is the necessity of using cavity QED to study coherent atom-photon interactions. In Subsection 2.3.2 we will go into much further detail describing the properties of Fabry-Perot optical cavities and how they relate to cavity QED.

2.2.2 The Master Equation Approach

In this subsection we will formalize our discussion of dissipation of excitation from atom and field. In particular, we want to consider coupling between our system and two distinct environmental reservoirs. The first is a reservoir of harmonic oscillator states to which the cavity electromagnetic field can couple, the Hamiltonian for which is:

$$\hat{H}_R = \sum_j \hbar\omega_j \hat{r}_j^\dagger \hat{r}_j. \quad (2.31)$$

Here the operators \hat{r}_j are the raising and lowering operators for the mode associated with frequency ω_j . Likewise, we will assume that the atom is coupled to a similarly constructed reservoir of states:

$$\hat{H}_{R'} = \sum_{\vec{k},l} \hbar\omega_l \hat{r}_{\vec{k},l}^\dagger \hat{r}_{\vec{k},l}, \quad (2.32)$$

where \vec{k} indicates a sum over all possible wave vectors. Both reservoirs are assumed to be in thermal equilibrium at some temperatures, T, T' with associated mean occupation numbers, \bar{n}, \bar{n}' . In much the same way we modeled atom-field coupling when constructing the Jaynes-Cummings Hamiltonian in the rotating-wave approximation, we will assume

system-reservoir interaction Hamiltonians for each of the two reservoirs are given by:

$$\hat{H}_{SR} = \hbar \sum_j \left(\kappa^*(\omega_j) \hat{a} \hat{r}_j^\dagger + \kappa(\omega_j) \hat{a}^\dagger \hat{r}_j \right), \quad (2.33)$$

$$\hat{H}_{SR'} = \hbar \sum_{\vec{k}, l} \left(\kappa'^*(\vec{k}, \omega_l) \hat{\sigma}_- \hat{r}_{\vec{k}, l}^\dagger + \kappa'(\vec{k}, \omega_l) \hat{\sigma}_+ \hat{r}_{\vec{k}, l} \right). \quad (2.34)$$

The total atom-field-reservoir Hamiltonian is now given by:

$$\hat{H}_T = \hat{H}_0 + \hat{H}_R + \hat{H}_{SR} + \hat{H}_{R'} + \hat{H}_{SR'}, \quad (2.35)$$

where \hat{H}_0 is the Jaynes-Cummings Hamiltonian. Over the set of basis states for the system and both reservoirs, $S \otimes R \otimes R'$, we can define a global density of states operator $\hat{\chi}(t)$ and a density operator just for the atom-cavity system $\hat{\rho}(t) \equiv \text{tr}_R(\text{tr}_{R'}(\hat{\chi}(t)))$.

We now need to make two assumptions about the physical properties of the reservoirs. First, we will make what is known as the Markovian approximation which assumes that the reservoirs are “memoryless.” This can be expressed in a rigorous, mathematical sense [7]. However it will suffice here to say that it implies that excitations migrate from system to reservoir over time $\Delta t \sim 1/\omega$ and do not return to the system on larger timescales. In other words, the density operator for the atom-cavity system $\hat{\rho}(t)$ is not a function of the density operator at some earlier time, $\hat{\rho}(t')$, $t' < t$.

The second assumption is that both R and R' are at zero temperature (*i.e.*, $\bar{n} = \bar{n}' = 0$). Because we are operating at optical frequencies, this is a very reasonable assumption to make. In the frequency spectrum we are concerned with, the environment is everywhere approximately in the electromagnetic vacuum state (at room temperature the population in infrared modes of the field due to blackbody radiation are very, very small).

Using these approximations, we can use the integro-differential Schrödinger equation for $\chi(t)$ to derive the equation of motion for $\rho(t)$ in the interaction picture for a coupled

atom-cavity-reservoir system:

$$\begin{aligned} \dot{\hat{\rho}} = & -\frac{i}{\hbar} \left[\widehat{H}_0, \hat{\rho} \right] + \gamma (2\hat{\sigma}_- \hat{\rho} \hat{\sigma}_+ - \hat{\sigma}_+ \hat{\sigma}_- \hat{\rho} - \hat{\rho} \hat{\sigma}_+ \hat{\sigma}_-) \\ & + \kappa \left(2\hat{a} \hat{\rho} \hat{a}^\dagger - \hat{a}^\dagger \hat{a} \hat{\rho} - \hat{\rho} \hat{a}^\dagger \hat{a} \right). \end{aligned} \quad (2.36)$$

This is the so-called master equation for the atom-cavity system. Here, the rates γ and κ are defined as the products of the $\kappa(\omega_j)$ and $\kappa'(\vec{k}, \omega_l)$ with the densities of states $g(\omega_j)$ and $g'(\vec{k}, \omega_l)$ for both reservoirs, respectively. The interaction picture Jaynes-Cummings Hamiltonian which we will feed into the master equation is a slight generalization of (2.11):

$$\widehat{H}_0 = \hbar \Delta_A \hat{\sigma}_z + \hbar \Delta_F \hat{a}^\dagger \hat{a} + \hbar g(\vec{r}) \left(\hat{a}^\dagger \hat{\sigma}_- + \hat{a} \hat{\sigma}_+ \right) + (\varepsilon^* \hat{a} + \varepsilon \hat{a}^\dagger). \quad (2.37)$$

The final term in this expression now corresponds to an external source driving the cavity mode with a coherent state of strength ε and frequency ω_P . In order to obtain interesting, non-trivial results from this equation in the presence of dissipation, it is instructive to add this new term which deposits additional energy into the system over time. This Hamiltonian is written in a frame rotating with ω_P , such that $\Delta_A \equiv (\omega_A - \omega_P)$ and $\Delta_F \equiv (\omega_F - \omega_P)$.

I should also point out that the master equation can be re-written using the so-called superoperator formalism as:

$$\dot{\hat{\rho}} = \mathcal{L} \hat{\rho} \quad (2.38)$$

where \mathcal{L} is the Liouvillian superoperator. A superoperator is defined with respect to its action on standard quantum operators, *i.e.*,

$$\begin{aligned} \mathcal{L} \hat{O} = & -\frac{i}{\hbar} \left[\widehat{H}_0, \hat{O} \right] + \gamma \left(2\hat{\sigma}_- \hat{O} \hat{\sigma}_+ - \hat{\sigma}_+ \hat{\sigma}_- \hat{O} - \hat{O} \hat{\sigma}_+ \hat{\sigma}_- \right) \\ & + \kappa \left(2\hat{a} \hat{O} \hat{a}^\dagger - \hat{a}^\dagger \hat{a} \hat{O} - \hat{O} \hat{a}^\dagger \hat{a} \right). \end{aligned} \quad (2.39)$$

In principle, we could stop here and use this expression to model the system under numerical integration. However, there is quite a bit to be learned about the dynamics of the full, dissipative system by moving a bit farther analytically. We will proceed in the weak

driving limit (assuming that there is at most one quantum of excitation in the system at any point in time), and re-write the density matrix as the sum of two terms corresponding to the zero- and one-quantum subspaces of the system:

$$\hat{\rho}(t) \equiv \hat{\rho}_0(t) + \hat{\rho}_1(t) \quad (2.40)$$

$$\hat{\rho}_0(t) \equiv \mu(t) |g, 0\rangle \langle g, 0| \quad (2.41)$$

$$\hat{\rho}_1(t) \equiv (\alpha(t) |g, 1\rangle + \beta(t) |e, 0\rangle)(\alpha^*(t) \langle g, 1| + \beta^*(t) \langle e, 0|). \quad (2.42)$$

It is straightforward to see how the Liouvillian can be partitioned in order to write “master equations” for $\hat{\rho}_0(t)$ and $\hat{\rho}_1(t)$:

$$\mathcal{L} \equiv \mathcal{L}_0 + \mathcal{L}_1 \quad (2.43)$$

$$\mathcal{L}_0 \hat{O} \equiv \gamma \hat{\sigma}_- \hat{O} \hat{\sigma}_+ + \kappa \hat{a} \hat{O} \hat{a}^\dagger \quad (2.44)$$

$$\mathcal{L}_1 \hat{O} \equiv -\frac{i}{\hbar} [\hat{H}_0, \hat{O}] - \gamma (\hat{\sigma}_+ \hat{\sigma}_- \hat{O} + \hat{O} \hat{\sigma}_+ \hat{\sigma}_-) - \kappa (\hat{a}^\dagger \hat{a} \hat{O} + \hat{O} \hat{a}^\dagger \hat{a}) \quad (2.45)$$

such that:

$$\dot{\hat{\rho}}_0 = \mathcal{L}_0 \hat{\rho}_1 \quad (2.46)$$

$$\dot{\hat{\rho}}_1 = \mathcal{L}_1 \hat{\rho}_1. \quad (2.47)$$

Using these equations, we can write an expression for $\mu(t)$, the time-dependent population in the system’s ground state:

$$\dot{\mu}(t) = \kappa |\alpha(t)|^2 + \gamma |\beta(t)|^2. \quad (2.48)$$

Likewise, we can write a set of coupled first order differential equations for $\alpha(t)$ and $\beta(t)$:

$$\dot{\alpha}(t) = -(\kappa + i\Delta_F)\alpha(t) - ig(\vec{r})\beta(t) - i\varepsilon \quad (2.49)$$

$$\dot{\beta}(t) = -(\gamma + i\Delta_A)\beta(t) - ig(\vec{r})\alpha(t). \quad (2.50)$$

We proceed by finding the steady-state solution for the system, $\dot{\alpha}(t) = \dot{\beta}(t) = 0$:

$$\alpha_s = \frac{-i\varepsilon(\gamma + i\Delta_A)}{g^2(\vec{r}) + (\gamma + i\Delta_A)(\kappa + i\Delta_F)} \quad (2.51)$$

$$\beta_s = \frac{-g(\vec{r})\varepsilon}{(\gamma + i\Delta_A)(\kappa + i\Delta_F) + g^2(\vec{r})} \quad (2.52)$$

The physical significance of $\alpha(t)$ and $\beta(t)$ can be understood by considering the expectation values of the atomic and field number operators [6]:

$$\langle \hat{a}^\dagger \hat{a} \rangle = \text{Tr}(\hat{a}^\dagger \hat{a} \hat{\rho}) = |\alpha(t)|^2 \quad (2.53)$$

$$\langle \hat{\sigma}_z \rangle = \text{Tr}(\hat{\sigma}_z \hat{\rho}) = |\beta(t)|^2. \quad (2.54)$$

It follows that $|\alpha(t)|^2$ and $|\beta(t)|^2$ quantify the amount of excitation in the cavity mode and atom, respectively.

Given these relations, the steady-state transmission spectrum of the coupled system is given by:

$$n_s(\Delta_A, \Delta_F) = |\alpha_s \alpha_s^*| = \frac{|\varepsilon|^2 (\gamma^2 + \Delta_A^2)}{(g^2(\vec{r}) + \gamma\kappa - \Delta_A \Delta_F)^2 + (\gamma \Delta_F + \kappa \Delta_A)^2}. \quad (2.55)$$

To understand the implications of this expression, we will temporarily “turn off” the atom by setting $g(\vec{r}) = \gamma = 0$:

$$n_s(\Delta_A, \Delta_F) = \frac{|\varepsilon|^2}{\kappa^2} \frac{1}{\Delta_F^2/\kappa^2 + 1}. \quad (2.56)$$

This is the expression for a Lorentzian with halfwidth κ as plotted in Figure 2.2a. The model we have assumed for the coupling of the cavity to a reservoir corresponds to an exponential decay of the intracavity intensity at a rate κ . We will return to this expression when we introduce the classical description of Fabry-Perot electromagnetic cavities in Section 2.3.2. In this context, we will see how κ is defined in purely physical terms by the losses and geometry of the cavity. Note that we also see that on resonance, $\Delta_F = 0$, that the driving term we incorporated into the Hamiltonian produces an intracavity photon number $n = |\varepsilon|^2/\kappa^2$.

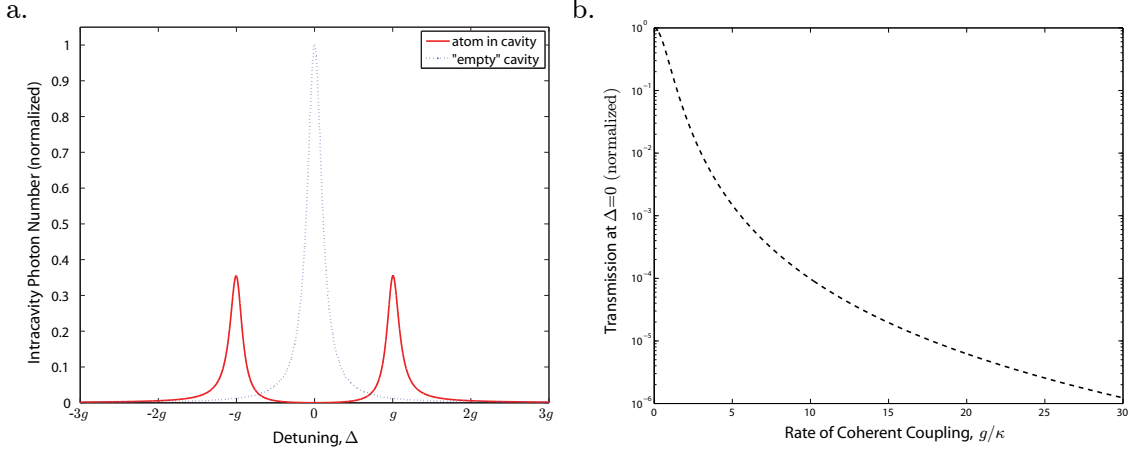


Figure 2.2: a. Normalized empty cavity photon number and vacuum Rabi splitting for an atom coupled to a cavity with the coupling parameters $(g, \gamma, \kappa) = (2\pi)(33.7, 2.6, 3.8)$ MHz with no atom-cavity detuning. These values were chosen for their particular relevance to our experiment and in order to demonstrate the characteristic spectroscopic feature of the coupled system in the strong coupling regime, $g \gg (\gamma, \kappa)$. b. Normalized intracavity photon number for a probe field driving the empty cavity resonance ($\Delta = 0$) as a function of g .

Returning to Equation (2.55), we will next consider the case of a shared atom-cavity resonance $\Delta \equiv \Delta_A = \Delta_F$:

$$n_s(\Delta) = |\alpha_s \alpha_s^*| = \frac{|\varepsilon|^2 (\gamma^2 + \Delta^2)}{(g^2(\vec{r}) + \gamma\kappa - \Delta^2)^2 + \Delta^2(\gamma + \kappa)^2}. \quad (2.57)$$

As can be seen in Figure 2.2a and Figure 2.3a, this is a two-peaked structure as a function of Δ exhibiting maxima at $\Delta = \pm g(\vec{r})$. Not surprisingly, the eigenvalue spectrum (Equation (2.16)) for the system which we calculated for the dissipation-free Jaynes-Cummings model is still valid for the master equation approach. This effect of the external reservoirs is to broaden the the two resonances by the mean of γ and κ . Figure 2.2b shows how the transmission of a resonant probe field is suppressed as a function of g . This signal will, as it turns out, be important to us in the laboratory - the presence of just one strongly coupled atom is sufficient to swing the intensity of a cavity probe signal by a few orders of magnitude.

In Figure 2.3b we return to Equation (2.55) and treat the case of a variable probe frequency, Δ_P , as well as a variable atom-cavity detuning $\Delta_{AC} = \Delta_F - \Delta_A = (\omega_F - \omega_C)$ but a fixed atomic resonance frequency. The resulting signal - a so-called “avoided crossing” - demonstrates how the vacuum Rabi splitting evolves and develops asymmetry as the atom-cavity detuning changes. This asymmetry will be important as we discuss real atoms and the differential atom-cavity detunings introduced via their complicated multilevel structures.

Finally, we will consider the coupled differential equations for $\alpha(t)$ and $\beta(t)$ ((2.49) and (2.50)) in the absence of an external probe ($\varepsilon = 0$), but under the initial conditions $(\alpha(0), \beta(0)) = (0, 1)$. We want to look at the temporal evolution of the system where the population is initially placed in a superposition of atom-cavity eigenstates (*i.e.*, entirely in the atomic excited state). Solving the differential equations for zero atom-cavity detuning, we find:

$$n(t') = |\alpha(t')\alpha^*(t')| = e^{-(\kappa+\gamma)t'} \frac{g^2(\vec{r})}{g^2(\vec{r}) - 1/4(\kappa - \gamma)^2} \sin^2 \left[\sqrt{g^2(\vec{r}) - 1/4(\kappa - \gamma)^2} t' \right] \quad (2.58)$$

The first thing we notice about this solution is that the excitation in the system decays at the arithmetic mean of κ and γ . Next, we notice that for values of $g(\vec{r}) > 1/2|(\kappa - \gamma)|$ the intracavity photon number oscillates. In the absence of damping ($\gamma = \kappa = 0$), it is not surprising that we recover Equation (2.23). In Figure 2.4a, we plot the intracavity photon number as a function of time for a system in the strong coupling regime, $g \gg (\gamma, \kappa)$. The resulting coherent oscillation at frequency $2g(\vec{r})$ is the time-domain equivalent of the vacuum Rabi splitting in the frequency-domain and corresponds to nutation between the two eigenstates of the system. Notice that it takes a half-cycle for the initial distribution of population (in the atomic excited state, $|e, 0\rangle$) to redistribute fully into the cavity, $|g, 1\rangle$. From Figure 2.4b, we can clearly see that outside of the strong coupling regime, the oscillation becomes indistinct and quickly washes out as dissipation occurs on timescales faster than and comparable to the coherence.

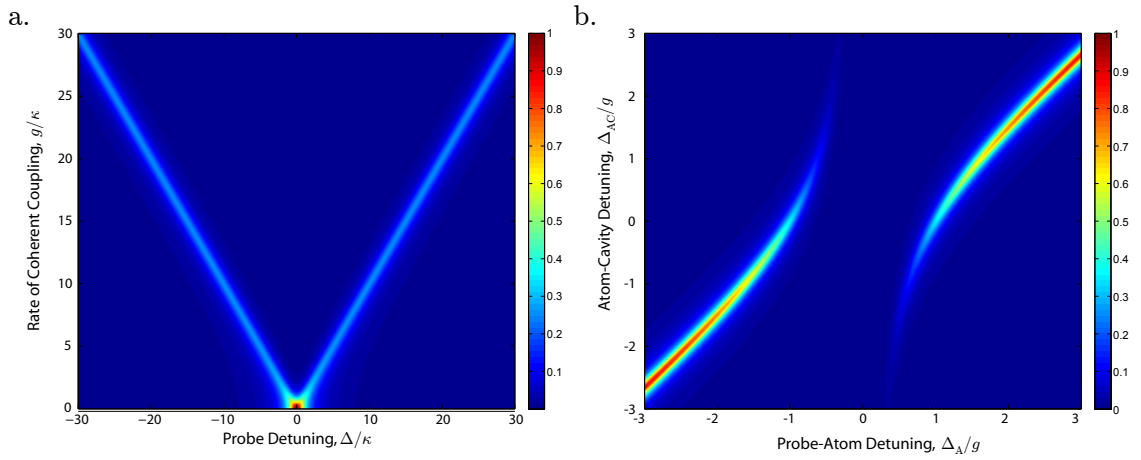


Figure 2.3: a. Normalized intracavity photon number (color) as a function of probe detuning and g , for a shared atom-cavity resonance and with $\gamma = \kappa$. As the system enters the strong couple regime, the empty cavity behavior near $g = 0$ disappears and the eigenvalue spectrum of the coupled system becomes evident. b. Normalized intracavity photon number (color) as a function of probe detuning and atom-cavity detuning, $\Delta_{AC} = (\omega_F - \omega_C)$. The coupling parameters are $(g_0, \gamma, \kappa) = (2\pi)(33.7, 2.6, 3.8)$ MHz.

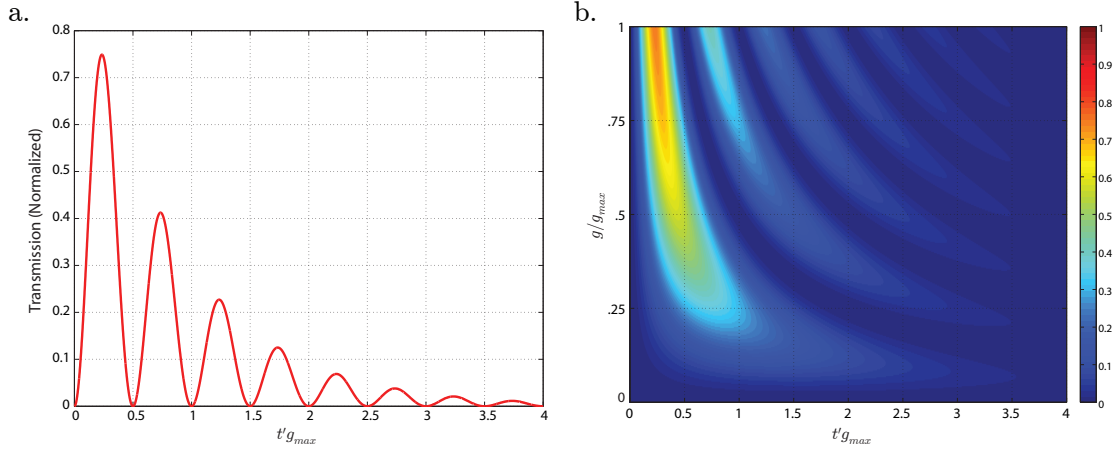


Figure 2.4: a. Vacuum Rabi nutation in the intracavity photon number for an atom coupled to a cavity with $(g_{max}, \gamma, \kappa) = (2\pi)(33.7, 2.6, 3.8)$ MHz. Note the oscillation at $2g_{max}$. b. Intracavity photon number (color) as a function of time for values of g ranging from $g_{min} = 0$ to $g_{max} = 33.7$ MHz. As the system enters the strong coupling regime, coherent vacuum Rabi nutation begins to manifest itself.

2.3 Practical Considerations

So far, this chapter has focused on the interaction of a single mode of the electromagnetic field with an idealized two-state atom. In the previous section we made an effort to model important dissipative processes and define the constraints which those processes place upon the parameterization and design of an experimental system. Ultimately, the motivation for this discussion is to provide a working model for the interactions and phenomena we measure in the laboratory, so it is necessary to make a few more refinements to the model in order to consider the use of real, multi-state atoms and optical resonators which can, in general, accommodate multiple near-degenerate modes.

2.3.1 Multi-State Atom: Cesium

The $D2$ line of cesium 133, at $\lambda_{D2} = 852.4$ nm, was used as our atomic system for each of the measurements described in this dissertation. Working with cesium in the context of cavity QED has a number of benefits. As an example, in certain spin configurations

and for coupling to light of a certain wavelength and polarization, cesium can very closely approximate a two-state atom (*i.e.*, it exhibits a number of cycling transitions - features which will be discussed more thoroughly later). In these configurations, the behavior of the coupled system is very closely approximated by the simple two-state models described in previous sections. Additionally, the dipole matrix elements for transitions within the full $D2$ manifold of transitions are relatively large and are therefore conducive to obtaining proportionately large rates of coherent coupling, g_0 . Ultimately this dissertation is as much about the atomic physics of single cesium atoms as it is about cavity QED and therefore understanding these matrix elements as well as the spectroscopic structure of cesium is extremely important. For further information about the $D1$ and $D2$ lines of cesium and elaboration on the discussion in the following subsections please see [11].

Spectroscopic Structure

Cesium 133 is an alkali metal (group I, period 6) with atomic number $Z = 55$ and atomic mass $A = 132.91$ amu. Like all alkali metals, ^{133}Cs is a hydrogen-like system in the sense that it contains a single, unpaired valence electron (here, with ground state principle quantum number $n = 6$). The spectroscopic properties of the atom are the result of transitions between the stable $6S$ ground state and higher lying excited states for this outer shell electron. The $D1$ and $D2$ lines, in particular, refer to the manifold of transitions coupling $6S$ to $6P$. Note that we have assumed standard spectroscopic notation wherein S corresponds to states exhibiting orbital angular momentum $L = 0$ and P corresponds to $L = 1$.

The $6P$ manifold of states exhibits fine structure splitting as a result of orbital spin coupling to intrinsic electron spin, $\vec{J} = \vec{L} + \vec{S}$. Here, $S = 1/2$ is the electron spin and therefore $J \in \{1/2, 3/2\}$ in the $6P$ manifold. In the $6S$ manifold there is only one possible spin-orbit configuration corresponding to $J = 1/2$. The set of energy levels with which we will concern ourselves, the $D2$ line, encompasses transitions between singlet $6S_{1/2}$ and triplet $6P_{3/2}$, where the subscript indicates the magnitude of J for those states (likewise, $D1$ corresponds to $6S_{1/2} \leftrightarrow 6P_{1/2}$).

There is further splitting of each of these fine structure levels into hyperfine structure levels which are the result of coupling to the atom's nuclear spin, \vec{I} . We can express the

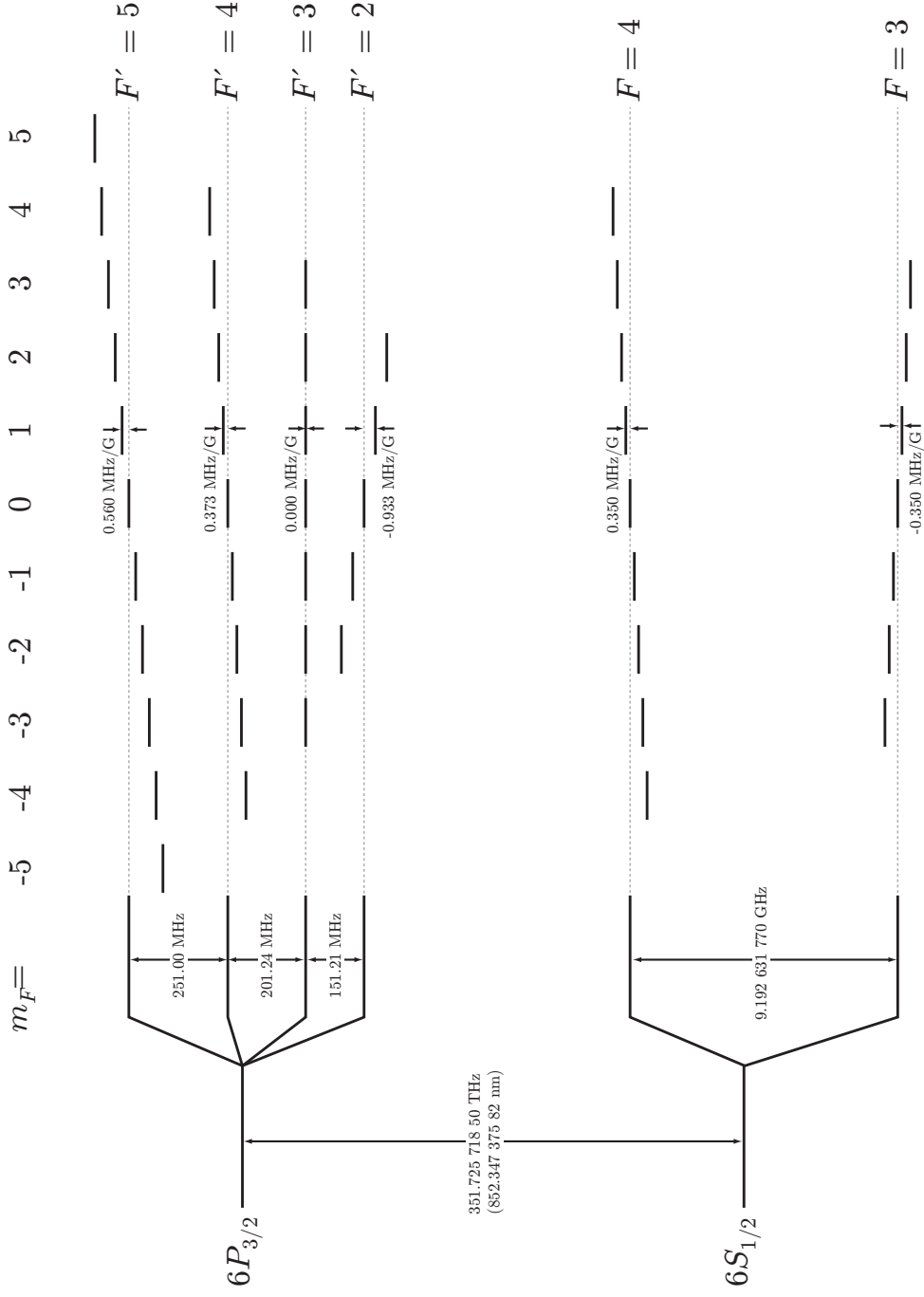


Figure 2.5: Atomic energy level diagram for cesium 133 D_2 line. Fine and hyperfine splitting numbers are taken from [11]. Detailed calculations for the weak-field Zeeman splittings depicted here are provided in Subsection 2.3.1.

total spin vector for the atom, $\vec{F} = \vec{L} + \vec{S} + \vec{I}$. For ^{133}Cs , $I = 7/2$. Therefore, $6S_{1/2}$ and $6P_{1/2}$ permit $F \in \{3, 4\}$ while $6P_{3/2}$ permits $F \in \{2, 3, 4, 5\}$. The values for gross, hyperfine and Zeeman splittings in each of the manifolds of states for the $D2$ line are depicted in Figure 2.5. In particular, note that the splitting between $(6S_{1/2}, F = 3)$ and $(6S_{1/2}, F = 4)$ is exactly $\Delta_{HF} = (2\pi)(9\,192\,631\,770 \text{ Hz})$ and is currently the international standard by which the SI unit of time is measured.

Weak-Field Zeeman Splitting

The final complication to the ^{133}Cs spectrum that we will consider here is the weak-field Zeeman splitting resulting from coupling between the total atomic spin and an uniform, externally-applied magnetic field (we need not consider the intermediate- and strong-field Zeeman effects for purposes of this discussion as our experiment never enters these parameter regimes). In general, the perturbative interaction term added to the atomic Hamiltonian to account for the Zeeman effect is:

$$\hat{H}_Z = -\hat{\mu} \cdot \vec{B}. \quad (2.59)$$

Since \vec{B} is (ideally) an experimentally-controlled parameter, it remains to calculate the atomic magnetic moment $\hat{\mu}$, which is a vector operator over the spin bases for the atom:

$$\hat{\mu} = \frac{e}{2m_e} \left(g_S \vec{S} + g_L \vec{L} + g_I \vec{I} \right), \quad (2.60)$$

where (g_S, g_L, g_I) are the electron, orbital and nuclear dimensionless magnetic moments (or “g-factors”). The values for each of these g-factors have been experimentally determined to be $(g_S = 2.002\,319\,304\,3622(15), g_L = 0.999\,995\,87, g_I = 0.000\,398\,853\,95(52))$ [12, 13]. Such precision is generally not required for any of the experimental results described herein and therefore, where necessary, we will make the approximation $(g_S = 2, g_L = 1, g_I \ll (g_S, g_L))$.

In order to evaluate $\hat{\mu}$, it is useful to use the quantum projection theorem [6] for an

arbitrary spherical vector operator \vec{A} :

$$\langle J, m'_J | \vec{A} | J, m_J \rangle = \frac{\langle J, m_J | \vec{J} \cdot \vec{A} | J, m_J \rangle}{\hbar^2 J(J+1)} \langle J, m'_J | \vec{J} | J, m_J \rangle. \quad (2.61)$$

This definition, which is a consequence of the Wigner-Eckart Theorem, is presented here in the \vec{J} angular momentum basis but holds equivalently in the \vec{F} basis.

It is useful to begin in the $\vec{J} = \vec{L} + \vec{S}$ basis and re-write $\hat{\mu}$ as:

$$\hat{\mu} = \hat{\mu}_J + \hat{\mu}_I$$

$$\mu_J = \frac{e}{2m_e} (g_L \vec{L} + g_S \vec{S}) \quad (2.62)$$

$$\mu_I = \frac{e}{2m_e} g_I \vec{I} \quad (2.63)$$

As long as the magnitude of the perturbative term added to the Hamiltonian is small on the scale of the fine structure splittings for a particular set of states with quantum numbers (J, m_J) then those states, $|J, m_J\rangle$, can be treated as “good” eigenstates of the perturbed system. Using (2.61), we can evaluate $\hat{\mu}_J$ with respect to $|J, m_J\rangle$:

$$\langle J, m'_J | \hat{\mu}_J | J, m_J \rangle = \frac{e \langle J, m'_J | g_L \vec{L} \cdot \vec{J} + g_S \vec{S} \cdot \vec{J} | J, m_J \rangle}{2m_e \hbar^2 J(J+1)} \langle J, m'_J | \vec{J} | J, m_J \rangle. \quad (2.64)$$

The matrix elements in the numerator on the right-hand side of this expression can be evaluated by using the spin identities:

$$\vec{L} \cdot \vec{J} = \frac{1}{2} (\vec{J}^2 + \vec{L}^2 - \vec{S}^2), \quad (2.65)$$

$$\vec{S} \cdot \vec{J} = \frac{1}{2} (\vec{J}^2 + \vec{S}^2 - \vec{L}^2). \quad (2.66)$$

Substituting these into (2.64), gathering terms and taking expectation values, we find:

$$\langle J, m'_J | \hat{\mu}_J | J, m_J \rangle = \frac{e \langle J, m'_J | (g_L + g_S) \vec{J}^2 + (g_L - g_S) (\vec{L}^2 - \vec{S}^2) | J, m_J \rangle}{4m_e \hbar^2 J(J+1)} \langle J, m'_J | \vec{J} | J, m_J \rangle \quad (2.67)$$

$$= \frac{e}{4m_e} \frac{(g_L + g_S) J(J+1) + (g_L - g_S) (L(L+1) - S(S+1))}{J(J+1)} \langle J, m'_J | \vec{J} | J, m_J \rangle. \quad (2.68)$$

Using the approximations for g_S, g_L :

$$\begin{aligned} \hat{\mu}_J &= \frac{e}{2m_e} \left(1 + \frac{J(J+1) - L(L+1) + S(S+1)}{2J(J+1)} \right) \vec{J} \\ &= \frac{e}{2m_e} g_J \vec{J}. \end{aligned} \quad (2.69)$$

We have written $\hat{\mu}_J$ in terms of g_J , the spin-orbit Landé g-factor.

Using the same reasoning and in the limit where $\langle H_Z \rangle$ is small compared to the hyperfine splitting energies then $|F, m_F\rangle$ are “good” eigenstates and we can perform the same procedure using the projection theorem in the \vec{F} basis for the total magnetic moment operator, $\hat{\mu}$. In analogy with (2.64):

$$\langle F, m'_F | \hat{\mu} | F, m_F \rangle = \frac{e \langle F, m'_F | g_J \vec{J} \cdot \vec{F} + g_I \vec{I} \cdot \vec{F} | F, m_F \rangle}{2m_e \hbar^2 F(F+1)} \langle F, m'_F | \vec{F} | F, m_F \rangle. \quad (2.70)$$

Using the identities

$$\vec{J} \cdot \vec{F} = \frac{1}{2} (\vec{F}^2 + \vec{J}^2 - \vec{I}^2), \quad (2.71)$$

$$\vec{I} \cdot \vec{F} = \frac{1}{2} (\vec{F}^2 + \vec{I}^2 - \vec{F}^2), \quad (2.72)$$

and taking expectation values, we find:

$$\hat{\mu} = \frac{e}{2m_e} \left(g_J \frac{F(F+1) + J(J+1) - I(I+1)}{2F(F+1)} + g_I \frac{F(F+1) - J(J+1) + I(I+1)}{2F(F+1)} \right) \vec{F}. \quad (2.73)$$

Gross State	J	F	g_J	g_F	$(2\pi)(\mu_B g_F / \hbar)$ (MHz/G)
$6S$	1/2	3	2	-1/4	-0.350
		4	2	1/4	0.350
$6P$	1/2	3	2/3	-1/12	-0.117
		4	2/3	1/12	0.117
	3/2	2	4/3	-2/3	-0.933
		3	4/3	0	0
		4	4/3	4/15	0.373
		5	4/3	2/5	0.560

Table 2.1: The values of g_J, g_F and $(2\pi)(\mu_B g_F / \hbar)$ (the frequency shift per unit magnetic field for the state $|F, m_F = 1\rangle$) calculated for each of hyperfine manifolds within the cesium D -lines.

The values of g_J for the $6S_{1/2}$ and $6P_{3/2}$ states in atomic cesium are $g_J = 2$ and $g_J = 4/3$, respectively. Both are approximately a factor of 10^4 larger than the experimentally obtained value for g_I , and therefore we will ignore the second term in the expression on the right:

$$\begin{aligned}\hat{\mu} &= \frac{e}{2m_e} g_J \frac{F(F+1) + J(J+1) - I(I+1)}{2F(F+1)} \vec{F} \\ &= \frac{e}{2m_e} g_F \vec{F}.\end{aligned}\quad (2.74)$$

We have finally arrived at an approximate expression for the total atomic spin Landé g -factor:

$$g_F = \left(1 + \frac{J(J+1) - L(L+1) + S(S+1)}{2J(J+1)}\right) \left(\frac{F(F+1) + J(J+1) - I(I+1)}{2F(F+1)}\right). \quad (2.75)$$

Finally, we will orient our coordinate system such that the quantization (\hat{z} -) axis lies along \vec{B} (*i.e.*, $\vec{B} = B_z \hat{z}$) which will allow us to evaluate the expectation value of \hat{H}_Z for

arbitrary $|F, m_F\rangle$:

$$\begin{aligned}\langle F, m_F | \hat{H}_Z | F, m_F \rangle &= \frac{e}{2m_e} g_F B_z \langle F, m_F | F_z | F, m_F \rangle \\ &= \frac{e\hbar}{2m_e} g_F B_z m_F = \mu_B g_F B_z m_F,\end{aligned}\quad (2.76)$$

where μ_B is the Bohr magneton, and fundamental constants give:

$$\frac{\mu_B}{\hbar} \simeq (2\pi)(1.399 \text{ MHz/G}). \quad (2.77)$$

The Zeeman effect shifts the state $|F, m_F\rangle$ by an amount $\Delta\omega_{F,m_F} = \mu_B g_F B_z m_F / \hbar$.

As a reference, Table 2.1 provides g_J, g_F and $(2\pi)(\mu_B g_F / \hbar)$ in units of MHz/Gauss for each of the hyperfine manifolds within the $D1$ and $D2$ lines of cesium.

Dipole Matrix Elements

In the first section of this Chapter, we defined the scalar rate of coherent coupling between atom and field (2.10). In order to quantify g_0 , we need to consider the values of the dipole matrix elements, d , for each of the cesium $|F, m_F\rangle \leftrightarrow |F', m'_F\rangle$ transitions. In this notation, unprimed quantum numbers correspond to atomic ground states in the $6S_{1/2}$ fine structure manifold and primed quantum numbers correspond to excited states in the $6P_{3/2}$ fine structure manifold. For any single transition, the expression for d which we need to evaluate is:

$$d = \langle F', m'_F | e\hat{r} | F, m_F \rangle \quad (2.78)$$

The operator \hat{r} is the spherical tensor position operator for the valence electron of cesium and is denoted with a hat to prevent confusion with the position of the atom relative to the electromagnetic field, \vec{r} .

Using the Wigner-Eckart Theorem [6, 14, 15] it is straightforward to express the matrix elements (2.78) as the product of dynamic and purely geometric terms:

$$\langle F', m'_F | e\hat{r}_q | F, m_F \rangle = \langle F' || e\hat{r} || F \rangle \langle F', m'_F | F; 1, m_F; q \rangle. \quad (2.79)$$

Here $\langle F' || e\hat{r} || F \rangle$ is the so-called reduced matrix element of the spherical tensor operator \hat{r} and q represents the index of \hat{r} in spherical coordinates. The second term on the right-hand side of this expression is called the Clebsch-Gordan coefficient, and can be represented as a Wigner 3- j symbol:

$$\langle F', m'_F | F; 1, m_F; q \rangle = (-1)^{1-F+m'_F} (2F' + 1)^{1/2} \begin{pmatrix} 1 & F & F' \\ q & m_F & -m'_F \end{pmatrix} \quad (2.80)$$

Note that the 3- j symbol is nonzero (*i.e.*, selection rules permit transitions between the two states) only when $q = (m'_F - m_F) \in \{0, \pm 1\}$ and $(F' - F) \in \{0, \pm 1\}$. Physically, q represents the angular momentum imparted to the atom by absorption or emission of a photon and the conservation rule represents the fact that photons are spin-1 systems. Specifically, $q = \pm 1$ corresponds to absorption of σ^\pm -polarized light (*i.e.*, right- and left-circularly polarized light with respect the quantization axis, \hat{z}), and $q = 0$ represents absorption of π -polarized light (*i.e.*, linearly polarized with respected to \hat{z}).

In order to simplify the reduced matrix element for the (F, m_F) basis, we must again apply the Wigner-Eckart Theorem considering $\vec{F} = \vec{J} + \vec{I}$ coupling:

$$\begin{aligned} \langle F || e\hat{r} || F' \rangle &= \langle J', I', F' | e\hat{r} | J, I, F \rangle \\ &= (-1)^{1+J+I+F'} (2J' + 1)^{1/2} (2F + 1)^{1/2} \begin{Bmatrix} 1 & J & J' \\ I & F' & F \end{Bmatrix} \langle J' || e\hat{r} || J \rangle. \end{aligned} \quad (2.81)$$

This result is expressed in terms of a Wigner 6- j symbol and is the nontrivial consequence of multipartite addition of angular momentum [15]. For reference, in Appendix C the normalized geometric portions of the matrix elements $\langle F', m'_F | e\hat{r} | F, m_F \rangle$ are calculated, in units of $\langle J' || e\hat{r} || J \rangle$, using (2.80) and (2.81) for each allowed transition within the $D2$ line.

It should be noted that for the transitions $|4, \pm 4\rangle \leftrightarrow |5', \pm 5'\rangle$, corresponding to absorption and emission of σ^\pm -polarized photons, Appendix C indicates

$$\left(\frac{\langle 5', \pm 5' | e\hat{r} | 4, \pm 4' \rangle}{\langle 6P_{3/2} || e\hat{r} || 6S_{1/2} \rangle} \right)^2 = 1. \quad (2.82)$$

Effectively, the branching ratio for decay of the $(6P_{3/2}, F' = 5)$ edge states to the $(6S_{1/2}, F' =$

4) edge states is unity. Population in these states, coupled to light of the appropriate polarization, remains there and the transition functions as an effective two-state atom with respect to that electromagnetic field. These particular transitions are “closed” or “cycling” transitions and exhibit the largest possible dipole moment, d , of any transition within the $D2$ manifold.

Finally, in order to ascribe a properly dimensioned value to each total matrix element, we must consider the reduced matrix element $\langle J' || e\hat{r} || J \rangle$. As our experimental interest is limited to the $D2$ line, we are especially concerned with $\mathcal{D} \equiv \langle 6S_{1/2} || e\hat{r} || 6P_{3/2} \rangle$. We need not apply another iteration of the Wigner-Eckart Theorem, however. This quantity may be calculated using the expression for the excited state lifetime, γ_{D2} , for the $6P_{3/2}$ manifold of states [16]:

$$\mathcal{D} = \sqrt{\frac{6\pi\hbar\epsilon_0\gamma_{D2}c^3}{\omega^3}} \quad (2.83)$$

$$\simeq 3.16ea_0, \quad (2.84)$$

Here, $\gamma_{D2} = (2\pi)(2.6 \text{ MHz})$ is the free-space atomic lifetime (in the cavity the lifetime $\tau = 1/2\gamma_{D2}$) discussed in the previous section and a_0 is the Bohr radius. An alternative definition can be framed in terms of the atomic saturation intensity:

$$\mathcal{D} = \sqrt{\frac{\hbar^2 c \epsilon_0 \gamma_{D2}^2}{I_{sat}}}, \quad (2.85)$$

where I_{sat} is defined as:

$$I_{sat} = \frac{\hbar\omega^3\gamma_{D2}}{6\pi c^2} \quad (2.86)$$

$$= 1.102 \text{ mW/cm}^2. \quad (2.87)$$

This result, the numeric value of \mathcal{D} , when multiplied by the dimensionless, geometric matrix elements listed in Appendix C, provides us the full dipole matrix element d for each transition. We are now able to determine the scalar coupling rate g_0 , transition-by-transition, for a given cavity geometry.

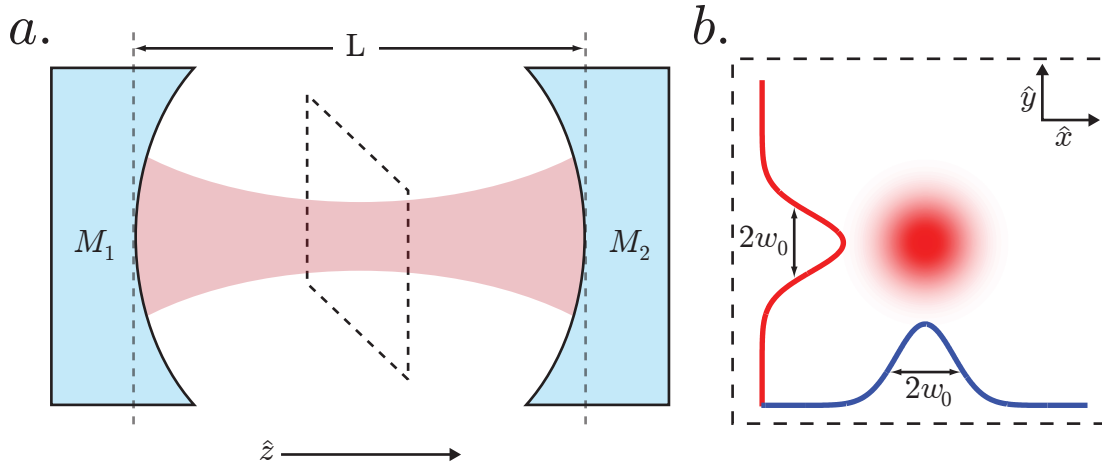


Figure 2.6: **a.** Schematic diagram of a Fabry-Perot optical cavity. Two cylindrical, concave mirrors (M_1, M_2) aligned such that they are concentric. The mirrors are spaced by a distance L , as measured from the center of one mirror surface to the other. **b.** The \hat{z} -axis is specified along the length of the cavity, while a cross section of the fundamental (TEM_{00}) mode of the cavity field (taken at $z = 0$, in the \hat{x}, \hat{y} -plane) exhibits a waist spot size w_0 .

2.3.2 Fabry-Perot Resonators

In Section 2.2 we arrived at the conclusion that in order to study coherent atom-field dynamics, placing the atom in the mode of an optical cavity was extremely beneficial. The effect of the cavity is to significantly constrain the volume of the mode, thereby commensurately increasing the maximum single photon Rabi frequency, g_0 . There are a wide variety of optical resonator geometries which can be used, in principle, to enhance the coupling between an atom and the electromagnetic field but only a few of these geometries have been pursued experimentally in the context of cavity QED. The focus of this discussion will be the type of cavity which was used throughout these experiments and is perhaps the most intuitive to understand - the Fabry-Perot resonator.

Fabry-Perot Design

A Fabry-Perot cavity (Figure 2.6a) is the simplest stable optical resonator. It consists of two spherical concave mirrors, (M_1, M_2), with radii of curvature (ρ_1, ρ_2), respectively. The

mirrors are placed side-by-side such that the two reflective surfaces face each other and their cylindrical substrates are concentric along the \hat{z} -axis. The center of the reflective surfaces for each of the two mirrors is placed at $z = (z_1, z_2)$, respectively, and the distance between them is

$$L = z_2 - z_1. \quad (2.88)$$

In general, this dissertation will concern itself with symmetric Faby-Perots, wherein $\rho = \rho_1 = \rho_2$ and $z_2 = -z_1 = L/2$.

Mode Structure

In the planar limit ($\rho \rightarrow \infty$), an optical field with associated wavelength λ and angular frequency $\omega = 2\pi c/\lambda$ receives a propagation phase shift,

$$\phi(\omega) = \frac{2\omega L}{c} \quad (2.89)$$

as it travels from M_1 to M_2 and back. Here we have simplified the problem to ignore small phase shifts imparted to the light due to finite interaction with the mirror coatings. A particular set of optical frequencies

$$\omega_n = n \frac{\pi c}{L}, \quad (2.90)$$

where n is a non-zero integer, satisfy the cavity resonance condition:

$$\phi(\omega_n) = 2\pi n. \quad (2.91)$$

At these specific frequencies the field returning from M_2 folds neatly back upon itself and the cavity boundary conditions support a standing wave consisting of n half-wavelengths with field nodes at the mirror surfaces (assuming no penetration of the field into the optical coating). These fundamental mode frequencies are spaced from each other by the free

spectral range (FSR),

$$\Delta\nu_{FSR} = \frac{(\omega_{n+1} - \omega_n)}{2\pi} = \frac{c}{2L}. \quad (2.92)$$

Determining the mode structure of resonators constructed from non-planar spherical mirrors, however, requires a more general formalism. Importantly, the geometry of the mirrors establishes boundary conditions dictating that the wavefront of any circulating light must be spherical with wavefront radius of curvature ρ at the mirror surfaces. It can be shown that for weakly divergent circulating beams, the most general solution to the paraxial wave equations for a field with these boundary conditions ([17], Chapter 16) is a TEM_{lm} Hermite-Gaussian beam (expressed here in the form of a scalar wave amplitude, ψ):

$$\begin{aligned} \psi(x, y, z) = & \left(\frac{e^{2i(2l+1)\xi(z)}}{2^l l!} \right)^{1/2} \left(\frac{e^{2i(2m+1)\xi(z)}}{2^m m!} \right)^{1/2} H_l \left(\frac{\sqrt{2}x}{w(z)} \right) H_m \left(\frac{\sqrt{2}y}{w(z)} \right) \\ & \times \exp \left[-i \left(\frac{2\pi z}{\lambda} + \frac{\pi(x^2 + y^2)}{R(z)\lambda} \right) - \frac{x^2 + y^2}{w^2(z)} \right]. \end{aligned} \quad (2.93)$$

Here, $\xi(z)$ is the Gouy phase shift term, $w(z)$ is the beam spot size, $R(z)$ is the wavefront radius of curvature, and H_j is the j th order Hermite polynomial. The first three of these terms are defined relative to the Rayleigh range, z_R , for our symmetric cavity:

$$z_R = \frac{L}{2} \sqrt{\frac{(2\rho - L)}{L}}. \quad (2.94)$$

The Gouy phase shift, resulting whenever a beam passes through a focal region, is given by:

$$\xi(z) = \arctan \left(\frac{z}{z_R} \right). \quad (2.95)$$

The local spot size, $w(z)$, is:

$$w^2(z) = w_0^2 \left[1 + \left(\frac{z}{z_R} \right)^2 \right] \quad (2.96)$$

where w_0 is the spot size of the beam measured at the waist ($z = 0$):

$$w_0^2 = \frac{cL}{\omega} \sqrt{\frac{(2\rho - L)}{L}}. \quad (2.97)$$

Finally, the radius of curvature of the wavefront at z is:

$$R(z) = z + \frac{z_R^2}{z}. \quad (2.98)$$

Rather than anticipating frequency modes which satisfy the simple planar round-trip phase condition (2.91), we must consider a new round-trip phase which accounts for the Gouy phase shifts present in (2.93):

$$\tilde{\phi}(\omega) = \frac{2\omega L}{c} - 2(l + m + 1)(\xi(L/2) - \xi(-L/2)) \quad (2.99)$$

$$= \frac{2\omega L}{c} - 2(l + m + 1) \arccos \left[1 - \frac{L}{\rho} \right]. \quad (2.100)$$

The resonance condition $\tilde{\phi}(\omega) = 2\pi n$ implies resonant modes at frequencies:

$$\omega_{l,m,n} = \frac{c}{2L} \left[2\pi n + 2(l + m + 1) \arccos \left[1 - \frac{L}{\rho} \right] \right]. \quad (2.101)$$

As with the planar cavity, the $(n + 1)$ th TEM_{lm} mode is spaced from the n th by the free spectral range, $\Delta\nu_{FSR}$. Importantly, the fundamental (TEM_{00}) mode frequencies (Figure 2.6b) are identical to those in the planar case with the addition of a (generally) small term resulting from the Gouy effect.

Classical Fields and Finesse

Now that we have some understanding of the spatial and temporal resonant mode structure of a symmetric Fabry-Perot resonator, it is important that we also understand how classical optical fields propagate in a lossy cavity. It is useful to decompose the field in and around the cavity into four components (Figure 2.7):

- E_{inc} , the field incident on M_1 ,

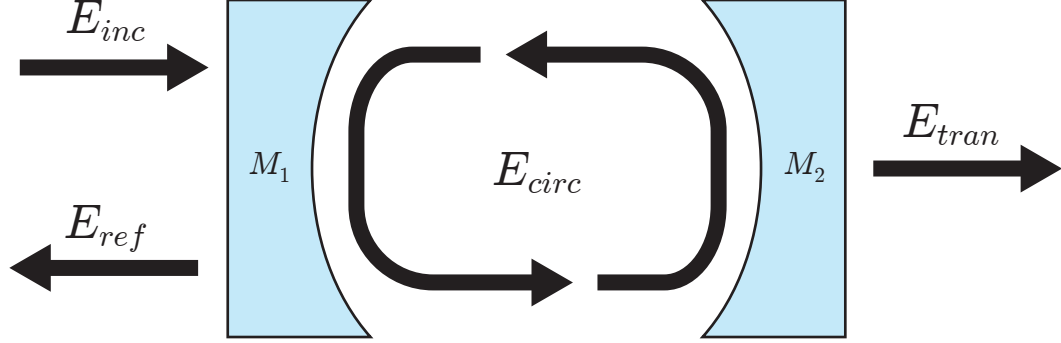


Figure 2.7: The electric fields coupled to and from a Fabry-Perot resonator. We can decompose these fields into four distinct components.

- E_{ref} , the field reflected from M_1 ,
- E_{circ} , the field circulating between M_1 and M_2 , and
- E_{tran} , the field transmitted through M_2 .

In order for this analysis to be valuable, we must ascribe some losses to our mirrors. We will assume that each mirror is characterized by a transmission coefficient t and a reflection coefficient r . Using these coefficients, we can express each of E_{ref} , E_{circ} , E_{tran} in terms of E_{inc} :

$$E_{ref} = E_{inc} \left[r - rt^2 e^{2i\omega L/c} \sum_{j=0}^{\infty} \left(r^2 e^{2i\omega L/c} \right)^j \right] \quad (2.102)$$

$$E_{circ} = itE_{inc} (e^{i\omega z/c} + re^{-i\omega z/c}) \left[\sum_{j=0}^{\infty} \left(r^2 e^{-2i\omega L/c} \right)^j \right] \quad (2.103)$$

$$E_{tran} = -E_{inc} t^2 e^{i\omega L/c} \sum_{j=0}^{\infty} \left(r^2 e^{2i\omega L/c} \right)^j. \quad (2.104)$$

On an experimental level, fields are often not very practical quantities. It is more instructive to reframe these expressions in terms of intensities, and, in particular, the fraction of the

incident intensity reflected, transmitted and circulating in the cavity:

$$\frac{I_{ref}}{I_{inc}} = \left| \frac{E_{circ}^2}{E_{inc}^2} \right| = \frac{R[(1 - (R + T))^2 + 4(R + T)\sin^2(\omega L/c)]}{(1 - R)^2 + 4R\sin^2(\omega L/c)}, \quad (2.105)$$

$$\frac{I_{circ}}{I_{inc}} = \left| \frac{E_{circ}^2}{E_{inc}^2} \right| = \frac{T(1 + R + 2\sqrt{R}\cos(2\omega z/c))}{(1 - R)^2 + 4R\sin^2(\omega L/c)}, \quad (2.106)$$

$$\frac{I_{tran}}{I_{inc}} = \left| \frac{E_{tran}^2}{E_{inc}^2} \right| = \frac{T^2}{(1 - R)^2 + 4R\sin^2(\omega L/c)}. \quad (2.107)$$

To arrive at these expressions, we have used the Taylor expansion for $(1 - x)^{-1}$ and the definitions of the mirror reflectivity, $R = |r|^2$, and transmissivity, $T = |t|^2$. When the loss due to scattering and absorption from the mirror surfaces becomes comparable to the loss due to transmission through the mirror (generally, in the limit $R \approx 1$ unless you had a really, really bad coating run) it is important to consider these losses in the above set of equations. We can redefine the total reflectivity using conservation laws as:

$$R = 1 - (T + l), \quad (2.108)$$

where $l = S + A$ is the total non-transmissive (*i.e.*, scattering, S , and absorption, A) loss per mirror. In the limit $R \approx 1$, we find:

$$\frac{I_{ref}}{I_{inc}} = \left| \frac{E_{circ}^2}{E_{inc}^2} \right| = \frac{(l^2 + 4\sin^2(\omega L/c))}{(T + l)^2 + 4\sin^2(\omega L/c)}, \quad (2.109)$$

$$\frac{I_{circ}}{I_{inc}} = \left| \frac{E_{circ}^2}{E_{inc}^2} \right| = \frac{4T\sin^2(\omega z/c)}{(T + l)^2 + 4\sin^2(\omega L/c)}, \quad (2.110)$$

$$\frac{I_{tran}}{I_{inc}} = \left| \frac{E_{tran}^2}{E_{inc}^2} \right| = \frac{T^2}{(T + l)^2 + 4\sin^2(\omega L/c)}. \quad (2.111)$$

Equation (2.111) is a particularly useful expression. It provides the transmission spectrum, \mathcal{T} , for a cavity driven by a variable detuning probe beam. In a more familiar form,

$$\mathcal{T} = \left(\frac{T}{T + l} \right)^2 \frac{1}{1 + 4/(T + l)^2 \sin^2(\omega L/c)}. \quad (2.112)$$

Near angular frequencies, ω_n , which satisfy the resonance condition (2.91), \mathcal{T} exhibits a Lorentzian lineshape:

$$\mathcal{T} = \left(\frac{T}{T+l} \right)^2 \frac{1}{1 + \left[\frac{2L}{c(T+l)} \right]^2 (\omega - \omega_n)^2}. \quad (2.113)$$

with halfwidth:

$$\kappa = \frac{c}{2L} (T+l). \quad (2.114)$$

This is the same rate κ which was discussed in 2.2 and corresponds physically to the quantum mechanical field decay which we described earlier. The prefactor of \mathcal{T} is the maximum transmission coefficient,

$$\mathcal{T}_{max} = \left(\frac{T}{T+l} \right)^2, \quad (2.115)$$

and is a measure of the fraction of the power transmitted through the cavity as opposed to dissipated in the mirror surfaces.

A final, particularly useful quantity is what is known as the cavity finesse, given as the ratio of the free spectral range to the fullwidth:

$$\mathcal{F} \equiv \frac{\Delta\omega_{FSR}}{2\kappa} \quad (2.116)$$

$$= \frac{\pi}{T+l}. \quad (2.117)$$

The finesse can be interpreted physically as the number of round trip interactions with the cavity mirrors a circulating field undergoes before its intensity has decayed by a factor of e^{-1} . Not surprisingly then, the finesse tends to appear in situations where the effect of interest scales in proportion to the number of interactions the field makes with mirrors. For instance, the ratio of peak circulating power to input power (the cavity build-up factor, \mathcal{B})

can be expressed in terms of the finesse and the maximum, on-resonance transmission:

$$\mathcal{B} \equiv \max \left(\frac{P_{circ}}{P_{inc}} \right) = 4\sqrt{\mathcal{T}_{max}} \frac{\mathcal{F}}{\pi}. \quad (2.118)$$

Inside the cavity, the injected intensity is increased by a factor of the finesse and reduced by a factor of the the square-root of the maximum cavity transmission. For very high finesse systems with low losses, l , this build up can be quite significant. In the following subsection, we will explore another effect which scales with the finesse.

Polarization and Birefringence

An important aspect of any real Fabry-Perot cavity which we have not yet considered is that the mirrors can simultaneously support two, orthogonal polarization eigenmodes in the (x, y) -plane. In an idealized model, both mirrors exhibit perfect radial symmetry and the single, physical Fabry-Perot resonator behaves effectively as two, decoupled resonators, both exhibiting the same spectral characteristics with respect to the (degenerate) polarization modes.

Experimentally, it is difficult to realize this situation. If a mirror, M_1 , is held in a way which is anisotropic with respect to its rotational geometry, this defect can break the symmetry of the (x, y) -plane by inducing a small amount of stress preferentially along one direction, l_+ , on the mirror's surface. This stress does not appreciably alter the geometry of the mirror but it does, however, induce a very small optical phase shift, φ , upon reflection of an incident field linearly polarized along \hat{l}_+ (why this is the case will be discussed in Chapter 3 when we describe the optical coatings of real mirrors).

If this mirror is configured to form a cavity with another mirror, M_2 , which is similarly stressed along \hat{l}_+ , these small phase shifts will build up in proportion to the cavity finesse. To see this, we generalize Equation (2.104) to two polarization eigenmodes in the l_{\pm} basis:

$$\begin{pmatrix} E_{tran}^+ \\ E_{tran}^- \end{pmatrix} = -t^2 e^{-i\omega L/c} \sum_{j=0}^{\infty} \left[\left(r^2 e^{2i\omega L/c} \right) \begin{pmatrix} e^{-2i\varphi} & 0 \\ 0 & 1 \end{pmatrix} \right]^j \begin{pmatrix} E_{inc}^+ \\ E_{inc}^- \end{pmatrix}. \quad (2.119)$$

After a bit of algebra, and under the assumption we are driving with linearly polarized light

along either \hat{l}_{\pm} , we arrive at:

$$\frac{E_{tran}^+}{E_{inc}^+} = \left[\frac{t^2 e^{-i\omega L/c}}{1 - r^2 e^{2i(\omega L/c - \varphi)}} \right] \quad \text{or,} \quad (2.120)$$

$$\frac{E_{tran}^-}{E_{inc}^-} = \left[\frac{t^2 e^{-i\omega L/c}}{1 - r^2 e^{2i\omega L/c}} \right]. \quad (2.121)$$

In terms of intensities, we have two, orthogonally polarized eigenmodes with respective lineshapes:

$$\mathcal{T}^+ = \mathcal{T}_{max} \frac{1}{1 + 4/(T+l)^2 \sin^2(\omega L/c - \varphi)}, \quad (2.122)$$

$$\mathcal{T}^- = \mathcal{T}_{max} \frac{1}{1 + 4/(T+l)^2 \sin^2(\omega L/c)}. \quad (2.123)$$

Note that \mathcal{T}^{\pm} have different resonance conditions for the n th longitudinal mode:

$$\omega^+ = \frac{2n\pi c}{L} + \frac{c\varphi}{L} \quad \text{and} \quad \omega^- = \frac{2n\pi c}{L}. \quad (2.124)$$

The frequency spacing between these modes, as a fraction of the cavity linewidth, is therefore:

$$\frac{\Delta\omega^{\pm}}{\kappa} = \frac{c\varphi}{L\kappa} = \frac{2}{\pi} \mathcal{F}\varphi. \quad (2.125)$$

The effect of the cavity is to enhance what is, by itself, a small single pass phase shift by a factor of the finesse. For very high finesse cavities, even a small anisotropy in the stress along the mirrors can result in an experimentally significant frequency splitting between the two polarization eigenmodes. In the context of cavity QED, we must adjust our model to treat the case of an atom coupled to two cavities, each of which has a unique atom-cavity detuning and support for only one linear polarization.

The other significance of this effect is that it requires us to treat the cavity as a birefringent optical element, exhibiting “fast” and “slow” optical axes (referred to as \hat{l}_{\pm} , above). While we will consistently orient our coordinate frame such that the longitudinal axis of the cavity lies along \hat{z} (*i.e.*, for purposes of atomic spin projection), cavity birefringence breaks

the symmetry of the \hat{x} - and \hat{y} -axes, which must be defined with respect to \hat{l}_\pm .

We should briefly mention that although we have assumed here that the birefringent axes of both mirrors coincide with \hat{l}_\pm , there is no physical reason why this is necessarily the case. In fact it can be shown with a good deal of simple algebra (or a bit more gracefully using quaternion algebra) that regardless of how the linear birefringent axes of the mirrors are oriented with respect to each other we can still define a single, overall set of birefringent axes for the system. The results of this analysis are valid, regardless.

Fabry-Perot Cavity QED

Finally we return to cavity QED, now in the context of the above discussion of Fabry-Perot resonators. Consider a single atom located at \vec{r} with respect to the center of the cavity. We can, in principle, observe atom-field coupling for any Hermite-Gaussian ($\text{TEM}_{l,m}$) mode of our choosing so long as the cavity supports that mode with only a small detuning from atomic resonance [18]. In practice, the additional spatial transverse mode structure associated with higher-order Gaussian beams adds unwanted complexity to the system and will be completely avoided experimentally. We will work only with the fundamental (TEM_{00}) mode.

The Mode Volume

Combining equations (2.10) and (2.93), the rate of coherent coupling for this atom is given by:

$$g(x, y, z) = \sqrt{\frac{d^2\omega}{2\hbar\epsilon_0 V_m}} \exp\left[-i\frac{\omega z}{c} + \frac{x^2 + y^2}{w_0^2}\right]. \quad (2.126)$$

It should be noted that we have neglected transverse phase shifts due to the local wavefront curvature and the variations in spot size as a function of z by assuming that the cavity is near-planar, $\rho \gg L$. Also, the boundary conditions dictate that $\psi(x, y, \pm L/2) = 0$. It follows that for even-parity frequency modes ($\omega_{2q} : q \in \mathbb{Z}$), $g(\vec{r})$ varies as $\sin[\omega z/c]$ whereas for odd-parity modes ($\omega_{2q+1} : q \in \mathbb{Z}$) the field goes like $\cos[\omega z/c]$.

Calculating the mode volume for the cavity is straightforward:

$$\begin{aligned}
V_m &= \int_{\mathcal{V}} |\psi(\vec{r})|^2 d\vec{r} \\
&= \int_{-L/2}^{+L/2} \int_{-\infty}^{\infty} \int_{-\infty}^{\infty} \cos^2[\omega z/c] \exp\left[-2\frac{x^2+y^2}{w(z)^2}\right] dx dy dz \\
&= \frac{\pi w_0^2 L}{4} = \frac{\pi c}{4\omega} \sqrt{L^3(2\rho - L)}.
\end{aligned} \tag{2.127}$$

We are now able to express g_0 in terms of cavity parameters:

$$g_0 = \sqrt{\frac{2d^2\omega^2}{\pi\hbar c\epsilon_0}} \frac{1}{\sqrt[4]{L^3(2\rho - L)}}. \tag{2.128}$$

Note that $g_0 \propto L^{-3/4}$ in the planar cavity limit (in comparison with the cavity linewidth, $\kappa \propto L^{-1}$). Simply shortening the cavity length for mirrors of a given finesse will approach the undesirable limit $\kappa \gg g_0$. Fortunately, the cavity finesse is also a free parameter. By using mirrors with extremely low transmission and loss coefficients we can still approach the cavity strong coupling criterion $g_0 \gg \kappa$ by requiring:

$$\begin{aligned}
\left(\frac{\kappa}{g_0}\right)^2 &= \frac{\pi^2}{\mathcal{F}^2} \sqrt{\frac{(2\rho - L)}{L}} \left(\frac{\pi c^3 \epsilon_0 \hbar}{8d^2 \omega^2}\right) \\
&= \frac{\omega \pi^2}{24\gamma \mathcal{F}^2} \sqrt{\frac{(2\rho - L)}{L}} \ll 1.
\end{aligned} \tag{2.129}$$

Here we have made use of equation (2.25).

We can undertake a similar analysis for the other strong coupling criterion, $g_0 \gg \gamma$:

$$\begin{aligned}
\left(\frac{\gamma}{g_0}\right)^2 &= \sqrt{L^3(2\rho - L)} \left(\frac{\pi c \epsilon_0 \hbar}{2d^2 \omega^2}\right) \gamma^2 \\
&= \frac{\gamma \omega}{12c^2} \sqrt{L^3(2\rho - L)} \ll 1.
\end{aligned} \tag{2.130}$$

Expressing the two strong coupling criteria in this way alludes to an interesting physical interpretation of two parameters - the critical photon (n_0) and critical atom (N_0) numbers.

Critical Parameters and Strong Coupling

The critical photon number n_0 is the number of photons present in the cavity necessary to saturate the response of the atom. This occurs when the circulating intensity, I_{circ} , of an n -photon intracavity field, $|n\rangle$, reaches the atomic saturation parameter, I_{sat} . From equations (2.7) and (2.86), we find:

$$I_{circ} \equiv \frac{\epsilon_0}{2c} \langle n | E_{circ}^2 | n \rangle = \frac{n\hbar\omega^2}{\pi} \frac{1}{\sqrt{L^3(2\rho - L)}} \quad (2.131)$$

$$\begin{aligned} n_0 &\equiv \frac{\pi I_{sat}}{\hbar\omega^2} \sqrt{L^3(2\rho - L)} \\ &= \frac{\gamma\omega}{6c^2} \sqrt{L^3(2\rho - L)} = \frac{\gamma^2}{2g_0^2} \end{aligned} \quad (2.132)$$

Comparing this result with (2.129), the strong coupling criterion $g_0 \gg \gamma$ evidently corresponds to $n_0 \ll 1/2$. In physical terms, a strongly coupled atom-cavity system is one in which much less than “half” of a photon is necessary to appreciably affect the dynamics of the system.

Similarly, we can define a critical atom number, N_0 , which corresponds to the number of intracavity atoms necessary to significantly alter the field state to which they are coupled. While we won’t explore the theory of N-atom cavity QED in any detail here, the analogous model is known as the Tavis-Cummings (as opposed to Jaynes-Cummings) Hamiltonian [19] and the dressed state splitting scales like $g_0\sqrt{N}$ in the presence of a single, shared excitation. In order for the atom to coherently affect the field, this splitting should be greater than or equal to the square root of the product of the dissipative rates in the picture, $\sqrt{\gamma\kappa}$ (using a simple argument based on our ability to spectroscopically resolve the dressed state splitting in spite of broadening due to dissipation). Therefore, we estimate:

$$\sqrt{N_0}g_0 = \sqrt{\gamma\kappa}, \quad \Rightarrow \quad N_0 = \frac{\gamma\kappa}{g_0^2}. \quad (2.133)$$

Historically, N_0 is defined in the context of optical bistability theory [20], and is modified

by a factor of 2 from our estimate:

$$N_0 = \frac{2\gamma\kappa}{g_0^2} \tag{2.134}$$

$$= \frac{\omega\pi}{12\mathcal{F}_c} \sqrt{L(2\rho - L)}. \tag{2.135}$$

It follows from equation (2.130) that the strong coupling criterion $g_0 \gg \kappa$ corresponds to $N_0 \ll \gamma/\kappa$.

2.3.3 A Note on Numerical Simulations

As a final aside, the entirety of this Chapter, in conjunction with certain experimental elements taken from Chapter 3 (particularly our technique for optically confining an atom in Fabry-Perot cavity), is distilled into a single piece of `MATLAB` code as described in Appendix B. Written for use with the Quantum Optics Toolbox API, this code relies on an implementation for the complete cesium $D2$ line of the master equation approach described earlier in this chapter. Periodically throughout the remainder of the dissertation, aspects of this simulation software will be used to provide theoretical modeling of experimentally observed phenomena.

Chapter 3

Experimental Apparatus

In this Chapter, I will present a bottom-up view of the experimental apparatus in Lab 11. This instrumentation has been documented elsewhere, particularly in the theses of former group members [1, 21, 22, 23], but the ever-changing nature of the experiment requires that thoroughly updated description accompany this thesis. It is my goal that this Chapter, in conjunction with the descriptions of commonly-used experimental protocols detailed in Chapter 4, will provide a point of departure for discussions in subsequent Chapters of the experimental measurements undertaken during my time in the Kimble group.

This dissertation will not go into great detail regarding techniques for optical cavity assembly, characterization and selection of “good” cavity mirrors, and vibration isolation requirements for high finesse cavities. These topics have been discussed at great length in the theses of Christina Hood [24], Teresa Lynn [25], David Vernooy [1], and Tracy Northup [26]. Assembling Fabry-Perot resonators from “scratch” requires a great deal of craftsmanship, and I refer you to their detailed notes on these subjects.

3.1 The Physics Cavity

The central component in the experiment is an ultrahigh finesse Fabry-Perot resonator in which we perform cavity QED measurements. The “physics cavity” was constructed in 1998-9 by David Vernooy and Jun Ye and has remained in continuous, uninterrupted operation since.

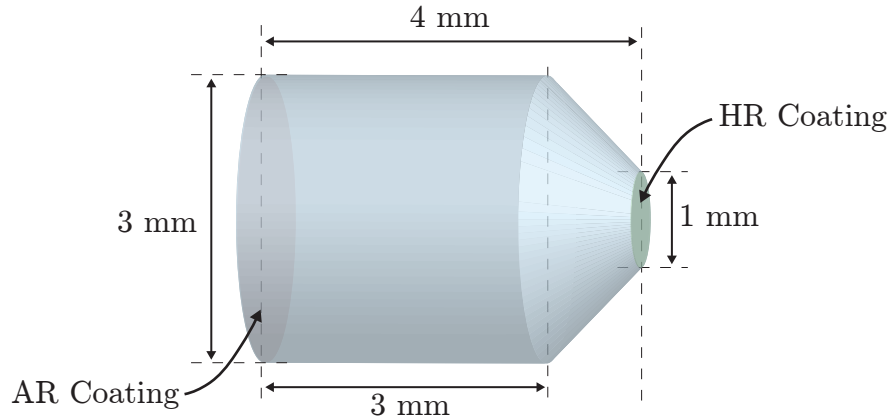


Figure 3.1: Schematic representation of a physics cavity mirror (to scale). The radius of curvature, $\rho = 20$ cm, is large enough that the HR coated surface appears flat to the human eye.

3.1.1 The Mirrors

The physics cavity is a symmetric Fabry-Perot resonator, comprised of two superpolished fused silica substrates coated with a highly-reflective (HR) stack of alternating layers of tantalum pentoxide (Ta_2O_5) and silicon dioxide (SiO_2), each coated $\lambda_{D2}/4$ thick. An anti-reflective (AR) coating is applied to the reverse side of each substrate in order to facilitate input and output coupling and to prevent unwanted interferometric effects within the substrate itself. The mirrors were custom made at our group’s request to exhibit maximum reflectivity at the Cesium D2 line by Research Electro-Optics (REO) of Boulder, CO.

The mirrors were originally coated onto a cylindrical substrate with a 7.75 mm outer diameter (OD), then turned on a lathe to the dimensions depicted in Figure 3.1. The radius of curvature of the polished portion of the substrate is nominally $\rho = 20$ cm. The HR coated surface of the substrate is “coned” to a 1 mm OD, whereas the OD of the AR coated surface is 3 mm. The reason for this conical structure is purely practical - the experiment requires optical access through the side of the cavity and for spherical mirrors of large OD, this access is obscured by unnecessary substrate material. We can quantify this by writing down an

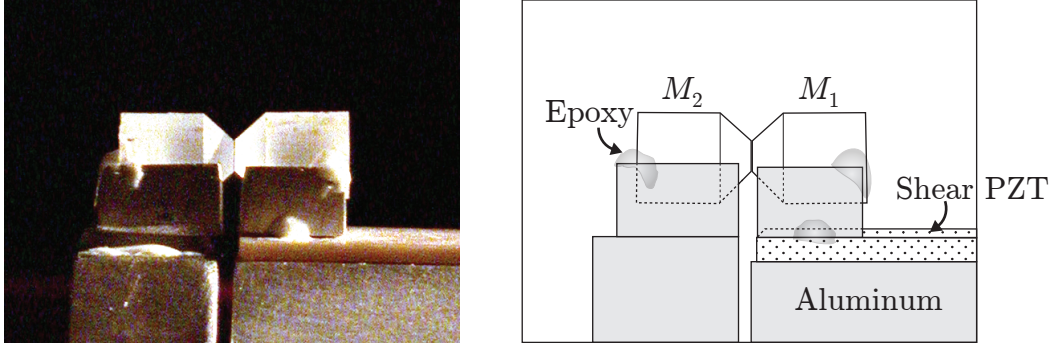


Figure 3.2: Photograph (left) and schematic diagram (right) of the physics cavity assembly. The physical separation between the mirrors, $L = 42.2 \mu\text{m}$, is barely visible in the photograph.

expression for the size, d , of the aperture between the mirror surfaces:

$$d = L - L_{min}, \quad (3.1)$$

$$L_{min} = 2\rho - \sqrt{4\rho^2 - D^2}. \quad (3.2)$$

Here, L is the length of the cavity, D is the OD of the HR coated surface, and L_{min} is the minimum possible cavity length for a given set of mirrors (which would be attained if the ODs of both mirrors were in direct physical contact).

3.1.2 The Cavity Assembly

The cavity assembly consists of two mirrors of the type discussed in the previous subsection, each held in place by vacuum-compatible epoxy in a solid aluminum v-block (Figure 3.2). The v-block containing the input mirror (*i.e.*, M_1 , the mirror into which light is coupled experimentally) is epoxied onto a shear-mode piezoelectric transducer (PZT). A user-controlled voltage applied to this PZT allows us to servo the cavity length *in situ* (up to a maximum bandwidth of ~ 11 kHz). The PZT is itself epoxied onto a tension-mounted

aluminum base assembly. The v-block containing the output mirror (*i.e.*, M_2 , the mirror from which transmitted fields are measured) is fixed in place on the same base.

This base assembly consists of two separate machined aluminum blocks held together by a tensioned thread rod (Figure 3.3a). These blocks are milled so as to allow optical access to the inter-mirror aperture across a 270° arc. One of the two mounted mirrors resides on each of the blocks. The housing is hollow and contains a 1/2 inch cylindrical PZT which was originally intended to provide coarse adjustment of the cavity length. After the entire system was under vacuum, it became clear that the shear PZT provided a full free spectral range of tunability and the cylinder was deemed unnecessary. It has remained grounded and unused since work began on the experiment.

The aluminum housing is itself rigidly bolted onto a large, copper damping weight (Figure 3.3b). The damping weight is machined to fit in the bottom of the spherical octagon vacuum chamber where the cavity resides under ultra-high vacuum (see Section 3.2). Underneath the damping weight are small pieces of viton rubber which cushion the copper weight on the chamber and form the rest of the in-vacuum passive vibration isolation system.

3.1.3 Cavity Parameters

As was discussed in Chapter 2, Section 2.3.2, a lossy, symmetric Fabry-Perot resonator can be effectively characterized in terms of four parameters: L , the cavity length; ρ , the mirror radius of curvature; \mathcal{F} , the Finesse; and φ , the differential birefringent phase shift. The value $\rho = 20$ cm is specified by REO and measurements of the transverse mode structure of the cavity are in good agreement with this specification. In this subsection I will describe measurements made to determine the value of each of the other three quantities, especially in the context of cavity QED with atomic cesium.

Cavity Length

The discussion of Fabry-Perot resonators in Section 2.3.2 treated mirror surfaces as exhibiting zero-thickness and as precise antinodes of any resonant field. The cavity length L was then uniquely determined by the maximum surface-to-surface distance between the mirrors. In this approximation, and for planar mirrors, the resonant frequency of the m th

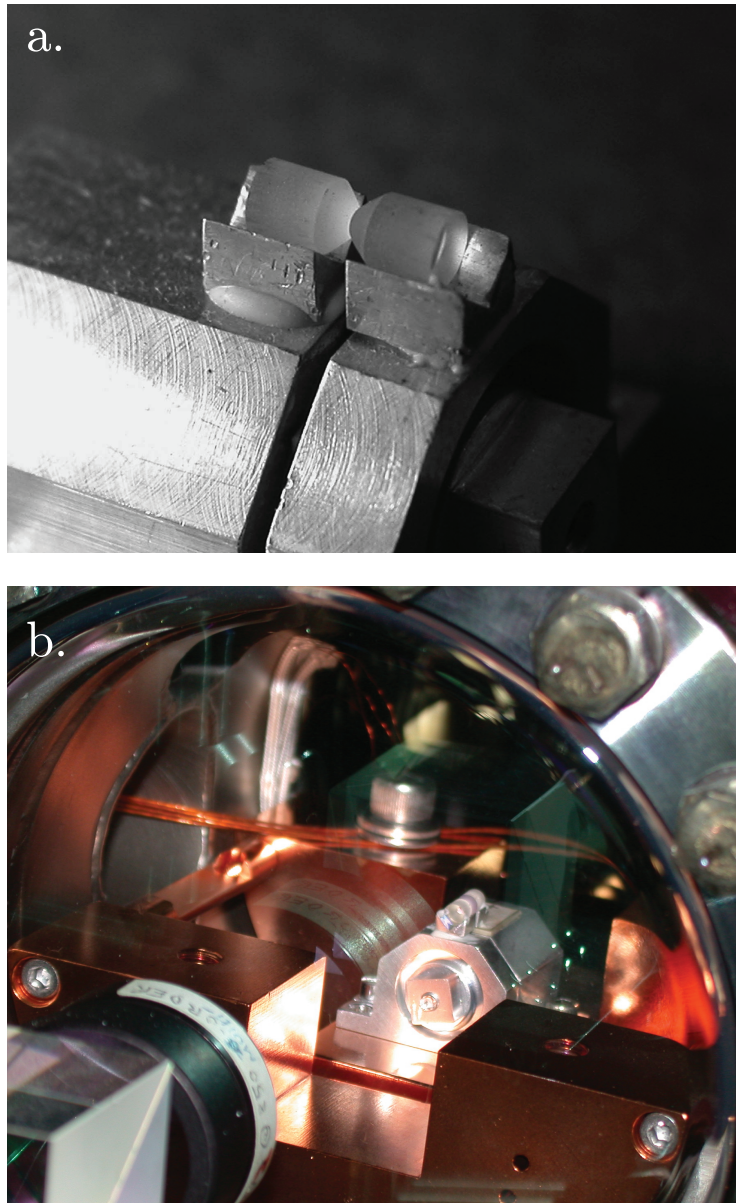


Figure 3.3: a. Reverse angle photo of the physics cavity and aluminum mounting structure. M_1 , the shear PZT-mounted mirror, is now positioned on the left. The tensioned nut holding the baseplate assembly together is clearly visible at bottom right. b. Perspective view of the full physics cavity assembly resting on the copper damping weight inside the UHV chamber 3.2. From this angle, M_1 is the rear mirror.

order (TEM₀₀) mode is given simply by the cavity resonance condition:

$$\omega_m = \frac{m\pi c}{L}.$$

In Equation (2.101) we added a correction to this expression corresponding to phase shifts resulting from the Gouy effect:

$$\omega'_m = \frac{c}{2L} \left[2\pi m + 2 \arccos \left[1 - \frac{L}{\rho} \right] \right].$$

For the nominal cavity design length, $L_d = 44.6 \mu\text{m}$, the Gouy effect provides a correction to the effective cavity length on the order of about 3 nm, or 0.007%. While the Gouy phase does manifest itself as an appreciable frequency shift ($|\omega_m - \omega'_m| \sim 23 \text{ GHz}$) and also gives rise to transverse mode structure, its contribution to the effective cavity length is minimal and we will therefore overlook this term.

A much more significant contribution arises from frequency-dependent phase shifts associated with penetration of the cavity mode into the dielectric HR mirror coating stack. The frequency-dependence results from the variations from layer-to-layer of the index of refraction, from $n_H = 2.0564$ for the Ta₂O₅ layers to $n_L = 1.4440$ for the SiO₂ layers. We can model this effect as:

$$\omega''_m = s(\omega''_m) [2\pi m + \phi(\omega''_m)]. \quad (3.3)$$

Here we have replaced the prefactor corresponding to the cavity free spectral range (FSR) with one that accounts for the finite extent of the mode in the coating stack (an “effective free spectral range”):

$$s(\omega''_m) \equiv \frac{c}{2L + 2\pi c \delta\phi / \delta\omega''_m}. \quad (3.4)$$

We will also define an “effective cavity length”, L_{eff} with respect to $s(\omega)$:

$$L_{eff} = \frac{c}{2s(\omega)}. \quad (3.5)$$

Wavelength (nm)	ω_m (THz)	m (inferred)
827.685	$(2\pi)(362.206)$	102
835.750	$(2\pi)(358.711)$	101
852.357	$(2\pi)(351.722)$	99
935.586	$(2\pi)(320.043)$	90
945.545	$(2\pi)(317.058)$	89

Table 3.1: Resonant wavelengths and optical frequencies for TEM₀₀ longitudinal modes of the Lab 11 physics cavity. Uncertainty (not shown in the table) is ± 0.001 nm, due to fluctuations in Wavemeter reading.

The term $\phi(\omega''_m)$ corresponds to the frequency-dependent phase shift added to the light during its interaction with the mirror coating. It can be shown [27] that by performing a power series expansion of $\phi(\omega)$ around a frequency ω_c for which the mirror reflectivity $R(\omega)$ is locally maximal, the first derivative of the mirror phase shift near ω_c is:

$$\left. \frac{\delta\phi}{\delta\omega} \right|_{\omega_c} = \left[\frac{1}{\omega_c(n_H - n_L)} \right]. \quad (3.6)$$

Experimental frequency resolution of a number of resonant longitudinal modes near $\omega_c \approx (2\pi)(352 \text{ THz})$ provides us a direct method for determining L_{eff} . To do this, we fix the length of the cavity and vary the frequency of mode-matched probe light (derived from three lasers, tuned to four distinct wavelengths). In varying the wavelengths we are in search of cavity resonances exhibiting a TEM₀₀ spatial profile (indicating a fundamental longitudinal mode). When we observe resonant transmission of a probe laser, the wavelength is then determined by redirecting a portion of the field to a Burleigh Wavemeter which resolves it via Michelson interferometry. Experimentally measured values for these wavelengths are presented in Table 3.1.

For optical frequencies detuned slightly from ω_c with respect to $R(\omega)$ (which is first-order insensitive to variations in ω near a local maximum), we can neglect the frequency dependence of L_{eff} . Under this approximation, it is possible to infer the mode order,

$m = \{89, 90, 99, 101, 102\}$, for each of the ω_m presented in Table 3.1 by assuming a linear relationship between m and ω_m . From this data we can also infer an effective (local, with respect to the maximum of $R(\omega)$) FSR, $\nu_{FSR} = 3.495 \pm 0.001$ THz which corresponds to an effective length $L_{eff} = 42.89 \pm 0.01$ μm (uncertainties correspond to the 68% confidence interval in a linear regression fit to the data).

Using Equations (3.6) and a power series expansion of (3.5) about ω_c , we can derive an expression for the surface-to-surface mirror spacing L as a function of L_{eff} and ω_c to first order [28]:

$$L = L_{eff} - \frac{c\pi}{\omega_c} \left(\frac{1}{n_H - n_L} \right) \quad (3.7)$$

$$= L_{eff} - 0.8165\lambda_c. \quad (3.8)$$

From this relationship we can make an estimate of the physical cavity length, $L = 42.19 \pm 0.01$ μm . This agrees favorably with a more detailed calculation yielding $L = 42.207 \pm 0.005$ μm carried out by Kevin Birnbaum and described in his thesis [29].

Linewidth and Finesse

In Chapter 2, Section 2.3.2 we took note of the functional relationship between cavity halfwidth κ and finesse \mathcal{F} . We can generalize this relationship to consider effective, as opposed to physical, cavity length:

$$\kappa = \frac{c}{2L_{eff}} \frac{\pi}{\mathcal{F}}. \quad (3.9)$$

The finesse is a function only of the transmissive and dissipative losses in the mirror. The two are reciprocal quantities and can be inferred indirectly from the other by independent measurement of L_{eff} . As a practical matter, the value of κ at $\lambda_{D2} = 852.4$ nm (with its relative importance as a parameter in the cavity QED strong coupling criteria) is the more experimentally relevant quantity. In this section I describe a direct measurement of the cavity halfwidth from which I infer the finesse. For a discussion of direct measurements of the mirror losses, see Andreea Boca's dissertation [23].

There are three common approaches to measuring the cavity linewidth used by our group. The first, cavity ring-down spectroscopy, involves a time-domain measurement. This is done by driving the fixed-length cavity on resonance with a probe field through mirror M_1 and measuring the intensity of the field transmitted through M_2 as a function of time. If the probe field is switched OFF over a timescale much shorter than κ^{-1} , the transmitted signal will exhibit an exponential decay as the circulating field leaks from the cavity mirrors. The time constant of this decay is the cavity linewidth, κ . In practice, for very short, high-finesse cavities such as the Lab 11 physics cavity, this is not an effective method due to the rapid decay of the field.

The other two techniques involve frequency-domain measurements. In a fixed-length cavity we can monitor the transmission spectrum $\mathcal{T}(\omega)$ of a probe beam for which the frequency-detuning from the cavity resonance is swept. It follows from Equation (2.113) that (in the absence of birefringent effects) $\mathcal{T}(\omega)$ will exhibit a Lorentzian lineshape with halfwidth κ . This type of measurement is commonly employed in the laboratory and will be discussed in Chapter 6. I omit discussion here as there is some experimental overhead associated with calibrating $\mathcal{T}(\omega)$ against beam-steering and intensity modulation effects as the probe detuning is varied.

The final technique, which is the one which will be used here to measure κ , involves monitoring the transmission of a fixed-frequency probe which is injected into a cavity of variable length, L . We are, again, sweeping the probe-cavity detuning, however we are doing so now by varying the round-trip resonance condition of the cavity. This technique is the most robust of the three against experimental defect and has yielded the most consistent measurements.

To understand how the cavity length is swept it is first necessary to understand how the length is actively stabilized. A thorough discussion of the frequency chain that leads to the cavity lock servo loop will follow in Section 3.4. For now, it is sufficient to understand that a frequency-stabilized laser drives the $m = 101$ longitudinal mode at 835.750 nm (the probe field drives $m = 99$). An error signal for stabilizing the cavity is derived from the transmission of this beam such that by changing the frequency of the laser, the cavity length follows. To understand this effect, note that for a frequency change $\Delta\omega_{101}$ in the laser, the

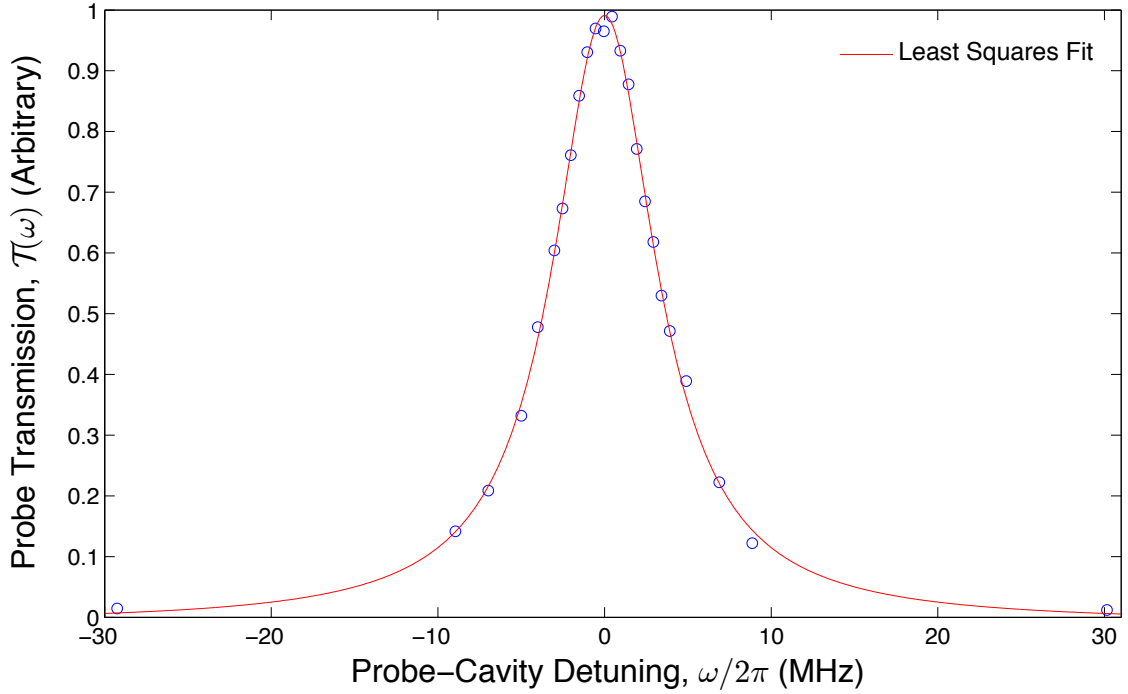


Figure 3.4: Transmission spectrum $\mathcal{T}(\omega)$ (\circ) of a fixed-frequency probe beam through a variable-length physics cavity. A nonlinear least squares fit ($-$, `fit` routine in MATLAB) yields $\kappa = (2\pi)(3.76 \pm 0.06)$ MHz. Uncertainty represents a 68% confidence interval for the fit.

resulting change in wavelength (and therefore cavity length, as the servo follows the laser) is:

$$\Delta L_{eff} = \frac{101}{2} \Delta \lambda_{101} = \frac{100\pi c}{\Delta \omega_{101}}. \quad (3.10)$$

As the effective cavity length changes, the resonant frequency ω_{99} shifts by:

$$\Delta \omega_{99} = \frac{99\pi c}{\Delta L_{eff}} \quad (3.11)$$

$$= \frac{99}{101} \Delta \omega_{101}. \quad (3.12)$$

In order to map out the transmission spectrum for a fixed-frequency probe, it is sufficient to scan the frequency of the locking laser and record $\mathcal{T}(\omega_{101})$, then rescale the frequency axis by a factor of 99/101.

Figure 3.4 contains an experimental measurement of $\mathcal{T}(\omega)$ as recorded on single-photon counting avalanche photodiodes. The vertical axis has been normalized and the frequency axis has been properly rescaled. A nonlinear least squares fit to a Lorentzian distribution gives $\kappa = (2\pi)(3.76 \pm 0.06)$ MHz, which is representative of mean linewidth measured using this technique during my time at Caltech. Performing the same technique using heterodyne detection in lieu of single photon counting tends to produce $\sim 25\%$ variations in κ , however these fits are generally of lower quality and deviate strongly from the data in the wings of the distribution.

Based on this measurement, and using the previous result $L_{eff} = 42.89 \pm 0.01 \mu\text{m}$, we calculate the finesse $\mathcal{F} = (4.648 \pm 0.007) \times 10^5$. This corresponds to total losses in the mirror $T + l = (6.7 \pm 0.03)$ ppm. A serious concern in atom-cavity experiments [25] is that over time a background vapor of cesium gas might condense on the mirror surfaces, gradually degrading the finesse. Michael Chapman and Christina Hood observed this effect in early implementations of this type of experiment. In the context of the Lab 11 experiment, however, we have observed no measurable degradation of the finesse or cavity linewidth over the course of ten years. Measurements consistently yield $\kappa \sim (2\pi)(3.8)$ MHz with only small variations due to measurement technique and error.

Birefringence

In Chapter 2, I described a subtle effect which manifests itself in high-finesse resonators whereby small anisotropies in the mirror surfaces give rise to a large birefringent splitting between orthogonally polarized cavity modes, $\Delta\omega^\pm$. The general consensus in our group among students who have built cavities is that the birefringence manifests itself only when the mirrors are epoxied into the cavity assembly and is not inherent to the mirrors themselves (*i.e.*, not as a result of the substrate coning process, for instance). The most likely physical mechanism for this effect is that as the epoxy cures it causes uneven stress across the mirror surfaces which gives rise to variations in the coating stack indices of refraction, (n_H, n_L) .

These variations, in turn, alter the mirror phase shift (3.6) inducing a small differential phase φ along the linear axis of the stress, \hat{l}_+ , with respect to the unstressed axis, \hat{l}_- .

Regardless of the underlying mechanism, it is empirical fact that the Lab 11 physics cavity exhibits a modicum of birefringent splitting. In order to obtain the cavity lineshape in Figure 3.4, the probe field was necessarily polarized along \hat{l}_+ , thereby only driving the higher frequency of the two modes. Likewise, the output field of the cavity was directed through a $\lambda/2$ -waveplate and polarizing beamsplitter such that only transmitted light polarized along \hat{l}_+ was detected. In the absence of these precautions, the transmitted spectrum would be a convolution of the lineshapes for the two modes. To see why this is the case, consider Equation (2.119) in the context of an arbitrarily polarized input field, $\vec{E}_{inc} = E_{inc}^+ \hat{l}_+ + E_{inc}^- \hat{l}_-$. We are concerned with measuring the transmitted intensity along an arbitrary axis, $\hat{m} = \cos \theta \hat{l}_+ + \sin \theta \hat{l}_-$. This situation can be analyzed using Jones matrix formalism:

$$\vec{E}_{tran} \cdot \hat{m} = T e^{-i\omega L/c} \mathcal{R} \begin{pmatrix} 1 & 0 \\ 0 & 0 \end{pmatrix} \begin{pmatrix} \frac{1}{1+Re^{2i(\omega L/c-\varphi)}} & 0 \\ 0 & \frac{1}{1+Re^{2i\omega L/c}} \end{pmatrix} \begin{pmatrix} E_{inc}^+ \\ E_{inc}^- \end{pmatrix}. \quad (3.13)$$

Here we have rotated the projection matrix from the \hat{l}_+ -axis to the \hat{m} -axis using the rotation matrix:

$$\mathcal{R} = \begin{pmatrix} \cos \theta & -\sin \theta \\ \sin \theta & \cos \theta \end{pmatrix}. \quad (3.14)$$

This yields an expression for the transmitted field along \hat{m} :

$$\vec{E}_{tran} \cdot \hat{m} = E_{inc}^+ \frac{T e^{-i\omega L/c} \cos \theta}{1 - Re^{2i(\omega L/c-\varphi)}} + E_{inc}^- \frac{T e^{-i\omega L/c} \sin \theta}{1 - Re^{2i\omega L/c}} \quad (3.15)$$

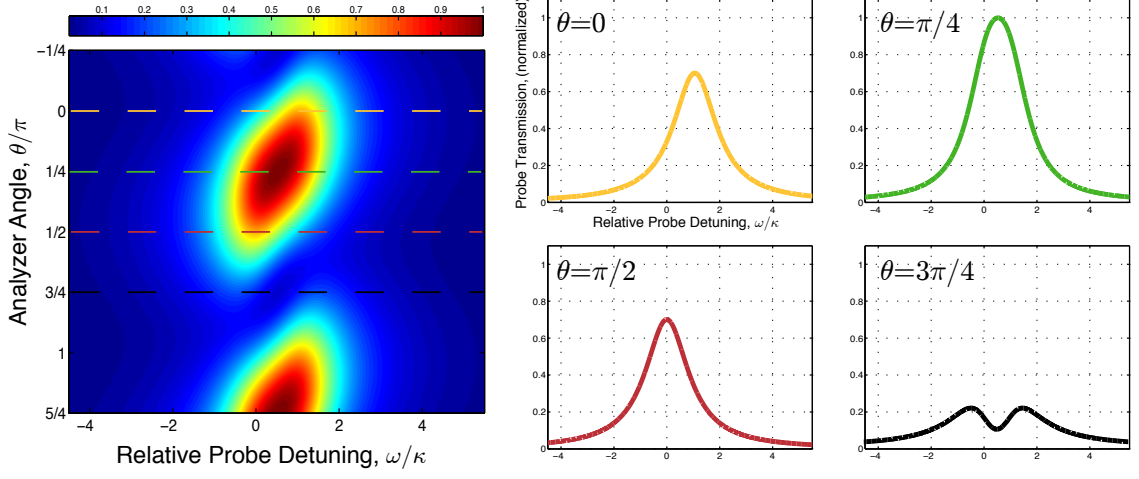


Figure 3.5: Theoretical normalized transmission intensity (colormap) for a circularly polarized probe field as a function of analyzer angle and probe detuning. In this model, the quantity $\Delta\omega^\pm/\kappa \approx 1.06$ is the same as for the Lab 11 physics cavity. Individual Transmission spectra for $\theta = 0$ (lower-frequency eigenmode), $\theta = \pi/4$ (constructive interference), $\theta = \pi/2$ (higher-frequency eigenmode), $\theta = 3\pi/4$ (destructive interference).

And, likewise the transmitted intensity for $\omega \sim \omega_n$:

$$\begin{aligned}
 I_{tran,m}(\omega) &= \frac{c\epsilon_0}{2} |\vec{E}_{tran} \cdot \hat{m}|^2 & (3.16) \\
 &= \frac{c\epsilon_0}{2} \left(\frac{T}{T+l} \right)^2 \left[|E_{inc}^+|^2 \frac{\cos^2 \theta}{1 + \frac{(\omega - \omega_n - c\varphi/L)^2}{\kappa^2}} + |E_{inc}^-|^2 \frac{\sin^2 \theta}{1 + \frac{(\omega - \omega_n)^2}{\kappa^2}} \right] \\
 &\quad + T^2 \frac{c\epsilon_0 \sin 2\theta}{4} \left(\frac{|E_{inc}^{+*} E_{inc}^-|}{(1 - Re^{i\varphi})^2 + 4e^{i\varphi} (L/c[\omega - \omega_n] - \varphi/2)^2} + \text{c.c.} \right).
 \end{aligned}$$

The first two terms are the familiar Lorentzian lineshapes for the two polarization eigenmodes. The third and fourth terms represent mixing between the two eigenstates when measured and driven off eigenaxis.

Figure 3.5 reveals the dependence of the transmission spectrum on the analyzer angle. Using the prescribed model we find that the transmission of a circular polarized probe field

is:

$$\vec{E}_{inc} = \frac{|E|}{\sqrt{2}} (i\hat{l}_+ + \hat{l}_-), \quad (3.17)$$

is monitored as a function of both θ and the detuning of the probe from resonance with the lower frequency polarization eigenmode. For values $\theta_+ = n\pi$ and $\theta_- = (n+1)\pi/2$, the analyzer is aligned with \hat{l}_\pm and we cleanly resolve the transmission spectra for the two eigenmodes. However for $\theta = n\pi/4$, the polarizer is oriented at a 45° with respect to either eigenaxis and the transmission spectrum alternately exhibits constructive and destructive interference.

In order to measure the magnitude of the birefringent splitting in the laboratory, the deconstructively interfered signal is a particularly useful observable. The procedure is to obtain a probe transmission spectrum $\mathcal{T}(\omega)$ for an off-axis value of θ and obtain a numerical fit to the model described in Equation (3.17). $\mathcal{T}(\omega)$ exhibits birefringent effects most prominently for analyzer angles where $\sin\theta\cos\theta$ is at its minimum (*i.e.*, $\theta = (2n+1)\pi/4$). I should quickly note that there are a variety of other experimental methods for measuring cavity birefringence which are described in great detail in Teresa Lynn's thesis. However the particular technique used here is, in my experience, the most straight forward and reliable.

Figure 3.6 contains one such fit with $\{\varphi, \theta\}$ left as free parameters. This spectrum was measured using the same technique as was used for Figure 3.4, with a fixed-frequency probe field and variable-length cavity. MATLAB's `fit` routine yields $\theta = (0.74 \pm 0.05)\pi$ and $\varphi = (3.6 \pm 0.2) \times 10^{-6}$, with error bars representing 68% confidence intervals (the quality of the fit reflects what was likely a probe field with a slight elliptical polarization rather than pure circular). Recalling Equation (2.125), we can calculate the total birefringent splitting:

$$\frac{\Delta\omega^\pm}{\kappa} = \frac{2}{\pi} \mathcal{F}\varphi = 1.06 \pm 0.03 \quad (3.18)$$

$$\Delta\omega^\pm = (2\pi)(4.0 \pm 0.1) \text{ MHz}. \quad (3.19)$$

I should quickly mention that this result is representative (see Andreea Boca's thesis for other measurements). During my six years in Lab 11 we have never observed significant

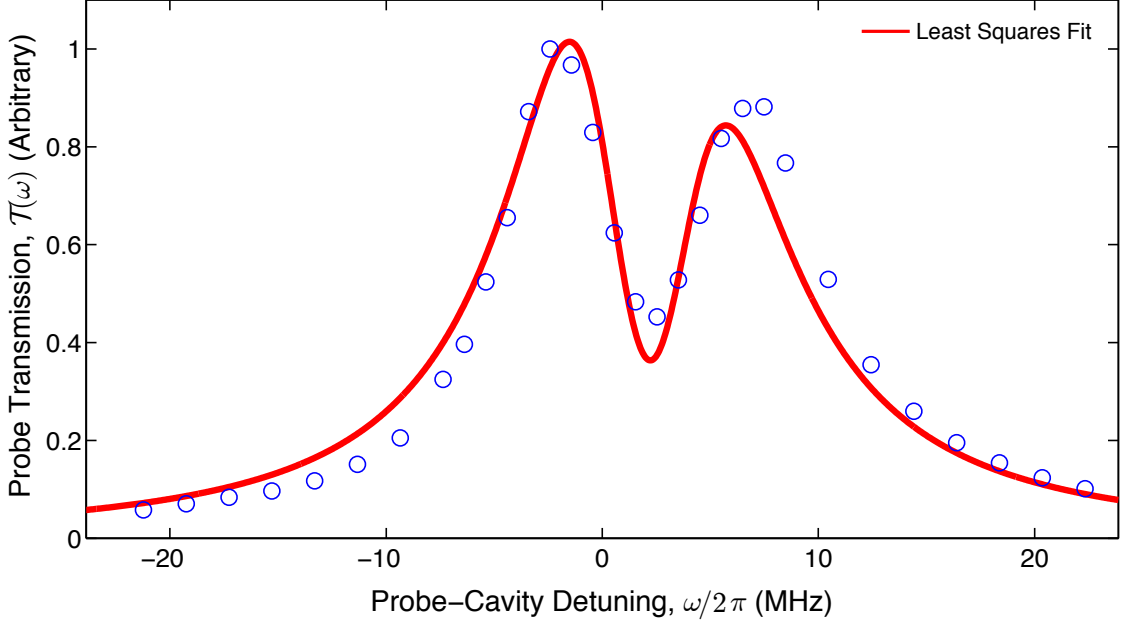


Figure 3.6: Transmission intensity spectrum for a circularly polarized probe beam through a polarizing beam splitter oriented at an angle $\theta \sim 3\pi/4$ with respect to the \hat{l}_+ cavity eigenaxis. A numerical fit to Equation (3.17) yields $\varphi = (3.6 \pm 0.2) \times 10^{-6}$ and a birefringent splitting $\Delta\omega^\pm = (2\pi)(4.0 \pm 0.1)$ MHz.

variation in the splitting of the QED mode. Also, it seems to be the case that the polarization eigenaxes are universal across longitudinal modes (this has been verified for $m \in \{89, 90, 99, 101\}$) which would agree with the hypothesis that the physical mechanism for the birefringence is geometric (*i.e.*, stress planes) as opposed to spectral. The splitting at modes other than $m = 99$, however, grows considerably smaller as the coating curve rolls off (along with the finesse).

This leads to the question, “to what extent is the cavity birefringence a relevant concern when studying cavity QED?” The answer this question, it is important to realize that our cavity lies in a unique regime. For $\Delta\omega^\pm \gg (g_0, \kappa, \gamma)$, we can far-detune one of the two modes and thereby treat only the resonant one. In the other limiting case, $\Delta\omega^\pm = 0$, the two modes are fully degenerate and, while both polarizations are simultaneously supported, the

cavity is not birefringent. The physics cavity, however, satisfies $\Delta\omega^\pm \sim (\gamma, \kappa)$. Irrespective of the atom-cavity detuning, the atom couples strongly to both modes and these modes potentially exhibit mixing of the type predicted in Equation (3.17). Even if we probe and measure only along eigenaxes, a strongly coupled atom will depolarize the field at a rate close to g_0 (consider transitions from excited state Zeeman levels to ground states which satisfy $\Delta m_F = \pm 1$).

In Chapter 6, I will describe the series of experiments where we first began to understand the importance of cavity birefringence in our system and even, to a certain extent, use it advantageously to observe the photon blockade effect.

3.1.4 Summary of Cavity Parameters

Table 3.2 provides a thorough summary of the relevant parameters for the Lab 11 physics cavity. The discussion in Chapter 2 and the previous subsections of this chapter offer detailed explanations of how each of these quantities was either measured or deduced from other measurables. Importantly, it should be noted that for our system (on the $F = 4 \leftrightarrow F' = 5$ transition):

$$(g_0, \kappa, \gamma) = (2\pi)(33.7, 3.76, 2.61) \text{ MHz} \quad (3.20)$$

placing our experiment well into the regime of strong coupling.

3.2 The Vacuum Chamber and MOTs

The Lab 11 physics cavity resides under ultra high vacuum (UHV) at a pressure $P_{low} \approx 4 \times 10^{-10}$ Torr. There are a variety of reasons for keeping the cavity under vacuum - a UHV environment allows us to laser cool and trap atomic samples and facilitates decoupling of an intracavity atom from its environment. Both the vacuum chamber and the magneto-optical traps which provide a source of cold atoms to the cavity have been thoroughly discussed in other dissertations [21, 1]. I provide only a brief explanation of them here, for the sake of completeness and in order to make clear their role in the experimental timing schemes to be discussed in Section 3.6.

Parameter	Description	Value	Uncertainty	Units
Geometric Properties:				
ρ	mirror radii of curvature	20	-	cm
L_{eff}	effective cavity length	42.89	0.01	μm
L	physical cavity length	42.207	0.005	μm
d	cavity aperture width	41.41	0.005	μm
w_0	waist spot size at λ_{D2}	23.70	0.001	μm
V_m	mode volume at λ_{D2}	1.893×10^4	0.0007×10^4	μm^3
Mode Structure:				
ν_{FSR}	free spectral range	3.495	0.001	THz
ω_T	transverse mode spacing	$(2\pi)(22.9)$	$(2\pi)(0.4)$	GHz
$\Delta\omega^\pm$	peak-to-peak birefringent splitting	$(2\pi)(4.0)$	$(2\pi)(0.1)$	MHz
\mathcal{F}	finesse	4.648×10^5	0.007×10^5	-
Cavity QED Parameters:				
$\max(g_0) _{4,5'}$	maximum g_0 ($F = 4 \leftrightarrow F' = 5$)	$(2\pi)(33.72)$	$(2\pi)(0.006)$	MHz
$\max(g_0) _{4,4'}$	maximum g_0 ($F = 4 \leftrightarrow F' = 4$)	$(2\pi)(23.03)$	$(2\pi)(0.004)$	MHz
$\max(g_0) _{4,3'}$	maximum g_0 ($F = 4 \leftrightarrow F' = 3$)	$(2\pi)(14.87)$	$(2\pi)(0.003)$	MHz
κ	cavity half width at λ_{D2}	$(2\pi)(3.76)$	$(2\pi)(0.06)$	MHz
γ	atomic half width at λ_{D2}	$(2\pi)(2.611)$	$(2\pi)(0.003)$	MHz
Critical Numbers:				
n_0	min. critical photon number	3.00×10^{-3}	8×10^{-6}	-
N_0	min. critical atom number	1.73×10^{-2}	2.8×10^{-4}	-

Table 3.2: Summary of Lab 11 physics cavity parameters. Experimentally measured quantities are $(L_{eff}, \kappa, \Delta\omega^\pm, \gamma$ [11]). All others are inferred from these values.

3.2.1 Vacuum Chamber

The overall vacuum chamber (Figure 3.7) is divided into two functionally separate chambers - “upper” and “lower.” Both are octagonal, supporting $2\frac{3}{4}$ ” ($1\frac{1}{3}$ ”) and $4\frac{1}{2}$ ” ($2\frac{3}{4}$ ”) conflat windows, respectively, on their axial (radial) ports. The lower chamber contains the physics cavity assembly and rests freely on a stack of steel plates and viton rubber which provides passive vibration isolation. The cavity is nominally located at the geometric center of the chamber. The upper chamber is connected to a temperature-controlled reservoir of metallic cesium through a series of flanges and a gate valve. Generally this reservoir is thermoelectrically cooled but in the absence of cooling, and with the valve open, an appreciable background pressure of cesium vapor can develop in the upper chamber.

The chambers are themselves joined by a narrow (inner diameter, 3 mm) differential pressure tube. The tube offers a low conductance path between the two chambers, which allows us to maintain a pressure difference of about $P_{up}/P_{low} \sim 25$ between them [21]. Both chambers are also attached to dedicated ion pumps which remain in nonstop operation. Pressure readings on ion gauges attached to each chamber indicate $P_{up} \sim 1 \times 10^{-8}$ Torr and $P_{low} \sim 4 \times 10^{-10}$ Torr.

The use of a differential pressure tube between the cesium reservoir and the physics cavity chamber has been an extremely beneficial design feature of this system as it allows us to isolate the cavity from excessive exposure to cesium. In earlier implementations of this type of apparatus within our group, atomic samples of cesium were laser cooled from background gas in the same chamber as the physics cavity. Over six month to one year time scales, the finesse of the cavity would gradually degrade as cesium slowly condensed on the mirror surfaces and lead to significant scattering and absorption losses. The Lab 11 configuration, however, has been in operation for almost a decade now with no measurable degradation of any cavity parameters (and with no apparent shortage of cesium gas in the upper system, as well).

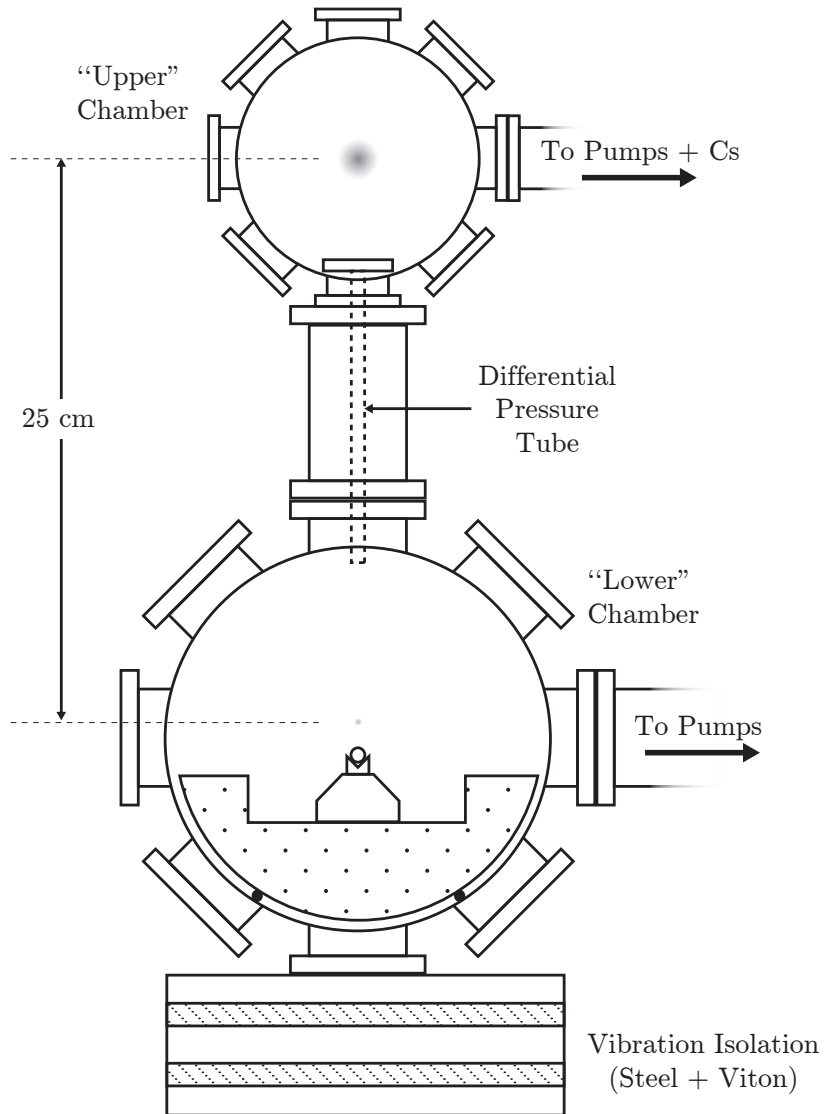


Figure 3.7: Schematic of the Lab 11 two-chamber UHV system (not to scale). Flanges drawn without connections lead to conflat windows. Larger conflat windows are also attached to both sides of the lower ($4\frac{1}{2}$ "") and upper chambers ($2\frac{3}{4}$ "") in the plane of the drawing.

3.2.2 A Source of Cold Atoms

Magneto-optical trapping (MOT) is now a broadly used technique in the atomic physics world. Using a combination of magnetic field gradients and properly tuned laser fields, MOTs allow for the confinement and cooling of atomic samples. They are perhaps so prevalent because they are relatively inexpensive (relying on only modest field gradients and low-cost diode lasers) and yet offer sub-mK atomic samples. In our experiment the physics of the MOT, once understood and implemented, is largely superfluous to the subsequent cavity QED physics which is the real focus of our work. To a greater or lesser extent, the MOT serves only as source of cold atoms. Once those atoms enter the cavity mode, as we will see in the next section, they are cooled into another kind of trap which governs the dynamics of the atomic motion as it undergoes coupling to the cavity field. For this reason, what follows is not intended to be a complete review of radiation pressure cooling but rather a short overview of some MOT principles as they pertain to our work.

MOT Physics

A magneto-optical trap relies on a combination of magnetic field gradients and counter-propagating polarized laser beams in order to create an atomic potential [30, 31]. We will assume that the absolute magnetic field is initially null through some volume of space in which we will form our trap. In order to generate the potential, we affect a magnetic spherical quadrupole field in the region. Near the center of the field pattern it takes the approximate form:

$$B_{x'} = \frac{\partial B_{x'}}{\partial x'} \cdot x', \quad B_{y'} = \frac{\partial B_{y'}}{\partial y'} \cdot y', \quad B_{z'} = \frac{\partial B_{z'}}{\partial z'} \cdot z'. \quad (3.21)$$

I have primed the coordinates to make absolutely clear that there is no correspondence between this coordinate frame and that set by the cavity's longitudinal and birefringent axes. The effect of these magnetic field gradients in the weak-field limit, as we saw in Section 2.3.1, is to induce Zeeman shifts on atomic energy eigenstates which are proportional to those states' spin projection quantum number, m_F .

The trapping force is derived from three pairs of counter-propagating σ^{+-} and σ^{-} -

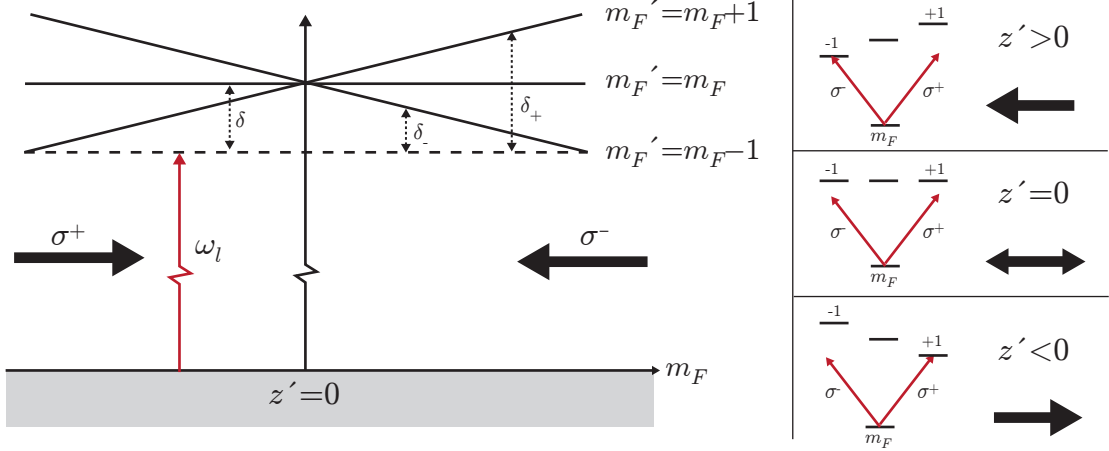


Figure 3.8: One-dimensional representation of the magneto-optical trapping force.

polarized beams which are oriented in the $\pm \hat{z}'$ -direction and also in two, transverse, orthogonal directions $\pm \hat{x}'$, $\pm \hat{y}'$. These beam pairs spatially intersect the others near the center the trapping region, $(x', y', z') = 0$ and are each red-detuned from the $(6S_{1/2}, F = 4, m_F = 0) \leftrightarrow (6P_{3/2}, F' = 5, m_F' = 0)$ clock transition by a small frequency δ .

Figure 3.8 depicts a one-dimensional toy model of a MOT. At $z' = 0$ the magnetic field is nulled and all transitions $|4, m_F\rangle \leftrightarrow |5', m_F \pm 0, 1\rangle$ weakly scatter both left- and right-going beams equally. If the atom moves towards $z' > 0$, however, the $|4, m_F\rangle \leftrightarrow |5', m_F - 1\rangle$ transition shifts closer to resonance (*i.e.*, $\delta_- \rightarrow 0$) with the σ^- -polarized field which is traveling along $-\hat{z}'$. As this resonance shifts, the atom beings scattering more of this right-going beam than the left-going σ^+ -beam and a photon recoil tends to push the atom back towards $z' = 0$. Likewise, if the atom moves towards $z' < 0$, the symmetric effect occurs for the σ^+ -polarized field and the $|4, m_F\rangle \leftrightarrow |5', m_F + 1\rangle$ transition.

We can express the total force on the atom as a sum of left and right scattering forces:

$$\begin{aligned}
 F_{tot} &= F_+ + F_- \\
 &= \frac{\hbar \vec{k} \gamma I}{I_{sat}} \left[\frac{1}{1 + I/I_{sat} + (\delta_+/\gamma)^2} - \frac{1}{1 + I/I_{sat} + (\delta_-/\gamma)^2} \right] \quad (3.22)
 \end{aligned}$$

Here we have assumed both beams are of equal intensity and opposite wave vector, and

have used the common expression for the free-space scattering rate of a driven atom. We can also formally express the detunings as:

$$\delta_{\pm} = \delta \mp \vec{k} \cdot \vec{v} + \mu_B \vec{B} \cdot \hat{z}' [2/5(m_F \pm 1) - 1/4m_F]. \quad (3.23)$$

This one-dimensional model easily generalizes to the three-dimensional case. Ignoring passive polarization gradient effects, the cooling limit for a MOT is the Doppler limit:

$$\begin{aligned} T_{Doppler} &= \frac{\hbar\gamma}{k_B} \\ &= \frac{\hbar(2\pi)(2.6 \text{ MHz})}{k_B} \approx 125 \mu\text{K} \end{aligned} \quad (3.24)$$

Two-Stage MOT

In order to deliver cold atoms to the cavity volume, we begin by collecting a MOT from background vapor in the upper chamber. Laser beams for this MOT (total intensity $I \sim 20$ mW) are directed into the upper chamber as shown in Figure 3.9. This light is tuned $\delta = -7.5$ MHz (red) from the $|4, 0\rangle \leftrightarrow |5', 0\rangle$ transition (the lasers from which these beams are derived will be discussed in Section 3.4). The magnetic spherical quadrupole field is achieved by driving current through two coils in an anti-Helmholtz configuration which produce the desired field gradients at the midpoint between the coils. Generally the upper MOT is allowed to form for ~ 150 ms, during which time $\sim 10^7$ atoms are collected. We can, however, generate a larger upper MOT at the expense of a longer gathering time and a slower experimental duty cycle.

Following the upper MOT interval, we switch **OFF** the anti-Helmholtz coils (using a TTL-controlled flyback-buffered solid state relay) and polarization gradient (PG) cool the remaining atoms for ~ 10 ms (PG cooling will be described in some detail in Section 3.3, but is generally a technique for sub-Doppler cooling an atomic sample). All trapping beams are then turned **OFF** and the newly cold atoms are allowed to undergo free fall. A fraction of these atoms exhibit a ballistic trajectory which sends them through the differential pressure

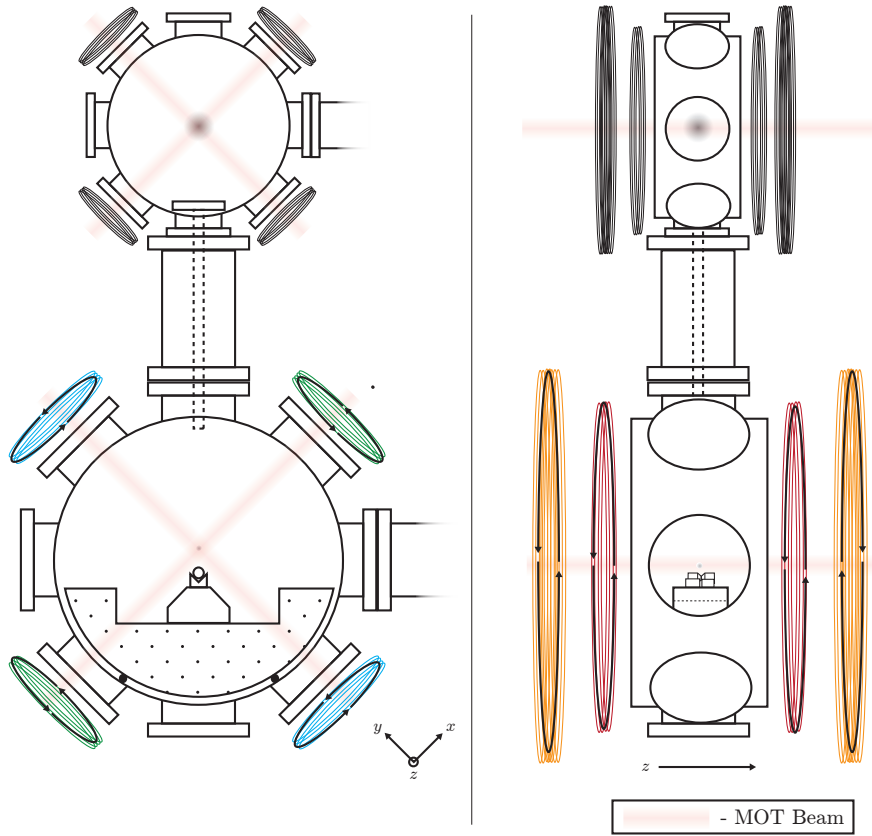


Figure 3.9: Schematic of the Lab 11 vacuum system in the context of MOT beams and coils (not to scale). The MOT beam geometry is depicted in light orange. The lower chamber coils are colored according their pairings and are marked to indicate the direction in which current flows through them. See Table 3.3 for more information about the bias coil pairs (*i.e.*, red, green and blue).

tube and into the lower chamber. The purpose of the sub-Doppler cooling step is to reduce the expansion of the cloud as it is released - a smaller distribution of velocities transverse to axis of the differential pressure tube ensure more atoms pass through.

A second, lower MOT is formed from those atoms which successfully transit the tube (generally $\sim 10^5$ atoms). The geometry of the MOT beams and coils is similar to that for the upper MOT (Figure 3.9, though due to the dimensions of the lower chamber, a larger pair of anti-Helmholtz coils is required). The quadrupole field and laser beams (total intensity, $I \sim 11$ mW) for this MOT are oriented such that their intersection is ~ 5 mm above the spacing between the two cavity mirrors. The lower MOT begins forming (fields and beams switched ON) 180 ms after the upper MOT is released and continues to collect atoms for a further 150 ms. After the lower MOT is formed, we once again PG cool and release the sample (here, again, the PG cooling serves to minimize the expansion of the cloud as it is released). The atoms again fall via gravity and a very small fraction (on the order of 10 atoms, depending on day-to-day drifts in the relative MOT-cavity alignment) pass through the aperture between the mirrors and into the cavity mode volume. These atoms are now at a temperature given approximately by their ballistic kinetic energy:

$$T = \frac{mgh}{k_B} \approx 800 \mu\text{K}. \quad (3.25)$$

In the absence of intracavity trapping or cooling, they will transit the cavity QED mode waist with velocity $v \approx 0.3$ m/s in $\tau_{transit} \approx 150 \mu\text{s}$.

As will be discussed in Section 3.3, we are ultimately able to slow this falling motion and to load the atoms into an all-optical standing wave trap which will enable us to extend these transit times by up to four orders of magnitude.

Coils and Magnetic Field Control

As previously described, both the upper and lower chambers have a set of anti-Helmholtz coils associated with them in order to generate the MOT potential. In addition to this pair, there are an additional three, orthogonally-oriented coil pairs per chamber which manipulate the static magnetic bias fields in three-dimensions (the currents in these coil pairs flow in

Axis	‘Colloquial’ Name	Kepeco Model	Curr./Input (A/V)	B_{cavity} /Input (G/V)
x	fed-from-above	BOP 20-5M	0.5	0.07
y	fed-from-below	BOP 20-10M	1.0	0.14
z	axial	BOP 20-5M	0.5	0.97

Table 3.3: Properties of the Lab 11 lower chamber bias coils. ‘Colloquial’ names are a historical remnant and are written on labels and power supplies throughout the laboratory to describe the coil pairs. Current-to-field calibrations were performed using Raman magnetometry as described in Chapter 4. Voltages listed are control voltages input to the Kepco, not voltages applied across the coils.

parallel, as opposed to the anti-parallel configuration in the anti-Helmholtz pair). The bias coils in the upper chamber are operated at continuous, fixed current and are tuned so as to form the upper MOT at the geometric center of the chamber.

The lower chamber has three similar, orthogonally-oriented pairs of coils (Figure 3.9: green, blue and red coil pairs) in addition to the lower anti-Helmholtz pair (orange coils). These coil pairs serve two purposes - during the lower MOT timing interval they provide a static magnetic field null at the location of the MOT, just above the cavity substrates (whereas the quadrupole pair provides the field gradient). After the lower MOT is released, the coil currents are switched to an “experimental” setting which determines the static magnetic field at the location of the atom inside the cavity. This allows us to set manually set a quantization axis for the atom as it undergoes cavity QED dynamics.

Only after the first set of experiments in which I was involved (in 2004) did we address the importance of being able to switch to this “experimental” setting (all prior work was done with the MOT setting still in place, and therefore an arbitrarily oriented static magnetic field at the location of the cavity mode). Our solution was to replace the fixed current supplies driving these coils with three Kepco Model BOP-20 high-current switching operational amplifiers. In current mode, these supplies accept an analog input voltage and output a proportional current (the constants of proportionality are a property of the Kepco model and are given in Table 3.3). The analog voltages are derived from the D/A converter built

into the same ADWin Gold controller which is used to manage the overall timing for the experiment (Section 3.6).

With slight user modification, these supplies exhibit a slew rate of $1 \text{ A}/\mu\text{s}$ across a resistive load. Across an inductive load, however, the reverse voltage spike associated with fast current switching (*i.e.*, $V = -L dI/dt$) has the proven ability to seriously damage the power supplies (the measured inductance of each axial coil is $250 \mu\text{H}$ and the radial coils are each about $20 \mu\text{H}$). We therefore low-pass (time constant, $\tau = 3.2 \text{ ms}$) and unity-gain buffer the analog signal from the ADWin in order to smooth the switching voltage and prevent electronic feedback from the supplies damaging the computer and control circuitry.

The properties of each coil pair are given in Table 3.3. The z -axis (axial) coil pair produces a field very well aligned with the cavity axis and we generally use these coils to determine the quantization axis where experimentally relevant. The x - and y -axis coils are not aligned with the cavity birefringent axes and so when transverse magnetic bias fields are required, we must take note of this fact as needed. In Section 4.3, I will describe a technique we have developed for performing single atom Raman magnetometry in order to (among other things) calibrate the bias coils and use them to locally null the static magnetic field. In Section 3.6, I will describe the timing scheme for switching coil current settings in the context of the overall experimental timing sequence.

3.3 Intracavity Optical Dipole Trapping

With the ability to introduce cold atoms to the cavity mode as they fall from the lower MOT, we are in principle now ready to undertake cavity QED measurements. Indeed, there is a large body of published work regarding observations of strong coupling between cold, freely-falling atoms and a Fabry-Perot cavity [32]. There has even been experimental demonstrations of a weak trapping force applied to an intracavity atom by the QED field, itself [33].

However, unlike these earlier “atom cavity microscope” experiments wherein the QED and trapping potential were necessarily intertwined, we want to study trapped-atom cavity QED in a fundamentally different way. By exerting a trapping force on the atom which is

decoupled from the QED field, we are able to continuously observe strong coupling between a single atom and the cavity for as many as four orders of magnitude longer than ever previously recorded. In doing so, we are able to perform entire experiments on one-and-the-same atom and to begin to exert some coherent control over the coupled system. In this Section, I will describe the all-optical technique we employ to trap atoms inside a cavity mode standing wave dipole trap.

3.3.1 The Optical Dipole Force

In this Subsection, I will present two pictures of the optical dipole force, classical and quantum. Ordinarily, I would skip completely over the classical picture as it is a gross approximation to the far more relevant quantum mechanical description; however the classical model does offer useful insight into the actual physical phenomena at work and so it worth giving it a very brief treatment.

Classical Picture

An atom characterized by an electric polarizability, α , will produce a dipole moment

$$\vec{p} = \alpha \vec{E} \quad (3.26)$$

when placed in an electric field (for cesium the static polarizability is $\alpha/(4\pi\epsilon_0) = 59.6 \times 10^{-30} \text{ m}^3$ [34]). That electric field, in turn, applies a force on the dipole:

$$\vec{F} = (\vec{p} \cdot \nabla) \vec{E} \quad (3.27)$$

which corresponds to a potential energy:

$$U_{dip} = -\vec{p} \cdot \vec{E} = -\alpha |\vec{E}|^2. \quad (3.28)$$

Or, for an electromagnetic wave of spatially-varying intensity $I(\vec{r})$:

$$U_{dip} = -\frac{2\alpha}{c\epsilon_0} I(\vec{r}). \quad (3.29)$$

This classical picture predicts two important phenomena - an electric field will distort the outer electron shell of an atom so as to create an induced dipole moment. At the same time, that induced dipole will interact with the field, producing a mechanical potential for the atom which varies linearly with optical intensity. As we will see, both predictions are accurate and the commonly used “optical tweezers” technique in biology and chemistry relies explicitly on this model [35]. However, as we will also discover, the classical picture neglects the important frequency dependence of the field. This dependence is made manifest in the quantum picture as we treat the discrete set of atomic energy levels to which the field can couple (and from which it can potentially scatter).

Two- and Three-State Quantum Picture

The quantum treatment of the dipole force follows a line of reasoning similar to the classical description. However, rather than assuming that the field induces a linear dipole moment in the atom, we instead will calculate the energy level shifts within the atom and explore how they vary spatially to create a potential. We will begin (as always) with a two-state atom for simplicity and scale the model up to the more complicated full cesium spectrum of energy levels in the next Subsection.

The problem we want to consider is a two-state atom with energy level spacing $E_A = \hbar\omega_A$ which is driven far-from-resonance by a field $\vec{E}(\vec{r}) = E_0(x, y)\hat{\epsilon} \cos(kz - \omega_D t)$. We will model the interaction between atom and field as a dipole coupling and construct a model perturbative Hamiltonian in analogy with the derivation of the Jaynes-Cummings Hamiltonian in Chapter 2 (here, however, the driving field is not treated quantum mechanically). Following from Equation (2.14), in the $\{|g\rangle, |e\rangle\}$ basis:

$$H_{dip} = \frac{\hbar}{2} \begin{pmatrix} (\omega_D - \omega_A) & \Omega \\ \Omega & (\omega_A - \omega_D) \end{pmatrix}. \quad (3.30)$$

Here we have made the same assumptions that lead to the earlier equation - particularly the rotating wave approximation. We have also defined Ω , the “classical” Rabi frequency

(as opposed to g_0 , the single-photon Rabi frequency):

$$\Omega = -\frac{\vec{E}(\vec{r})}{\hbar}d = \frac{e\vec{E}(\vec{r})}{\hbar}\langle e|\hat{r}|g\rangle. \quad (3.31)$$

The eigenenergies for the system represent the dressed states splittings:

$$E_{e',g'} = E_{e,g} \mp \frac{\hbar}{2}\sqrt{\Delta^2 + \Omega^2}. \quad (3.32)$$

In the easily obtainable limit $\Omega \ll |\Delta|$, Taylor-series expansion gives the AC Stark shifts (or light shifts):

$$\Delta E_g = \frac{\hbar\Omega^2}{4\Delta} \quad \text{and} \quad \Delta E_e = -\frac{\hbar\Omega^2}{4\Delta}. \quad (3.33)$$

Also, in the limit where $|\Delta| \gg \gamma$, we can largely ignore incoherent scattering of the classical field and therefore the potential that the atom experiences is given by:

$$U_{e,g}(\vec{r}) = \pm \frac{e^2}{2c\epsilon_0\hbar\Delta} I(\vec{r}) |\langle e|\hat{r}|g\rangle|^2 \quad (3.34)$$

$$= \pm \frac{\hbar\gamma^2}{2\Delta I_{sat}} I(\vec{r}). \quad (3.35)$$

Note that the quantum theory and the classical theory agree with respect to the functional dependence of potential energy on field intensity. The energy shifts associated with the AC Stark splitting can be interpreted physically as a small perturbation to the shape of the valance electron shell giving the atom a small extrinsic dipole moment.

For red (blue) detuned light, the atomic ground state sees an attractive (repulsive) potential and the excited state sees a repulsive (attractive) potential. From an experimental point-of-view, while it is useful that one state is trapped, this is a fundamentally undesirable circumstance. We can circumvent this problem by adding an ancillary third energy level, $|u\rangle$ to the atom which exhibits a dipole coupling only to state $|e\rangle$ (in a real atom with a multiplicity of higher-lying excited states, this addition is far less ad hoc). We assume the classical field is detuned by Δ' with respect to the transition between $|u\rangle$ and $|e\rangle$, which has characteristic halfwidth γ' . Following the previous derivation, the potential felt by

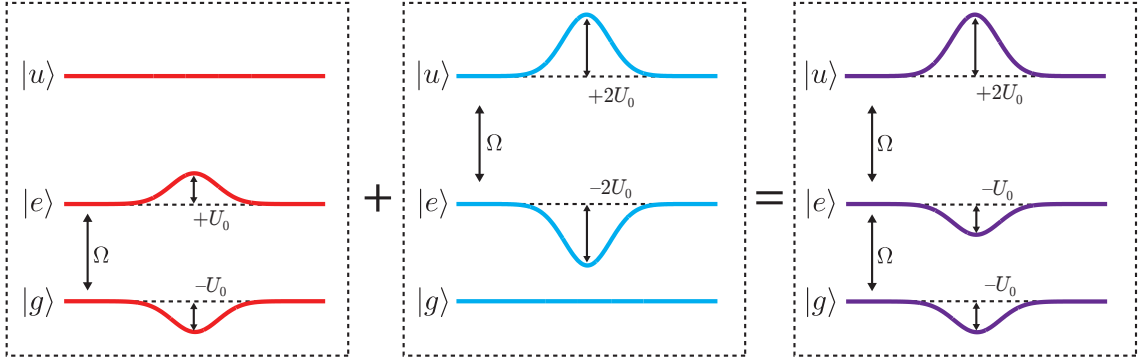


Figure 3.10: Schematic illustration of the “magic” wavelength effect for a three-state atom. By way of dipole coupling to an ancillary state $|u\rangle$, the state $|e\rangle$ sees an attractive potential of maximum depth, $-U_0$, which is approximately equal to the potential seen by the ground state, $|g\rangle$.

population in state $|e\rangle$ is now:

$$U_e(\vec{r}) = \frac{\hbar}{2} \left(\frac{\gamma^2}{\Delta I_{sat}} - \frac{\gamma'^2}{\Delta' I'_{sat}} \right) I(\vec{r}). \quad (3.36)$$

The ground state potential is unchanged. Therefore, for favorable parameters $(\Delta', \gamma', I_{sat})$ we can produce a trapping potential of equal depth for both states in which we are interested. This effect is depicted graphically in Figure 3.10. Wavelengths at which this serendipity occurs are colloquially referred to as “magic” wavelengths, and the application of this principle to atomic cesium will be the focus of the next Subsection.

3.3.2 Cesium’s “Magic” Wavelength

The most significant difference between treating the light shifts on the three-level atom and on a real cesium atom is that we can no longer simply fold the dipole matrix elements for each state into the linewidth, γ . In Chapter 2 we went through the details of calculating the geometric and angular components of atomic dipole matrices via reduced matrix elements and Wigner 3- j and 6- j symbols, so I won’t go into any detail here (for a more thorough discussion see the excellent notes in the dissertations of David Boozier [15] and

Jason McKeever [22]).

As an example we can calculate the light shifts on the $|4, m_F\rangle$ states which result from coupling to the $D1$ and $D2$ transitions [22]:

$$U_{4,m_F}(\vec{r}) = \frac{\pi c^2 \gamma_{D2}}{\omega_{D2}^3} \left[\frac{2 + qg_F m}{\Delta_{D2}} + \frac{1 - qg_F m_F}{\Delta_{D1}} \right] I(\vec{r}) \quad (3.37)$$

where $q \in \{0, \pm 1\}$ corresponds to a linear, left- or right-circularly polarized classical field, Δ_{D1}, Δ_{D2} are the detunings of the field from the two cesium D lines and g_F is the Landé g -factor. Note that when calculating U_3 , the detunings differ from those for U_4 by the cesium ground state hyperfine splitting (*i.e.*, $(\Delta_{D1} + \Delta_{HF}), (\Delta_{D2} + \Delta_{HF}), \Delta_{HF} \sim 9.2$ GHz) which produces a small, differential light shift between the two states:

$$\Delta U_{4-3,m_F}(\vec{r}) = \frac{\pi c^2 \gamma_{D2}}{\omega_{D2}^3} \left[\frac{\Delta_{HF}}{\Delta_{D2}} \frac{2 + qg_F m}{\Delta_{D2} + \Delta_{HF}} + \frac{\Delta_{HF}}{\Delta_{D1}} \frac{1 - qg_F m_F}{\Delta_{D1} + \Delta_{HF}} \right] I(\vec{r}). \quad (3.38)$$

Also, note that there is a linear dependence on the projection quantum number, m_F , and on q such that for an elliptically or circularly polarized classical field the effect on the atom is to shift the Zeeman states as if they were in the presence of a uniform, weak magnetic field along the polarization axis of the light. This magnetic “pseudo-field” effect will prove to be important within the context of cavity birefringence.

We can generalize Equation (3.37) to states within the $6P_{3/2}$ excited state manifold by considering couplings to $nS_{1/2}$, $n'D_{3/2}$ and $n'D_{5/2}$ states with principle quantum numbers $n \geq 6$ and $n' \geq 5$. Similarly, we can expand (3.37) to include terms corresponding to $6S_{1/2}$ to $nP_{1/2}$ and $nP_{3/2}$, $n > 6$. Using this model, the Stark shifts on the Zeeman substates within the $(6S_{1/2}, F = 4)$ and $(6P_{3/2}, F' = 5)$ hyperfine manifolds are shown in Figure 3.11 for a linearly-polarized classical field. Note that the $(6S_{1/2}, F = 3, 4)$ ground states exhibit no m_F -dependent stark shift, while the excited states generally show a quadratic dependence of m_F . A “magic” wavelength occurs where the shifts for the two states intersect and are both negative (*i.e.*, trapping) - for cesium this occurs near $\lambda \sim 935$ nm.

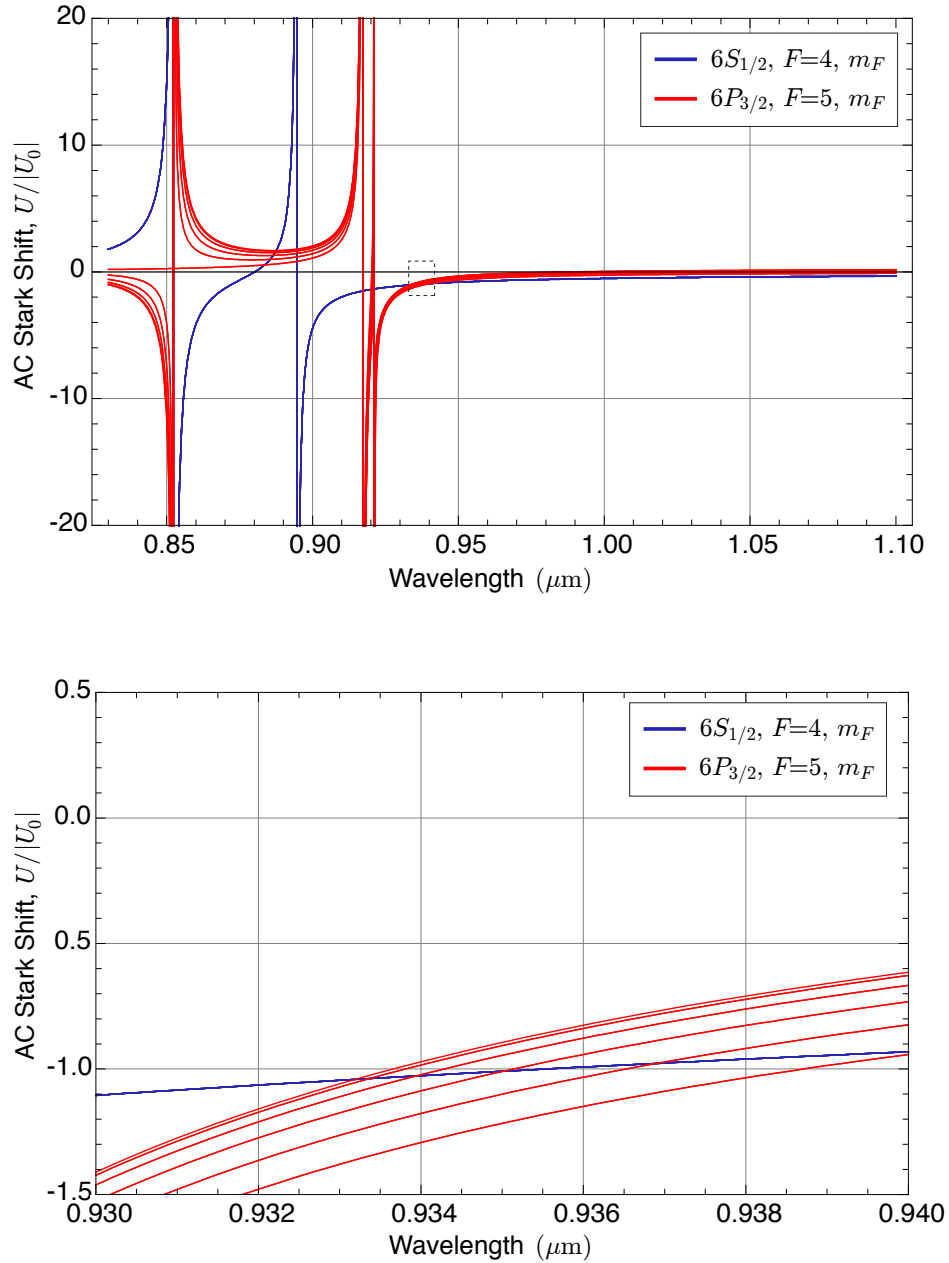


Figure 3.11: AC Stark shifts on all Zeeman states within the $(6S_{1/2}, F = 4)$ (green) and $(6P_{3/2}, F' = 5)$ (red) hyperfine levels for linearly-polarized light. The inset view shows the range of wavelengths over which both states see trapping potentials of approximately equal depth. Shifts are given in units of $|U_0|$, the magnitude of the shift on the $6S_{1/2}, F = 4$ clock state at $\lambda_F = 935.568$ nm.

3.3.3 A State-Insensitive Trap

In order to form a trap using the optical dipole force (also known as a far off-resonance trap, or FORT) we take advantage of the physics cavity and drive a resonant mode. The standing wave associated with that mode constitutes the classical trapping field. This has two advantages: first, the transverse structure of the trap and the QED field are well-overlapped (the longitudinal registration, however, is more complicated) and second, the cavity build up factor \mathcal{B} (Equation (2.118)) allows for a very deep trap at the expense of very little input optical power.

The Trap

When the cavity length is locked such that mode $m = 99$ corresponds to resonance with the cesium ($6S_{1/2}, F = 4$) \leftrightarrow ($6P_{3/2}, F' = 5$) transition, mode $m' = 90$ is resonant at $\lambda_F = 935.568$ nm which very near the cesium “magic” wavelength. As far as I know, this was not by design - before our group implemented the “magic” wavelength technique, FORT wavelengths of 869 nm and 906 nm were used to very little success (trapping times, $T < 100$ ms) [21].

At λ_F , the cavity mode waist is $w_F = 24.83$ μ m and the measured halfwidth is $\kappa_F = 0.79$ GHz. This far from the center of the mirror coating curve, the dominant loss mechanism is transmissive ($T \sim 1.4 \times 10^{-3}$) not dissipative ($l \sim 10$ ppm, which is largely insensitive to wavelength). It follows that cavity finesse is $\mathcal{F}_F \sim \pi/T = 2.2 \times 10^3$ and the maximum transmission coefficient for a mode-matched beam is $\mathcal{T}_{max} \sim 1$. The maximum intensity of the FORT, as a function of cavity output power, P_{tran} , measured at an antinode of the field is:

$$I_0 = \frac{2\mathcal{B}}{\pi w_F^2} P_{tran} = \frac{8\mathcal{F}}{\pi^2 w_F^2} P_{tran}. \quad (3.39)$$

We choose to define I_0 in terms of transmitted power instead of incident power because transmission is more straightforward to measure experimentally. For this intensity, the simple model from Equation (3.37) predicts that the trap depth for the ($6S_{1/2}, F = 4$) clock

state per milliwatt of output power is:

$$U'_0/P_{tran}\hbar = -39.4 \text{ MHz/mW} \quad \text{or} \quad |U'_0|/P_{tran}k_B = 1.9 \text{ mK/mW}. \quad (3.40)$$

The more complete picture, which includes counter-rotating terms and coupling to states with larger principle quantum numbers, gives a small correction:

$$U_0/P_{tran}\hbar = -40.9 \text{ MHz/mW} \quad \text{or} \quad |U_0|/P_{tran}k_B = 2.0 \text{ mK/mW}. \quad (3.41)$$

The small differential shift between the $F = 3, 4$ hyperfine ground states (Equation (3.38)) is:

$$\Delta U_{0,4-3}/|U_0| = 530 \text{ Hz/MHz}. \quad (3.42)$$

At the trap depths we commonly use in the laboratory ($U_0 \sim 40$ MHz), this shift is small but easily measurable and will be discussed in Chapter 4.

The Stark shifts on each of the Zeeman states within the $6P_{3/2}$ fine structure manifold are calculated in Figure 3.12, again for a linearly polarized trap at λ_F with states projected along the polarization axis of the field. These states lie in a $\sim 30\%$ spread around $|U_0|$, which means that for a trap depth of $U_0 \sim -40$ MHz, the $(6P_{3/2}, F' = 5, m_F = 0)$ state is split from the edge states within the same manifold by ~ 13 MHz. This is an important effect, and one which any complete model of our atom-cavity system will have to consider. I should briefly mention that for our nominal trap depth, the magnetic “pseudo-field” effect mentioned in the previous subsection can produce differential shifts between ground and excited state Zeeman levels in excess of 50 MHz. We have observed that for a circularly-polarized input to the FORT mode, the laser beams generally used to load, cool and address the atom in a linearly-polarized configuration are shifted so far away from resonance that they have no appreciable effect on the atoms and therefore we are unable to load atoms into the FORT in this configuration.

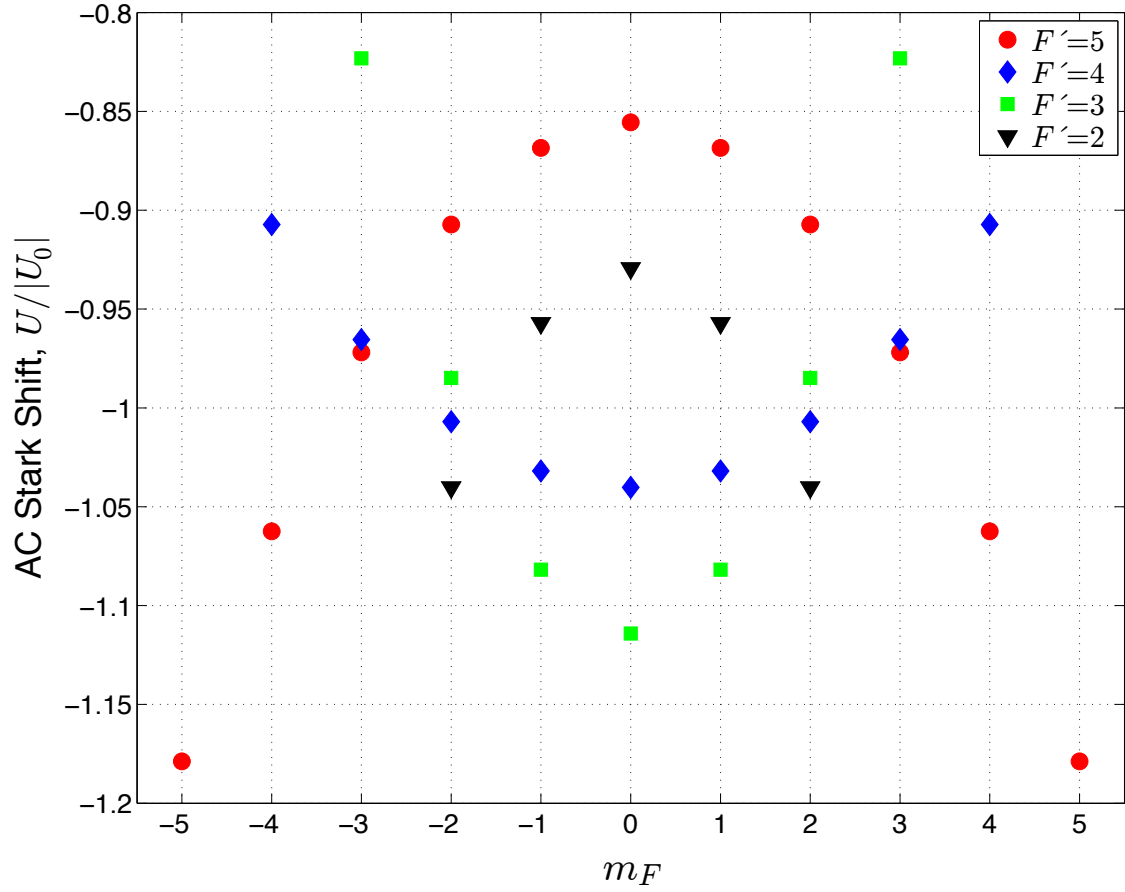


Figure 3.12: Zeeman state AC Stark shifts within the $6P_{3/2}$ fine structure manifold of states for a linearly polarized FORT. The quantization axes lies along the polarization vector of the field. Shifts are given as a fraction of the nominal trap depth U_0 for the $(6S_{1/2}, F = 4)$ clock state.

The FORT mode is even-parity ($m' = 90$) and so the shape of the trap is:

$$U(x, y, z) = U_0 \sin^2 \left(\frac{\omega_F z}{c} \right) \exp \left[-2 \frac{x^2 + y^2}{w_F(z)^2} \right]. \quad (3.43)$$

While generally anharmonic, around local maxima (*i.e.*, radially, near $(x, y) = 0$, and longitudinally, near $z = (n + 1/2)[\pi c/\omega_F]$) we can perform Taylor expansion of $U(x, y, z)$ and make a harmonic approximation. In this approximation, near the bottom of the trap, the axial and radial oscillation frequencies are:

$$\omega_{ax} = \sqrt{\frac{2\omega_F^2 |U_0|}{c^2 m}} \quad \Rightarrow \quad \frac{\omega_{ax}}{P_{tran}} = (2\pi)(530 \text{ kHz})/\text{mW} \quad (3.44)$$

$$\omega_{rad} = \sqrt{\frac{4|U_0|}{m w_F^2}} \quad \Rightarrow \quad \frac{\omega_{rad}}{P_{tran}} = (2\pi)(4.5 \text{ kHz})/\text{mW}. \quad (3.45)$$

The axial vibrational frequencies are, of course, larger because the confinement along that axis (trap dimension $\sim \lambda_F/2\pi$) is much tighter than along the transverse axes (trap dimension $\sim w_F$).

It is also possible to treat the problem of 1-dimensional motion along the cavity axis analytically. The Shrödinger equation for the system is:

$$-\frac{\hbar^2}{2m} \frac{\partial^2}{\partial z^2} \psi(z) + U_0 \sin^2 [\omega_F z/c] \psi(z) = E \psi(z). \quad (3.46)$$

We can rewrite this in the convenient form:

$$\psi''(z) + (a - 2q \cos [2\omega_F z/c]) \psi(z) = 0, \quad (3.47)$$

where:

$$a = -\frac{m c^2}{\hbar^2 \omega_F^2} (U_0 - 2E) \quad \text{and} \quad q = -\frac{m c^2 U_0}{2 \hbar^2 \omega_F^2}. \quad (3.48)$$

This is the well-known Mathieu equation [36]. The eigenvalues of this equation, a_n , cannot be expressed in closed form, but appear rather as an infinite recursion relation (Mathematica's `MathieuCoefficientA` routine will calculate the a_n for an arbitrary Floquet parameter, q).

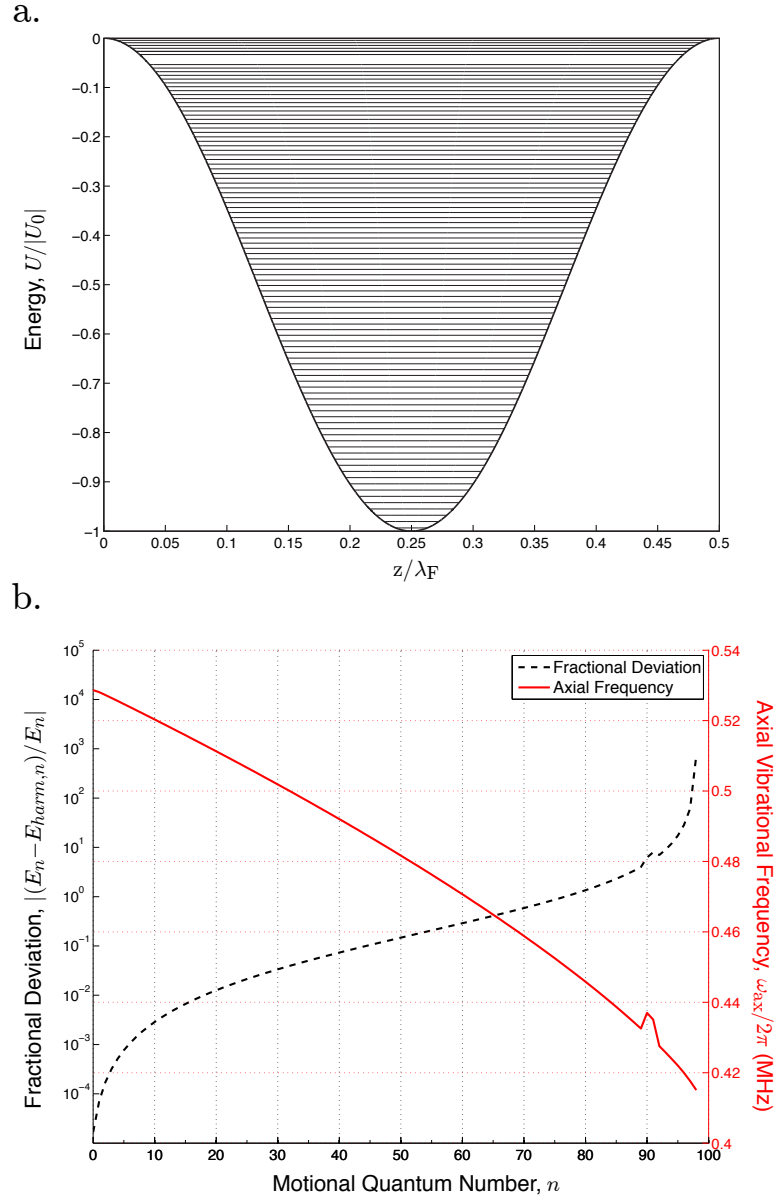


Figure 3.13: a. Motional energy eigenvalue spectrum a 1-D sinusoidal FORT with $|U_0| = 40$ MHz, $\lambda_F = 935.586$ nm. b. Deviation from the harmonic approximation of the full Mathieu picture (---) as a function of motional quantum number, n . Also, axial vibrational frequency $\omega_{ax}/(2\pi)$ (—) as a function of n .

The motional energy eigenvalue spectrum for a cesium atom in a FORT of depth $|U_0| = 40$ MHz at $\lambda_F = 935.586$ nm is calculated in Figure 3.13a. For this potential, the highest energy bound state corresponds to $n = 98$. Near the top of the well, the emergence of band structure (a consequence of tunneling within the full, periodic potential) starts to become visible.

The left-hand axis (dashed, black trace) of Figure 3.13b presents a calculation of the deviation of the energy of the n th eigenstate of the Mathieu potential, E_n , from the corresponding energy in the harmonic approximation, $E_{\text{harm},n} = \hbar\omega_{ax}(n + 1/2)$, as a fraction of E_n . Over more than half of the well depth we see that the two agree to at least the level of 10%. The right-hand axis (solid, red trace) of Figure 3.13b corresponds to the approximate vibrational frequency of the atom in the n th motional energy eigenstate (calculated by assuming $\omega_{ax}(n) = [E_n + |U_0|]/[\hbar(n + 1/2)]$). We can see that there's a variation of $\sim 27\%$ in ω_{ax} from the bottom of the well (where it agrees very nicely with the harmonic model) to the top.

Performing a similar analysis of the radial motion is a bit more complicated because Gaussian potentials do not support analytic solutions to Schrödinger's equation. One could, in principle, perform numeric integration, use the WKB method or use variational calculus. However, I will omit any discussion of the radial anharmonicity, as there is no further discussion of quantized motion along these degrees of freedom in this dissertation.

Loading the FORT

The force applied to the atom by the FORT is dominantly conservative. Therefore, in order to load an atom in the trap, we must apply some sort of initial damping force. The way we do this in the laboratory is to address the atoms as they fall through the cavity mode with two pairs of polarized, detuned, counter-propagating laser beams. These beams enter the cavity through the $d = 41.4$ μm gap between the mirrors and affect what is known as polarization gradient (PG) cooling.

The idea underlying PG cooling is that by counter-propagating two, orthogonally polarized beams (lin \perp lin, or $\sigma^+ - \sigma^-$) we create a field of polarization which varies spatially on the scale of the wavelength. An atom with zero velocity along the wave vectors, $\pm\vec{k}$, of the

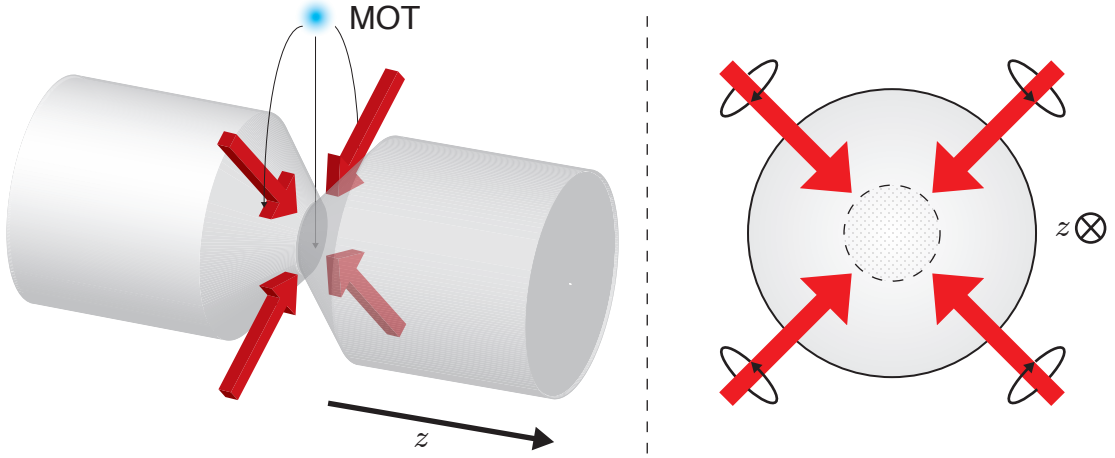


Figure 3.14: Configuration of the cavity loading lattice “side” beams for polarization gradient cooling falling atoms into the FORT. Nominally, each beam consists of light $\delta = +10$ MHz blue detuned from both $(6S_{1/2}, F = (3, 4)) \leftrightarrow (6P_{3/2}, F' = (3, 4))$ transitions. The $\sigma^+ - \sigma^-$ configuration of the beams is shown, at right.

beams will gradually be pumped into a dark state with respect to a quantization axis defined relative to the local polarization vector. However an atom with a sufficiently large velocity component along $\pm \vec{k}$ will move through the polarization gradient quickly enough that its internal state won't be able to adiabatically follow. Without adiabatic following, the atom remains coupled to the light and therefore, for fields of the proper detuning, absorption and scattering relative to movement along $\pm \vec{k}$ can apply a damping force.

In the laboratory, we have found that for loading into our FORT the slightly unusual “grey molasses” scheme presented by the group of C. Salomon in Paris [37] is useful. Whereas most PG cooling schemes [31] rely on detuning the cooling beams slightly red of a $F \rightarrow F' = F+1$ transition, this scheme works for light detuned blue of a $F \rightarrow F' \in \{F, F-1\}$ transition. Salomon's initial demonstration was for $(6S_{1/2}, F = 3) \leftrightarrow (6P_{3/2}, F' = 2)$, but we have implemented the analogous scheme for light $\delta = +10$ MHz blue of $(6S_{1/2}, F = (3, 4)) \leftrightarrow (6P_{3/2}, F' = (3, 4))$. I indicate both $F = (3, 4)$ because, as both transitions are not closed, we must implement a repumping field to prevent the atom from falling into an uncoupled hyperfine ground state. What we end up with is a ‘chicken and egg’ situation

where both the “cooling” field and the “repump” field are detuned from atomic resonance and are $\sigma^+ \text{-} \sigma^-$ polarized along the cooling axis. Which beam is doing the cooling and which is doing the repumping is entirely a matter of where the atomic population is distributed between the hyperfine ground states.

The spatial configuration of the two PG cooling (or “lattice”) pairs is shown in Figure 3.14. Each counter-propagating pair is $\sigma^+ \text{-} \sigma^-$ -polarized and consists both “cooling” and “repumping” fields. These beams are appropriately polarized and then focused through the cavity aperture via 15 cm cylindrical lenses. The total intensity in each arm (both “cooling” and “repumping” fields, with the power very roughly equally balanced between the two) is $\sim 200 \text{mW/cm}^2$. In Subsection 3.5.2 I will discuss how the intensity of these side beams is distributed in the center of the cavity following diffraction by the cavity aperture. However, for purposes of PG cooling, this diffraction effect is not significant.

The lattice beams are switched ON for 5 ms after the release of the lower MOT in order to damp the motion of any atoms which transit the cavity mode. This configuration, for standard operating characteristics of our lower MOT, is sufficient to load an atom into the FORT with, at most, probability $P_l \approx 0.1$ (because of the thermal distribution of atomic trajectories as the MOT cloud expands, the loading probabilities for 1, 2, 3 . . . atoms ($P_{l,1}, P_{l,2}, P_{l,3}, \dots$) are very well approximated by Poissonian statistics). Estimates, to be discussed in later Chapters, indicate that, after the cooling cycle is complete, atom remain in the trap with mean temperature $T \sim 200 \mu\text{K}$.

In the next Chapter, I will describe a slight modification to this scheme where we have replaced the “repump” field (in practice it doesn’t matter which) with a very large-Rabi frequency Raman pair which drives population directly between the $F = (3, 4)$ ground state manifolds. This pair has the decided advantage of repumping most strongly at locations of maximum FORT potential and ultimately provides a much more effective loading method (as measured by a greatly increased probability to observe a trapped atom post-MOT drop).

The first demonstration of this trapping technique [2] was in 2003, shortly before I joined the group. A FORT potential of $|U_0| \approx 50 \text{ MHz}$ in this configuration is characterized by trap lifetimes of $T_{avg} = 2.4 \pm 0.2 \text{ s}$ in the dark (*i.e.*, in the absence of any near-resonant optical fields). This is likely limited by collisions with background particles in the UHV

chamber [21]. In the presence of near resonant driving (cavity probes, “side” beams, etc.) the trap lifetime can, however, be considerably less than T_{avg} (the heating rate for any particular configuration of these fields is governed by the atom-field dynamics).

Cavity QED in the FORT

A final consideration we must make with respect to the intracavity FORT is how the trap affects cavity QED measurements. We have already discussed two of the most significant effects: Zeeman state splitting as a result of the “pseudo” magnetic field produced by a circularly-polarized trapping field and the differential shifts on Zeeman levels within excited state hyperfine manifolds, even for a linearly polarized trap. Both effects manifest themselves as state-dependent atom-cavity detunings. The first effect can be negated by driving the FORT mode only with light linearly-polarized along one of the cavity’s birefringent axes. The second effect is largely unavoidable and so we must include these shifts in any model of the system, where relevant.

The third effect we need to consider is the registration of the FORT wells with respect to the cavity QED field. There are $m = 90$ FORT wells in our cavity, with the $(q + 1)$ th well located at:

$$z_{max}(q) = (2q + 1) \frac{\lambda_F}{4} - \frac{L}{2}. \quad (3.49)$$

The value of $\psi_0(q) \equiv \psi(z_{max}(q), 0, 0)$, the dimensionless amplitude of the QED field, at each of these FORT anti-nodes is:

$$\begin{aligned} \psi_0(q) &= \cos\left(\frac{2\pi z_{max}(q)}{\lambda_{D2}}\right) \\ &= \cos\left(\pi \frac{(2q + 1)}{2} \frac{\lambda_F}{\lambda_{D2}} - \pi \frac{L}{\lambda_{D2}}\right) \end{aligned} \quad (3.50)$$

$$= -\cos\left(\pi \frac{(2q + 1)}{2} \frac{\lambda_F}{\lambda_{D2}}\right) \quad (3.51)$$

Therefore, each FORT well is associated with a local maximum rate of coherent coupling, $|g_q| \equiv g_0 |\psi_0(q)|$. The value of $|\psi_0(q)| = |g_q|/g_0$ at each of the 90 FORT well locations, $z_{max}(q)$, is shown in Figure 3.15a. The slight lateral asymmetry in this plot about $z = 0$ is

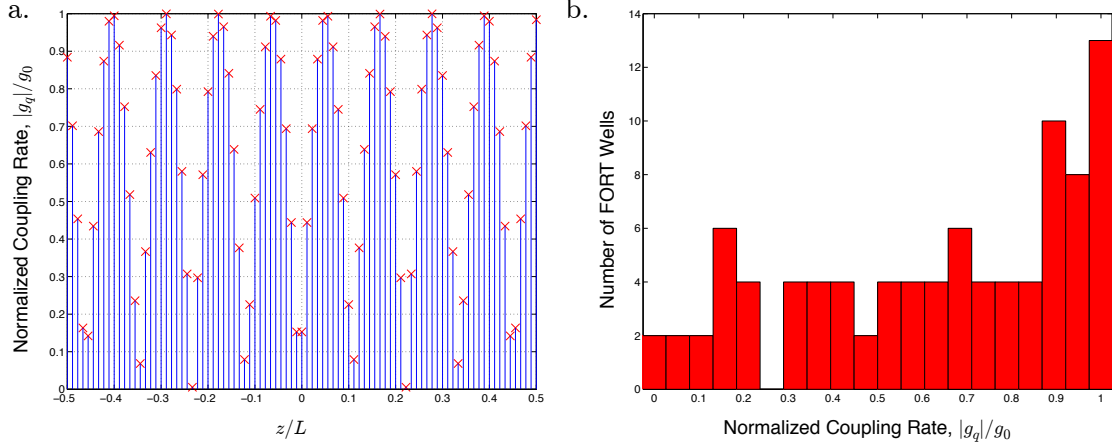


Figure 3.15: a. Stem plot of the normalized rates of coherent coupling, $|g_q|/g_0$ (\times) for each of the $m = 90$ FORT wells as a function of well location $z_{max}(q)$. b. Histogram of coupling rate $|g_q|/g_0$ versus number of wells exhibiting that rate. Each bin is $g_0/25$ wide.

due to the parity difference between the QED and FORT fields. Figure 3.15b. shows the distribution of coupling rates in histogram form. There are 46 unique values of $|\psi_0(q)|$ for this FORT-QED configuration, though they tend to be clustered.

In principle, our loading technique permits falling atoms to be cooled into any of the FORT wells (though likely not with uniform probability). At present, we have no viable experimental technique for measuring into which well a given atom is loaded. Especially for measurements where we perform ensemble averaging over multiple single atom loading events from multiple MOT drops, the distribution of atoms into well-coupled and poorly-coupled wells is an important experimental parameter.

The final consideration we need to make is the impact of the finite axial and radial temperatures of the atom on the QED coupling rate. Motion of an atom within a FORT well translates into modulation of the local vacuum Rabi frequency, $g(\vec{r})$. In general, the temperature of the atom during an experiment is given uniquely by the characteristics of that experiment - for instance an atom being strongly probed on resonance will experience rapid heating whereas an atom undergoing stimulated Raman cooling will likely exhibit longer trap lifetimes than in the dark. We therefore can make no *a priori* claims about this

effect, but instead must address it on a case-by-case basis.

3.4 Lasers and Frequency Servos

In this section I will describe the lasers and fields which are commonly used in the laboratory to near-resonantly address cesium atoms. I will primarily focus on the frequency stabilization techniques used to reference our three cesium principle lasers and how the same system is used to actively stabilize the physics cavity length. Finally, in the interest of space and concision, I will present a diagrammatic overview of how we derive from these lasers the fields and beams necessary to cool, trap and manipulate intracavity atoms.

3.4.1 Cesium Lasers

There are three lasers on the Lab 11 optics bench which are tuned to drive transitions within the cesium $D2$ manifold. I will refer to these three as “master”, “slave” and “repumper.” The significance of these names has become largely indistinct over the past 4-5 years; however, I will maintain the terminology in the interest of consistency with other theses and lab notebooks. The master and slave lasers are near-resonant with transitions from the $(6S_{1/2}, F = 4)$ hyperfine ground state and the repumper couples transitions from $(6S_{1/2}, F = 3)$. Throughout the remainder of this chapter I will refer to transitions between $(6S_{1/2}, F)$ hyperfine states and $(6P_{3/2}, F')$ hyperfine states as $(F \leftrightarrow F')$ transitions. All three are diode lasers - the master and repumper are external cavity diode lasers in a Littrow geometry and the slave is a free-running diode.

Master Laser and Transfer Cavity

The master laser optical configuration is depicted in Figure 3.16. A fraction of the total laser output power (~ 35 mW) is directed through an electro-optic modulator and used to stabilize the laser frequency to the length of an independently stabilized transfer cavity. The error signal for this lock is derived using the Pound-Drever-Hall technique in reflection from the transfer cavity [38].

With a portion of the light from the now cavity-stabilized master laser, the length of

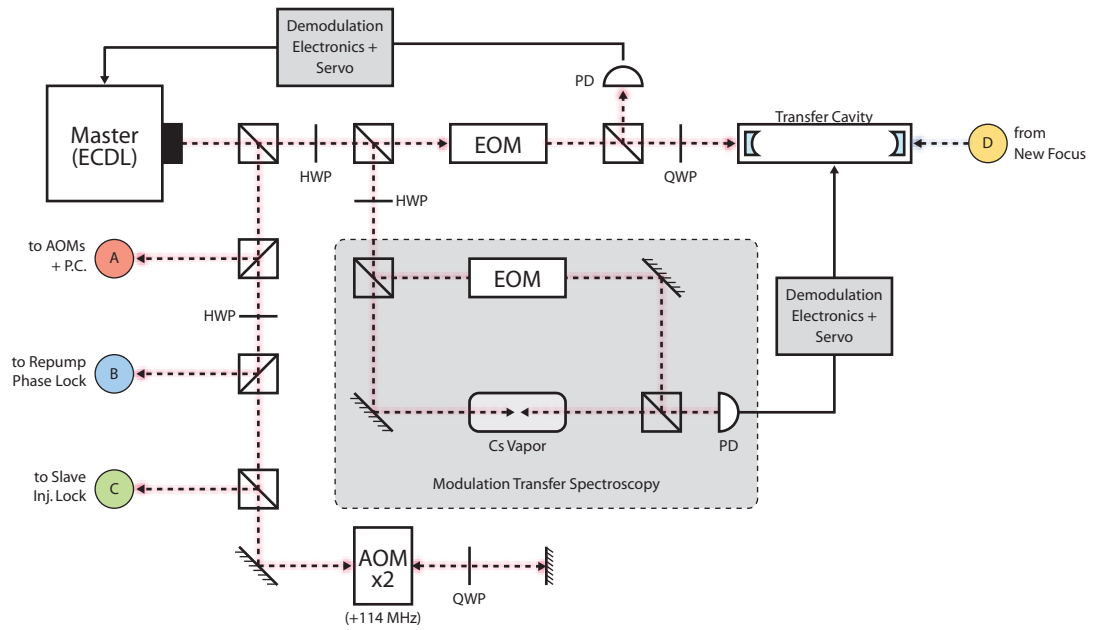


Figure 3.16: Schematic drawing of the master laser beam paths and servo configuration. In the interest of concision, this drawing does not represent the geometry of the beam paths on the optics bench. Abbreviations are for quarter-wave plate (QWP), half-wave plate (HWP), electro-optic modulator (EOM), acousto-optic modulator (AOM), and physics cavity (P.C.). All cubes are polarizing beam splitters (PBS). Colored circles and letters indicate a beam which enters another part of the apparatus as depicted schematically elsewhere in this Chapter.

the transfer cavity is then itself stabilized by modulation transfer spectroscopy in a small cesium vapor cell. We choose to lock the transfer cavity to the $(4 \leftrightarrow [4', 5'])$ “crossover” resonance. Crossover resonances are a common feature of pump-probe spectroscopy on transitions exhibiting multiple hyperfine states [39] - they are the result of the probe addressing transitions to one hyperfine level for a certain class of atomic velocities while the counter-propagating pump beam drives transitions to a second set of states. The resonant frequency of the crossover lies exactly midway between the resonances for each of the two hyperfine manifolds (so the master is detuned $\Delta = (2\pi)(125.5)$ MHz blue of $(4 \leftrightarrow 4')$ and red of $(4 \leftrightarrow 5')$).

As we will discuss in the next Subsection, in order to actively stabilize the physics cavity length we need a laser which is stable with respect to our QED probe field but detuned by $1 - 2$ FSR ($10 - 20$ nm) from the QED transition (in order to decouple any atomic physics from the servo). By design, the transfer cavity supports resonances over a broad spectrum in the near-infrared and we are thereby able to transfer the stability of its cesium-referenced lock to a laser at any wavelength within its optical bandwidth (hence the name transfer cavity). The transfer cavity is the only system in the entire lab which is independently stabilized with respect to a transition in cesium. The rest of the lasers are frequency locked either with respect to the transfer cavity or injection/phase locking to transfer cavity-stabilized beams.

As will be discussed in Section 3.5, the master laser provides the primary cavity QED probe field (*i.e.*, $(4 \leftrightarrow 5')$ or $(4 \leftrightarrow 4')$) as well as other beams coupling $(4 \leftrightarrow \{3', 4', 5'\})$, as needed.

Slave Laser

The slave laser (Figure 3.17) is a free-running diode with a maximum output power of ~ 105 mW. It is frequency-stabilized with respect to cesium by injection lock from the master laser [17]. A small amount of master laser power ($\sim 800 \mu\text{W}$) is frequency up-shifted by 228.0 MHz ($\Omega_1 = 114.0$ MHz-per-pass) using a double-passed acousto-optic modulator. This light, the injection beam, is then fiber coupled and directed into the “rejection” port of an Optics for Research-brand Faraday isolator located directly at the slave laser output. The

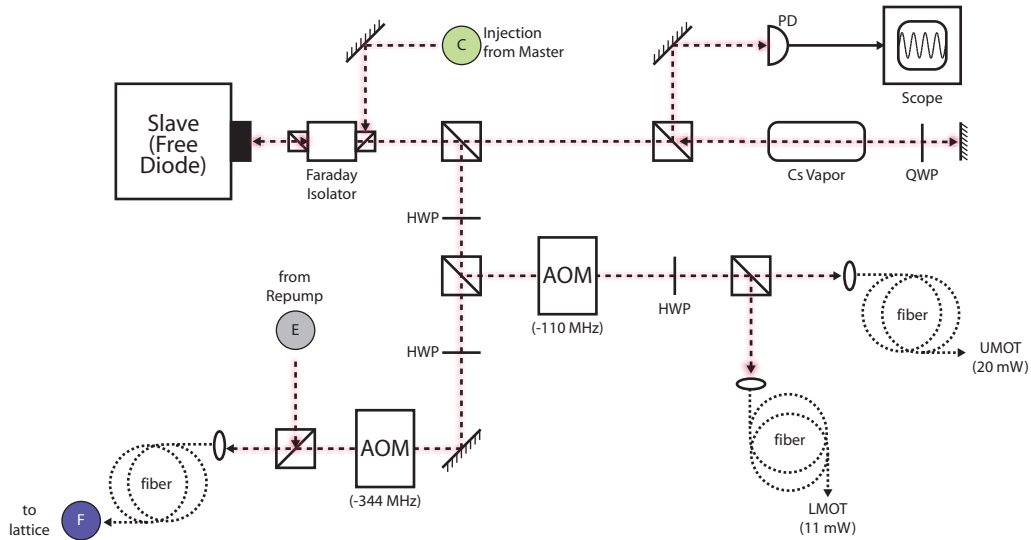


Figure 3.17: Schematic drawing of the slave laser beam paths and servo configuration. In the interest of concision, this drawing does not represent the geometry of the beam paths on the optics bench. Colored circles and letters indicate a beam which enters another part of the apparatus as depicted schematically elsewhere in this Chapter.

injection beam is transmitted back through the isolator and into the diode. For proper temperature and current tuning of the slave diode, as little as $\sim 50 \mu\text{W}$ of injection power can produce a very stable frequency lock at the injected wavelength (so for the laser in its normal configuration, $\Delta = (2\pi)(102.8)$ MHz blue of the $(4 \leftrightarrow 5')$ transition). Twice per experimental cycle we switch the frequency of the double-passed AOM which generates the injection beam to $\Omega_2 = 99$ MHz in order to quickly switch to a PG cooling setting. For more on this aspect of the lock, see Andreea Boca's dissertation [23].

A small portion of the laser's output power is directed to a cesium pump-probe spectroscopy setup in order to verify the quality of the injection lock. This measurement is purely diagnostic and there is no feedback to the laser from the photodiode. The remainder of the laser's power is distributed between MOT beams and lattice/side beams. The MOT

path is split off and downshifted by 110 MHz to be $\Delta = (2\pi)(7.5)$ MHz red of the $(4 \leftrightarrow 5')$ transition. This beam is then divided between the upper and lower MOTs and coupled into the vacuum chamber via polarization-maintaining single-mode optical fiber. The remaining power is downshifted by ~ 340 MHz (the exact value of the shift is determined by the application of the light) to be near-resonant with the $(4 \leftrightarrow 4')$ transition. This light is combined with $(3 \leftrightarrow 3')$ light from the repumper laser and directed to the vacuum chamber via optical fiber to provide lattice (see Section 3.3.3) and cavity side beams.

Repumper Laser

The repumper laser (Figure 3.18) is a diode laser in external cavity configuration. It exhibits a nominal output power of ~ 30 mW. In the present configuration (since mid-2007), approximately $300 \mu\text{W}$ is taken from this laser and combined with unshifted light directly from the master laser using a 50/50 optical fiber coupler. Using a large-bandwidth New Focus 1400-series 25 GHz photoreceiver we measure the optical beat note between the two lasers. The laser is manually tuned (piezo/current/temperature) to a frequency near the $(3 \leftrightarrow 4')$ resonance such that the beat note is near a frequency $\omega_{beat} = \Delta_{HF} - 1/2\Delta_{4'-5'} = (2\pi)(9.067)$ GHz. By mixing this beat note against a stable microwave source at $(2\pi)(9.125)$ GHz, we generate a signal at $(2\pi)(58.5)$ MHz. This signal is then, in turn, amplified and mixed against an RF reference also at 58.5 MHz. Finally the signal, now mixed down to DC, is conditioned (*c.f.*, David Boozer's thesis [15], especially Figure 1.15) and from it an error signal derived. This error signal is divided into two loops - a "slow" loop which feeds back to the laser's external cavity piezo up to ~ 10 kHz and a "fast" loop which is directly combined with the DC current to the diode via bias tee and provides feedback out to ~ 1 MHz. The result is an electronic lock between the phase (and therefore frequency) of the master laser and the repumper laser, with the microwave and RF sources used as local oscillators bridging the frequency difference.

This phase lock technique was implemented in order to address a very specific problem. From the inception of the experiment to early 2007, this laser was locked using a basic Pound-Drever-Hall scheme which was completely independent of the master and slave lasers. Previously this had been acceptable because the light derived from this laser was principally

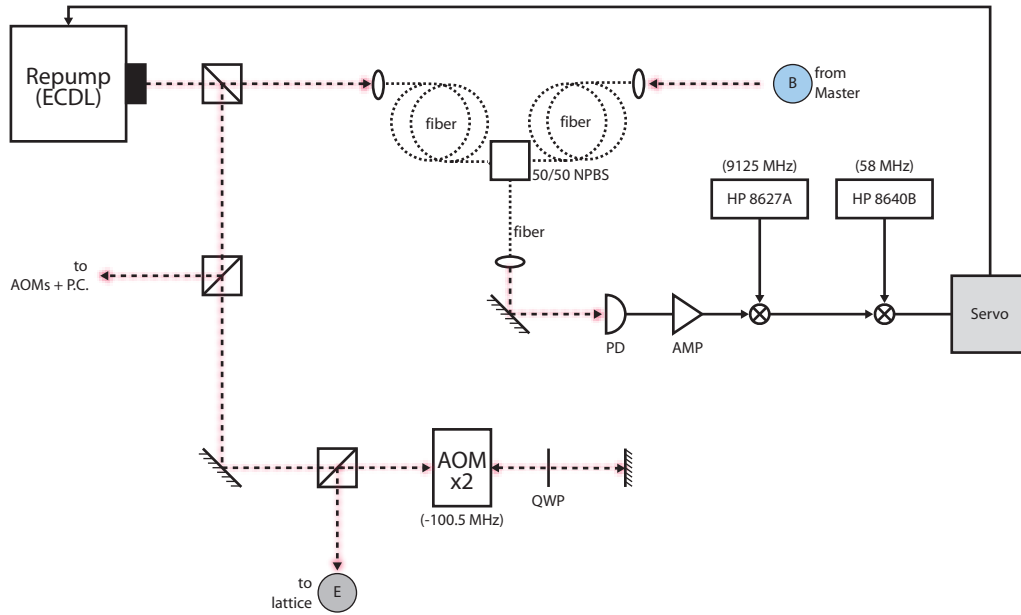


Figure 3.18: Schematic drawing of the repumper laser beam paths and servo configuration. In the interest of concision, this drawing does not represent the geometry of the beam paths on the optics bench. Colored circles and letters indicate a beam which enters another part of the apparatus as depicted schematically elsewhere in this Chapter. The photodiode (PD) in this diagram is a specialized New Focus 1400-series 25 GHz photorecieiver. The abbreviation “50/50 NPBS” represents a non-polarizing 50/50 fiber optic coupler.

used as a source for incoherently repumping MOTs and trapped atoms. Any small detunings relative to the other lasers in the laboratory were irrelevant in so far as the repumper was itself able to drive the cesium ($3 \leftrightarrow 3'$) transition with a reasonable Rabi frequency. However, it became clear as we were performing measurements in order to quantify the coherence of the atom-field state mapping process discussed in Chapter 5 that we would need a beam resonant with ($3 \leftrightarrow 3'$) and phase stable with respect to the QED field and cavity length. This beam would serve as one arm of a stimulated Raman process, and any frequency or phase jitter with respect to the other arm would contribute significantly to decoherence in the system. With this in mind we made the switch to the phase lock. Note that this servo suffers from the same unfavorable noise characteristics discussed in David Boozer's thesis in the context of stimulated Raman processes at another wavelength. These noise issues were much more of a concern in this other context, however, as they overlapped almost exactly with a particular set of spectroscopic features we were hoping to measure. Here there is no such overlap and the change in servo mechanism has proven quantifiably beneficial.

The repumper is the only laser in the lab which couples ($3 \leftrightarrow F'$) transitions, and so it is used wherever fields at those frequencies are needed. Following a frequency downshift of 201.0 MHz by double-passed AOM, the light (resonant with ($3 \leftrightarrow 3'$)) is coupled in free space to the upper and lower MOTs to serve as a repumper. A fraction of the same beams is also combined with ($4 \leftrightarrow 4'$) light from the slave laser in order to form the PG cooling lattice pair.

3.4.2 Physics Cavity Stabilization

As has been alluded to throughout the chapter, the length of the physics cavity is not passively stable enough to remain within a fraction of a linewidth of the QED transition during the course of an ordinary experiment. It follows that we need to actively stabilize the cavity length by feeding back to the voltage across the shear-mode piezo on which the input mirror is fixed. The most straightforward way to do this is implement feedback derived from photodetection of a beam transmitted through the cavity on-resonance. The cavity length is so short that, for all but the few modes closest to the peak of the mirror coating curves,

the bandwidth of the cavity limits the resolution of the lock. We clearly can't use the QED field because, first, it is necessarily very weak and, second, it is modulated strongly by the atom-cavity coupling in a way not conducive to trapping or cavity stabilization. We choose to drive the fundamental mode two FSR blue of the QED mode ($m = 101$, or $\lambda_\nu = 835.750$ nm).

The laser which drives this mode is a New Focus model 6200 Littman configuration ECDL which offers ~ 10 mW of total output power and is broadly tunable over a range of nearly 30 nm. The diode's output is split between two arms. The first arm is mode matched into the transfer cavity through the mirror opposite to that coupling the master laser light. By weakly modulating the current of the diode at 11 MHz we lock the carrier of the laser to a longitudinal mode of the transfer cavity using the Pound-Drever-Hall technique [38]. This stabilizes the frequency of the New Focus laser with respect to each of the cesium lasers in the laboratory and, ultimately, to a spectroscopic feature in cesium itself.

In general, the frequency at which there exists a resonance in the transfer cavity for locking the New Focus does not correspond to the resonant frequency of the $m = 101$ mode in the physics cavity when $m = 99$ corresponds to the QED transition. To bridge this frequency difference, the second arm of the laser is directed through a traveling wave EOM which is used to apply sidebands to the light at 500 MHz (variable, depending on drifts in the absolute length of the transfer cavity from day-to-day and the transition in cesium which we are attempting to use for QED). The RF source for these sidebands is an Agilent ESG2000 signal generator. We lock the physics cavity in transmission to the blue sideband applied to the light by the EOM, allowing us to tune the length of the cavity into resonance with the QED field by simply adjusting the sideband frequency. On top of this sideband, smaller sidebands are put on the light at 8 MHz (*i.e.*, $\sim 2\kappa$) using FM modulation of the signal from the ESG2000. These are the sidebands which are used to derive a Pound-Drever-Hall error signal for locking the length of the physics cavity.

The ability to tune the cavity length by varying the sideband frequency at the EOM is a useful feature of this system. The general protocol for establishing the lock is to manually align the system "by eye," looking for concurrent resonances between the New Focus sideband and the probe field derived from the master laser as the physics cavity

length is swept. When the two are close, the New Focus laser lock to the transfer cavity is then switched ON, the physics cavity sweep is turned off and the cavity then locked to the New Focus laser transmission. We then manually sweep the frequency of the New Focus sideband until we observe the QED field is exactly co-resonant in transmission (usually to within ~ 0.1 MHz). This type of technique is the same as was used (and very briefly described) in Section 3.1.3 to measure the linewidth of the cavity at the QED wavelength.

There is generally on the order of 35 nW of power mode matched into the cavity from the New Focus laser during the course of any QED experiment. Conservative estimates suggest that the perturbation to the FORT potential from the locking light will be on the order of 120 kHz, with a 80 kHz spread across Zeeman states in the hyperfine manifolds. For our usual FORT depths ($U_0/h = 40\text{-}50$ MHz), this effect is largely negligible.

3.5 Beam Paths

In this section I will describe two of the more important beam paths on our optics bench. First will be the path used to combine, polarize and mode-match the beams at the input to the cavity and those optics along the cavity output path which lead to a series of detectors. The second set of paths we will consider are those available to address the atom in the cavity through the aperture separating the mirrors. This will include the lattice beams from Section 3.3.3 and a single, unbalanced side beam not yet mentioned.

3.5.1 Cavity Input and Output Paths

The Lab 11 physics cavity is a symmetric resonator and therefore regardless of on which mirror input fields are incident, there will be significant transmission through both mirrors as the field resonates. In practice, we choose to only detect light transmitted through mirror M_2 and to only drive the cavity through M_1 . For light generated intracavity (*i.e.*, deposited directly in the cavity mode by an atom), this results in an “attenuation” with respect to our measurements of $\alpha_{2s} = 0.50$.

λ (nm)	Mode Order	axis ($\pm: \hat{l}_{\pm}$)	Description
852.357	99	+	“bright” cavity QED probe field
852.357	99	–	“dark” cavity QED probe field
835.750	101	+	New Focus cavity stabilization field
935.586	90	+	FORT field
935.613	90	–	Raman field (FORT-Raman config.)
945.556	89	+	Raman field 1 (Raman-Raman config.)
945.533	89	–	Raman field 2 (Raman-Raman config.)

Table 3.4: List of fields coupled into mirror M_1 of the physics cavity. Each of these fields is nominally linearly polarized and oriented along either the \hat{l}_{\pm} axis as denoted in third column of the table.

Input Path

The physics cavity input path is shown on the left hand side of Figure 3.19. Depending on the nature of the experiment there can be as many as six fields simultaneously mode matched into the cavity at any given time. The wavelengths, mode numbers, polarization orientations with respect to cavity birefringent eigenaxes and functions of each of these fields are described in Table 3.4. These fields are combined with fields of dissimilar frequency along the input path using a series of short- and long-wave pass dichroic mirrors from CVI Corporation.

The final optic before the mode-matching lense and cavity is a broadband CVI calcite Glan-Laser polarizer (CPAD-10.0-670-1064 with a specified extinction ratio of 1 : 1000). This polarizer is oriented and fixed in place such that light transmitted along its axis is aligned with the higher frequency birefringent mode of the cavity, \hat{l}_+ . We also inject light into the “rejected” port of the polarizer in order to drive the \hat{l}_- mode.

Mode-matching is accomplished using a fixed 20 cm lens. Admittedly our mode matching efficiency is very poor ($< 10\%$ for some fields). However this is generally acceptable for most applications simply because the fields we are injecting into the cavity are derived from lasers with ample power to compensate and produce whatever circulating intracavity field

we specify. For applications in the future where one might wish to inject very weak states of light (single photon states, for instance) this mode-matching efficiency would need to be improved.

Output Path

The output path for the physics cavity is depicted schematically in the right hand side of Figure 3.19. We collect transmission only from mirror M_2 . The transmitted light is immediately directed through a half waveplate specified for operation at 852 nm followed by a broadband infrared polarizing beamsplitter (PBS) cube. The orientation of the waveplate is such that QED light polarized along \hat{l}_+ is reflected from the cube. The same waveplate functions reasonably well at 836 nm and so the majority of the New Focus locking laser signal is also reflected from the cube. The beams at 936 nm and 945 nm, however, are highly ellipticized by the waveplate (these wavelengths sit well outside it's design range) and are generally transmitted and reflected in equal parts by the PBS. The transmitted portion of the field (dominated by FORT and Raman signal) is directed to a standard New Focus photodiode.

The light reflected from the PBS is directed through a collimation lens and to an angle-tuned short-wave pass dichroic mirror. This mirror is designed to transmit light at 836 nm (the New Focus locking laser signal) and reflect light at wavelengths longer than this (each of the other beams). The portion of the field transmitted through dichroic is directed to an avalanche photodiode which is used to derive the cavity locking error signal (Section 3.4.2).

The remainder of the output path is dedicated to stripping the remaining FORT and Raman light (usually on the order of 0.5 mW of optical power) from the QED signal (consisting of 1 fW to 10 pW, depending on the experiment being conducted). The filtering optics consist of 4 long wave-pass dichroic mirrors which transmit, on average, 30% of the incident FORT and Raman per mirror (and reflect 97% of an incident QED beam). In addition, there are two specially coated 852.3 nm interference filters which transmit 85 – 90% of an incident QED probe (dependent on angle tuning) and attenuate the FORT and Raman pair by a factor of 1×10^6 . These two interference filters do the vast majority of the spectral filtering but the dichroic mirrors serve an important purpose as well - light

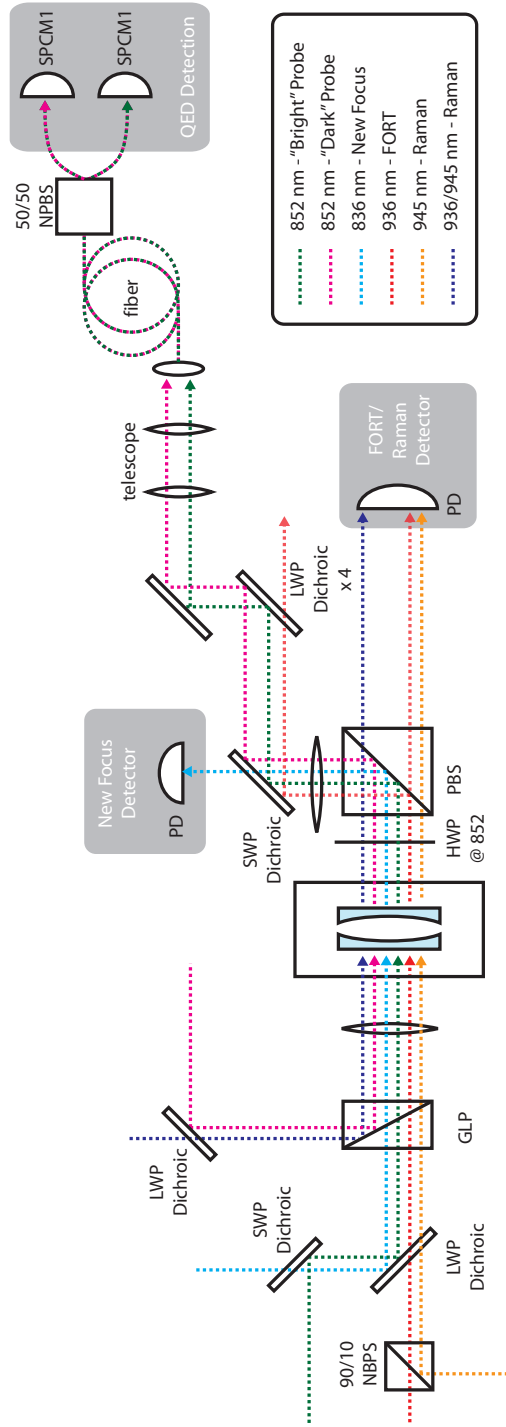


Figure 3.19: Physics cavity input and output paths. Abbreviations are for long-wave pass (LWP) and short-wave pass (SWP) dichroic mirrors, non-polarizing beam splitters (NPBS), polarizing beam splitters (PBS), single photon counting modules (SPCM), and photodetectors (PD). Figure does not represent the geometry of the beam paths on the optics bench.

designed to be transmitted by the mirrors but instead reflected penetrates much farther into the dichroic coating than does light which is designed to be reflected. The significance of this effect is that it adds a small angular displacement between the QED signal and the FORT/Raman at each bounce and this angular displacement can be used for spatial filtering.

The remaining power is mode matched into a length of single mode optical fiber - the fiber input alignment provides the spatial filter for the remaining FORT/Raman power. The signal is then transmitted through a non-polarizing 50/50 fiber coupler which directs the signal to two avalanche photodiode single photon counting modules (Perkin-Elmer SPCM-AQR-14-FC). We choose to use a splitter and two detectors because the modules have an intrinsic 50 ns “dead” time after registering a photodetection event during which the module resets and cannot register any further photodetections. The two-detector Hanbury-Brown-Twiss configuration allows us to perform correlation measurements in spite of this dead time by cross-correlating data between the two SPCMs. Upon registering a photodetection event, the module emits a TTL-compatible voltage pulse into 50Ω impedance. The quantum efficiency for converting a photon incident upon the APD into an electronic photodetection event is specified (and independently measured) to be $\alpha_{qe} = 0.53 \pm 0.05$ at 852.4 nm. SPCM1(2) exhibits a 60 (120) Hz rate of dark counts, or randomly distributed erroneous photodetections caused by thermal fluctuations in the module. These modules also exhibit a 1.2% probability, conditioned on a valid photodetection event, to generate a second, erroneous “after-pulsing” event a time 53 ns after the initial detection. For more information about this effect and its pertinence to our work please see Jason McKeever’s dissertation [22].

The quality of the spectral and spatial filtering of the FORT light is sufficient that the contribution to the dark count rate from the FORT is indistinguishable from Poisson fluctuation of dark counts (at this wavelength the quantum efficiency of the detectors is $\sim 30\%$). This corresponds to less than 0.05 fW of incident optical power from the FORT and Raman pair. From the PBS at the cavity output to the input of the SPCM, the total attenuation of these beams is $\alpha_{FORT} \sim 5 \times 10^{-15}$.

We have also fully characterized the efficiency with which we can detect a single photon

Symbol	Value	Error	Description
α_e	0.65	0.09	cavity transmission coefficient
α_{2s}	0.50	-	detecting one side of a two-sided cavity
α_p	0.50 [†]	0.05	propagation losses
α_{qe}	0.53	0.05	SPCM quantum efficiency
α	0.086	0.02	total detection efficiency
† - maximal value measured 11/16/2006			

Table 3.5: Accounting of cavity output path losses and efficiencies.

from the mode of the cavity to TTL pulse. Table 3.5 offers an item-by-item breakdown of the losses which diminish this efficiency. The cavity transmission or escape efficiency, α_e , is equal to $\sqrt{\mathcal{T}_{max}}$ (Equation (2.115)) the one-way cavity transmission coefficient. This represents the fraction of the circulating power transmitted through the mirrors as opposed to dissipated in the coatings. The equal probability that the photon will escape from the “output” mirror M_2 as opposed to M_1 is quantified as $\alpha_{2s} = 0.50$ (of course, for a driven cavity the escape efficiency for the two mirrors is not equal, but we are assuming the photon is generated inside the cavity mode and neither mirror is being actively driven). The total efficiency with which the photon travels through the output path to the SPCM input is given by α_p . Finally, α_{qe} is the quantum efficiency of the SPCM. This leads to a total detection efficiency:

$$\alpha = \alpha_e \times \alpha_{2s} \times \alpha_p \times \alpha_{qe}. \quad (3.52)$$

I should mention that the value for α_p , the propagation efficiency, given in Table 3.5 is not the same as that given in *e.g.*, reference [40] or dissertations [22, 23]. We have gradually made improvements to the output path which have increased α_p by a factor of 1.5 over the interceding years.

The final step in the photodetection process is to measure and record the arrival times of the detection events relative to the experimental cycle. This is done using a 4-channel

FAST ComTec P7888 Time Multiscaler board. The card accepts a single “start” input and as many as four “stop” inputs. Discrimination of a TTL-level event on any of the “stop” channels produces a computer data record of the arrival time of that “stop” relative to the discrimination of an initial “start” pulse. The data record takes the form of an ASCII text file containing a list of 32-bit numbers corresponding to the “stop” events measured for a user-specified number of “starts.” The first two bits of the number denote the channel on which the event was recorded and the remaining 30 bits are the relative arrival time in nanoseconds. The card has 2 ns pulse resolution in 4-channel mode (and can be converted to a 2-channel mode with 1 ns resolution if necessary). We generally synchronize the beginning of the experimental cycle (see Section 3.6) with the “start” pulse and use the digital output from the two SPCMs as “stop” channels A and B. “Stops” C and D are usually reserved to record “time stamp” or “milestone” events so we can compare the arrival times of the photodetections with specific timing events of interest in the experiment and which occur on a shorter timescale than does the overall experimental timing (this eliminates any concern over nonlinearities in the internal timebase of the P7888).

3.5.2 Cavity “Side” Beams

The cavity lattice beams were discussed in Section 3.3.3. They are two pairs of ($4 \leftrightarrow 4'$) and ($3 \leftrightarrow 3'$) beams in a $\sigma^+ - \sigma^-$ counter-propagating configuration. The four beams are each focused through the $d = 41.4 \mu\text{m}$ gap between the cavity substrates in order to provide a damping force for loading atoms into the FORT as they fall through the cavity mode. This focus is achieved by 20 cm cylindrical locating just outside of the UHV chamber. As we will see in later Chapters, these beams are used not only for initial cooling of the atom, but also throughout the experiment where classical fields near these frequencies are needed. In addition to the lattice beams, there is also one additional side beam which has no counter-propagating equivalent. This beam can be configured to drive any of a number of transitions within the atom via a conveniently hot-swappable optical fiber mount and is linearly polarized either along, or at 90° with respect to the cavity axis.

The paths of these beams, themselves, are not very interesting. Instead, we need to be concerned with how the intensity of the beams is distributed at the center of cavity and

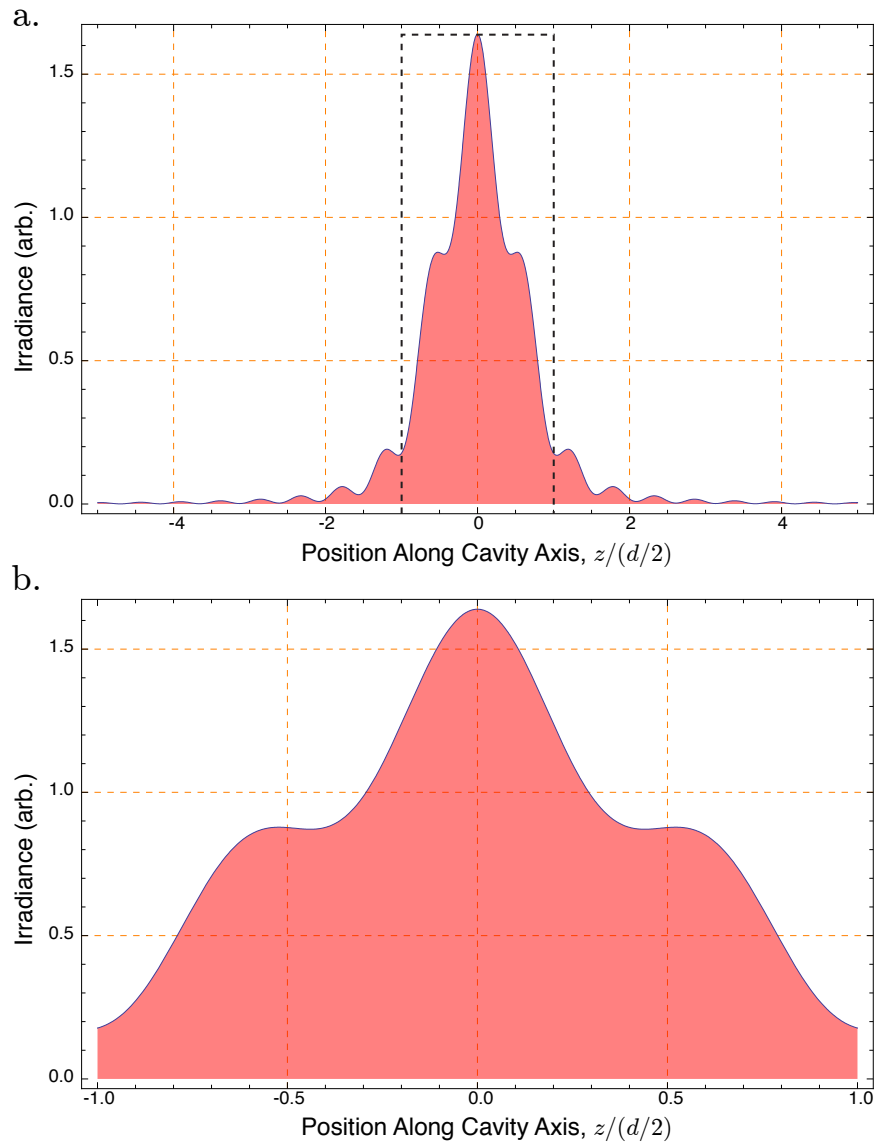


Figure 3.20: a. Fresnel diffraction pattern of the lattice and side beams by the cavity, calculated with the plane of observation at the center of the cavity mode and in the approximation that the cavity aperture is rectangular. The Fresnel number for the system is $N = 0.96$. The dashed black lines indicate the boundaries of the aperture. b. Diffraction pattern with limits of the plot set at the positions corresponding to the locations of the two mirror surfaces.

whether diffraction by the cavity aperture is a concern. We will approximate the aperture of the cavity by a rectangle. At the QED wavelength, these beams have a Fresnel number given by:

$$N \equiv \frac{d^2}{4D\lambda} \quad (3.53)$$

where $D = 5 \times 10^{-4}$ m is the physical distance from the center of the cavity mode to the edge of the substrate. For our cavity geometry, $N = 0.96$, which places the system right at the boundary between the Fresnel and the Fraunhofer diffraction limits [17]. We should therefore expect near-field diffraction to be a concern and that a geometric interpretation of the intensity distribution of the beam across the cavity will not hold.

We can calculate the irradiance pattern of the beams across the cavity length (here defined to lie along \hat{z}) using the Fresnel integral expression for the amplitude of the diffracted field:

$$u(z) = \frac{1}{\sqrt{2}} \left(F \left[\sqrt{2N}(1-z) \right] - F \left[-\sqrt{2N}(1+z) \right] \right) \quad (3.54)$$

where $F(x)$ is the Fresnel integral function:

$$F(x) \equiv \int_0^x e^{i\frac{\pi\tau^2}{2}} d\tau. \quad (3.55)$$

Performing the integrals numerically using Mathematica, the irradiance

$$\mathcal{I}(z) = |u(z)u^*(z)| \quad (3.56)$$

as a function of position along the cavity axis, is shown in Figure 3.20. Note that over the length of the cavity, $\mathcal{I}(z)$ varies by as much as 90%. The Rabi frequencies of the lattice and side beams depend strongly on in which well of the FORT an atom is located.

This has a few important consequences. First, it suggests that the lattice loading scheme is likely most effective near the center of the cavity where the intensities of the four beams are maximal. This effect would reduce the overall loading probability as those atoms which

enter the FORT near the extrema of the cavity will be less effectively cooled. This estimate agrees with results from the next Chapter where we replace the lattice repump field with a field driving a resonant cavity mode exhibiting none of these spatial fluctuations.

A second, more important, consequence is that any sort of coherent process we want to implement using side or lattice beams will be washed out if we choose to ensemble average over multiple atoms. Each atom, at a unique position with respect to the diffraction pattern, will experience a different Rabi frequency for the beam and will therefore undergo nutation at a different rate. For adiabatic coherent processes, we can moderately correct for this effect by ensuring that the asymptotic Rabi frequency for the process is sufficiently large across the entire diffraction pattern. However, as will be discussed in the next Chapter, preserving the coherence of non-adiabatic Raman processes is virtually impossible in this configuration.

This result sums up the technical difficulty of experimental cavity QED in a nutshell. In order to achieve strong atom-field coupling, the requirements on the geometry of the system are so restrictive as to complicate tasks that would be otherwise straightforward in free-space. In this regard, our approach over the last 6 years has been to take advantage of the presence of the cavity whenever possible and use resonant modes other than QED mode to carry out coherent manipulation of atom-cavity system. Chapter 4 will focus on the set of tools we have developed for doing this.

3.6 Experimental Timing

The timing of the experiment is carried out almost exclusively with TTL-level digital logic. Pulse sequencing is done using an ADWin Gold digital I/O controller with a custom front end programming language written by David Boozer (see Appendix B). The ADWin system provides 32 digital outputs and 4 16-bit analog outputs, with a minimum pulse duration of 150 ns and a timing resolution of 25 ns. The Appendix offers a complete description of the syntax and function of the ADWin programming interface as it pertains to our work.

The laboratory's timing is generally defined on two different scales, slow (millisecond to microsecond) and fast (sub-microsecond). This is particularly true for experiments which

involve very precise, iterative pulse sequences. The experimental cycle is usually as follows:

1. Initialize slow (millisecond) time-scale subsystems (~ 10 ms)
 - (a) set function generator frequencies via TTL-to-IEEE 488 convertors
 - (b) reset MOT bias magnetic fields
2. Cavity loading protocol (~ 500 ms)
 - (a) upper MOT form/drop
 - (b) lower MOT collect/drop
 - (c) PG cooling into FORT
 - (d) (optional) verify atom presence, reset as necessary
3. Physics ($\sim 0.5 - 2.0$ s)
 - (a) delegate fast-time scale (sub-microsecond) pulse sequencing to SRS DG535
 - (b) trigger and time stamp FASTComTec P7888 photon counting card
 - (c) loop as needed

This process is repeated with a period of $\tau_{expt} \sim T_{avg} \approx 1.0 - 2.0$ s while data is collected.

The ADWin controller manages the overarching system timing (steps 1 and 2). When necessary, particularly for physics measurements, the ADWin is used to trigger a series of externally gated Stanford Research Systems DG535 delay generators. These two-channel devices offer a nominal time resolution of 5 ps with < 25 ps edge jitter and a good deal more flexibility on these time scales than does the ADWin. By devoting a single channel of our photon counting card to time stamp pulses from the DG535 units we are able to ensure that data we collect is properly registered with respect to the overall system timing on whichever timescale the experiment requires.

I will omit a complete description of the full array of RF electronics and digital logic circuitry necessary to run our experiment because it is both well-documented in the group's laboratory notebooks and not terribly interesting reading. Instead, Figure 5.5 offers a process-level block timing diagram of the experimental cycle necessary to prepare the upper

and lower MOTs and to load the cavity. Of course, the final timing block - the physics timing - varies from experiment-to-experiment and will be discussed on a case-by-case basis.

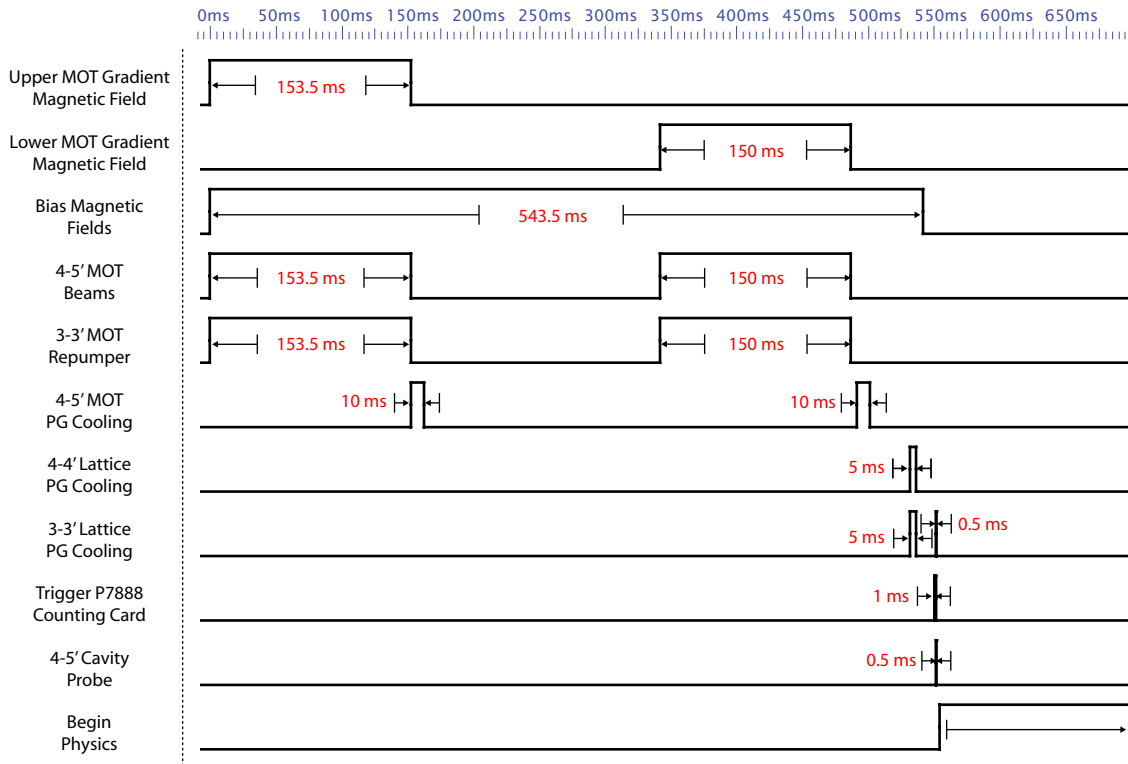


Figure 3.21: Block timing diagram for the preparation of the Lab 11 MOTs and loading of atoms from those MOTs into the intracavity FORT. Pulses high (low) correspond to that subsystem ON (OFF) with the exception of Bias Magnetic Field pulse which indicates switching between two discrete field settings (high: forming the lower MOT, low: establishing the desired bias field at the physics cavity center).

Chapter 4

Raman Transitions in an Optical Cavity

This Chapter describes a set of frequently used experimental protocols. The techniques and methods discussed here, many of which are unique to our group, are commonly used in the work we do in the laboratory. They form the experimental building blocks upon which the more complex experiments described in Chapters 5 and 6 are built.

In Section 4.1, I will briefly survey the techniques at our disposal for performing state detection on the atom-cavity system. In particular, I will focus on measuring so-called “down-goer” events and the information about the system which can be extracted from this signal.

The principle focus of this chapter, however, will be a technique our group has developed for driving stimulated Raman transitions between the hyperfine ground states of single, optically trapped atoms. The ability to coherently manipulate and measure the state of a trapped atom, *in situ* and using the uniform mode structure of the physics cavity, offers a level of control which is absolutely vital to understanding the inherent complexity of the system.

4.1 Atomic Hyperfine State Detection

As will become clear later in this Chapter, the ability to projectively measure the internal state of an atom bound to our cavity with high certainty is broadly useful in this type of research. Frequently the signal of interest in one of our experiments is the amount of atomic population in a particular cavity-coupled (or uncoupled) hyperfine ground state. We

have three distinct methods at our disposal for performing this type of measurement in the laboratory. Each has situational advantages and disadvantages which are discussed below.

4.1.1 “Down-goer” Detection

The most straightforward and robust technique we use relies on measuring the intensity fluctuations in a resonant probe field as a function of atomic ground state. The probe field is resonant in the sense that there is nominally zero detuning between the probe light, the empty cavity resonance and a ($4 \leftrightarrow N'$) atomic transition of our choosing. We should emphasize that the probe is “nominally” resonant because, as was discussed in Chapter 3, there can be a variety of small, differential shifts between internal atomic states within a given hyperfine manifold. Recall Equation (2.55) which states that the cavity transmission spectrum in the presence of dissipation for a probe field tuned to resonance ($\Delta = 0$) with an empty single-mode cavity and detuned from resonance with a two state atom by Δ_A is given by:

$$I_3 \equiv I_0(\Delta = 0) = \beta I_{inc} \frac{\kappa^2(\gamma^2 + \Delta_A^2)}{(g^2(\vec{r}) + \gamma\kappa)^2 + (\kappa\Delta_A)^2}. \quad (4.1)$$

Here β is a constant which describes the losses associated with coupling light through the cavity. If the atomic population resides completely within the $F = 3$ hyperfine ground state manifold, then the atom is far-detuned from resonance with the cavity ($\Delta_A = \Delta_{HF}$, the cesium hyperfine ground state splitting). Because this atom-cavity detuning is larger than the experimental values of $g(\vec{r})$, κ and γ for our system by at least two orders of magnitude, we can simplify I_3 by keeping only terms of highest order in Δ_{HF} :

$$I_3 \approx \beta I_{inc} \quad (4.2)$$

This is just the empty-cavity resonant transmission - in any of the $F = 3$ hyperfine states, the atom is effectively “transparent” to a field probing the cavity and therefore a resonant probe will exhibit high transmission.

Population in $F = 4$, however, exhibits generally small atom-cavity detuning, $\Delta_A \approx 0$.

Here, the transmission of a resonant probe field will go as:

$$I_4 \equiv I_0 \propto I_{inc} \frac{\kappa^2 \gamma^2}{(g^2(\vec{r}) + \gamma \kappa)^2}, \quad (4.3)$$

(as plotted in Figure 2.2). For our experimental values (g_0, κ, γ) this model predicts $I_4/I_3 \sim 7 \times 10^{-5}$. However, because the two-state model used to derive these expressions begins to break down in the context of multi-state cesium, we typically measure $I_4/I_3 \sim 1 \times 10^{-2}$. Nonetheless, in the laboratory it is straightforward to distinguish between I_3 and I_4 using photon counting. The suppression of cavity transmission as a function of atomic hyperfine level (*i.e.*, $F = 3$ or $F = 4$) serves as the basis for this state detection scheme. Because the characteristic signal for this method is a drop in cavity transmission when coupled to an atom it is commonly referred to as a “down-goer” signal.

It should be noted that for open atomic transitions (*i.e.*, $(4 \leftrightarrow 3')$ or $(4 \leftrightarrow 4')$) this scheme is of limited usefulness - any atomic population in $F = 4$ will optically pump into the $F = 3$ hyperfine manifold over short timescales and the information with which we are concerned (the current hyperfine ground state of the atom) will be irreversibly lost. We are therefore restricted to using this technique only in experiments which permit that the cavity to be tuned into resonance with the closed $(4 \leftrightarrow 5')$ transition. However, even on this transition, off-resonant scattering of a modest intensity probe field will drive population from $F = 4$ to $F = 3$ over hundreds of microseconds. These off-resonant scattering timescales place an upper limit on the integration times, or the amount of time we are permitted to measure the atom in order to discriminate the internal state before that state is destroyed.

A slight modification of this technique to include a beam (or beams) resonant with $(3 \leftrightarrow N')$ transitions allows us to very quickly and efficiently gather information about whether an atom is present in the cavity or not. These additional beams ensure that the atom is quickly repumped into the cavity-coupled $F = 4$ hyperfine ground state if it happens to scatter into (or begin in) decoupled $F = 3$. Therefore the presence of an atom in the cavity will always result in a down-goer signal. It is common to follow a state-detection down-goer measurement with an atom-presence down-goer measurement in order to discriminate no-atom data from data corresponding to an atom present in the $F = 3$

ground state.

A typical procedure for making a down-goer measurement begins by first preparing the atom in whichever state is to be measured. Following this initial preparation, we apply a resonant probe field to the cavity for a time τ_p . Typically τ_p can be as short as 100 μs , but can in principle be tailored as needed within the off-resonant pumping constraints described above. The transmitted intensity of the probe field is measured using the single photon counting modules described in Chapter 3 while the number of photons detected in that interval, $N(\tau_p)$, is recorded to computer memory.

Figure 4.1 presents an ensemble of representative down-goer measurements in histogram form for atoms prepared in a mixture of initial hyperfine ground states. Over 7.5×10^5 trials, the probability P_N to measure $N(\tau_p)$ photons during the integration window is plotted. The result is the sum of two Poisson distributions. The shapes of both features are set by the photon counting statistics of the coherent (laser) light source from which the probe field is derived. The mean value of each feature is characteristic of either a coupled ($F = 4$) or uncoupled ($F = 3$) atom. For this set of data, the high-transmission feature centered near $\bar{N}_3 = 33.2$ is the result of atomic population in $F = 3$ (or, potentially, absence of an atom within the cavity mode). The mean number of photons detected within this feature corresponds to a steady-state probe count rate of ~ 330 kHz, or an average intracavity photon number of ~ 1 . The feature near $\bar{N}_4 = 0.45$ corresponds to the those events wherein transmission through the cavity was suppressed by the presence of an atom in the $F = 4$ ground state.

We can either systematically or arbitrarily determine the discrimination thresholds n_3 (n_4) such that measurement of $N(\tau_p) > n_3$ ($N(\tau_p) < n_4$) photons during a detection interval corresponds in analysis to determination of the atomic state to be $F = 3$ ($F = 4$) with some related certainty. In recent versions of my own MATLAB-based data-analysis code, the program pre-analyzes small chunks of data (typically 50 atoms worth of data at a time) in order to numerically fit the bimodal probability distribution. This allows the program to specify n_3, n_4 as a user-defined number of standard deviations away from the respective centers of the two features while adapting for small fluctuations in experimental parameters. Generally in the past, however, these values have set arbitrarily relative to the empty cavity

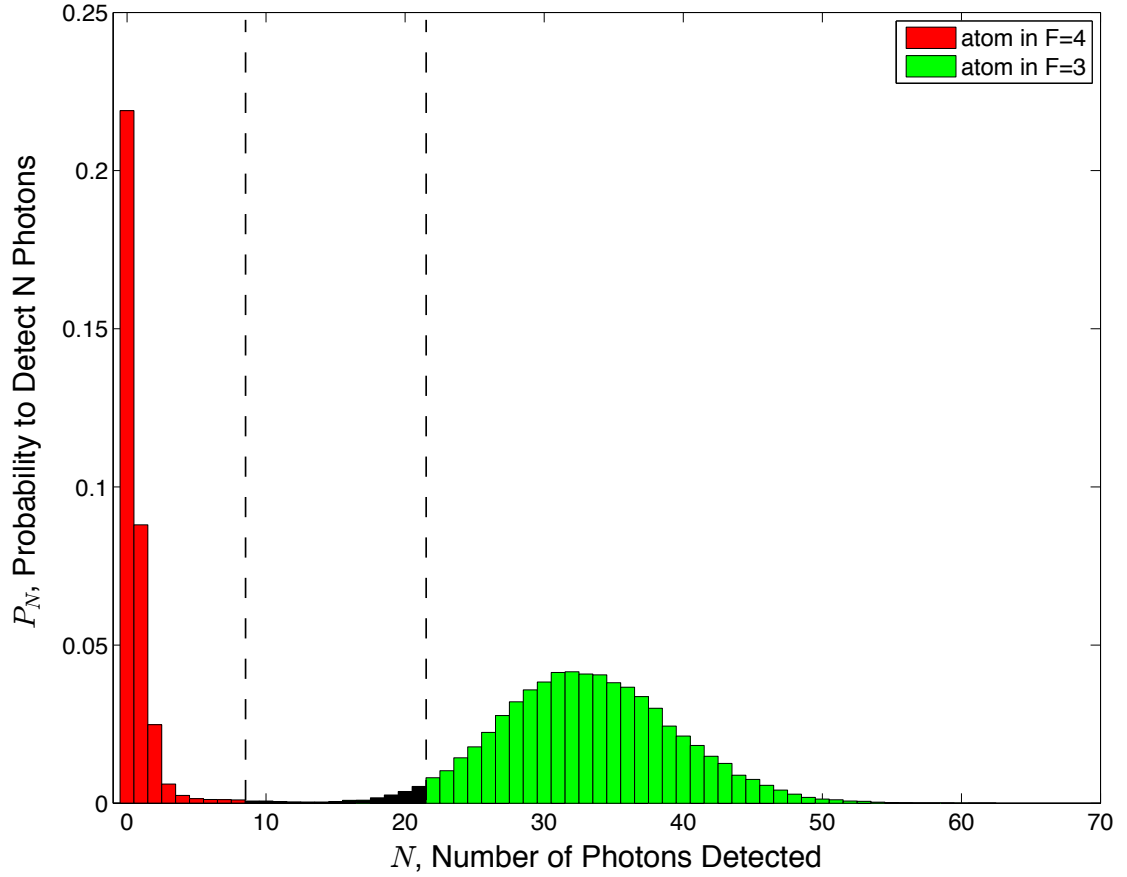


Figure 4.1: Histogram of typical “down-goer” type data for atoms prepared in an initial mixture of hyperfine ground states and measured for probe pulses of duration $\tau = 100 \mu\text{s}$. Dashed vertical lines correspond to state discrimination thresholds set at $n_3 = 0.25N_e$ and $n_4 = 0.75N_e$, where $N_e = 33.2$, is the average number of photons detected during on-resonance transmission of the probe through an empty cavity.

transmission level, N_e , in such a way that there is only a very small probability that a given event would be misclassified. Typical values are $n_3 = 0.75N_e$ and $n_4 = 0.25N_e$. These particular values were used in Figure 4.1 in order to delineate $F = 3$ data (green) from $F = 4$ (red).

A small sample of data ($\sim 4\%$) falls within the gap between the two thresholds and is left unclassified (black). We are therefore able to discriminate between states in this data set with 96% certainty. This is not a statement of our confidence in this classification (or the error associated with the discrimination procedure). We can, however, quantify the error associated with this procedure by exploring the overlap of the two distributions into the opposing discrimination regions. The result varies from measurement to measurement, but our discrimination fidelity is typically in excess of 99%.

4.1.2 “Up-goer” Detection

An alternative approach to the same problem, and along the same lines, is to probe the cavity not at zero detuning from a shared atom-cavity resonance but at $\Delta = \pm g_0$ (*i.e.*, at the vacuum-Rabi sidebands). Instead of measuring a transmission drop if the atom is cavity-coupled, we will instead expect to see a transmission increase as the system shifts into resonance with the probe light. Following the naming convention given the previously described method, we refer to this technique as looking for “up-goers.”

The up-goer method is viable, but suffers a number of limitations which down-goer detection does not. First, assuming we are driving the cavity with probe light tuned to a transmission maximum of the vacuum-Rabi spectrum for an atom, the dynamic range of the signal is roughly a factor of three smaller than that for down-goers. Also, and more importantly, we have seen throughout Chapter 3 that there are a variety of experimental factors which can significantly alter the local rate of atom-cavity coupling for a particular atom. These include differential atom-cavity detunings born from FORT-induced Zeeman state shifts and residual magnetic fields as well as variations from measurement-to-measurement in $g(\vec{r})$ as the atomic position \vec{r} fluctuates. A series of individual measurements of the system will each potentially correspond to different rates of coherent coupling between atom and field. In short, the signal which one derives from up-goer measurement is generally less

straightforward to interpret and less efficient to measure [41].

Moreover, whereas down-goers are characterized by rejection from the cavity of light which otherwise would interact (both internally and externally) within the atom, up-goer type measurements allow that light into the cavity mode. As a result, depending on the frequency at which we are probing, there is the potential for so-called cavity cooling of the atomic motion [42], but also for cavity-induced heating. As the coupling constant changes from atom-to-atom and measurement-to-measurement, these heating and cooling parameters also change and the result is typically shortened FORT lifetimes. In general it is desirable to decouple motion from QED effects, and therefore up-goer measurements are undesirable in this respect.

Up-goer measurements do have situational uses, however. For instance, up-goer detection can be useful in experiments where information about the system can be transferred from the atom to the strength of the probe field in cavity mode. In this context, I refer the reader to a specific example in the thesis of Andreea Boca (Reference [23], Chapter 3) where Fourier analysis of an up-goer signal reveals modulation at the oscillation frequency of the atom in the FORT. This measurement allowed us to visualize for the first time the distribution of vibrational frequencies, both radial and axial, for atoms trapped within our cavity. This distribution conveys a significant amount of information about the mean temperature of atoms trapped in our system due to the anharmonic dispersion of vibrational energies in each FORT well. Up-goer light can also exhibit some remarkable quantum photon statistics as will be discussed briefly in Chapter 6 and in some detail in Reference [29].

4.1.3 Photon Generation-Based Techniques

A third, more situational approach is to map the internal state of the atom onto the cavity photon number state. Photon generation as a means for state detection will be discussed at length in Chapter 5. I point to it in this context only to discuss its relative strengths and weaknesses. Photon generation as a state detection method is particularly viable when we are constrained to operate with the cavity on resonance with an open set of atomic transitions (*i.e.*, $4 \leftrightarrow 3'$ or $4'$). With high (near-unity) efficiency we can map population in $F = 3$ onto the one-photon component of the cavity mode, $|1\rangle$. Meanwhile, population in

$F = 4$ maps onto the ubiquitous cavity vacuum state $|0\rangle$. Subsequent detection of a photon in the cavity output mode during an anticipated arrival window indicates that the atom began in the $F = 3$ manifold.

The drawback of this scheme is that detection of QED light in the cavity output mode is relatively inefficient for our system ($\alpha = 0.086$ is the largest detection efficiency we have measured, as described in Chapter 3). If the photon is attenuated anywhere along the detection path, all information about the measurement is irreversibly lost. This places a stringent upper limit on the certainty with which we can infer the atomic state for any given measurement. We are also unable to directly measure population in the cavity-coupled atomic ground state manifold, $F = 4$ - the corresponding signal for which is simply the *de facto* vacuum state in the cavity mode. Instead, we are left to infer the average total probabilities that the atom is in $F = 4$ and $F = 3$ from the measured probability to detect a photon and the output path losses.

In summary, state detection by way of photon generation and detection can be effective under circumstances when down-goer and up-goer detection are generally not. However, due to the likelihood that the signal will be lost in the detection path, down-goer detection is still highly preferable because it guarantees that our measurement will discriminate the atomic state with high certainty. Photon generation as a state detection scheme is generally avoided in the work described throughout this thesis at all but those circumstances wherein we are not able to address closed atomic transitions.

4.2 Stimulated Raman Transitions in an Optical Cavity

As was discussed in Chapter 3, the presence of the optical cavity around the atom simultaneously restricts our physical access to the system (due to the small solid angle accessible through the inter-mirror spacing) yet provides us with a unique opportunity to regain that access through creative use of secondary cavity modes. The remainder of this Chapter will be devoted to discussion of a technique which our group has developed for using excitation in cavity modes other than the QED mode to drive stimulated Raman transitions between the hyperfine ground states of a trapped atom (including between adjacent Zeeman and

motion-coupled states). This method has proved to be a very useful tool in almost every aspect of our work - from initial preparation, coherent control and even measurement of the system's degrees of freedom. In this section I will describe the theoretical mechanism which underlies the Raman technique as well as how we go about physically implementing the necessary beams and fields.

4.2.1 Theoretical Model

In this Section we will begin by describing Raman transitions in the context of the simplest possible non-trivial physical system which permits them. We will then scale the description to the full cesium atom. This discussion will follow the formalism established by David Boozer in a related paper [43]. We begin by treating a three-state atom with two ground states, $|a\rangle$ and $|b\rangle$ each with associated energies $E_{b,a} \equiv \pm 1/2\hbar\Delta_{HF}$ and an ancillary excited state $|e\rangle$ with energy $E_e \equiv \hbar\omega_A$ (see Figure 4.2) . Raman processes are inelastic scattering processes involving absorption and reemission of a photon which is detuned from atomic resonance and accompanied by the transfer of atomic population from one ground state of the atom to the other [44]. Stokes-type Raman scattering moves atomic population from the lower-energy ground state $|b\rangle$ to the higher-energy state $|a\rangle$. As this takes place, a photon is scattered from a virtual energy level in the atom such that the photon has lost an amount of energy $(E_b - E_a) = \hbar\Delta_{HF}$ and thus conserving the amount of energy in the atom+photon system. Anti-Stokes-type processes involve inelastic scattering where energy is instead imparted from the atom to the photon. However, if we instead initially populate both the Stokes and anti-Stokes modes of the “ Λ ” configuration shown in Figure 4.2, we can affect what are known as stimulated Raman transitions. As we will see, this leads to a coherent oscillation of population between the two energy levels (these transitions are “stimulated” in the sense that the excitation in the two Raman field modes is stimulating the transfer of atomic population between the two coupled states).

To understand how this process takes place, we can begin by writing down a Hamiltonian

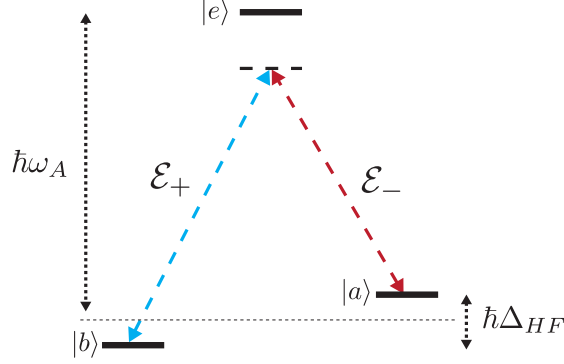


Figure 4.2: A typical Raman Λ -type atomic energy level diagram.

for the atom in the usual way:

$$\hat{H}_A = \hbar\omega_A |e\rangle \langle e| + \frac{1}{2}\hbar\Delta_{HF} (|a\rangle \langle a| - |b\rangle \langle b|) \quad (4.4)$$

$$= \hbar\omega_A \sigma_z + \frac{1}{2}\hbar\Delta_{HF} \sigma'_z. \quad (4.5)$$

Here σ'_z is a Pauli matrix over the basis of the effective two-state system between $|a\rangle$ and $|b\rangle$. We will assume that two laser fields, \mathcal{E}_\pm , are driving the cavity near a resonant fundamental mode. These fields oscillate at frequencies $\omega_\pm = \omega_L \pm 1/2\delta_R$, respectively and are far-detuned from atomic resonance, *i.e.*, $\Delta = (\omega_L - \omega_A) \gg \Delta_{HF}$. In order to generate a Raman pair, we require:

$$\delta_R = \Delta_{HF} + \delta, \quad (4.6)$$

where $\delta \ll \Delta_{HF}$ is a small, user-controlled Raman detuning. We can write the Hamiltonian for the interaction between atom and fields:

$$\hat{H}_I = \hbar (\Omega_+ \cos \omega_+ t + \Omega_- \cos \omega_- t) (|e\rangle (\langle a| + \langle b|) + (|a\rangle + |b\rangle) \langle e|) \quad (4.7)$$

where Ω_\pm are single-beam “semiclassical” Rabi frequencies for \mathcal{E}_\pm , as defined in Chapter 2.

The total system Hamiltonian $\hat{H} = \hat{H}_A + \hat{H}_R$ can be simplified using the rotating wave

approximation, by assuming that the Rabi frequencies Ω_{\pm} are much smaller than Δ and by transforming the system into a frame of reference which rotates at ω_A . Under these approximations, we can rewrite the Hamiltonian:

$$\hat{H} = \frac{1}{2}\hbar\Delta_{HF}\sigma'_z + \hbar\left(\frac{\Omega_+\Omega_-}{2\Delta}\cos\delta_R t - \frac{\Omega_+^2 + \Omega_-^2}{4|\Delta|}\right)(1 + |a\rangle\langle b| + |b\rangle\langle a|) \quad (4.8)$$

$$= \frac{1}{2}\hbar\Delta_{HF}\sigma'_z + \hbar(\Omega_E\cos\delta_R t - V_E/\hbar)(1 + |a\rangle\langle b| + |b\rangle\langle a|) \quad (4.9)$$

In this expression, V_E and $\Omega_E\cos\delta_R t$ are time-independent and -dependent AC Stark shifts on the energy levels $|a\rangle$ and $|b\rangle$. We can simplify the Hamiltonian by eliminating terms which do not contribute significantly to the dynamics of the system. For instance, the state-dependent, time-independent shift ($V_E/\hbar[|a\rangle\langle b| + |b\rangle\langle a|]$) is orders of magnitude smaller than the hyperfine splitting, Δ_{HF} , and may be neglected. Also, the time-dependent, state-independent contribution to the FORT potential ($\Omega_E\cos\delta_R t$) oscillates at a frequency $\delta_R \sim \Delta_{HF}$, which is typically four orders of magnitude larger than the frequency at which the atom oscillates in the static FORT potential. This term tends to average to zero over experimentally pertinent timescales. This allows us to write a simplified Hamiltonian in a frame which rotates at $\omega_A + \delta_R$:

$$\hat{H} = -\frac{1}{2}\hbar\delta\sigma'_z - V_E + \frac{1}{2}\hbar\Omega_E(|a\rangle\langle b| + |b\rangle\langle a|). \quad (4.10)$$

We are left with three terms, each of which has a straightforward physical interpretation. The first corresponds to the internal structure of the atom. The second corresponds to the sum of two FORT-like AC Stark shifts applied to the atom by \mathcal{E}_{\pm} . This can be seen by comparing Equation (3.33), the FORT depth for a two-state atom calculated in Chapter 3, with the expression for V_E :

$$V_E = \frac{\hbar\Omega_+^2}{4|\Delta|} + \frac{\hbar\Omega_-^2}{4|\Delta|}. \quad (4.11)$$

The third term, in particular, is the one with which we are interested. This is the interaction Hamiltonian for a two-state system ($|a\rangle$ and $|b\rangle$) which is driven by a classical field with

Rabi frequency, Ω_E :

$$\Omega_E = \frac{\Omega_+ \Omega_-}{2\Delta}. \quad (4.12)$$

The dynamics of this system are well-known in the context of the optical Bloch equations [31] and take the form of a coherent ‘‘Rabi oscillation’’ between the two, coupled states at a frequency $\Omega'_E = \sqrt{\delta^2 + \Omega_E^2}$.

4.2.2 Cavity Modes and Raman Configurations

In the treatment above, we see that the effective Hamiltonian for the off-resonantly double-driven three-state atom is the sum of terms corresponding to a FORT-like potential and a coherent exchange of excitation between ground states. Of course, because we have gone to great lengths to establish a state-insensitive dipole trap at a carefully chosen optical frequency (ω_F , as described in Chapter 3), the trap-like term of this Hamiltonian generally constitutes an undesirable perturbation to our FORT potential. With this consideration in mind, we must choose a cavity mode with which \mathcal{E}_\pm will be near-resonant.

FORT-Raman Configuration

One possibility is to eliminate the need to treat V_E as a perturbation and instead use the FORT, itself, as one leg of the Λ -pair (*i.e.*, $\omega_+ = \omega_F$). The second leg would then be a field at frequency $\omega_- = \omega_F - \delta_R$. This configuration, which we refer to as the FORT-Raman configuration, will be described first. It was first proposed and discussed by David Boozer in his dissertation [15].

As described in Chapter 3, we rely on the resonant enhancement of the cavity mode to produce a large FORT potential. It follows that the FORT beam \mathcal{E}_+ must be resonant with the cavity and that the Raman beam will be required to drive the cavity off-resonance by $\delta_R \sim (2\pi)(9.192 \text{ GHz})$. The cavity linewidth at ω_F has been measured to be $\kappa_F = (2\pi)(0.79 \text{ GHz})$, and so we expect the circulating power at ω_- to be suppressed from its resonant value by a factor of ~ 400 . Without going into any detail of how this scheme generalizes to the full cesium hyperfine ground state (see Subsection 4.2.3), we can qualitatively evaluate how

large a contribution to the trapping potential \mathcal{E}_- will make. A typical Rabi frequency we might use in our experiments is $\Omega_E = (2\pi)(100 \text{ kHz})$ and a typical FORT depth might be $U_+/h = 40 \text{ MHz}$. From this we are able to calculate the ratio of the contribution to the potential from the Raman beam to that from the FORT beam, U_-/U_+ :

$$\frac{U_-}{U_+} = \frac{\Omega_-^2}{\Omega_+^2} = \frac{h^2\Omega_E^2}{4U_0^2} \approx 1 \times 10^{-6}. \quad (4.13)$$

The Raman beam only negligibly perturbs the FORT potential. In practice, as will be discussed, when we wish to turn Raman processes in this configuration **OFF**, we simply turn **OFF** the Raman field using an acousto-optic modulator.

Finally, though our discussion has thus far neglected it, it is important to note that the effective Rabi frequency of the Raman pair varies spatially with structure of the cavity mode, $\psi_R(\vec{r})$, *i.e.*,

$$\Omega_E(\vec{r}) = \Omega_E |\psi_R(\vec{r})|^2. \quad (4.14)$$

By using the FORT mode to produce a Raman pair, we are guaranteed that $\psi_R(\vec{r}) = \psi_F(\vec{r})$, which is important in that it ensures that regardless of into which FORT well it is loaded, each atom will experience a homogenous Rabi frequency (with small variations due to atomic temperature). However, this also means that for motion near the bottom of a FORT well, the intensity of the Raman pair necessarily varies in a manner symmetric with respect to the potential. This has important implications, as we will see, for the types of transitions we can drive between eigenstates of atomic motion in the FORT.

The majority of the measurements presented in this Chapter were made using the FORT-Raman configuration. There are two principal reasons for this. First, the FORT-Raman configuration requires us to add only one additional beam to the experiment and is therefore a good deal more practical. Secondly, because the trapping potential and Raman pair are registered in this configuration and because the effective Rabi frequency is uniform from well-to-well it is considerably more straightforward to treat Raman processes in this context. Ensemble averaging over multiple Rabi frequencies, as would be necessary for the same experiments in Raman-Raman configuration, typically leads to unnecessary complication in

interpreting the results of our measurements.

Raman-Raman Configuration

The second possible configuration of beams involves using a cavity mode other than that used for the FORT. For this purpose, we need a mode which is far-detuned from both the $D1$ and $D2$ resonances and which has favorable characteristics in terms of FORT registration, cavity finesse, and maximum effective Rabi frequency. With these considerations in mind, we have chosen to use the $n = 89$ mode of the cavity, one longitudinal mode red of the FORT. The Raman pair consists of two beams at frequencies $\omega_{\pm} = \omega_R \pm 1/2\delta_R$ where ω_R is the resonant frequency of the cavity mode associated with longitudinal mode number $n = 89$ while the cavity length is stabilized such that the cesium transition of interest is resonant with mode $n = 99$. We refer to this configuration as the Raman-Raman configuration.

As in the previous Section, we can compute the perturbation to the FORT potential from this pair of beams. Here we are driving the cavity at $\lambda_+ = 945.533$ nm and $\lambda_- = 945.556$ nm, where the cavity resonance lies midway between the two wavelengths. Each beam is detuned from resonance by $\delta_R/2 \sim (2\pi)(4.596$ GHz), where the cavity linewidth is $\kappa_R = (2\pi)(5.9$ GHz). If the two fields are of equal intensity (*i.e.*, $\Omega_+ = \Omega_-$) and $\Omega_E = (2\pi)(100$ kHz), then we can express the perturbation to the FORT potential:

$$\frac{V_E}{U_0} = \frac{\Omega_E}{U_0} = 2.5 \times 10^{-3}. \quad (4.15)$$

Under these assumptions, the contribution to the FORT from Raman beams is on the order of 0.1% of the total potential depth. Though small, this perturbation is large enough that repeated switching of the Raman pair **ON** and **OFF** to apply rotations to the atomic state will also apply a significant mechanical force to the atom. In order to avoid this, we have implemented a technique which will be discussed later in this Chapter for maintaining a constant optical power in the cavity near the Raman wavelength (and, therefore, a constant perturbation to the FORT) while still allowing us to still gate the Raman process.

Finally, we note that the dimensionless mode shape for the FORT potential, $|\psi_F(\vec{r})|^2$, and the spatial dependence of the effective Rabi frequency in this configuration, $|\psi_R(\vec{r})|^2$, do

not exhibit uniform spatial overlap due to the frequency difference between the two fields. We can evaluate the spatial variations in $\Omega_E(\vec{r})$ from well-to-well by writing $|\psi_R(\vec{r})|^2$ in the form:

$$|\psi_R(\vec{r})|^2 = \exp\left[2\frac{x^2 + y^2}{w_R^2}\right] \sin^2\left[\frac{\omega_R z}{c} + \alpha\right] \quad (4.16)$$

where $\alpha = (\omega_F - \omega_R)z_r/c$ is the phase difference between the Raman pair and the FORT at the bottom of the r th FORT well, located at z_r .

The only experiment in this Chapter which makes use of the Raman-Raman configuration is our demonstration of first-order resolved-sideband Raman cooling to the motional ground state for atoms in the FORT potential. This will be described in Section 4.6.1. As we will see, this application benefits uniquely from inhomogeneous phase difference, α , between the FORT and Raman pair.

4.2.3 Generalization to Cesium

The generalization of these schemes to cesium involves more angular momentum addition and atomic physics of the type described in Chapter 2. Rather than going into the intricate details of these calculations, I refer the reader Reference [43] and present only the major results.

For cesium, we can write down a Hamiltonian in analogy with Equation (4.10):

$$\hat{H} = -\frac{1}{2}\hbar\delta(\hat{P}_4 - \hat{P}_3) - \hat{V}_E + \frac{1}{2}\hbar\Omega_E(\hat{\Sigma} + \hat{\Sigma}^\dagger). \quad (4.17)$$

Here, $\hat{P}_{3,4}$ are projection operators onto the $F = 3, 4$ manifolds of states and $\hat{\Sigma} + \hat{\Sigma}^\dagger$ is an operator which couples Zeeman states within these two manifolds. We can also calculate Ω_E and V_E by considering off-resonant interaction with both cesium D lines:

$$V_E = \hbar\frac{\gamma^2}{6}\frac{I_+ + I_-}{I_{sat}}\left(\frac{2}{\Delta_{D2}} + \frac{1}{\Delta_{D1}}\right) \quad (4.18)$$

$$\Omega_E = \frac{\gamma^2}{3}\frac{\sqrt{I_+ I_-}}{I_{sat}}\left(\frac{1}{\Delta_{D2}} + \frac{1}{\Delta_{D1}}\right). \quad (4.19)$$

Notice that, as expected, the expression for V_E is just Equation (3.36) - the predicted ground state FORT shifts for cesium. In this model, the Raman term in the Hamiltonian is a cross-term between complex conjugates and therefore the polarization vectors of the two fields must exhibit orthogonal components in order for the Raman coupling to be nonzero. In the experiment, we linearly polarize the two beams along the cavity orthogonal birefringent axes, \hat{l}_\pm (see Section 3.5.1) .

Most of our experiments will take place with either the low-frequency ambient magnetic fields nulled locally at the atom or with a static magnetic bias field along the cavity axis, which is then taken to be the quantization axis. In general, however, we can work with an arbitrary quantization axis \hat{z} and in an arbitrary coordinate frame $\{\hat{x}, \hat{y}, \hat{z}\}$ with the cavity axis oriented along, $\vec{k} = \cos \phi \sin \theta \hat{x} + \sin \phi \sin \theta \hat{y} + \cos \theta \hat{z}$. In this frame, the Rabi frequency for transitions between two Zeeman states in the $F = 3$ and $F = 4$ manifolds is:

$$\begin{aligned}\Omega_E(|3, m_F\rangle \leftrightarrow |4, m_F\rangle) &= \Omega_0(1 - m_F^2/16)^{1/2} \cos \theta \\ \Omega_E(|3, m_F\rangle \leftrightarrow |4, m_F + 1\rangle) &= \frac{\Omega_0}{8}(4 + m_F)^{1/2}(5 + m_F)^{1/2} e^{-i\phi} \sin \theta \\ \Omega_E(|3, m_F\rangle \leftrightarrow |4, m_F - 1\rangle) &= \frac{\Omega_0}{8}(4 - m_F)^{1/2}(5 - m_F)^{1/2} e^{i\phi} \sin \theta\end{aligned}\quad (4.20)$$

where Ω_0 is the effective Rabi frequency on the $(|3, 0\rangle \leftrightarrow |4, 0\rangle)$ transition for atoms located at an intensity maximum of the FORT.

4.2.4 Experimental Implementation

Regardless of which Raman pair configuration we choose (Raman-Raman or FORT-Raman), the basic experimental tools which we need to drive Raman transitions using this technique are two laser beams which are frequency locked $\delta_R \sim (2\pi)(9.192 \text{ GHz})$ from one another and then coupled into the cavity with polarizations along orthogonal cavity eigenmodes. There are a variety of ways to modulate a laser field in order to apply sidebands at microwave frequencies. However, these sidebands generally are emitted with uniform polarization, and are therefore ill-suited to our needs. So rather than deriving both arms of the Raman pair from a single laser field, we have developed techniques to frequency stabilize two lasers in such a way that they emit light at frequencies separated by a user-controlled microwave

offset frequency.

Electronic Phase Lock (2004-2006)

During our early Raman measurements (from 2004-2006), our approach to this problem was to frequency stabilize two lasers with respect to each other using direct electronic feedback derived from an optical beatnote between the two (see Figure 4.3 for a schematic overview of the lock circuitry). This system was the precursor to the phase lock currently used in the laboratory to stabilize the “repumper” cesium laser with respect to the “master” cesium laser (Chapter 3). The frequencies, ω_+ and ω_- , of the two external cavity lasers used to generate the pair are tuned such that a direct beatnote between the two is measured at a frequency near $(\omega_+ - \omega_-) \approx \omega_{beat} \equiv \Delta_{HF} + \delta_{AOM}$. This beatnote signal is amplified and mixed against a frequency reference derived from a Hewlett Packard 8672C microwave synthesizer tuned to $\omega_{ref} \equiv \Delta_{HF} + \delta_{AOM} - \delta_0$. The resulting mixed-down signal component at frequency $(\omega_{beat} - \omega_{ref}) \approx \omega'_{beat} \equiv \delta_0$ is again mixed against an RF reference source at frequency δ'_0 . From the DC and low-frequency components of this signal, an analog integrating circuit is used to provide piezo (slow) and current (fast) feedback to one of the two Raman lasers such that $\delta'_0 - \delta_0 = 0$. Typically in the laboratory $\delta_{AOM} = (2\pi)(85.0$ MHz) and $\delta_0 = (2\pi)(50.0$ MHz). With the lock switched ON, the higher frequency laser (generally the FORT, in the FORT-Raman configuration) operates at a detuning of $\delta_T = \omega_+ - \omega_- = \Delta_{HF} + \delta_{AOM}$ with respect to the lower frequency laser (to which the electronic feedback is applied).

In order to set $\delta_T = \delta_R$ as required for a proper Raman pair, we upshift the lower-frequency laser using an acousto-optical modulator driven at $\omega_{AOM} = \delta_{AOM} + \delta$. The first order shifted beam is then detuned from the higher frequency Raman laser by $\delta_T = \Delta_{HF} + \delta = \delta_R$, as required. The higher frequency beam is linearly-polarized and directed along the cavity input path such that it couples to the higher-frequency birefringent mode of the cavity, \hat{l}_+ , whereas the lower-frequency beam takes another path to the cavity input and is linearly-polarized along \hat{l}_- . This technique can be used in principle for either the FORT-Raman or Raman-Raman beam configurations, but in practice it was only ever used for FORT-Raman measurements.

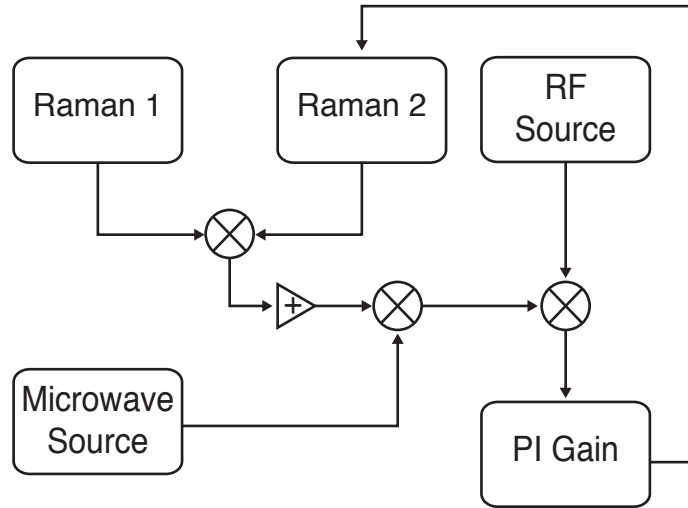


Figure 4.3: Schematic of the “old” style electronic phase lock apparatus for stabilizing the two Raman lasers.

As a diagnostic tool, we usually monitor the optical beatnote between the two lasers on a spectrum analyzer. A typical power spectrum measurement for this frequency locking method is shown in blue in Figure 4.4b. Characteristic of this beatnote are noisy sidebands suppressed from a narrow carrier signal by typically 25 – 35 dB and detuned from the carrier by 0.5 – 1 MHz. These sidebands are an artifact of the electronics used to servo the laser current and their shape and position can be manipulated by varying the feedback gain in this arm of the servo (Figure 4.4a.). Within the range of gains shown in this Figure, the lock is typically stable. However, outside of this range the stability of the lock drops off sharply and the lasers will not lock.

The sideband noise, though suppressed relative to the carrier, is not innocuous. As is discussed in Section 1.9.10 of David Boozer’s thesis, for typical Rabi frequencies it provides a sufficiently large spectral density of optical power to drive an appreciable amount of atomic population from state-to-state if it happens to overlap with particular motional or atomic transitions which are off-resonant with respect to a transition of interest. Effectively the FORT laser and the noise component of the Raman laser form an “incoherent” Raman pair.

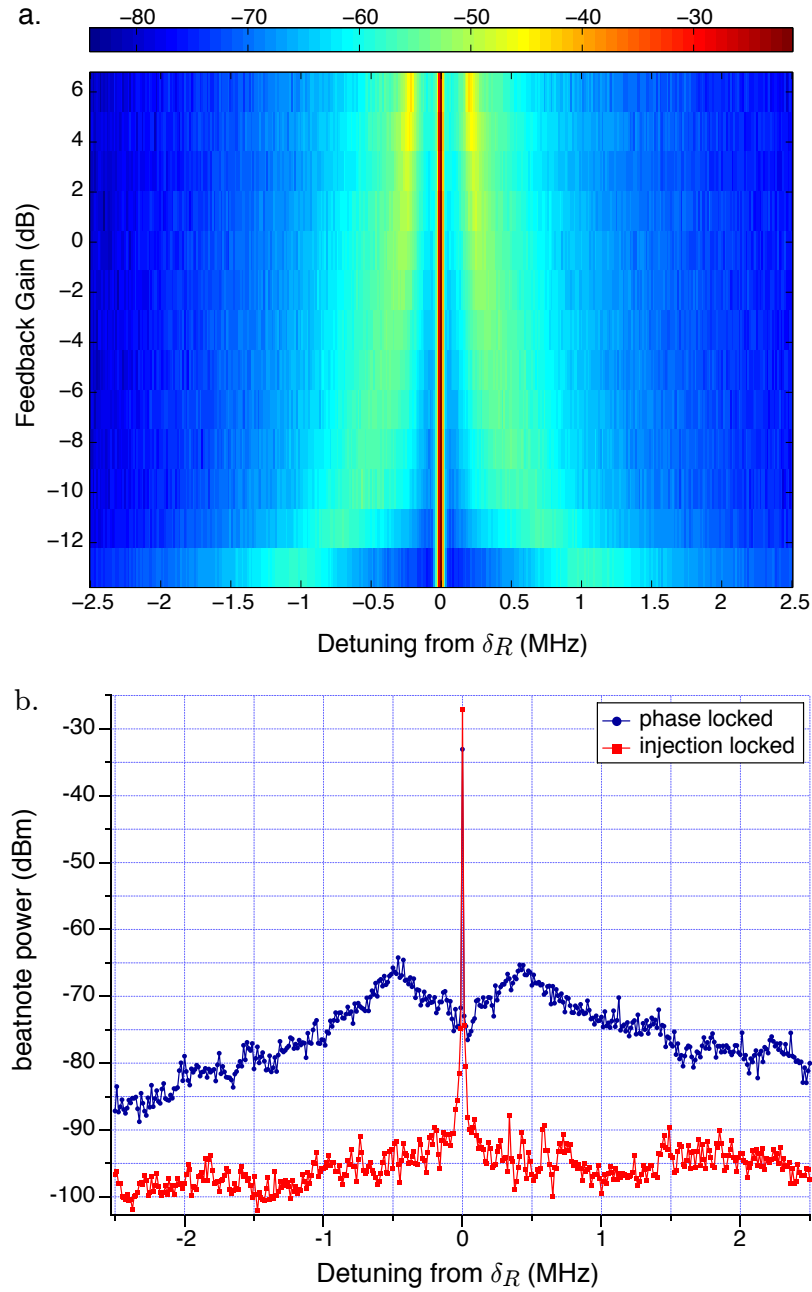


Figure 4.4: a. Beatnote between FORT and Raman lasers using the electronic phase lock technique with variable gain on the current arm of the feedback to the Raman laser. The color indicates RF power in a 1 kHz bandwidth. b. Comparison of phase lock and injection lock optical beatnotes.

While incoherent Raman transitions have their uses (*c.f.*, Section 4.5), the presence of this noise substantially limits the types of coherent Raman effects we can measure and control with the lasers locked in this way.

Direct Injection Locking (2006-Present)

After some effort to electronically filter the servo loop which was applying noise to the Raman laser, it became clear that to eliminate the noise would require a substantial redesign of servo electronics and the laser current controller. Rather than take that approach, we decided to re-think how we generate the lock and to instead use diode laser injection locking.

Figure 4.5 depicts our injection locking technique schematically. We take a small fraction of the higher-frequency Raman laser (operating at frequency ω_+) and direct it via optical fiber to an EOSpace PM-0K1-10-PFA-FFA-850-UL (S/N 73904) lithium niobate waveguide-integrated electro-optic modulator. These modulators, due to their relatively small physical size, allow for broadband (> 15 GHz) response with low modulation voltage requirements ($V_\pi = 2.5$ V is typical at DC). We modulate the EOM at $\omega_m = \Delta_{HF} + \delta_{AOM}$. For an amount of optical power injected into the EOM, P_i , the modulated signal is a comb of frequencies ($\omega_+, \omega_+ \pm \omega_m, \omega_+ \pm 2\omega_m, \dots$) with the optical power in n th component given by

$$P_n = \beta P_i J_n^2(\phi). \quad (4.21)$$

Here, β is the transmission efficiency for the modulator, J_n is the n th order Bessel function of the first kind and ϕ , the modulation index, is a function of V_{RF} , the RMS drive voltage provided to the EOM at ω_m . The modulated light emitted from the EOM serves as our injection light.

The lower-frequency laser in this configuration is unlike other injection-locked lasers in our laboratory because it is external cavity-stabilized and not free-running. In fact, we rely on the external cavity of the laser as a filter to remove frequency components of the injected light other than that at $\omega_+ - \omega_m$. With the external cavity tuned such that the laser is lasing near $\omega_- \sim \omega_+ - \omega_m$, we direct the injection light through the rejected port of a Faraday optical isolator. For modest input powers (typically $P_i = 1$ mW, and $P_{-1} = 100$ μ W) we can

achieve a stable injection lock. The capture range of the lock, typically ~ 100 MHz, is largely power-insensitive and is given by the parameters of the external cavity. For cavity lengths which support operation near $(\omega_+ - \omega_m)$, the laser acquires the frequency of the injected light. However, if the external cavity length drifts during the course of the experiment, it begins to support laser operation at other frequencies. These frequencies beat with the injected light to produce a characteristic comb of output frequencies which is the hallmark of the injection lock beginning to fail. However, the optomechanics which control the external cavity length are usually passively stable on the order of hours for fluctuations in the cavity length of the sort necessary for the lock to fail. In order to counteract this effect, we monitor the beatnote between the two lasers and manually correct for drifts. The injection-locked light is directed through an acousto-optic modulator driven at $\omega_{AOM} = \delta_{AOM} + \delta$. The up-shifted diffracted first order is sent to the cavity polarized along \hat{l}_- to complete the Raman pair.

The optical beatnote for two Raman lasers injection locked in this way is shown as the red curve in Figure 4.4b. Notice that noise in the wings of the signal is reduced by as much as a factor of 30 dB relative to the same signal taken in phase locked configuration. In order to verify that the output of the lower-frequency laser is, in fact, single mode at the desired frequency and not injection locked to any other electro-optically modulated sideband, we can generate a beatnote between the higher-frequency laser and the lower-frequency laser after it is upshifted signal by acousto-optic modulation. Any spectral component of the lower-frequency laser at the higher-frequency would appear as a beatnote at ω_{AOM} . At this frequency (as well as at $\omega_m - \omega_{AOM}$) we measure nothing above shot noise, indicating that the injection lock is single mode.

4.3 Raman as a Diagnostic Tool

The ability to drive Raman transitions between ground state hyperfine manifolds provides a powerful diagnostic tool for measuring population distributions, temperature, ambient magnet field and other relevant properties of our system. In this Section we will describe two commonly-used protocols for performing diagnostics of this sort. The first is a method for

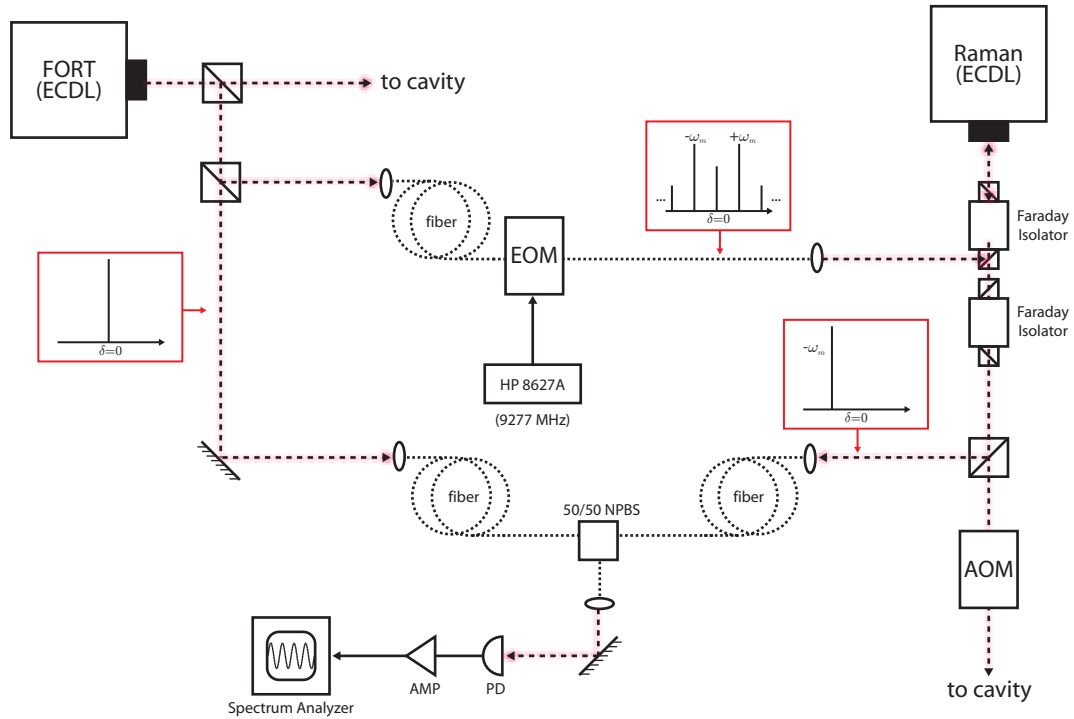


Figure 4.5: Schematic of the injection lock-based Raman pair generation scheme. Light from the FORT (or higher-frequency Raman laser for Raman-Raman configuration) is modulated in an EOSpace brand in-fiber electro-optic modulator at frequency ω_m . The modulated light is injected into the lower-frequency EC DL which is manually tuned to accept the first-order lower sideband and reject the remainder of the incident signal.

inferring the distribution of population between Zeeman states by measuring the spectrum of allowed Raman transitions for a given configuration of the system. The second is a related technique for measuring and iteratively nulling the ambient magnetic field at the location of the atom.

4.3.1 Raman Spectroscopy

We begin by preparing the atom in some distribution of Zeeman states within the $F = 3$ ground state manifold and with the Raman pair in FORT-Raman configuration. Following the initial state preparation, we switch the AOM for the lower-frequency beam ON for a period of time τ_R and with detuning δ . After τ_R , we perform state detection on the system using the down-goer technique to measure the probability P_4 that atomic population was transferred to the $F = 4$ manifold of states. By ensemble averaging over a large number of measurements of this sort and for many atoms, we can formulate a Raman spectrum - the spectrum of transfer probability (P_4) as a function of Raman detuning (δ).

In order to understand what exactly a Raman spectrum describes, we need to understand the dynamics of the system. In the absence of any decoherence (*i.e.*, exponential decay of the off-diagonal terms in the two-state density matrix for the system), the effect of the Raman pair at a fixed, resonant Raman detuning δ is to induce Rabi oscillation between the two coupled states indefinitely at frequency Ω_E . Using the optical Bloch equations [31], we can calculate the probability P_4 to find the atom in $F = 4$ after a fixed duration pulse at a given detuning from a Raman resonance:

$$P_4(\Omega_E, \delta, \tau_R) = \frac{1}{1 + \frac{\delta^2}{\Omega_E^2}} \sin^2 \left[\frac{1}{2} \sqrt{\Omega_E^2 + \delta^2} \tau_R \right]. \quad (4.22)$$

This is a Lorentzian envelope of width Ω_E modulated by a sinusoid and should look familiar from the master equation discussion of Chapter 2. However, as we will see in Section 4.4, our system is not decoherence-free and the oscillation exponentially decays at a rate T_2^* , averaging away the sinusoidal component of (4.22). We will explore the physical significance of T_2^* and the sources of decoherence in our system later, but it suffices for now to note that after the oscillation is fully damped away that the asymptotic state of the system for

on-resonance driving is a mixed state with equal probability $P_3 = P_4 = 0.5$ to detect the atom in $F = 3$ and $F = 4$, respectively. As a function of detuning, the Raman spectrum involving n Raman resonances at frequencies ω_n takes the shape:

$$P_4(\delta) = \frac{1}{2} \sum_n p_n \frac{\Omega_E^2(n)}{\Omega_E^2(n) + (\delta - \omega_n)^2} \quad (4.23)$$

where p_n is the probability that the system is initially in one of the two states coupled by the resonance with index n .

Informed by these dynamics, we must choose a Raman pulse duration τ_R in order to map a Raman spectrum. Under certain circumstances it can be useful to select a pulse length $\tau_R = \pi\Omega_0^{-1}$ (a so-called π -pulse) such that for the $m_F = 0, \Delta m_F = 0$ transition in an axial magnetic field we have ideally transferred all of the population initially in $|3, 0\rangle$ to $|4, 0\rangle$ when $\delta = 0$. More generally, it is useful to choose a Raman pulse length $\tau_R \gg T_2^*$ so as to allow the Rabi oscillation to damp away and measure the resulting asymptotic population distribution.

In the laboratory, the protocol for measuring a Raman spectrum is as follows. Before the experiment begins, we manually set the Raman and FORT powers to produce the desired effective Rabi frequency. A typical range of values is $\Omega_0 = 125\text{-}200$ kHz for the ($|3, 0\rangle \leftrightarrow |4, 0\rangle$) clock transition, depending on the application. The ADWin Gold system is programmed to readjust the frequency of the lower-frequency Raman AOM via IEEE 488 communications just prior to each attempt to load an atom into the FORT. This sets the value of δ which will then be used for all measurements involving that particular atom. The ADWin also sends a train of TTL-level pulses to channel D of the P7888 counting card before the measurement begins which encodes information about the value of δ . This information is stored on an atom-by-atom basis and is subsequently decoded in post-processing. A few milliseconds after the ADWin is finished programming the system, the MOT sequence loads an atom into the cavity mode and the experiment begins. Following each state preparation event, a fixed-duration ($\tau_R = 25 \mu\text{s}$ typical) TTL pulse is used to gate ON the lower-frequency Raman AOM at the preprogrammed frequency. A short time (typically $\sim 30 \mu\text{s}$) after the Raman is gated OFF, a $\tau_p = 200 \mu\text{s}$ pulse of ($4 \leftrightarrow 5'$) probe light is coupled

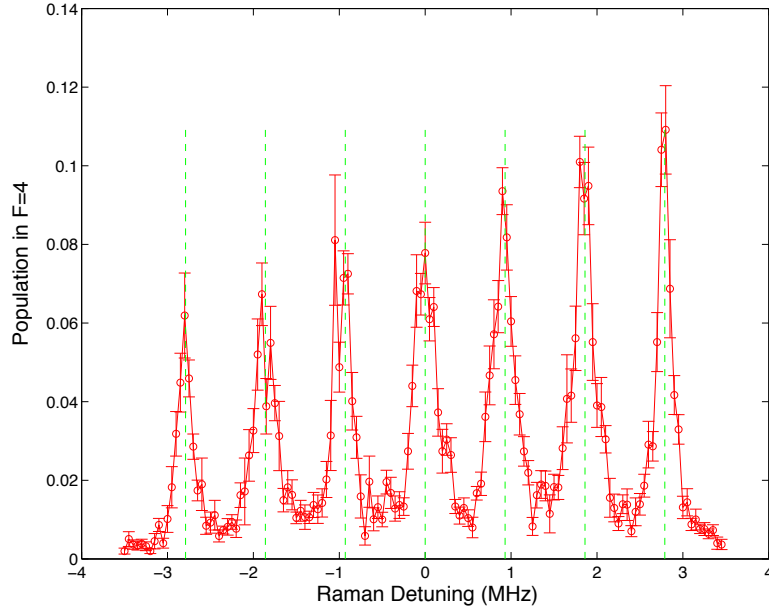


Figure 4.6: A typical Raman spectrum for our system with a pure axial magnetic field and no initial Zeeman state preparation.

to the cavity to perform down-gate detection. The last $100 \mu\text{s}$ of the probe sequence is accompanied by ($3 \leftrightarrow 3'$) resonant light from the lattice side beams to verify the presence of an atom in the cavity for that measurement. The experiment then starts over and again prepares the initial state of the atom for measurement. This process is iterated between 250-1500 times per atom depending on the average trap lifetime of the atoms undergoing measurement. The Raman spectrum is calculated by taking the average probability to find the atom in $F = 4$ over all measurements involving atoms loaded into the FORT at a given preprogrammed Raman detuning δ . A typical Raman scan involves somewhere from 5-20 atoms-per-frequency.

A typical, representative example of the type of the Raman spectrum this procedure produces is shown in Figure 4.6. Notice that there are seven discrete resonances in this particular spectrum and that the spectrum is symmetric in frequency (though not in amplitude, due to pumping effects) about $\delta = 0$. For this measurement, the atom was initially prepared in the $F = 3$ manifold but no care was taken to optically pump into a particular

Zeeman substate. We also applied a small magnetic bias field along the cavity axis ($B_z = 1.3$ G). As described by equation (4.20) a magnetic field directed along the cavity axis permits only $\Delta m_F = 0$ transitions between states ($|3, m_F\rangle \leftrightarrow |4, m_F\rangle$). For this magnetic field configuration we expect to address seven transitions corresponding to ($|3, m_F\rangle \leftrightarrow |4, m_F\rangle$), $m_F \in \{0, \pm 1, \pm 2, \pm 3\}$ (these are the seven resonances shown in Figure 4.6). The resonant frequency of each is given by the sum of the ground state hyperfine splitting Δ_{HF} and the magnitude of the weak-field Zeeman splitting for the pair of states involved in the transition:

$$\omega_0(m_F) = (g_4 - g_3)\mu_B B_z m_F \quad (4.24)$$

$$= \frac{1}{2}\mu_B B_z m_F \quad (4.25)$$

$$= (2\pi)(700 \text{ kHz/G})B_z m_F \quad (4.26)$$

For the magnetic field used in this measurement we predict a resonance-to-resonance splitting of $\Delta\omega = |\omega_0(m_F) - \omega_0(m_F - 1)| = (2\pi)(930 \text{ kHz})$. The vertical green lines in Figure 4.6 indicate the Raman detunings which we expect should correspond to the resonant frequencies of the allowed transitions in this magnetic bias field. Clearly the measurement is in good agreement with theory. We can now generalize Equation (4.23) to this set of experimental parameters:

$$P_4(\delta) = \frac{1}{2} \sum_{m_F=-3}^3 p_3(m_F) \left[1 + \frac{(\delta - \omega_0(m_F))^2}{\Omega_0^2(1 - m_F^2/16)} \right]^{-1}. \quad (4.27)$$

By fitting to this function we can infer the values $p_3(m_F)$ which are the amplitudes of the atomic population in the states $|3, m_F\rangle$ following the initial state preparation procedure. Effectively, Raman spectroscopy allows us to adapt the down-goer technique for measuring atomic hyperfine states to also read out the distribution of Zeeman state population in the atom.

We can observe a couple of interesting effects by narrowing the focus of our scan to just the ($|3, 0\rangle \leftrightarrow |4, 0\rangle$) transition (Figure 4.7). First, notice that there is a small oscillatory component convolved with the Lorentzian envelope of the feature. The oscillation is the signature of small amount of coherence left in the system even after the full pulse duration,

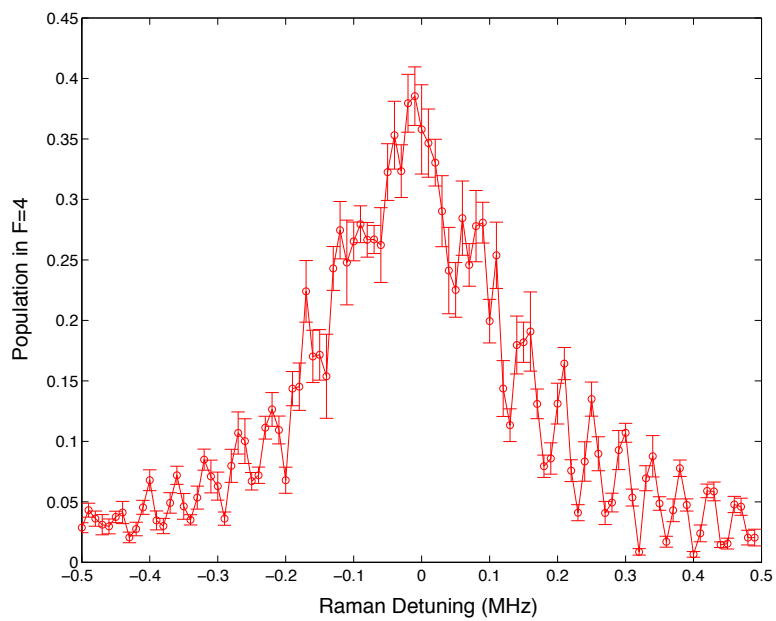


Figure 4.7: High-resolution Raman spectrum of the ($|3,0\rangle \leftrightarrow |4,0\rangle$) clock transition. The small oscillation on the Lorentzian envelope indicates that after this particular choice of Raman pulse duration there is still a small amount of coherence left in the system. Also notice that the peak is shifted $\Delta U_{0,4-3} \approx -20$ kHz to the red due to the differential FORT shift on the two ground states.

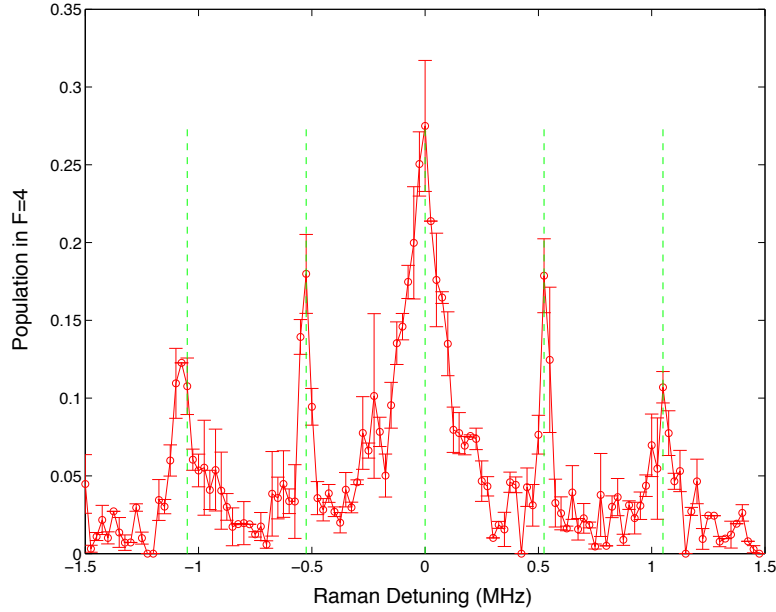


Figure 4.8: Raman spectrum for an atom-cavity system with a strong axial magnetic field $B_z \approx 1.3$ G in addition to a weaker transverse magnetic perturbation $B_x \approx 0.7$ G. Vertical green lines indicate the expected locations of the allowed Raman transitions based on the total magnetic field.

τ_R . As predicted by Equation (4.22), the frequency of this oscillation grows larger as the Raman detuning is swept away from resonance. The second interesting feature of this measurement is that the envelope of the transition is offset from $\delta = 0$ by $U_{0,4-3} = -20$ kHz. This offset is the result of the small hyperfine state-dependent residual AC Stark shift caused by the FORT and discussed in Chapter 3. This shift, as we will see in Subsection 4.4 has a very subtle and profound impact on the coherent dynamics of the system as a whole.

The discussion thus far has focused on Raman spectra measured with a purely axial magnetic bias field. Although the magnitudes of the magnetic fields which we can apply along directions transverse to the cavity axis are typically an order of magnitude smaller than that which can apply along the cavity axis, we can still induce a small perturbative transverse magnetic field in order to observe the effect of this sort of field on the system.

Figure 4.8 shows a partial Raman spectrum for atoms in a large axial magnetic bias field $B_z \approx 1.3$ G in addition to a smaller transverse bias field $B_x \approx 0.7$ G. The total magnetic field is $|\vec{B}| \approx 1.5$ G and the angles which specify the orientation of the cavity axis with respect to the quantization axis are $\theta = 0.15\pi$ and $\phi = 0$. Based on Equation (4.20) we expect two types of features in the Raman spectrum for this field. The first are transitions of the sort we have seen in previous spectra, coupling ($|3, m_F\rangle \leftrightarrow |4, m_F\rangle$) with Rabi frequency

$$\Omega_E = 0.89(1 - m_F^2/16)^{1/2}\Omega_0. \quad (4.28)$$

As before, these transitions exhibit Raman resonance at detunings given by:

$$\delta = \omega_0(m_F) = (2\pi)(700 \text{ kHz/G})|\vec{B}|m_F. \quad (4.29)$$

The second type of resonance corresponds to frequency-degenerate pairs of transitions coupling ($|3, m_F\rangle \leftrightarrow |4, m_F + 1\rangle$) and ($|3, m_F + 1\rangle \leftrightarrow |4, m_F\rangle$) with Rabi frequencies

$$\Omega_E(|3, m_F\rangle \leftrightarrow |4, m_F + 1\rangle) = 0.06\Omega_0(4 + m_F)^{1/2}(5 + m_F)^{1/2}, \quad (4.30)$$

$$\Omega_E(|3, m_F + 1\rangle \leftrightarrow |4, m_F\rangle) = 0.06\Omega_0(3 - m_F)^{1/2}(4 - m_F)^{1/2}. \quad (4.31)$$

The resonant detunings for these transitions are equal and given by:

$$\omega_{\pm 1}(m_F) = (2\pi)(700 \text{ kHz/G})|\vec{B}|\left(m_F + \frac{1}{2}\right). \quad (4.32)$$

The partial spectrum of transitions shown in Figure 4.8 exhibits three broad resonances corresponding to ($|3, m_F\rangle \leftrightarrow |4, m_F\rangle$), $m_F \in \{0, \pm 1\}$ and two narrow resonances corresponding to ($|3, 0\rangle \leftrightarrow |4, \pm 1\rangle$) and ($|3, \pm 1\rangle \leftrightarrow |4, 0\rangle$). The vertical green lines transposed over the spectrum correspond to the anticipated resonant frequencies $\omega_{0, \pm 1}$ of the transitions and are in good agreement with the data. Notice also that the $\Delta m_F = \pm 1$ features exhibit much narrower resonances than the $\Delta m_F = 0$ features. If we recall that the spectral widths of these features are set by the effective Rabi frequencies for the transitions in question, then it is clear that this effect is a result of the smaller Rabi frequencies expected

for $\Delta m_F = \pm 1$ transitions in this configuration of magnetic fields.

4.3.2 Raman Magnetometry and Field Nulling

With an understanding of how the shapes of Raman spectra vary as a function of the magnetic field applied to the system, we can use this type of measurement to perform magnetometry with the Zeeman splitting of the atom serving as the “sensor.” Careful measurement of the widths of each spectral feature in addition to their resonant frequencies offers all of the information necessary to deduce the magnitudes of the axial and transverse magnetic fields at the location of the atom. Determination of the direction of the transverse field is not possible from this single measurement due to the radial symmetry of the problem. However, by applying a transverse calibration magnetic field of known magnitude and orientation we can break this symmetry and resolve the direction of the ambient transverse field.

In addition to being able to infer the magnetic field strength, we have also developed a method in the laboratory for zeroing a static magnetic field at the location of the atom. To understand how this method works, first consider a system in which the magnetic fields at the atom are already nulled. In this system there is no magnetic field to determine a quantization axis or to introduce Zeeman splitting. All Raman transitions coupling $\Delta m_F = 0, \pm 1$ are allowed and all are frequency degenerate. Regardless of where the atomic population is initially distributed, the Raman spectrum for the system will manifest itself as a single Lorentzian envelope centered at $\delta = 0$ with height $P_4(0) = 0.5$.

Next, consider how the system responds if an arbitrarily-oriented magnetic field is slowly ramped on, starting from zero amplitude. The effect of this field will be to introduce a quantization axis and to gradually break the frequency degeneracy between Raman resonances. This will manifest itself in Raman spectroscopy with the initial Lorentzian distribution at $\delta = 0$ splitting out into the full spectrum of transitions we explored in the previous Subsection. In the limit of a large magnetic field, the asymptotic value of the Raman spectrum at zero detuning is given simply by the shape of the feature corresponding to the $(|3, 0\rangle \leftrightarrow |4, 0\rangle)$ clock transition, or $P_4(0) = 0.5p_3(0)$. Recall that $p_3(0)$ is the initial population in $|3, 0\rangle$.

There is also an intermediate regime wherein the magnetic field is large enough to break the degeneracy between the transitions but the widths of the Lorentzian features corresponding to transitions involving $m_F \neq 0$ overlap significantly with the envelope of the carrier. Here, the amplitude of the Raman spectrum at zero detuning is a complicated function of the initial population distribution, the magnetic field and the Rabi frequency of the Raman pair, but is generally $0.5 \geq P_4(0) \geq 0.5p_3(0)$.

This effect constitutes the mechanism for our field nulling scheme. The signal we are concerned with is $P_4(0, \vec{B})$ which is $P_4(0)$ as a function of the static magnetic bias field \vec{B} produced by the three, orthogonal pairs of current-carrying coils which surround the chamber. Assume that there is initially a small ambient DC magnetic field \vec{B}' which we want to zero by applying feedback to the coil pairs. This initial field is comprised of components $\{B'_x, B'_y, B'_z\}$ along each of the axes $\{\hat{x}, \hat{y}, \hat{z}\}$ determined by the orientations of the coils. We need to determine the amounts of current through each coil pair necessary to produce a magnetic field $\vec{B} = (-B'_x, -B'_y, -B'_z)$ of equal and opposite magnitude along each of these axes such that $\vec{B}' + \vec{B} = 0$. The way in which we do this is by looking for maxima in $P_4(0, \vec{B})$ - coil settings for which the field along that axis is most nearly zeroed.

We begin by selecting a single pair of coils to determine an initial axis along which to apply the nulling technique. Prior to the FORT loading sequence, we use the digital-to-analog convertor built into the ADWin Gold to provide a programming voltage to the power supply controlling the current through those coils. As described in Section 3.2.2, the programming voltage is proportional to the steady-state current applied through the coil. The value of this programming voltage is varied discretely from loading attempt-to-loading attempt over a pre-determined range of values. For each coil current setting, an atom is loaded into the FORT and typically 1×10^3 measurements are made of $P_4(0, \vec{B})$ for that atom. The ADWin also sends a series of TTL pulses to channel D of the P7888 photon counting card to identify which measurements correspond to a particular power supply setting.

By averaging all measurements of $P_4(0, \vec{B})$ corresponding to a specific current through the coil pair, we are able to determine the functional dependence and maximal value over all programming voltages. We then fix the current through that set of coils at the value

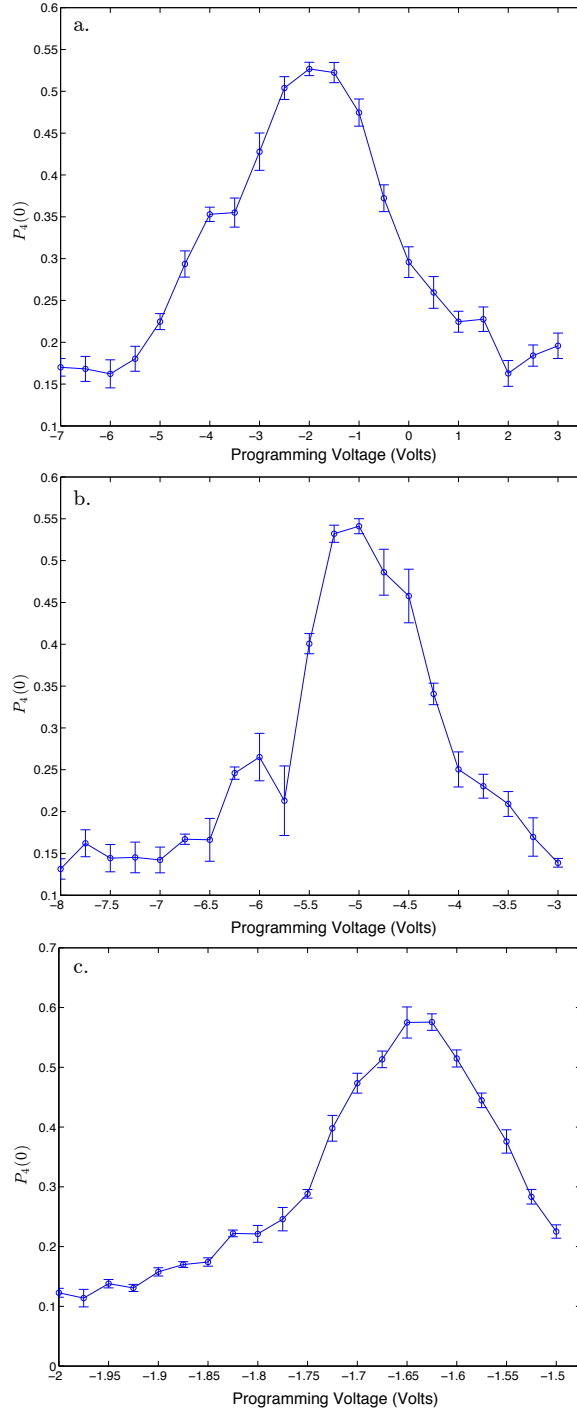


Figure 4.9: Measurements of $P_4(0, \vec{B})$ for bias fields applied along the a. \hat{x} -, b. \hat{y} -, and c. \hat{z} -axes. Maxima indicate null field settings. Calibrations for coil programming voltages are given in Table 3.3. These measurements were made with $\Omega_E \approx 125$ kHz.

which produced the maximum and perform the same set of measurements with another coil pair. By repeating this procedure a number of times for all three coil pairs, we gradually converge on a set of programming voltages which null the static magnetic field at the atom.

Figure 4.9 demonstrates the results of this type of measurement for each of the coil pairs in our system. Along all three axes we are able to clearly resolve a maximal value of $P_4(0, \vec{B})$. For the step sizes in programming voltage and Rabi frequency, Ω_E , used for this particular set of measurements we are able to null the field to within $|\vec{B}'| < 1.5 \times 10^{-2}$ G. These measurements are representative of the results we obtain after only 1 – 2 iterations of the field nulling protocol. Note that the widths of each of these features are complicated functions of Ω_E and if we chose to, we could increase the resolution of the measurement by decreasing the Rabi frequency. Finally, it should be emphasized that this procedure takes 10 – 15 minutes to perform in the laboratory is therefore insensitive to all but DC magnetic fields. Any field fluctuations faster than few thousandths of a Hertz will average away over the duration of our measurement.

4.4 Rabi Nutation and Decoherence

4.4.1 Decoherence Theory

In the previous section, in the context of Raman spectroscopy, we alluded to how the temporal dynamics of an atom undergoing stimulated Raman transitions between hyperfine ground states are functionally equivalent to the dynamics of a classically driven two-state atom. We can define a density operator over the basis of hyperfine states coupled by the Raman pair:

$$\hat{\rho} = \begin{pmatrix} \rho_{33} & \rho_{34} \\ \rho_{43} & \rho_{44} \end{pmatrix}. \quad (4.33)$$

Here $\rho_{33} = P_3$ and $\rho_{44} = P_4$ are the probabilities to measure the atom in the $F = 3$ or $F = 4$ hyperfine states and $\rho_{34} = \rho_{43}^*$ are coherence terms. The dynamics of the classically

driven system are governed by the well-known optical Bloch equations (OBEs) [31]:

$$\frac{d\rho_{33}}{dt} = \frac{i}{2}(\Omega_E^* \tilde{\rho}_{34}^* - \Omega_E \tilde{\rho}_{34}) \quad (4.34)$$

$$\frac{d\rho_{44}}{dt} = \frac{i}{2}(\Omega_E \tilde{\rho}_{34} - \Omega_E^* \tilde{\rho}_{34}^*) \quad (4.35)$$

$$\frac{d\tilde{\rho}_{34}}{dt} = \frac{i}{2}\Omega_E^*(\rho_{44} - \rho_{33}) - i\delta\tilde{\rho}_{34}, \quad (4.36)$$

where $\tilde{\rho}_{34} = e^{-i\delta t}\rho_{34}$. The OBEs follow from the equation of motion for the density matrix in the Schrödinger picture. From conservation laws, we can also add the constraint $\rho_{33} + \rho_{44} = 1$. If we assume the initial conditions $\rho_{33} = 1$ and $\rho_{44} = \rho_{34} = \rho_{43} = 0$ (*i.e.*, that we have initialized the state of the system to $F = 3$), then the solutions to these equations take the form:

$$\rho_{44}(t) = \frac{\Omega_E^2}{\Omega_E^2 + \delta^2} \sin^2 \left(\frac{1}{2} \sqrt{\Omega_E^2 + \delta^2} t \right) \quad (4.37)$$

$$\begin{aligned} \rho_{34}(t) = \frac{\Omega_E}{\Omega_E^2 + \delta^2} \sin \left(\frac{1}{2} \sqrt{\Omega_E^2 + \delta^2} t \right) & \left[-\delta \sin \left(\frac{1}{2} \sqrt{\Omega_E^2 + \delta^2} t \right) \right. \\ & \left. + i \sqrt{\Omega_E^2 + \delta^2} \cos \left(\frac{1}{2} \sqrt{\Omega_E^2 + \delta^2} t \right) \right]. \end{aligned} \quad (4.38)$$

Notice that the expression for $\rho_{44}(t)$ is equivalent to Equation (4.22) from the previous Section.

It is particularly instructive to treat this problem in terms of what is known as the Bloch sphere. In general, we can decompose the density operator into a sum of products between the Pauli spin matrices $\hat{\sigma}_i$ and the components of a vector \vec{S} :

$$\hat{\rho} = \frac{1}{2}(1 + \vec{S} \cdot \vec{\sigma}), \quad (4.39)$$

where the individual components of \vec{S} are given by:

$$S_1 = 2\text{Re}(\rho_{34}) \quad (4.40)$$

$$S_2 = 2\text{Im}(\rho_{34}) \quad (4.41)$$

$$S_3 = \rho_{44} - \rho_{33}. \quad (4.42)$$

Geometrically, the Bloch vector \vec{S} represents a point on a three-dimensional unit sphere. The projection of the vector onto the \hat{z} -axis corresponds to what is known as the inversion, or the difference in population between the $F = 4$ and $F = 3$ states. The \hat{x} - and \hat{y} -components of vector correspond to the real and imaginary components of the coherence. We can visualize the effect of the OBEs as the motion of this vector on the surface of the sphere.

For resonant driving ($\delta = 0$), the system undergoes coherent Rabi nutation (or, more colorfully, “flopping”) between between the coupled states, $|3, m_F\rangle$ and $|4, m'_F\rangle$, at frequency Ω_E . This can be pictured on the Bloch sphere (Figure 4.10a) as rotation at Ω_E of the Bloch vector about a great circle in the plane of the \hat{y} -axis. By applying Raman pulse of finite duration we can use this oscillation to prepare arbitrary coherent superpositions of the two atomic states. For instance, a Raman pulse of duration $\tau_R = \pi/2\Omega_E$ (a “ $\pi/2$ -pulse”) will generate the state $|\psi\rangle = 1/\sqrt{2}(|3, m_F\rangle + i|4, m'_F\rangle)$ whereas a pulse of duration $\tau_R = \pi/\Omega_E$ (a “ π -pulse”) will completely invert the atomic population.

In the case of non-zero detuning, the state of the system oscillates at a larger frequency $\Omega'_E = \sqrt{\delta^2 + \Omega_E^2}$ but the Raman pair can only invert a fraction of the initial population. In the Bloch vector picture, this corresponds to oscillation of the state vector on a small circle of the Bloch sphere with radius $\Omega_E^2/\Omega_E'^2$. (Figure 4.10b). For a fixed-phase Raman pair this can also be viewed as precession about a fixed vector $\vec{Q} = (\Omega_E/\Omega'_E, 0, \delta/\Omega'_E)$. By introducing an optical phase difference to the Raman pair we can offset this precession in the \hat{x} - \hat{y} -plane.

It is important to note that this treatment of the OBEs is idealized - under the current model a driven atom will undergo Rabi nutation indefinitely. In actual practice there are a variety mechanisms by which noise can couple to the system and significantly alter the dynamics. A typical approach to modeling sources of noise is to tack a variety of *ad hoc*, phenomenological terms onto the OBEs. Rather than begin by doing this, we will take a slightly different approach and use the (equally *ad hoc*) quantum operations formalism of Nielsen and Chuang [45]. In particular we will assume that the environment performs some quantum operation \mathcal{E} , a superoperator, on the atom such that the density matrix undergoes

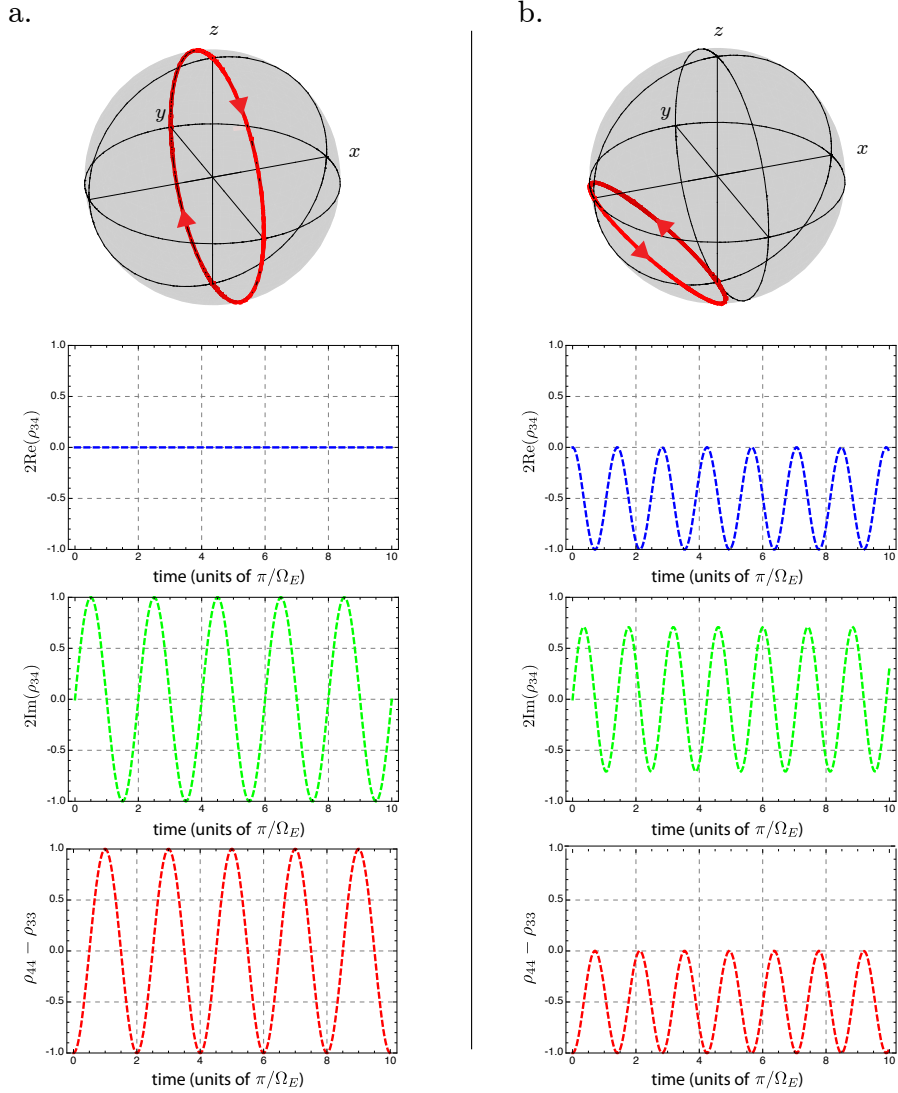


Figure 4.10: a. Bloch sphere representation and time-dependent Bloch vector components for a resonantly driven ($\delta = 0$) atom. Note the Rabi oscillation at frequency Ω_E between $|3, m_F\rangle$ and $|4, m'_F\rangle$. Geometrically, this takes the form of nutation on the Bloch sphere along a great circle perpendicular to the \hat{y} -axis. b. Off-resonantly driven case ($\delta = \Omega_E$). The Bloch vector oscillates along a small circle of the Bloch sphere at frequency $\Omega'_E = \sqrt{\Omega_E^2 + \delta^2}$.

the following transformation:

$$\rho(t) = \begin{pmatrix} \rho_{33}(t) & \rho_{34}(t) \\ \rho_{34}^*(t) & \rho_{44}(t) \end{pmatrix} \xrightarrow{\mathcal{E}} \rho(t) = \begin{pmatrix} 1 - e^{-t/T_1} \rho_{44}(t) & e^{-t/T_2} \rho_{34}(t) \\ e^{-t/T_2} \rho_{34}^*(t) & e^{-t/T_1} \rho_{44}(t) \end{pmatrix} \quad (4.43)$$

This transformation encompasses two unique classes of effects. The first is an exponential decay of the diagonal elements of $\hat{\rho}$ at a rate T_1 (here the nomenclature - T_1 and T_2 - is a holdover from similar work in the nuclear magnetic resonance community). This type of noise is also commonly known as “amplitude damping” (or, in the NMR literature, as the “spin-lattice” or “longitudinal” relaxation). A particular form of amplitude damping with which we are already familiar is spontaneous decay from one state to another as a result of coupling between the atom and an environmental reservoir of electromagnetic vacuum states. However spontaneous decay also exhibits the second type of noise mechanism modeled in \mathcal{E} - decay of off-diagonal elements, or coherences, at a rate T_2 . This type of process is commonly known as “decoherence” (due to its effect on the coherence terms of the density matrix) and “phase damping” (also in NMR jargon, “spin-spin” or “transverse” relaxation). There are a variety of experimental phenomena which can potentially contribute to phase damping. As we will discuss later, these include frequency and intensity noise on the Raman lasers, off-resonant scattering of photons from the FORT laser, and fluctuations in Ω_R and δ as a function of atomic position and motion. The times T_1 and T_2 are generally discussed in terms of ensemble averages over, for example, a large number of spins in crystal lattice. While we deal with only one spin (and one atom) at a time in our system, the measurements we make are typically averaged over thousands of repetitions of the experiment and can be treated with the same formalism.

To good approximation we can ignore amplitude damping effects and omit contributions from T_1 . Typical Rabi frequencies for our experiments are orders of magnitude larger than the linewidth of the cesium hyperfine ground state and so spontaneous decay does not contribute significantly to dynamics over the timescales in which we are interested. Instead we will focus on dephasing, which can be seen to play a prominent role in the system. Regardless of how phase noise affects the transient dynamics of the atom, it is clear that at times long compared to T_2 , an initial pure state of the system will decay into a mixed

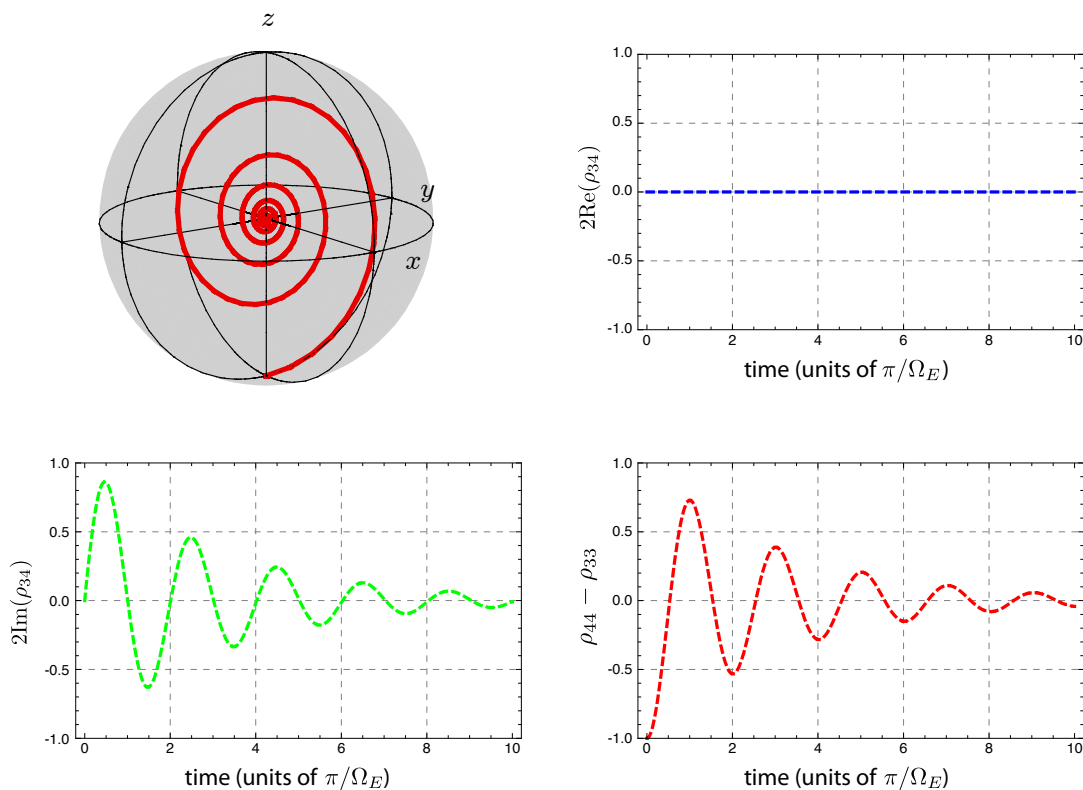


Figure 4.11: Effect of phase damping on the Bloch vector of a resonantly driven system with $T_2 = 5\Omega_E^{-1}$. Dephasing damps out Rabi oscillation as the system asymptotically approaches the maximally mixed state, $\hat{\rho} = 1/2 |3, m_F\rangle \langle 3, m_F| + 1/2 |4, m'_F\rangle \langle 4, m'_F|$.

state (or classical, probabilistic mixture). In the Bloch vector representation, mixed states correspond to points inside (as opposed to on the surface of) the Bloch Sphere.

To see how the evolution from pure to mixed state takes place, we can reformulate our *ad hoc* quantum operation as either as set of new terms in the OBE or, equivalently, as a quantum Monte Carlo simulation. Figure 4.11 shows the evolution of the phase damped Bloch vector and its three components for $T_2 = 5\Omega_E^{-1}$ for a resonantly-driven atom. The system undergoes damped Rabi oscillation and asymptotically approaches the maximally

mixed state:

$$\hat{\rho} = \frac{1}{2} |3, m_F\rangle \langle 3, m_F| + \frac{1}{2} |4, m'_F\rangle \langle 4, m'_F| \quad (4.44)$$

(the maximally mixed state for a system is the mixed state for which it is equally probable to measure the system in any of its pure eigenstates). In the Bloch sphere picture, this corresponds to nutation about the \hat{y} -axis as the vector spirals inward towards $\vec{S} = (0, 0, 0)$. The probability to detect the atom in $F = 4$ after a Raman pulse of duration τ_R , the observable which we measure in the laboratory, takes the functional form:

$$P_4(\tau_R) = \frac{1}{2} [1 - e^{-\tau_R/2T_2} \cos(\Omega_E \tau_R)]. \quad (4.45)$$

An important question now is whether our makeshift noise model has a phenomenological basis in reality. To address this issue, we begin by assuming that instead of applying a constant damping term to the density matrix coherences that the beams which are driving the Raman transitions have either a small amount of intensity or frequency noise on them. The effect of the optical cavity is to perform FM-to-AM conversion on transmitted light and so the effects of both are similar. As the intensity and/or detuning from the atom of the beams fluctuates, we can model this in terms of its effect on an arbitrary state vector of the system:

$$|\psi\rangle(t) = c_3(t) |3, m_F\rangle + c_4(t) |4, m'_F\rangle \quad \longrightarrow \quad (4.46)$$

$$|\psi'\rangle(t) = c_3(t) |3, m_F\rangle + \mathcal{P}(\theta', t) e^{i\theta'} c_4(t) |4, m'_F\rangle. \quad (4.47)$$

Here θ' is a random phase imparted to the atom by the Raman pair and $\mathcal{P}(\theta', t)$ represents the probability that at time t that the value of the random phase will be given by θ' . If we assume that the noise on the lasers is Gaussian distributed then we can model $\mathcal{P}(\theta', t)$ as random walk with zero mean and phase diffusion which is linear in time $\sigma^2 = 2\chi t$:

$$\mathcal{P}(\theta(t), t) = \frac{1}{\sqrt{4\pi\chi t}} e^{-\theta^2/4\chi t}. \quad (4.48)$$

Integrating the density matrix for this state over all possible phases θ' yields:

$$\hat{\rho} = \int_{-\infty}^{+\infty} |\psi'\rangle \langle \psi'| d\theta' = \begin{pmatrix} |c_3|^2 & e^{-\chi t} c_3 c_4^* \\ e^{-\chi t} c_4 c_3^* & |c_4|^2 \end{pmatrix}. \quad (4.49)$$

Under the substitution $\chi = 1/T_2$ we have reclaimed our original, *ad hoc* noise model:

$$\hat{\rho} = \begin{pmatrix} \rho_{33} & e^{-t/T_2} \rho_{34} \\ e^{-t/T_2} \rho_{34}^* & \rho_{44} \end{pmatrix}. \quad (4.50)$$

We should note that noise on the Raman beams is not the only source of this type of dephasing. Two other examples include: motion of an atom in the FORT effectively modulating the intensity and phase of the Raman pair at the position of the atom; and mapping magnetic field noise onto the atom via the Zeeman effect. Moreover, this is not the only physical model of noise which can lead to decoherence. Another example is off-resonant scattering of FORT light which causes the system to undergo a “quantum jump”. These jumps instantaneously project the system into one of the two eigenstate and eliminate the coherence terms in the density matrix. Averaging over an ensemble of these kinds of events, we recover the form of Equation (4.50).

This leads us to an interesting question. Although phase noise introduced because a particularly hot atom samples a large range of Rabi frequencies and phase noise resulting from scattering of stray light both lead to the same functional form for the noise-coupled density matrix, they are fundamentally different physical phenomena. In fact, there are generally two distinct classes of phase damping mechanisms. We can make that distinction by rewriting the spin-spin relaxation time constant as the sum of two terms:

$$\frac{1}{T_2^*} = \frac{1}{T_2'} + \frac{1}{T_2}. \quad (4.51)$$

The naming convention for each term is a strange holdover from the world of NMR and MRI, but the first term, T_2^* , is the total effective phase damping time constant. The second, T_2' , corresponds to reversible, or inhomogeneous, dephasing - these are types of noise which are unique to a particular configuration of the experiment (*i.e.*, inhomogeneous over the full,

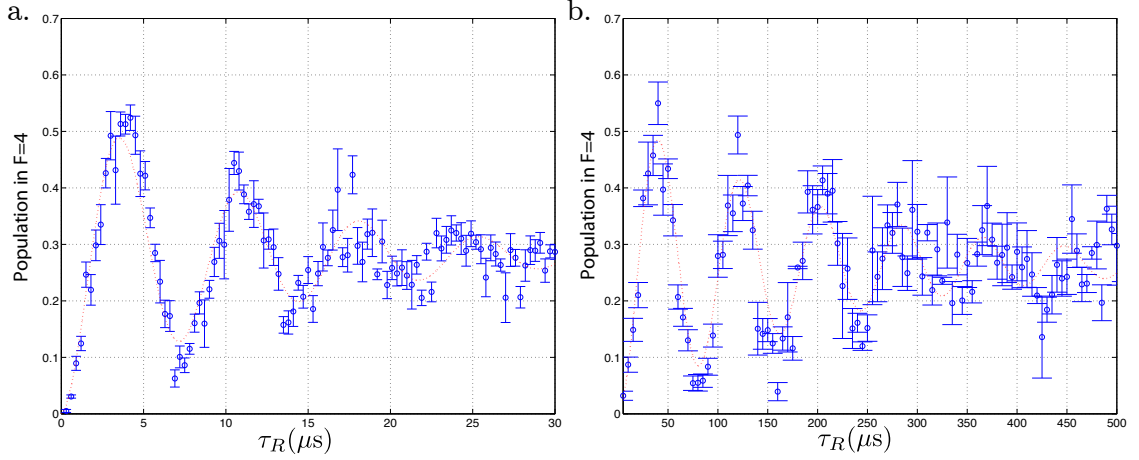


Figure 4.12: Rabi oscillation on the ($|3,0\rangle \leftrightarrow |4,0\rangle$) clock transition at zero detuning and with a. $\Omega_E = (2\pi)(137 \text{ kHz})$ and b. $\Omega_E = (2\pi)(12.3 \text{ kHz})$. Data is shown in blue with statistical error and the red dashed line constitutes a fit to Equation (4.45).

ensemble of data). Inhomogeneous dephasing effects include things like slow (atom-to-atom timescale) drifts in the power in the Raman pair, effects dependent on atomic temperature, and slow magnetic field drifts. Under a particular set of Raman pulses known as a spin echo, we effectively time reverse the noise and see a revival in the coherence of the system [26]. The third term, T_2 , represents irreversible, or homogeneous, dephasing. These are sources of noise which couple with uniform strength to all measurements in the ensemble. Homogenous effects include things like the rate of incoherent scatter of FORT light and fast-timescale Raman intensity fluctuations.

4.4.2 Measurements

This leads us finally to how we can characterize Rabi oscillation and decoherence in our experiment. The observable to which we have convenient access by way of down-goer detection is the population in each hyperfine state of the atom. Similar to Raman spectroscopy, we will measure $P_4(\tau_R, \delta)$, however now with variable Raman pulse duration, τ_R , and at fixed detuning. This type of measurement is also only possible in the FORT-Raman configuration - ensemble averaging over different phases α in the Raman-Raman configuration

leads to a broad distribution of Rabi frequencies to which atoms can couple which, in turn, leads to a T_2^* far too small to observe any coherence.

The experimental protocol is similar to that for spectroscopy - we begin by using the ADWin Gold to remotely program an SRS DG535 pulse generator to produce pulses of the desired length, τ_R , when externally triggered. For each attempt to load an atom into the FORT, that atom will interact only with Raman pulses of one, particular duration. A train of digital pulses to the P7888 is used to provide a “stamp” indicating which pulse duration is associated with each loading attempt. After an atom is loaded into the cavity, we iterate 500 – 1500 cycles of fixed-duration Raman, down-goer state detection and down-goer atom detection. From these measurements, an ensemble average of the total population in $F = 4$ as a function of τ_R is computed from the data. For this set of measurements there is a uniform DC magnetic bias field applied along the cavity axis so as to split out and resolve the individual $(|3, m_F\rangle \leftrightarrow |4, m_F\rangle)$, $\Delta m_F = 0$ transitions.

Figure 4.12a demonstrates resonant Rabi oscillation on the $(|3, 0\rangle \leftrightarrow |4, 0\rangle)$ transition with the optical power in the Raman beam tuned such that $\Omega_E = (2\pi)(137 \text{ kHz})$ (as determined by a fit to the data). For this measurement a fraction $p_3(0) = 0.6$ of the atomic population was initially prepared in $|3, 0\rangle$ using the incoherent Raman optical pumping protocol outlined in the next Section. Because we cannot expect to transfer more population to $|4, 0\rangle$ than we began with in $|3, 0\rangle$, the contrast of the oscillation is diminished by a factor of $p_3(0)$. This measurement is valuable because the two states being driven are first-order magnetic field insensitive which removes a potential noise source from the problem. In spite of this, it is clear that the oscillation exhibits T_2^* -type phase damping, as described in the previous Subsection. The dashed red line represents a least squares fit of the data to Equation (4.45) and yields a dephasing time $T_2^* = (5.91 \pm 0.97) \mu\text{s}$. We expect a number $n_R = 2T_2^*\Omega_E = 1.6$ of full Rabi cycles before the contrast of the fringe is reduced by a factor of 2.

In order to understand the sources of dephasing for this measurement, a useful check is to perform an analogous measurement at a lower Rabi frequency. We expect any noise resulting from sources which cause the Rabi frequency to fluctuate (*i.e.*, atomic motion within the FORT potential or high-frequency intensity or phase noise between the lasers)

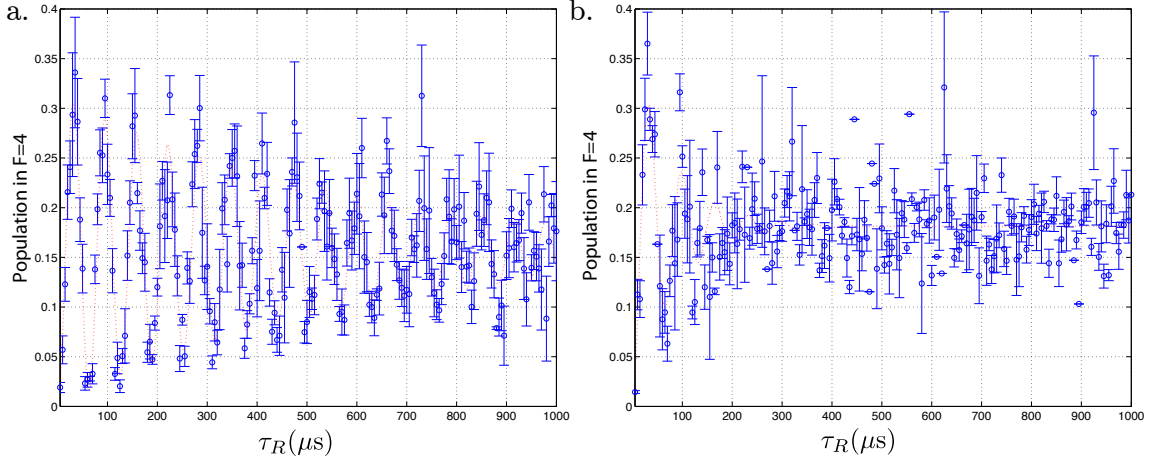


Figure 4.13: Rabi oscillation on the ($|3,0\rangle \leftrightarrow |4,0\rangle$) transition with $\Omega_E = (2\pi)(12.3 \text{ kHz})$ and a. $\delta = (2\pi)(-10 \text{ kHz})$ and b. $\delta = (2\pi)(+10 \text{ kHz})$. Notice that the red-detuned measurement exhibits a considerably larger phase damping time constant than the blue-detuned data.

to scale in proportion to the optical power in the two beams. Figure 4.12b shows resonant Rabi oscillation on the clock transition with $\Omega_E = (2\pi)(12.3 \text{ kHz})$, again deduced by fitting to the data. For this measurement, a least squares fit gives $T_2^* = (105 \pm 18) \mu\text{s}$ and $n_R = 2.6$. While n_R is only a factor of 1.6 larger than the equivalent measurement at higher Rabi frequency, T_2^* is a factor of 17 larger. That the dephasing time scales inversely with Rabi frequency strongly suggests that the dominant phase damping mechanism is either atomic motion or laser noise.

We have also investigated the dependence of the relaxation time on detuning and discovered a rather surprising effect. Figure 4.13a shows data taken for Rabi oscillations at $\Omega_E = (2\pi)(12.3 \text{ kHz})$ at a Raman detuning of $\delta = (2\pi)(-10 \text{ kHz})$ (here Ω_E was determined by first measuring Rabi nutation on resonance and fitting to that data). The measured Rabi nutation rate in the Figure is $\Omega_M = (2\pi)([15.8 \pm 0.1] \text{ kHz})$ and is in good agreement with theory, $\Omega_M \approx \Omega'_E = \sqrt{\Omega_E^2 + \delta^2} = (2\pi)(15.8 \text{ kHz})$. Also, the contrast of the oscillation is diminished as is expected for off-resonant driving. Strikingly, however, the phase damping time is now $T_2^* = (288 \pm 46) \mu\text{s}$ and $n_R = 7.1$. The analogous measurement with blue

detuning, $\delta = (2\pi)(+10 \text{ kHz})$ (Figure 4.13b) yields only $T_2^* = (41 \pm 16) \mu\text{s}$ and $n_R = 1.0$. Clearly some detuning-dependent effect is playing a very important role in the decoherence processes for this system.

We believe the most likely culprit is a subtle effect involving the differential AC stark shift $\Delta U_{0,4-3}$ between the two hyperfine ground state induced by the FORT (Section 3.3). Recall that the slight difference in detuning, Δ_{HF} , of the two manifolds from the atomic excited states causes the FORT to decrease the energy splitting between the two. In a given ensemble of measurements we can safely assume that there is a distribution of atomic temperatures determined by whatever heating and cooling rates are present and relevant. The “coldest” atoms in that ensemble are those with wavepackets which tend to better overlap the highest intensity regions of the FORT (*i.e.*, the “bottoms” of the FORT wells) as compared to “hot” atoms. Therefore these are also the atoms which experience both the largest differential shift $\Delta U_{0,4-3}$ and the smallest spread in Rabi frequency Ω_E due to their motion. “Hotter” atoms, on the other hand, will see a smaller average differential shift and a larger spread in Rabi frequency. By detuning our Raman beams by an amount $\delta \sim \Delta U_{0,4-3}$, we are effectively moving the “hot” atoms farther out of resonance than the “cold” atoms. The dominant contribution to the observed Rabi oscillation is from those atoms which are closer to resonance (we know that the amplitude of the oscillation falls off with detuning). From this model, we therefore can predict that the same atoms which dominate the measurement also happen to be those which experience less motion-induced dephasing. The result, which has been confirmed to order-of-magnitude by computer simulation, is that T_2^* is considerably longer for an appropriately red-detuned Raman pair. This also very strongly suggests that the principle dephasing mechanism for our system is fluctuations in Rabi frequency as a function of atomic motion.

In summary, we are able to observe coherent Rabi oscillation induced by the FORT-Raman configuration of beams. Although dephasing has a pronounced effect on the system, we have been able to develop a good understanding of the sources which contribute significantly to decoherence. Beyond what we have discussed in this Subsection, there are a number of techniques which we have also used to isolate different sources of phase damping in our system. These include Ramsey interferometry and the so-called spin echo protocol

which can isolate inhomogeneous from homogeneous phase damping. These measurements are described in the thesis of Tracy Northup [26]. However, because coherence persists long enough that $n_R > 1$, we are able to use this technique to prepare arbitrary coherent superpositions of the two coupled states and to perform finite rotations of the Bloch vector for the system. This provides us a powerful tool for coherently preparing and manipulating the internal state of the atom which, as we will see, has a diverse set of applications in the laboratory.

4.5 Incoherent Raman Optical Pumping

In this section we will describe an application of the cavity-based Raman technique to optical pumping of a trapped atom into a particular well-defined Zeeman state. Atomic state preparation is an extremely important task and one which is otherwise difficult to carry out when optical access to the atom is obscured by the presence of a cavity. Here we describe a novel method for performing optical pumping using a slight, incoherent variation on the coherent Raman processes described hereto. The discussion in this section follows from and expands upon my work and contributions to Reference [46].

4.5.1 Overview

A standard method for preparing an atom in a specific internal state is optical pumping [47, 39, 48], which involves driving the atom with light fields that couple to all but one of its internal states; these light fields randomly scatter the atom from one internal state to another until it falls into the uncoupled “dark” state. Various optical pumping schemes have been analyzed and demonstrated for alkali atoms [49, 50, 51] and today are well-established techniques. These schemes rely on dark states that are set by the polarization of the driving field, and this imposes restrictions on the possible Zeeman states in which the atom can be prepared. Specifically, one can prepare the atom in the $m_F = 0$ state by using light that is linearly polarized along the quantization axis, or in one of the edge states ($m_F = \pm F$) by using light that is circularly σ_{\pm} -polarized along the quantization axis.

In contrast, the scheme presented in this Section allows the atom to be prepared in

any of the Zeeman states within the lowest ground state hyperfine manifold of an alkali atom, which in our case is the $6S_{1/2}, F = 3$ manifold of Cesium. The key component of the scheme is the FORT-Raman technique described in the previous Sections. We apply a magnetic bias field along the cavity axis to split out the individual Zeeman transitions, and add broadband noise to lower-frequency Raman optical field, where the spectrum of the noise is tailored such that all but one of the $|3, m_F\rangle \leftrightarrow |4, m_F\rangle$ transitions are driven. The two Zeeman states corresponding to the undriven transition are the dark states of the system, and we exploit these dark states to perform optical pumping.

We verify the optical pumping procedure by measuring Raman spectra; these measurements show that a fraction 0.57 ± 0.02 of the total population is prepared in the desired state, with the remaining population distributed fairly uniformly among the six other states. Conventional optical pumping to a single Zeeman sublevel has been previously demonstrated within a cavity [52], but we find our new method to be particularly effective given the constraints of our system, in which optical access to the atom is limited and we must address the large multiplicity of Cesium sublevels. However, optical pumping via incoherent Raman transitions has much broader applications beyond the cavity QED setting, and can be used in a wide variety of atomic systems with hyperfine ground-state structure.

4.5.2 Experimental Configuration

For the particular set of results shown in this section, the depth of the FORT is tuned to be $U_0/h = 45$ MHz. The FORT-Raman beam configuration is used for these measurements, though in principle similar results could be obtained for a Raman-Raman type arrangement. We will prepare our system with a magnetic bias field directed along the cavity axis such that so only the $\Delta m_F = 0$ Raman transitions are driven. For the experiments described here, we typically set the axial bias field such that $\omega_0(m_F) \simeq (2\pi)(910 \text{ kHz})m_F$, as described by Equation (4.26).

4.5.3 Coherent vs. Incoherent Raman transitions

As we have previously described, if the FORT and Raman beams are both monochromatic, then they drive coherent Raman transitions between pairs of Zeeman states ($|3, m_F\rangle \leftrightarrow$

$|4, m_F\rangle$), and the atomic populations oscillate between the two states in each pair. For the experiments described in this Section, the powers in the Raman and FORT beams are chosen such that that $\Omega_0 \simeq (2\pi)(120 \text{ kHz})$. The effective detuning for the $(|3, m_F\rangle \leftrightarrow |4, m_F\rangle)$ transition is given by

$$\delta_E(|3, m_F\rangle \leftrightarrow |4, m_F\rangle) = \delta - \omega_0(m_F). \quad (4.52)$$

In addition to the already established protocols for driving coherent Raman transitions, we can also drive incoherent Raman transitions by using a monochromatic FORT beam and a spectrally broad Raman beam, where the spectral width is typically $\sim 10 \text{ MHz}$. In contrast to coherent Raman transitions, in which the atom undergoes coherent Rabi oscillations, for incoherent Raman transitions the atomic population decays at a constant rate from $|3, m_F\rangle \rightarrow |4, m_F\rangle$ and from $|4, m_F\rangle \rightarrow |3, m_F\rangle$. In Subsection 4.5.6, we show that these decay rates are proportional to $S(\Delta_{HF} + \omega_0(m_F))$, where $S(\omega)$ is the power spectrum of a beat note formed between the FORT and Raman beams.

4.5.4 Population Measurement via Raman Spectroscopy

Figure 4.14 shows a Raman spectrum for the initial state of the system in the absence of optical pumping and with comparable populations in all of the $F = 3$ Zeeman states. To prepare this state, we optically deposit the atom randomly in $F = 3$ by alternating 7 pulses of resonant ($4 \leftrightarrow 4'$) lattice light with 7 pulses of resonant ($4 \leftrightarrow 4'$) “unbalanced” side light (the cavity side beam with no counter-propagating component, as described in Section 3), where each pulse is 300 ns long. The beams that deliver the lattice and side light are those discussed in Chapter 3.

To determine the population $p_3(m_F)$ in the Zeeman state $|3, m_F\rangle$, we return to a slightly generalized version of Equation (4.27):

$$p_4(\delta) = p_b + \frac{1}{2} \sum_{m_F} \left[1 + \frac{(\delta - \omega_0(m_F))^2}{(1 - m_F^2/16) \Omega_0^2} \right]^{-1} p_3(m_F), \quad (4.53)$$

where p_b is a constant background. We fit the Zeeman state populations, the Rabi frequency

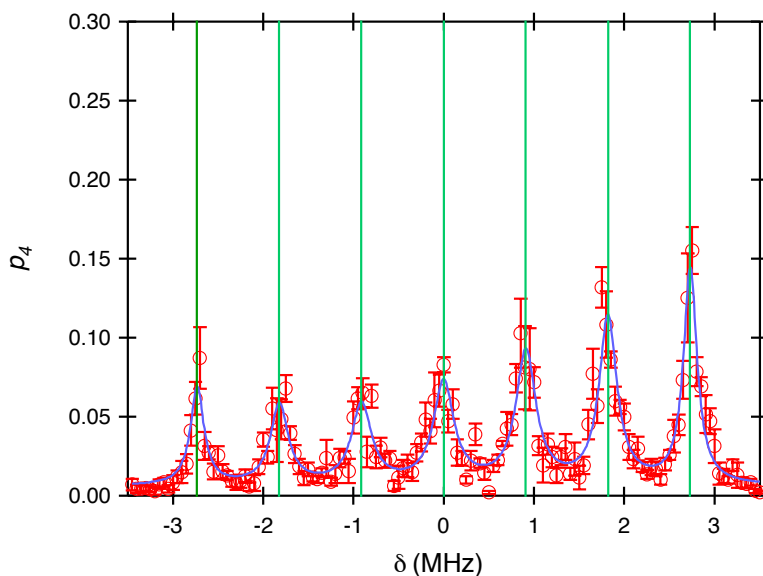


Figure 4.14: Raman spectrum for a random initial state. Shown is the transfer probability p_4 versus Raman detuning δ : the points are the experimental data, the curve is a fit of $p_4(\delta)$, as given by equation (4.53), and the vertical green lines indicate the predicted frequencies $\delta(|3, m_F\rangle \leftrightarrow |4, m_F\rangle)$ for individual Zeeman transitions.

Ω_0 , and the strength of the axial bias field, and perform an independent measurement to determine the background probability $p_b = 0.006$. The fitted value of Ω_0 agrees to within 14% with the value we would expect based on the measured optical powers in the FORT and Raman beams, and the fitted value of magnetic field strength agrees to within 5% with the value we would expect based on the known axial coil current and geometry. As a consistency check we sum the fitted populations and obtain the result 1.10 ± 0.03 , in reasonable agreement with the expected value of 1.

4.5.5 Optical Pumping Scheme

We can prepare the atom in a specific Zeeman state by using a Raman beam whose spectrum is tailored to incoherently drive all but one of the Zeeman transitions. As an example, Figure 4.15a shows the power spectrum of the noise used for pumping into $|3, 0\rangle$. This graph was obtained by measuring the power spectrum of a beat note formed between the FORT and Raman beams by mixing them on a photodetector with a non-polarizing beam splitter. For

comparison, Figure 4.15b shows the power spectrum for a monochromatic Raman beam tuned to Raman resonance, as would be used for driving coherent Raman transitions.

Comparing the noise spectrum shown in Figure 4.15a to the Raman spectrum shown in Figure 4.14, we see that the noise drives incoherent Raman transitions from ($|3, m_F\rangle \leftrightarrow |4, m_F\rangle$) for $m_F \neq 0$, but because of the notch around zero detuning, the ($|3, 0\rangle \leftrightarrow |4, 0\rangle$) transition is not driven. We optically pump the atom into $|3, 0\rangle$ by first driving incoherent Raman transitions for $10\ \mu\text{s}$, then pumping the atom to $F = 3$ using the method discussed in section 4.5.4, and iterating this sequence 40 times. It is straightforward to modify this procedure so as to pump into the $|3, m_F\rangle$ Zeeman state for any m_F ; we simply shift the notch in the noise so that it overlaps with the ($|3, m_F\rangle \leftrightarrow |4, m_F\rangle$) transition.

To characterize the optical pumping, we first pump the atom into a specific Zeeman state and then measure the Raman spectrum as described in the preceding section. Figure 4.16 shows Raman spectra measured after pumping into (a) $|3, 0\rangle$ and (b) $|3, 1\rangle$. We find that the fraction of the atomic population in the desired state is 0.57 ± 0.02 for pumping into $|3, 0\rangle$ and 0.57 ± 0.02 for pumping into $|3, 1\rangle$, where the remaining population is roughly equally distributed among the other Zeeman states (these numbers are obtained using the by fitting equation (4.53) to the data, as described in section 4.5.4). This value is likely limited by small but significant amounts of optical power which provide Raman coupling between the clock states in the system and result from deficiencies in how our incoherent noise spectrum is produced. Summing the fitted populations in all the Zeeman states, we obtain the value 1.02 ± 0.04 for (a) and 1.08 ± 0.04 for (b), in reasonable agreement with the expected value of 1.

To generate the Raman beam used in Figure 4.15a, we start with an RF noise source, which produces broadband noise that is spectrally flat from DC to ~ 10 MHz. The noise is passed through a high-pass filter at 500 kHz and a low-pass filter at 5 MHz, where both filters roll off at 60 dB per octave. The filtered noise is then mixed against an 85 MHz local oscillator, and the resulting RF signal is used to drive an acousto-optical modulator (AOM) that modulates a coherent beam from the injection-locked Raman laser. The first order diffracted beam from the AOM forms a Raman beam with the desired optical spectrum. Note that previous work has demonstrated the use of both synthesized incoherent laser

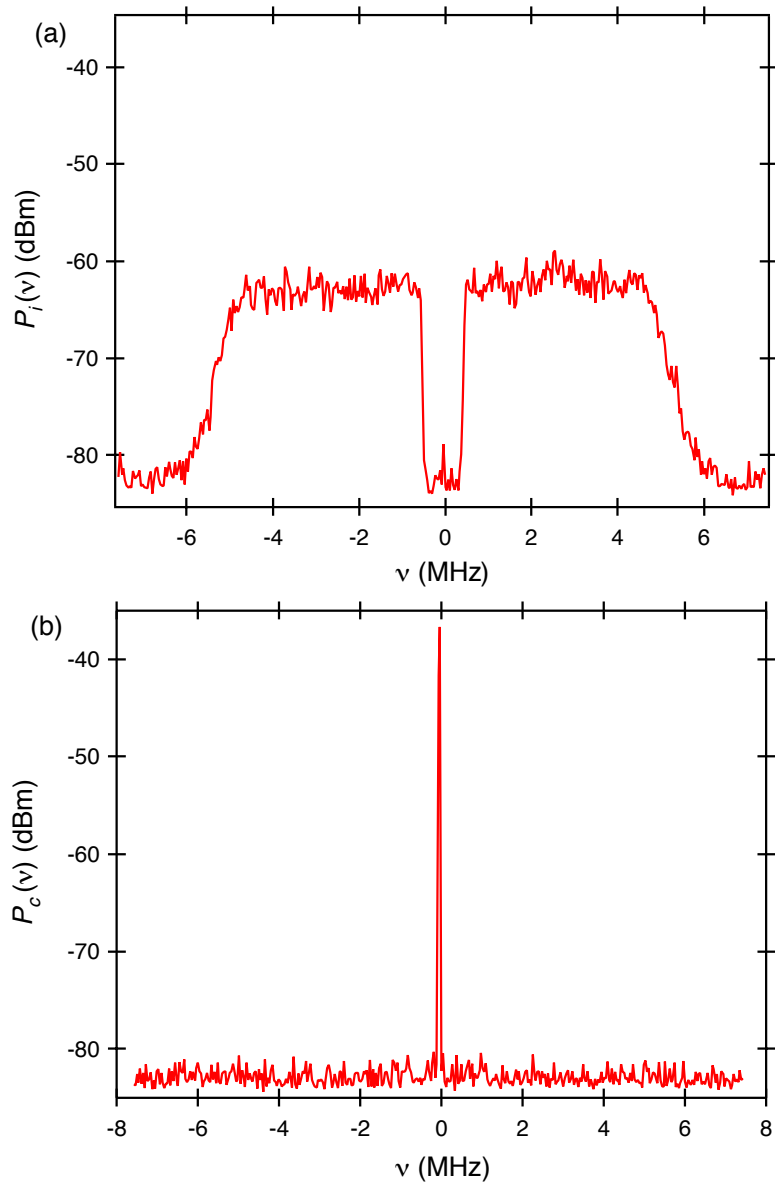


Figure 4.15: (a) Power spectrum of noise used for pumping into $|3, 0\rangle$. (b) Power spectrum of coherent signal used for driving coherent Raman transitions with $\Omega_0 = (2\pi)(120 \text{ kHz})$. Both curves are obtained by combining the FORT and Raman beams on a photodetector and measuring the spectrum of the photocurrent; shown is the RF power in a 3 kHz bandwidth versus detuning from Δ_{HF} .

fields [53, 54], such as that used here, as well as the noise intrinsic to free-running diode lasers [55, 56] to resonantly probe atomic spectra.

Although the scheme presented here relies on incoherent Raman transitions, it is also possible to perform optical pumping with coherent Raman transitions. The basic principle is the same: we simultaneously drive all but one of the Zeeman transitions, only instead of using a spectrally broad Raman beam, we use six monochromatic Raman beams, where each beam is tuned so as to resonantly drive a different transition. We have implemented such a scheme, and found that it gives comparable results to the incoherent scheme described above, but there are two advantages to the incoherent scheme. First, it is simpler to generate a Raman beam with the necessary spectral properties for the incoherent scheme. Second, when coherent Raman transitions are used, the six frequency components for the Raman beam must be tuned to resonance with their respective transitions, and hence are sensitive to the value of the axial magnetic field. When incoherent Raman transitions are used, however, the same Raman beam can be used for a broad range of axial field values.

4.5.6 Transition Rate for Incoherent Raman Transitions

As described in Section 4.5.3, we drive incoherent Raman transitions between pairs of Zeeman states ($|3, m_F\rangle \leftrightarrow |4, m_F\rangle$) by using a monochromatic FORT beam and a spectrally broad Raman beam. For incoherent Raman transitions the atomic population decays at a constant rate from $|3, m_F\rangle \rightarrow |4, m_F\rangle$ and from $|4, m_F\rangle \rightarrow |3, m_F\rangle$, and in this Section we calculate these decay rates.

We will consider a single Zeeman transition ($|3, m_F\rangle \leftrightarrow |4, m_F\rangle$), so we can treat the system as an effective two-level atom with ground state $g \equiv |3, m_F\rangle$ and excited state $e \equiv |4, m_F\rangle$, where the energy splitting between g and e is $\omega_A \equiv \Delta_{HF} + \omega_0(m_F)$. The FORT-Raman pair drives this effective two-level atom with broadband noise, which we can approximate as a comb of classical fields with optical frequencies ω_k and Rabi frequencies Ω_k . Let us assume that we start in the ground state g . If we only consider the coupling of the atom to field k , then the equation of motion for the excited state amplitude c_e is

$$i\dot{c}_e = \frac{\Omega_k}{2} e^{-i\delta_k t} c_g, \quad (4.54)$$

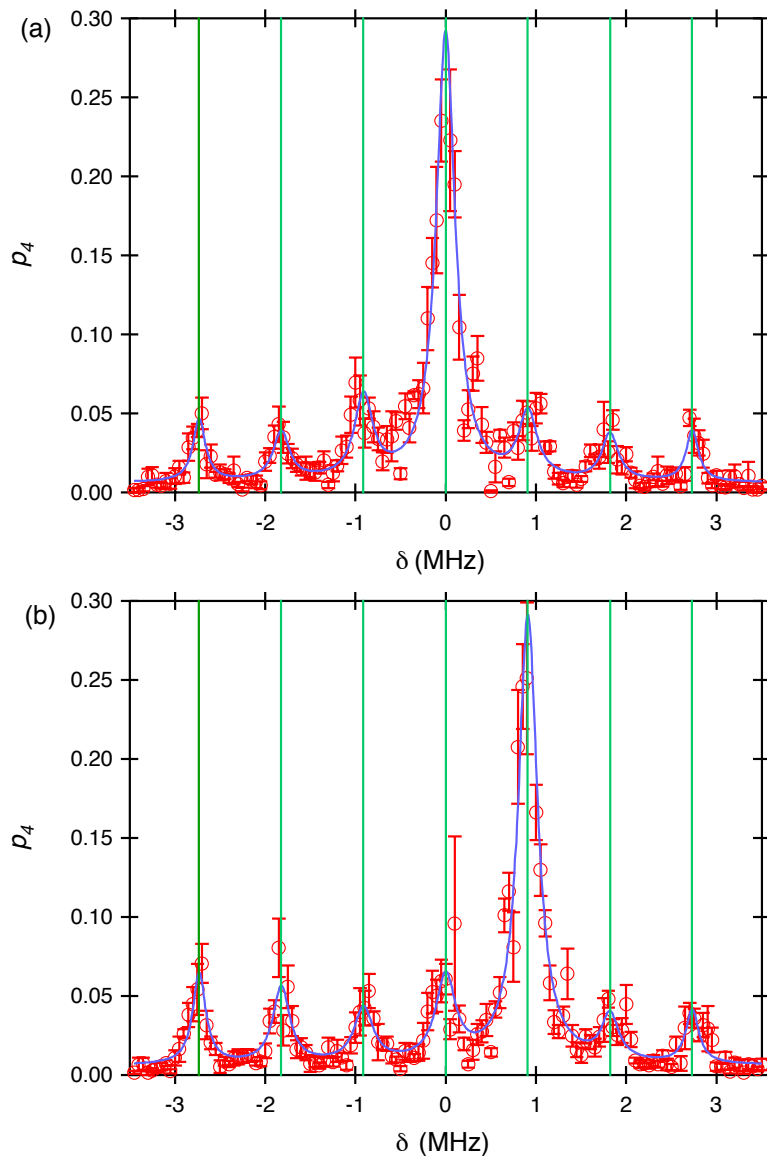


Figure 4.16: (a) Raman spectrum for optical pumping into $|3,0\rangle$. (b) Raman spectrum for optical pumping into $|3,1\rangle$. Raman spectrum for a random initial state. Shown is the transfer probability p_4 versus Raman detuning δ : the points are the experimental data, the curve is a fit of $p_4(\delta)$, as given by equation (4.53), and the vertical green lines indicate the predicted frequencies $\delta(|3, m_F\rangle \leftrightarrow |4, m_F\rangle)$ for individual Zeeman transitions.

where $\delta_k \equiv \omega_k - \omega_A$ is the detuning of the field from the atom. At small times the population is almost entirely in the ground state, so we can make the approximation $c_g = 1$ and integrate equation (4.54) to obtain

$$c_e(t) = \frac{\Omega_k}{2\delta_k} (e^{-i\delta_k t} - 1). \quad (4.55)$$

Thus, the transition rate from g to e for a single frequency ω_k is

$$\gamma_k = \frac{|c_e(t)|^2}{t} = \frac{\pi}{4} t \Omega_k^2 D(\delta_k t/2), \quad (4.56)$$

where

$$D(x) \equiv \frac{\sin^2 x}{\pi x^2}. \quad (4.57)$$

The total decay rate is obtained by summing the decay rates for all the fields in the comb:

$$\gamma = \sum_k \gamma_k = \frac{\pi}{4} t \sum_k \Omega_k^2 D(\delta_k t/2). \quad (4.58)$$

To evaluate this expression we need to know the distribution of Rabi frequencies Ω_k . This information can be obtained by forming a beat note between the FORT and Raman beams on a photodetector, and measuring the power spectrum $S(\omega)$ of the photocurrent using a spectrum analyzer. Let us first consider this measurement for a monochromatic Raman beam, and then generalize to a spectrally broad Raman beam. If both the FORT and Raman beams are monochromatic, with optical frequencies ω_F and ω_R , then the resulting photocurrent $i(t)$ is given by

$$i(t) = i_F + i_R + 2\eta \cos((\omega_F - \omega_R)t) \sqrt{i_F i_R}, \quad (4.59)$$

where i_F and i_R are the cycle-averaged photocurrents for the FORT and Raman beams taken individually and η is the heterodyne efficiency. Thus, the power spectrum of the

photocurrent has a spike at the difference frequency $\Delta \equiv \omega_F - \omega_R$:

$$S_c(\omega) = P_c \delta(\omega - \Delta), \quad (4.60)$$

where the integrated power P_c of the spike is proportional to $i_F i_R$. If the difference frequency Δ is tuned to Raman resonance ($\Delta = \omega_A$), then the FORT-Raman pair drives coherent Raman transitions with a Rabi frequency Ω_c that is proportional to $\sqrt{i_F i_R}$, so

$$\Omega_c^2 = \alpha P_c, \quad (4.61)$$

where α is a constant that depends on various calibration factors.

Now consider the case of a spectrally broad Raman beam, which results in a photocurrent with power spectrum $S_i(\omega)$. The effective Rabi frequency Ω_k corresponding to comb line k is given by

$$\Omega_k^2 = \alpha S_i(\omega_k) \delta\omega, \quad (4.62)$$

where $\delta\omega$ is the frequency spacing between adjacent comb lines. Substituting this result into equation (4.58), and replacing the sum with an integral, we obtain

$$\gamma = \frac{\pi}{4} \alpha t \int S_i(\omega) D((\omega - \omega_A)t/2) d\omega. \quad (4.63)$$

If the power spectrum near ω_A is flat over a bandwidth $\sim 1/t$, then we can approximate D as a delta function and perform the integral:

$$\gamma = \frac{\pi}{2} \alpha S_i(\omega_A). \quad (4.64)$$

It is convenient to use equation (4.61) to eliminate the calibration factor α :

$$\gamma = \frac{\pi S_i(\omega_A)}{2 P_c} \Omega_c^2. \quad (4.65)$$

The spectrum analyzer trace given in Figure 4.15a displays the power spectrum in terms of

the power $P_i(\nu) \simeq 2\pi B S_i(\omega)$ in a bandwidth $B = 3$ kHz, so we can also write this as

$$\gamma = \frac{1}{4} \frac{P_i(\omega_A/2\pi)}{P_c} \frac{\Omega_c^2}{B} = \frac{1}{4} (1 - m_F^2/16) \frac{\Omega_0^2}{B} \frac{P_i((\Delta_{HF} + \omega_0(m_F))/2\pi)}{P_c}, \quad (4.66)$$

where we have substituted $\Omega_c = (1 - m_F^2/16)^{1/2} \Omega_0$ and $\omega_A = \Delta_{HF} + \omega_0(m_F)$.

We can calculate the time evolution of the atomic populations using rate equations. It is straightforward to show that the decay rate $e \rightarrow g$ is also given by γ , and from the rate equations one can show that the excited state population is

$$p_e(t) = \frac{1}{2} (1 - \exp(-2\gamma t)). \quad (4.67)$$

We can calculate the decay rates for the noise spectrum shown in Figure 4.15. For this noise spectrum the power $P_i(\nu)$ has roughly the same value \bar{P}_i at the frequencies of all the $m \neq 0$ Zeeman transitions, so we can write the decay rates for these transitions as

$$\gamma(|3, m_F\rangle \rightarrow |4, m_F\rangle) = \gamma(|4, m_F\rangle \rightarrow |3, m_F\rangle) = (1 - m_F^2/16) \Gamma, \quad (4.68)$$

where

$$\Gamma \equiv (1/4)(\Omega_0^2/B)(\bar{P}_i/P_c). \quad (4.69)$$

From the power spectrum for the noise shown in Figure 4.15a we have that $\bar{P}_i = -63$ dBm, and from the power spectrum for the coherent signal shown in Figure 4.15b we have that $P_c = -36$ dBm, where the corresponding Rabi frequency is $\Omega_0 = (2\pi)(120$ kHz). Substituting these values into equation (4.69), we obtain $\Gamma = 0.084 \mu\text{s}^{-1}$.

4.5.7 Summary

We have measured the effectiveness of the optical pumping, and have shown that a fraction ~ 0.57 of the atomic population can be prepared in the desired Zeeman state. Some possible factors that could be limiting the effectiveness of the optical pumping include fluctuating magnetic fields transverse to the cavity axis, misalignment of the cavity axis with the axial

bias field, and slow leaking out of the dark state due to scattering from background light. We are currently investigating these factors.

The scheme presented here operates on a fundamentally different principle from existing optical pumping schemes, in that it relies on incoherent Raman transitions to create an atomic dark state. Raman transitions have many different applications in atomic physics, so there are often independent reasons for incorporating a system for driving Raman transitions into an atomic physics laboratory; our scheme shows that such a system can also be applied to the problem of atomic state preparation. The scheme should serve as a useful tool for experiments in atomic physics, both in a cavity QED setting and beyond.

4.6 Motional Effects and Cooling

Recall that in Section 3.3 we described the properties of the FORT used to confine atoms within the mode of our optical cavity. In particular, we described how for cold atoms (with motional wavepackets localized near the “bottom” of a FORT well) we can treat the axial and radial motion of the atom as two decoupled harmonic oscillators with oscillation frequencies ω_{ax} and ω_{rad} , respectively. For the geometry of our physics cavity we found $\omega_{ax}/\omega_{rad} \sim 10^2$. Because the axial frequency is so much larger than the radial frequency we will make the additional assumption that when describing only axial motion that the radial position of the atom can be assumed to be fixed.

Under this assumption we can write the effective instantaneous axial vibrational frequency at position (x, y) :

$$\omega'_{ax} = \omega_{ax} \exp \left[-\frac{(x^2 + y^2)}{w_F^2} \right]. \quad (4.70)$$

The quantum harmonic oscillator potential associated with this motion is characterized by creation and annihilation operators \hat{b} and \hat{b}^\dagger :

$$\hat{b} = \sqrt{\frac{m\omega'_{ax}}{2\hbar}} \left(\hat{z} + i \frac{\hat{p}_z}{m\omega'_{ax}} \right) \quad \text{and} \quad \hat{b}^\dagger = \sqrt{\frac{m\omega'_{ax}}{2\hbar}} \left(\hat{z} - i \frac{\hat{p}_z}{m\omega'_{ax}} \right). \quad (4.71)$$

Using these relations, we can write:

$$\hat{z} = \frac{\eta}{k_F} (\hat{b} + \hat{b}^\dagger) \quad (4.72)$$

where $k_F = \omega_F/c$ is the wave vector of the FORT field and $\eta = k_F \sqrt{\hbar/2m\omega'_{ax}}$ is called the Lamb-Dicke parameter. Physically, η represents the ratio of the spatial extent of the ground state wavepacket of a trapped atom to the wavelength of the FORT, λ_F . For our system, assuming a FORT depth $U_0/\hbar = -41.0$ MHz, the maximum value of the Lamb-Dicke parameter is $\eta_{max} = 5.6 \times 10^{-2}$.

Of course the FORT is not harmonic, but varies axially as $\sin^2(k_F z)$. For cold atoms we can more closely approximate the FORT Hamiltonian by keeping the two lowest-order terms of a Taylor series expansion of \sin^2 about a local minimum:

$$H_F = \frac{\hat{p}_z^2}{2m} + \frac{1}{2}m\omega'^2_{ax}z^2 - \frac{1}{6}m\omega'^2_{ax}k_F^2\hat{z}^4 \quad (4.73)$$

$$= \hbar\omega'_{ax} (\hat{b}^\dagger\hat{b} + 1/2) - \omega'_{ax}\frac{\eta^2}{12}(\hat{b} + \hat{b}^\dagger)^4. \quad (4.74)$$

To first order, the harmonic oscillator Fock states $\{|n\rangle\}$ are still “good” eigenstates of this system. Using this approximation we can write tensor product states describing both the internal and external state of the atom $|F, m_F, n\rangle \equiv |F, m_F\rangle \otimes |n\rangle$.

Now that we have a viable model Hamiltonian for the FORT potential, we can evaluate how Raman processes interact with motional states of the system. Recall that the interaction Hamiltonian for the Raman pair is given by Equation (4.17), omitting V_E :

$$\hat{H} = -\frac{1}{2}\hbar\delta(\hat{P}_4 - \hat{P}_3) + \frac{1}{2}\hbar\Omega_{rad}\sin^2\left(\frac{\omega_R\hat{z}}{c} + \alpha\right)(\hat{\Sigma} + \hat{\Sigma}^\dagger). \quad (4.75)$$

Here we have made the spatial dependence of $\Omega_E(\vec{r})$ explicit by decomposing the radial component

$$\Omega_{rad} = \Omega_E \exp\left(-\frac{(x^2 + y^2)}{w_F^2}\right) \quad (4.76)$$

from the axial component. This expression can apply either to the FORT-Raman configu-

ration wherein $\omega_R = \omega_F$ and $\alpha = 0$, or to the Raman-Raman configuration where $\omega_R \neq \omega_F$ and α can assume a different value in each FORT well. Note that because $\Omega_E(\vec{r})$ varies with z that the Raman pair is able to couple motional states. To see this, we can use Taylor expansion to order \hat{z}^2 about the bottom of a FORT well to rewrite \hat{H} in the form:

$$\hat{H} = -\frac{1}{2}\hbar\delta(\hat{P}_4 - \hat{P}_3) + \frac{1}{2}\hbar\Omega_{rad} [\cos^2 \alpha - k_F \sin 2\alpha \hat{z} - k_F^2 \cos 2\alpha \hat{z}^2] (\hat{\Sigma} + \hat{\Sigma}^\dagger) \quad (4.77)$$

$$= -\frac{1}{2}\hbar\delta(\hat{P}_4 - \hat{P}_3) + \frac{1}{2}\hbar\Omega_{rad} [\cos^2 \alpha - \eta \sin 2\alpha(\hat{b} + \hat{b}^\dagger) - \eta^2 \cos 2\alpha(\hat{b} + \hat{b}^\dagger)^2] (\hat{\Sigma} + \hat{\Sigma}^\dagger). \quad (4.78)$$

In order to understand how the Raman pair moves population between different motional states, we can evaluate matrix elements of \hat{H} to determine effective Rabi frequencies for those transitions:

$$\frac{\Omega_{n \leftrightarrow n}}{\Omega_{rad}} = \frac{2 \langle 3, m_F, n | \hat{H} | 4, m_F, n \rangle}{\hbar\Omega_{rad}(|3, m_F\rangle \leftrightarrow |4, m_F\rangle)} = \cos^2 \alpha - \eta^2(2n + 1) \cos 2\alpha \quad (4.79)$$

$$\frac{\Omega_{n \leftrightarrow n \pm 1}}{\Omega_{rad}} = \frac{2 \langle 3, m_F, n | \hat{H} | 4, m_F, n \pm 1 \rangle}{\hbar\Omega_{rad}(|3, m_F\rangle \leftrightarrow |4, m_F\rangle)} = -\eta\sqrt{n \pm 1} \sin 2\alpha \quad (4.80)$$

$$\frac{\Omega_{n \leftrightarrow n \pm 2}}{\Omega_{rad}} = \frac{2 \langle 3, m_F, n | \hat{H} | 4, m_F, n \pm 2 \rangle}{\hbar\Omega_{rad}(|3, m_F\rangle \leftrightarrow |4, m_F\rangle)} = -\eta^2\sqrt{n \pm 1}\sqrt{n \pm 2} \cos 2\alpha. \quad (4.81)$$

Evidently the Rabi frequency for transitions involving $\Delta n = \pm 1$ is suppressed by a factor of $\eta\sqrt{n}$ relative to transitions involving $\Delta n = 0$ and transitions for which $\Delta n = 2$ are suppressed by $\eta^2 n$. Where permitted, these transitions manifest themselves in Raman spectra as sidebands on spectral features corresponding to $(|3, m_F\rangle \leftrightarrow |4, m_F\rangle)$. These sidebands are located near $\omega_z^\pm = \omega_0(m_F) \pm \delta_n$ (or, $\omega_z^\pm = \omega_0(m_F) \pm 2\delta_n$) for $\Delta n = \pm 1$ (or, $\Delta n = \pm 2$) where $\delta_n \equiv \omega'_{ax} - \eta^2 \omega'_{ax} n$. The second term in the definition of δ_n represents a correction for the anharmonicity of the FORT as a function of the number of vibrational quanta in the system. The widths of the sidebands are generally dominated by the range of values which ω'_{ax} takes as the atom moves radially and the dispersion in δ_n as it samples the anharmonicity of the FORT.

In the FORT-Raman configuration, these expressions reduce to:

$$\frac{\Omega_{n \leftrightarrow n}}{\Omega_{rad}} = \frac{2 \langle 3, m_F, n | \hat{H} | 4, m_F, n \rangle}{\hbar \Omega_{rad}(|3, m_F\rangle \leftrightarrow |4, m_F\rangle)} = 1 \quad (4.82)$$

$$\frac{\Omega_{n \leftrightarrow n \pm 1}}{\Omega_{rad}} = \frac{2 \langle 3, m_F, n | \hat{H} | 4, m_F, n \pm 1 \rangle}{\hbar \Omega_{rad}(|3, m_F\rangle \leftrightarrow |4, m_F\rangle)} = 0 \quad (4.83)$$

$$\frac{\Omega_{n \leftrightarrow n \pm 2}}{\Omega_{rad}} = \frac{2 \langle 3, m_F, n | \hat{H} | 4, m_F, n \pm 2 \rangle}{\hbar \Omega_{rad}(|3, m_F\rangle \leftrightarrow |4, m_F\rangle)} = -\eta^2 \sqrt{n \pm 1} \sqrt{n \pm 2}. \quad (4.84)$$

It follows that any Raman pair which varies in intensity symmetrically with respect to the FORT potential can not couple states which differ by $\Delta n = \pm 1$. We can, however, implement a Raman-Raman configuration wherein α varies from well-to-well and for which $\Delta n = 1$ transitions are permitted in certain wells. In the next Subsection we will describe how these type of transitions can be used to cool the motion of an atom to its quantum ground state $n = 0$ and how we can use Raman spectroscopy to infer the temperature of the atom.

4.6.1 Ground State Cooling on the First Order Sideband

This Section is adapted from Reference [57].

Using the techniques outlined above, in this Section we will describe the implementation of a Raman cooling process to cool an atom trapped in our FORT to its quantum ground state of motion. This information is read out using standard down-goer techniques for recording Raman spectra. From these spectra, we are able to infer that the lowest vibrational level $n = 0$ of the axial potential is occupied with probability $P_0 \simeq 0.95$ for one trapped atom.

For this set of experiments, the FORT potential was set to be $U_0/h = -41$ MHz. Atoms near the bottom of the FORT potential experience an axial oscillation frequency $\omega_{ax} = (2\pi)(530$ kHz) and a radial oscillation frequency $\omega_{rad} = (2\pi)(4.5$ kHz). The experiment is tuned such that probability to load an atom into the FORT given an attempt to do so is ~ 0.3 . The Raman-Raman pair is configured as described in Section 4.2.2. We typically set the optical power transmitted on resonance through the cavity for each of the two Raman beams to $P_+ = P_- = 140$ μ W, which gives a Rabi frequency $\Omega_0 = (2\pi)(200$ kHz) for atoms

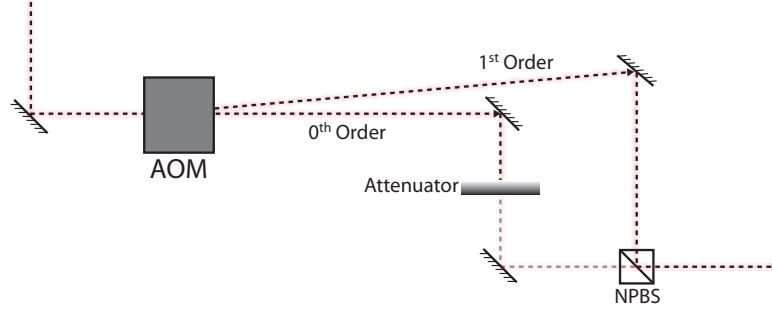


Figure 4.17: Switching apparatus for the higher-frequency of the two Raman beams in the Raman-Raman configuration. The 0th and 1st diffracted orders from an acousto-optic modulator are recombined at a non-polarizing splitting in such a way that the total power reflected from the splitter is held constant.

with $\alpha = 0$. Here, as usual, Ω_0 is the Rabi frequency for the transition ($|3, 0, 0\rangle \leftrightarrow |4, 0, 0\rangle$), where the quantization axis is along the cavity axis. The AC Stark shift due to these Raman beams adds a correction to the FORT potential of $V_E/h = 0.84$ MHz.

To avoid heating the atom induced by repeated switching of V_E , we have configured the higher-frequency Raman beam to remain at constant intensity, but far-detuned ($\delta_{AOM} = (2\pi)(85$ MHz)) from Raman resonance unless being used to drive transitions. This is accomplished as shown in Figure 4.17. The first diffracted order of an acousto-optic modulator at frequency ω_+ is recombined with the zeroth diffracted order at $\omega_+ - \delta_{AOM}$. The AOM can be switched between two discrete settings - either maximum power in the first order diffracted beam (Raman transitions **ON**) or maximum power in the zeroth order beam and no power in the first order beam (Raman transitions **OFF**). The amount of power in each of the two diffracted orders is managed using a variable attenuator such that in both configurations of the AOM, the total summed power is constant. In order to map out Raman spectra we fine-tune the frequency $\omega_- + \delta$ of the lower-frequency Raman beam using another AOM.

In the harmonic limit, we can define a set of Fock states $\{|n\rangle\}$ for the axial motion. Recall that for transitions coupling ($|3, 0\rangle \leftrightarrow |4, 0\rangle$) and to first order in η , the Rabi frequency for an $n \rightarrow n$ transition is $\Omega_{n \rightarrow n} = \cos^2 \alpha \Omega_0$, while for an $n \rightarrow n - 1$ transition, $\Omega_{n \rightarrow n-1} =$

$\eta\sqrt{n-1}\sin 2\alpha\Omega_0$. For the system parameters used in this set of measurements, $\eta = 0.056$. Note that the $n \rightarrow n-1$ transition is strongest for atoms with $\alpha = \pi/4$. The spatial dependence of the Raman coupling, together with the fact that the axial motion of the atom is in the Lamb-Dicke limit, allows us to implement Raman sideband cooling [58]. We tune the Raman pair to the red axial sideband ($\delta_c = -525$ kHz $\simeq -\omega_{ax}$) and apply the ($4 \leftrightarrow 4'$) lattice cooling beams (Chapter 3), which for consistency we shall refer to as Ω_4 . An atom that starts in $F = 3$ is coherently transferred by the Raman pair to $F = 4$, where it is incoherently repumped to $F = 3$ by Ω_4 . The coherent transfer lowers the axial vibrational quantum number n by one, while the incoherent repumping usually leaves n unchanged since n -changing transitions are Lamb-Dicke suppressed. Thus, the beams continually lower n , cooling the atom to the axial ground state. Also, the lattice light provides Sisyphus cooling [37] in the radial direction.

State detection and Raman spectroscopy are carried out in the usual way with $\tau_p = 100$ μ s pulses of ($4 \leftrightarrow 5'$) probe light serving as the source of the down-goer signal. We set the intensity of the probe light such that on average N_e photons are detected per probing interval with no atom in the cavity. If the number N of detected photons is such that $N < 0.25N_e$, we assume an $F = 4$ atom is present, if $N > 0.75N_e$ we assume an $F = 4$ atom is not present, otherwise the measurement is inconclusive (which happens $< 2\%$ of the time) and we ignore the result. As usual, whenever we detect the atomic state we perform two such measurements: the first with just probe light to measure $P_4(\delta)$ and the second with both probe and ($3 \leftrightarrow 3'$) repumper in order to detect an atom regardless of its internal state. For loading, the total power in the four lattice beams (both ($3 \leftrightarrow 3'$) and ($4 \leftrightarrow 4'$)) is $50I_4^{\text{sat}}$, where $I_4^{\text{sat}} \sim 3.8$ mW/cm². For detection, the intensity of the lattice ($3 \leftrightarrow 3'$) repump field is $5I_4^{\text{sat}}$.

We measure the Raman transfer probability $P_4(\delta)$ by preparing an atom in $F = 3$, applying a Raman pulse, and then detecting the atomic state using the above scheme (with $N_e \sim 22$). For each measurement cycle (or trial), we first Raman-sideband cool the atom for an interval τ_c . Next, we pump it into $F = 3$ by alternating 1 μ s pulses of ($4 \leftrightarrow 4'$) lattice light with 1 μ s pulses of linearly polarized resonant ($4 \leftrightarrow 4'$) light from the side of the cavity (10 pulses of each). After the atom is pumped to $F = 3$, we apply a $\tau_R = 500$ μ s

Raman pulse, which sometimes transfers it to $F = 4$. Finally, we measure the atomic state and check if the atom is still present. For each atom we fix the absolute value of the Raman detuning $|\delta|$, and alternate trials at $+\delta$ with trials at $-\delta$ (299 trials each). By combining data from atoms with different values of $|\delta|$, we map out a Raman spectrum. Note that because the initial Zeeman state of the atom is random, all allowed ($|3, m_F\rangle \leftrightarrow |4, m_F\rangle$) Zeeman transitions contribute to these spectra.

Two example Raman spectra are plotted in Fig. 4.18. For the (a) curve, we cool for $\tau_c = 250 \mu\text{s}$, for the (b) curve for $\tau_c = 5 \text{ ms}$. These scans are performed after nulling the magnetic field to within $\sim 40 \text{ mG}$; the widths of the peaks are set by the splitting of different Zeeman levels due to the residual magnetic field. For the curve in panel (a), we see peaks at the carrier ($\delta = 0$), as well as at the blue/red sidebands ($\delta \simeq \pm(2\pi)(530 \text{ kHz}) = \pm\omega_{ax}$). Already we note a sideband asymmetry, indicating that a significant fraction of the population is in the $n = 0$ vibrational state. For the (b) data, the red sideband at $\delta \simeq -(2\pi)(530 \text{ kHz})$ is suppressed to such an extent that it cannot be distinguished from the background and contribution from off-resonant excitation of the carrier.

The ratio r of transfer probabilities for the red and blue sideband gives information about the temperature of the atom. For a two-state atom in a thermal state, this ratio r_0 at $|\delta| = \omega_a$ is related to the mean vibrational quantum number \bar{n} by $r_0 = \bar{n}/(\bar{n} + 1)$ [58]. In Fig. 4.18c, we plot r as a function of $|\delta|$ for the $\tau_c = 5 \text{ ms}$ data. As shown in Fig. 4.18b, we fit a Lorentzian curve to the carrier, then subtract its contribution from both the red and the blue sideband data, with the result shown in panel (c). We find $r_0 \simeq \bar{n} = 0.01 \pm 0.05$, and the ground state population $P_0 = 1/(\bar{n} + 1) = 0.99 \pm 0.05$, where the error bars reflect fluctuations in the data around $|\delta| = \omega_a$. If instead we subtract the constant background of $P_4^B = 0.024$ but not the carrier's Lorentzian tail, we find $r_0 \simeq \bar{n} = 0.05 \pm 0.04$, and $P_0 = 0.95 \pm 0.04$. Finally, if we use the raw data from Fig. 4.18b with no subtractions, we obtain $r_0 = 0.10 \pm 0.03$, $\bar{n} = 0.12 \pm 0.04$ and $P_0 = 0.89 \pm 0.03$. Note, however, that because the atom is not a two-state system and the motional state is not known to be thermal, these estimates are approximate.

In addition to measuring the probability of the atom in the $n = 0$ axial ground state with high probability, the Raman cooling protocol was measured to significantly extend the

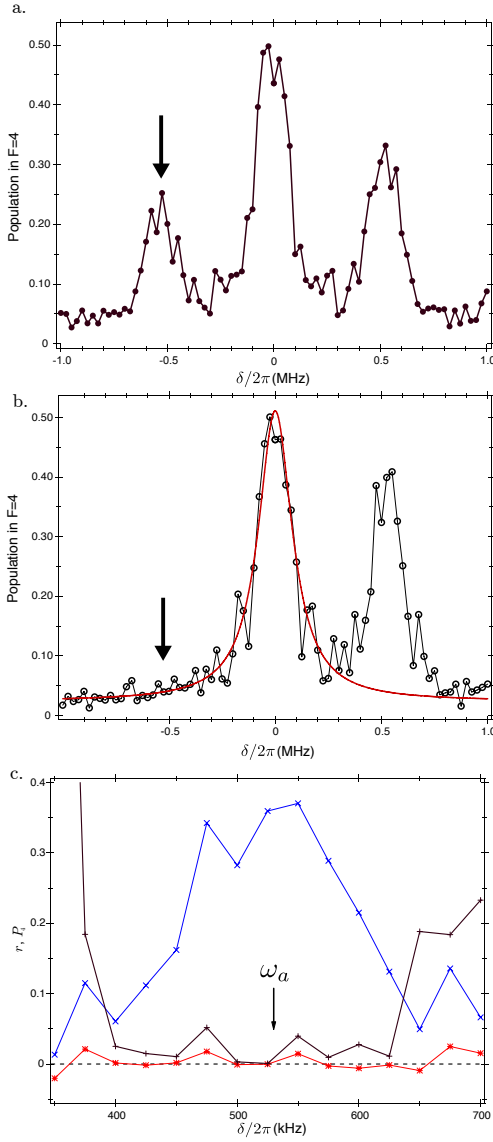


Figure 4.18: Population P_4 in the $F = 4$ state versus Raman detuning $\delta/2\pi$. The (a) data are taken with $\tau_c = 250 \mu\text{s}$ of cooling, and with an Ω_4 total 4-beam intensity $I_4 = 5I_4^{\text{sat}}$; the (b) data with $\tau_c = 5$ ms of cooling, and $I_4 = 0.5I_4^{\text{sat}}$ (on average, about 33 atoms per data point). The arrow marks the detuning used for sideband cooling. (c) Zoom-in on the two sideband regions for the (b) data, with detuning axis folded around $\delta = 0$. The red and blue sidebands, as well as their ratio r (black), are shown after subtracting a Lorentzian fit to the carrier (red curve in (b)).

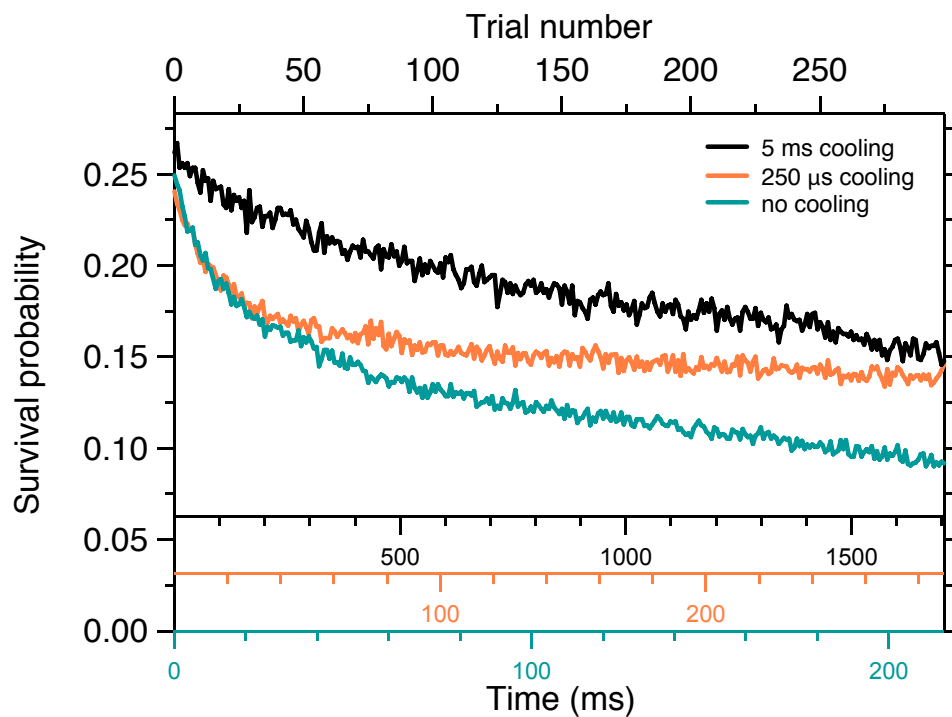


Figure 4.19: Probability to measure the presence of an atom the FORT as a function of the number of cooling cycles applied to the atom and as a function of time for three different sideband cooling settings. The time axes are color-coded to match the data to which they are paired.

lifetime of atoms in the FORT. This is demonstrated in Figure 4.19 where we have plotted the probability to measure the presence of an atom in the FORT as a function of the number of cooling intervals applied to the system. By fitting to an exponential we can determine the trap lifetime for $\tau_c = 250 \mu\text{s}$ cooling intervals, $T = (42 \pm 3) \text{ ms}$, and $\tau_c = 5 \text{ ms}$ cooling intervals, $T = (883 \pm 86) \text{ ms}$. In the absence of cooling the dominant heating mechanism for the atom is likely probe-induced motion during the state- and atom-detection intervals. The data in the absence of cooling therefore does not conform to an exponential fit. While the lifetime in the presence of ground state cooling does not exceed the measured lifetime “in the dark” (*i.e.*, in the absence of any probe light), it does greatly extend the lifetime in the presence of probing and is quite valuable for practical purposes.

The axial cooling rate and asymptotic value of \bar{n} depend on δ_c , on the Ω_{\pm} Rabi frequencies, and on the power and detuning of the Ω_4 lattice beams. We have performed computer simulations to help us choose optimal values for these parameters. A common feature of both our theoretical and experimental investigations is the robustness of \bar{n} under variations of the cooling parameters. As an example, in Fig. 4.20 we plot the measured sideband ratio r_0 at $\delta_c = -(2\pi)(500 \text{ kHz}) \simeq -\omega_a$ as a function of (a) the detuning δ_c used for sideband cooling, and (b) the recycling intensity I_4 . The sideband asymmetry is maintained over a range of at least 200 kHz in detuning, and of two orders of magnitude in the intensity I_4 of the Ω_4 beams. The insets give results from a simple 2-state calculation of r_0 , displaying similar insensitivity to the exact values of δ_c and I_4 . Unless otherwise noted, the settings for these measurements are: $I_4 = 0.3I_4^{\text{sat}}$, $\tau_c = 5 \text{ ms}$, $\delta_c = -(2\pi)(500 \text{ kHz})$, $\tau_R = 50 \mu\text{s}$; $P_4^B = 0.065$ was subtracted before computing r_0 .

We use two different methods for estimating the mean energy E_r for radial motion. The first method involves adiabatically lowering the FORT depth to zero, so that only the U_R trapping potential remains, and measuring the probability that the atom survives the process [59]. If we assume a thermal state for the radial motion, this method limits E_r to $\sim 200 \mu\text{K}$. The second method relies on the fact that radial motion would shift and/or broaden the axial sidebands observed in our Raman spectra. By applying a small axial bias field, we can resolve motional sidebands of transitions between specific magnetic sublevels; the positions and widths of these sidebands also place a limit on E_r of $\sim 200\mu\text{K}$. However,

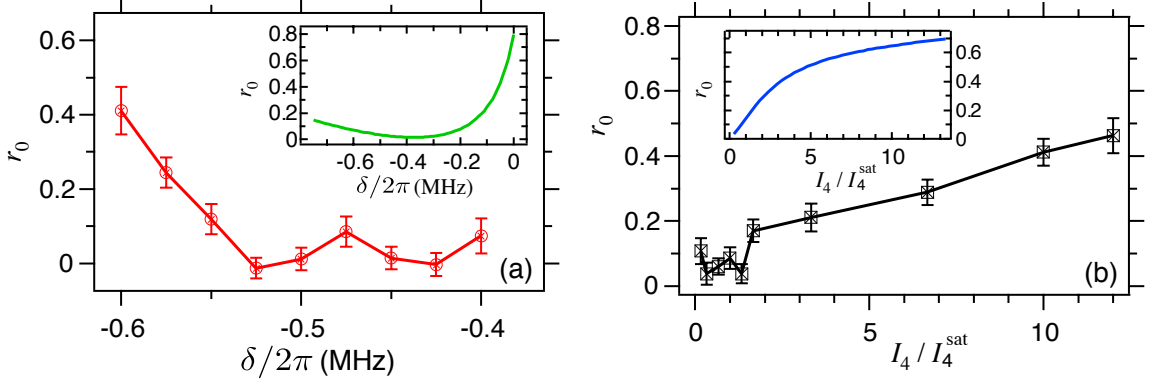


Figure 4.20: Varying cooling parameters. The sideband ratio r_0 is shown as a function of (a) the Raman detuning δ employed for cooling and (b) the $4 \rightarrow 3$ repumping intensity I_4 . Insets show the results from a simple calculation for a 2-state atom trapped in a FORT well with $\alpha = \pi/4$.

the Sisyphus cooling we use radially has been previously shown to reach temperatures of $\sim 1 \mu\text{K}$ [37], which corresponds to $n_{\text{rad}} \simeq 4$ for an atom in our FORT. Note that the ratio of the radial to the axial trapping frequencies ($\simeq 0.01$) is such that any modulation of the axial frequency due to radial motion would be adiabatic. As a result, we expect that an atom cooled to the axial ground state does not change its state due to radial motion.

In summary, we have demonstrated cooling to the ground state of axial motion for single Cesium atoms strongly coupled to the field of a small optical resonator. Together with existing capabilities for strong coupling of the internal degrees of freedom, control over the external center-of-mass motion in cavity QED could possibly enable a new set of phenomena to be explored at the light-matter interface. For example, arbitrary states of atomic motion can be prepared from the ground state by coherent Raman transitions [58], then mapped to the electromagnetic field by way of the strong atom-field coupling [60].

4.6.2 Cooling on the Second Order Sideband

We have also implemented a scheme for resolved sideband cooling on the second order motional sideband in analogy to that described in the previous section. This is done by driving $\Delta n = 2$ motional transitions using the FORT-Raman configuration of beams. For

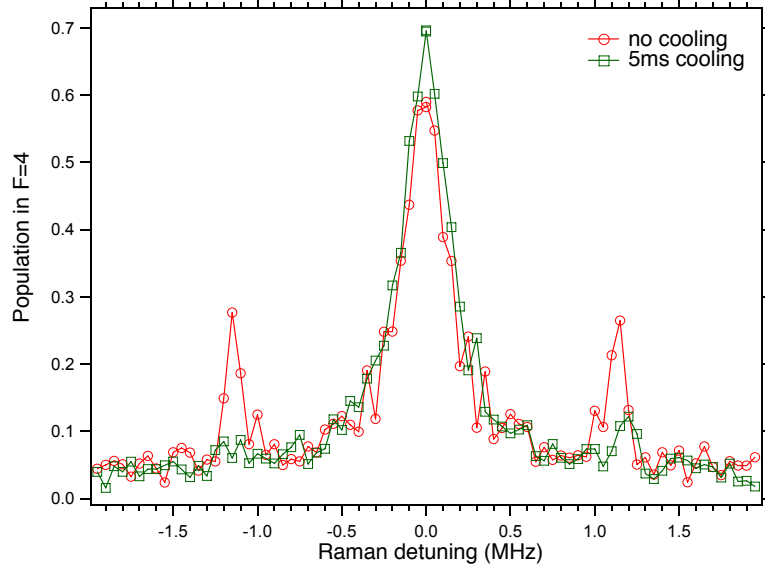


Figure 4.21: Raman spectra for uncooled atoms and for atoms undergoing $\tau_c = 5$ ms of second order resolve Raman sideband cooling. Note the sideband asymmetry and the change in sideband shape in the data with cooling.

the set of measurements described here, the intensity of the Raman beam was configured such that $\Omega_0 \approx 150$ kHz is the Rabi frequency for the ($|3, 0, 0\rangle \leftrightarrow |4, 0, 0\rangle$) transition. The depth of the FORT was measured to be $U_0/h = 45$ MHz. The intensity of the Ω_4 lattice light is set to be $I_4 \approx 0.5I_4^{sat}$. The timing for the experiment is the equivalent to that for the first order sideband measurement: a Raman cooling interval of duration τ_c followed by a variable detuning Raman pulse of duration τ_R and then $100 \mu\text{s}$ intervals of state- and atom-detection probe light.

The Raman spectra corresponding to this measurement for $\tau_c = 0$ ms and $\tau_c = 5$ ms are shown in Figure 4.21. For these measurements the magnetic fields are nulled to the level of $|\vec{B}| \approx 30$ mG and therefore, for both pieces of data, there is a clearly resolved carrier feature corresponding to all transitions ($|3, m_F, n\rangle \leftrightarrow |4, m_F, n\rangle$). We can also clearly see two second order motional sidebands located near $\delta = \pm 2\omega_{ax} = \pm 1.2$ MHz. These sidebands are much broader than the Rabi frequency with which they are being driven (and which is suppressed by a factor of $\sim \eta^2 n$ relative to the carrier) due to the anharmonic dispersion of the FORT

vibrational energies. In the data corresponding to $\tau_c = 5$ ms we see two important effects emerge. First, there is a clear asymmetry between the red and blue motional sidebands. This suggests a majority of the motional population resides either in the $n = 0$ or $n = 1$ states. Because we are driving $\Delta n = 2$ transitions, neither of these states can couple to lower-lying motional levels and both contribute to the asymmetry of the feature. Atoms initially in cooled into a Fock state exhibiting an odd number of vibrational quanta will cool asymptotically to $n = 1$ while atoms initially cooled into an even numbered Fock state will approach $n = 0$.

The second notable effect is that the shape of the blue sideband has changed with respect to the data for uncooled atoms. Recall that we expect the resonant frequency for the sideband transitions to be:

$$\delta_n \equiv \omega'_{ax} - \eta^2 \omega'_{ax} n. \quad (4.85)$$

As the atom gets colder and moves towards states exhibiting lower motional quantum numbers, the center of the sideband feature should shift towards ω'_{ax} . We can clearly see this effect in the data - for the spectrum in which cooling has been implemented the blue sideband has narrowed and the center shifted towards ω_{ax} .

As a matter of practical convenience, we frequently make use of second-order resolved sideband cooling the laboratory. As was observed for first order cooling, the effect of the second order cooling protocol is to significantly extend the trap lifetime of individual atoms in the presence of strong probing. However second order cooling is a good deal simpler and more efficient to set up and maintain as it requires only one beam in addition to the FORT as opposed to two additional beams in the case of first order cooling. In Chapter 6 we will describe an experiment wherein we are able to measure the complete vacuum Rabi spectrum for just one atom. This experiment, in which the atom undergoes prolonged periods of probing at probe-cavity detunings which can demonstrably heat the atom from the trap on experimentally small timescales, was made possible only by the implementation of second order sideband cooling which kept the atoms well-localized in the FORT for the entire duration of the measurement.

4.7 Sisyphus Cooling with Raman Repumper

In Chapter 3 we briefly described how polarization gradient (or Sisyphus) cooling is used to damp the falling motion of atoms from the lower MOT as they enter the FORT potential. The configuration for this cooling scheme involves two pairs of counter-propagating $\sigma^+ - \sigma^-$ -polarized “lattice” beams, each comprised of light at two distinct optical frequencies +10 MHz detuned from ($3 \leftrightarrow 3'$) and ($4 \leftrightarrow 4'$) transitions. Using this method, the typical probability with which we can load an atom into the FORT conditioned on the release of the lower MOT is $P_l < 0.1$. In mid-2006 we discovered, however, that by replacing one of the two Sisyphus cooling beams by a large Rabi frequency ($\Omega_E > (2\pi)(1.5 \text{ MHz})$) resonant Raman pair in FORT-Raman configuration, we can considerably increase P_l . We have observed that this scheme does not produce the same effect in Raman-Raman configuration.

While we don't have a quantitative understanding of how the combination of lattice and Raman is more effective than lattice alone we have developed a plausible, qualitative explanation. As we have seen in this Chapter, the effect of a coherent Raman pair is to induce Rabi oscillation between the hyperfine ground states of the atom. For an atom falling through the Raman beams, Ω_E will vary as a function of the position of the atom. This will lead to dephasing of the Rabi oscillation and can be modeled, like earlier, as an incoherent Raman process with population equilibrating in the maximally mixed state for the system.

Ordinarily, the atom undergoes PG cooling in lattice light with frequency corresponding to the populated hyperfine ground state of the atom until it scatters a photon which deposits the atom in the other ground state. In the lattice-lattice arrangement the atom then experiences PG cooling due to the other frequency of lattice light until it, again, scatters. Each time the atom scatters a “repump” photon (*i.e.*, a non-PG cooling photon), there is a random momentum kick imparted to the atom. However, in the Raman-lattice configuration (for instance, where we have replaced the ($3 \leftrightarrow 3'$) beam with the Raman pair) the Raman beams are acting as an “incoherent repumper” - constantly redistributing the population between the two ground states such that the atom remains effectively coupled to the PG cooling. There is no recoil associated with this redistribution of population. Also, because

the Raman pair is registered with the FORT, the effectiveness of this repump mechanism is greatest at the spatial locations of highest FORT intensity. These also happen to be the positions corresponding to maximum potential depth. Whereas the lattice-lattice configuration operates independently of the FORT potential, the Raman-lattice setup is most effective in at those locations where the atom is most likely to be trapped. It seems likely that the combination of registration and lack of repumper-induced recoil heating events contribute to the Raman-lattice configuration offering more effective cooling to the atom. Although we don't have a numerical model, in light of experimental evidence this hypothesis seems the most plausible explanation of observed phenomena.

This experimental evidence includes a general insensitivity of the loading probability to small detunings and a broad range in Rabi frequencies for the Raman pair. We had considered the possibility that the combination of lattice light and Raman was driving motional transitions and providing second-order sideband cooling to the atoms as they pass through the trapping region. However, we have found that there is no functional dependence of the loading probability on the Raman pair being blue- or red-detuned relative to the field-insensitive carrier transition. Moreover, for Rabi frequencies $\Omega_E \gtrsim (2\pi)(500 \text{ kHz})$, there seems to be no dependence of P_l on Ω_E .

We can, however, characterize the effectiveness of Raman-lattice loading versus lattice-lattice loading. For this measurement, we repeatedly load atoms in the cavity using one scheme or the other. The system is prepared with the magnetic fields nominally nulled at the center of the cavity. At the end of each MOT cycle and loading interval we begin by pumping the atoms into $F = 3$ and applying $\tau_R = 0.7 \mu\text{s}$ intervals of coherent Raman light resonant with all ($|3, m_F\rangle \leftrightarrow |4, m_F\rangle$) transitions followed by state and atom detection. The amount of optical power in the FORT-Raman pair is configured such that $\Omega_E = (2\pi)(140 \text{ kHz})$ and there is an observed dephasing time of $T_2^* \approx 5 \mu\text{s}$. Conditioned on the initial detection of an atom in the cavity, we can measure the population transfer probability for each of the different schemes. We expect that if $N = 1$ atom is present in the cavity that, after the Raman pulse, we should detect the presence of that atom in $F = 4$ with probability

$$P_4(\tau_R) = \frac{1}{2} \left(1 - e^{-\tau_R/2T_2^*} \cos[\Omega_E \tau_R] \right). \quad (4.86)$$

Loading Method	P'_4	\bar{N}
Both Lattice Beams	0.17 ± 0.03	1.5 ± 0.4
Both Lattice Beams and Raman	0.15 ± 0.04	1.4 ± 0.4
Raman and 3 – 3' Lattice	$.41 \pm 0.03$	3.7 ± 0.3
Raman and 4 – 4' Lattice	0.82 ± 0.02	7.5 ± 0.2

Table 4.1: Conditioned on the presence of at least one atom in the cavity, the probability $P_4(\tau_R)$ to measure atomic population in $F = 4$ following a resonant Raman pulse of length $\tau_R = 0.7 \mu\text{s}$. Also the inferred number of atoms present after the loading interval, \bar{N} .

For this experiment, $P_4(\tau_R) = 0.11$. Now, if $N = 2$ atoms are located in the cavity, the Raman pulse should act independently on both atoms, transferring a fraction $P_4(\tau_R)$ of the populations of both atoms to $F = 4$. Upon detection, we cannot discriminate between one or the other (or both) atoms being in the cavity-coupled $F = 4$ state. If the detection measurement projects either or both atoms into $F = 4$, we see a downgoer. Therefore, the total probability to measure any population of atoms in $F = 4$ is given by $P'_4(N = 2) = 2P_4(\tau_R) + P_4^2(\tau_R)$. In general, for N atoms in the cavity, the probability to measure a down-goer is given by:

$$P'_4(N) = \sum_{n=1}^N n P_4(\tau_R)^{N-(n-1)}. \quad (4.87)$$

However, because $P_4(\tau_R)$ is so much less than unity, we can ignore terms in this expression which are nonlinear in $P_4(\tau_R)$. We will assume that for \bar{N} atoms loaded into the cavity, that $P'_4(\bar{N}) = \bar{N}P_4(\tau_R)$.

Table 4.1 shows the values of $P_4(\tau_R)$ and inferred values for \bar{N} for each of four different configurations of the lattice and Raman beams. Notice that for configurations wherein both lattice frequencies are ON, that the probability (with error bars) to detect an atom in $F = 4$ is statistically consistent with the presence of just one atom in the cavity. Because this data is conditioned on the presence of an atom, this is to be expected. However, for configurations where only one of the two lattice frequencies is ON, we see a significant

increase in the Raman transfer probability and therefore the number of atoms in the cavity mode. In fact, for a properly-tuned configuration of ($4 \leftrightarrow 4'$) lattice light and Raman we are loading an mean of $\bar{N} = 7.5$ atoms per attempt. This is a very significant increase which opens the possibility for a variety of interesting measurements including the study of small atom number cavity QED with more than one atom in the cavity.

Chapter 5

Reversible Atom-Field State Transfer

Over the past 20 years atomic physics and quantum information science [45] have developed hand-in-hand. It is not difficult to understand why - a tabletop experiment involving laser cooling and trapping of small atomic samples offers one of the most accessible and potentially scalable points of entry into the “quantum world.” [61] Atomic hyperfine ground states, in particular, make an ideal quantum memory - they exhibit narrow linewidths, long coherence times and can be coherently manipulated using experimentally accessible techniques (see Chapter 4).

The challenge, then, is in how to implement controlled interactions between two physically separate quantum memories (as to, for instance, perform a quantum gate operation). Neutral atoms exhibit only weak collisional interactions with one another, so one potential approach is to instead singly ionize your atomic system and rely on the Coulomb repulsion between two adjacent memories to exchange quantum information. Ion trapping experiments of this sort have yielded amazing results, including demonstrations of multi-atom quantum gates and quantum state teleportation from ion-to-ion [62, 63, 64]. The difficulty, however, is in scaling these systems up. What works well for a few ions requires a considerable bit more overhead as the number of qubits grows [65].

More recently, ion trapping groups [66, 67, 68] and groups working with multi-atom ensembles [69, 70] have presented important results involving entanglement between an atomic memory and a quantum optical field. Photon number and polarization states are easily transported over long distances and, via dipole coupling, provide a robust interac-

tion with atomic systems. While these results are extraordinarily impressive, arguably no physical system is better suited to studying the coupling between atom and photon than is cavity quantum electrodynamics. In fact, one of the earliest demonstrations of a quantum gate operation came from the forbearer in the Kimble group of the experiment described in this thesis [71].

This Chapter will focus on experiments involving the reversible mapping of quantum information in the form of a field state to and from the hyperfine ground states of a trapped cesium atom. Section 5.3 will briefly summarize our 2004 demonstration of a push-button single photon source [40] using the cavity as one arm of a Raman Λ -type scheme. Following this work, in 2007, we used the same apparatus to demonstrate the inherent reversibility of this process by mapping the phase and amplitude of a weak coherent state of light onto a single atom and back [72]. Section 5.4 will describe that experiment.

5.1 Quantum Networking

An important goal in quantum information science is the realization of quantum networks for the distribution and processing of quantum information [73, 74], including for quantum computation, communication, and metrology [75, 76, 77, 78]. Figure 5.1a presents a simple, topological model of a quantum network. The two constituent parts of any such network are quantum nodes (places where quantum information can be locally stored and processed) and quantum channels (which connect adjacent quantum nodes and through which quantum information can be transmitted). In order for any quantum network to be viable, we require certain properties of these nodes and channels.

Figure 5.1b offers a “black box” model of a quantum node. Importantly, the node is characterized by some sort of interface between itself and the channels to which it is connected (as shown in red and associated with some rate of information exchange, κ). In general we also require that our node be able to implement some user-defined quantum algorithm or perform some quantum gate operation on the information which is stored there. This operation can be written succinctly in terms of the interaction Hamiltonian for that operation \hat{H}_{int} , or the energy associated with that interaction $\chi \sim \langle \hat{H}_{int} \rangle / \hbar$. In general

we also expect that real quantum nodes will exhibit some sort of (ideally weak) coupling to the environment which involves irreversible loss of quantum information at characteristic rate γ . Our requirements for quantum channels are a fair bit less complex. We assume that these channels will transport units of quantum information between two remote systems with some (ideally) high efficiency.

In the initial proposal for the implementation of quantum networks [79], atomic internal states with long coherence times serve as ‘stationary’ qubits, stored and locally manipulated at the nodes of the network. Quantum channels between different nodes are provided by optical fibers, which transport photons (‘flying’ qubits) over long distances by way of quantum repeaters [80]. A crucial requirement for this and other network protocols is the reversible mapping of quantum states between light and matter. Cavity quantum electrodynamics (QED) provides a promising avenue for achieving this capability by using strong coupling for the interaction of single atoms and photons (Figure 5.1c). Within this setting, reversible emission and absorption of one photon can be achieved by way of a dark-state process involving an atom and the field of a high-finesse optical cavity. For classical fields, this process, known as stimulated Raman adiabatic passage (or STIRAP) was first considered twenty years ago [81, 82], before being adapted to quantum fields [83] and specifically to the coherent transfer of quantum states between remote locations [79], with many extensions since then [84]. In the next Section we will describe this technique in detail.

5.2 Stimulated Raman Adiabatic Passage (STIRAP)

5.2.1 Theoretical Description

In this section we will describe stimulated Raman adiabatic passage (STIRAP) in the context of a single, three-level atomic system coupled to an ideal cavity in the regime of strong coupling. The atomic system consists of two ground states - $|g\rangle$ and $|u\rangle$ with energies $E_g = \hbar\omega_g$ and $E_u = \hbar\omega_u$, respectively - and a single excited state $|e\rangle$ with energy $E_e = \hbar\omega_e$. The cavity is coupled to the ($|g\rangle \leftrightarrow |e\rangle$) transition with coupling rate g . An externally applied field at frequency ω_T drives the transition ($|u\rangle \leftrightarrow |e\rangle$) with variable Rabi frequency $\Omega_T(t)$ in order to induce STIRAP. We will quantize the mode of the field resonant with

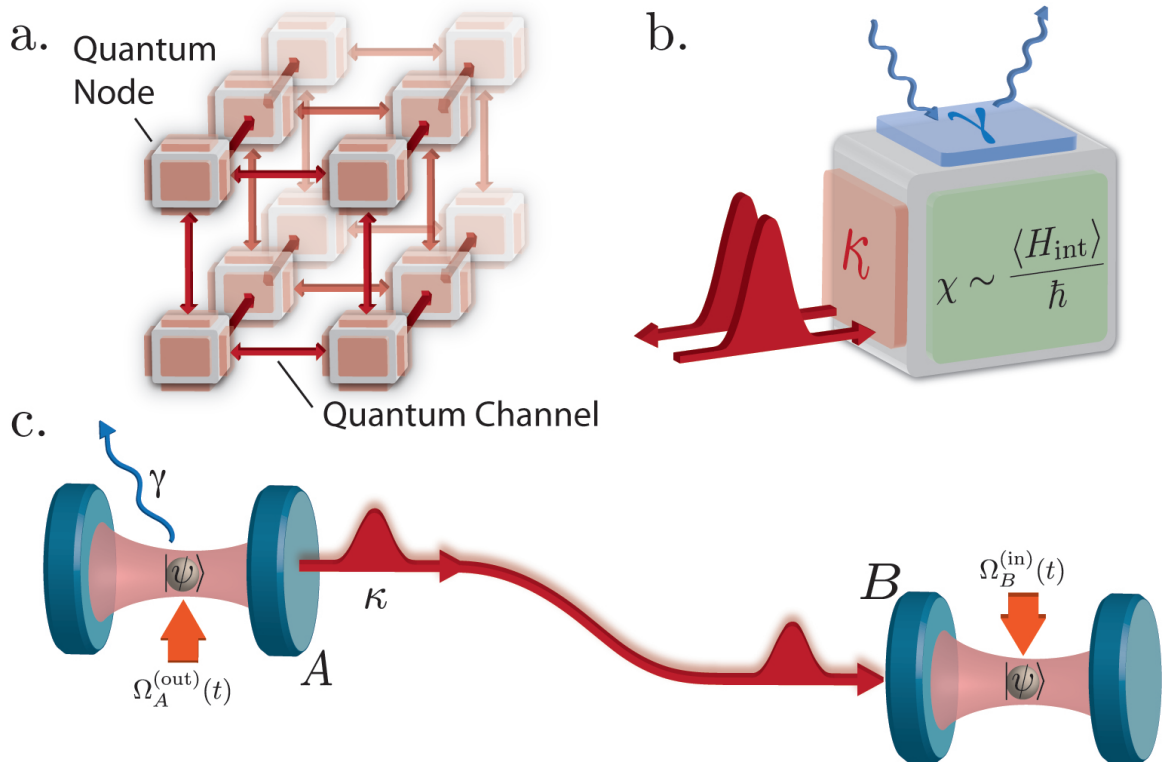


Figure 5.1: a. Simple topological model of a quantum network. b. Functional “black box” representation of a quantum node. Information is transmitted from node-to-node by way of an interface between the node and channel (as shown in red). c. A cavity QED implementation of quantum networking. Atoms trapped within optical cavities in the regime of strong coupling serve as nodes wherein quantum information is stored and processed. The strong atom-field coupling serves as the “network interface” by which quantum information is transmitted from node-to-node over optical fibers (which serve as quantum channels).

the cavity and treat the field which triggers the single photon emission as classical. First, we construct the Hamiltonian for the system in strict analogy with the two-level Jaynes-Cummings model in the rotating wave approximation:

$$\begin{aligned}\widehat{H} &= \widehat{H}_{\text{atom}} + \widehat{H}_{\text{field}} + \widehat{H}_{u-e} + \widehat{H}_{g-e} \\ &= \hbar(\omega_g |g\rangle \langle g| + \omega_u |u\rangle \langle u| + \omega_e |e\rangle \langle e|) + \hbar\omega_C \left(\hat{a}^\dagger \hat{a} + \frac{1}{2} \right) \\ &\quad + \frac{\hbar}{2}(\Omega_T e^{-i\omega_T t} |e\rangle \langle u| + \Omega_T^* e^{i\omega_T t} |u\rangle \langle e|) + \hbar(g\hat{a} |e\rangle \langle g| + g^* \hat{a}^\dagger |g\rangle \langle e|)\end{aligned}\quad (5.1)$$

With a bit of algebra, we can rewrite this Hamiltonian in the interaction picture:

$$\widehat{H}_I = \hbar\Delta |e\rangle \langle e| + \frac{\hbar}{2}(\Omega_T |e\rangle \langle u| + \Omega_T^* |u\rangle \langle e|) + \hbar(g\hat{a} |e\rangle \langle g| + g^* \hat{a}^\dagger |g\rangle \langle e|), \quad (5.2)$$

where $\Delta = (\omega_e - \omega_u) - \omega_T$. We will restrict ourselves to the weak excitation limit (within the manifolds of states exhibiting 0 and 1 excitations) and operate in a basis of uncoupled product states $|\mathcal{A}\rangle \otimes |n\rangle = \{|u, 0\rangle, |e, 0\rangle, |g, 1\rangle\}$ where $|\mathcal{A}\rangle$ denotes atomic state and $|n\rangle$ the cavity photon occupation state in the Fock basis. It is instructive to express the interaction picture Hamiltonian \widehat{H}_I in matrix form over this basis:

$$\widehat{H}_I = \frac{\hbar}{2} \begin{pmatrix} 0 & \Omega_T & 0 \\ \Omega_T^* & 2\Delta & 2g \\ 0 & 2g^* & 0 \end{pmatrix}. \quad (5.3)$$

Upon diagonalization of this matrix, the eigenenergies of the system are:

$$E = \frac{\hbar}{2}(0, -\Delta \pm \sqrt{\Delta^2 + 4g^2 + \Omega_T^2}), \quad (5.4)$$

whereas the eigenvectors are:

$$|a^{(0)}\rangle = -\frac{2g}{\Omega_T} \left(\frac{1}{\sqrt{1 + \frac{4g^2}{\Omega_T^2}}} \right) |u, 0\rangle + \left(\frac{1}{\sqrt{1 + \frac{4g^2}{\Omega_T^2}}} \right) |g, 1\rangle \quad (5.5)$$

$$|a^{(+)}\rangle = \beta \left(\frac{\Omega_T}{2g} |u, 0\rangle - \frac{(\Delta + \sqrt{\Delta^2 + 4g^2 + \Omega_T^2})}{2g} |e, 0\rangle + |g, 1\rangle \right) \quad (5.6)$$

$$|a^{(-)}\rangle = \beta \left(\frac{\Omega_T}{2g} |u, 0\rangle - \frac{(\Delta - \sqrt{\Delta^2 + 4g^2 + \Omega_T^2})}{2g} |e, 0\rangle + |g, 1\rangle \right). \quad (5.7)$$

Here β is a normalization constant:

$$\beta = \frac{1}{\sqrt{\left(1 + \frac{\Omega_T^2}{4g^2} + \frac{(\Delta - \sqrt{\Delta^2 + 4g^2 + \Omega_T^2})^2}{4g^2}\right)}}. \quad (5.8)$$

It is useful to define a set of mixing angles $\{\Theta, \Phi\}$ in order to simplify the expressions for the three eigenstates:

$$\sin \Theta = - \left(\frac{1}{\sqrt{1 + \frac{4g^2}{\Omega_T^2}}} \right) \quad (5.9)$$

$$\cos \Theta = - \frac{2g}{\Omega_T} \left(\frac{1}{\sqrt{1 + \frac{4g^2}{\Omega_T^2}}} \right) \quad (5.10)$$

$$\sin \Phi = \beta \frac{(\Delta + \sqrt{\Delta^2 + 4g^2 + \Omega_T^2})}{2g} \quad (5.11)$$

$$\cos \Phi = -\beta \frac{(\Delta - \sqrt{\Delta^2 + 4g^2 + \Omega_T^2})}{2g}. \quad (5.12)$$

We can also express the mixing angles as:

$$\begin{aligned}\tan \Theta &= \frac{\Omega_T}{2g} \\ \tan \Phi &= \sqrt{\frac{-\Delta + \sqrt{4g^2 + \Delta^2 + \Omega_T^2}}{\Delta + \sqrt{4g^2 + \Delta^2 + \Omega_T^2}}} \\ &= \frac{\sqrt{4g^2 + \Omega_T^2}}{\Delta + \sqrt{4g^2 + \Delta^2 + \Omega_T^2}}.\end{aligned}$$

It follows that we can rewrite the system eigenvectors in terms of these mixing angles:

$$|a^{(0)}\rangle = \cos \Theta |u, 0\rangle - \sin \Theta |g, 1\rangle \quad (5.13)$$

$$|a^{(+)}\rangle = \cos \Phi \sin \Theta |u, 0\rangle - \sin \Phi |e, 0\rangle + \cos \Phi \cos \Theta |g, 1\rangle \quad (5.14)$$

$$|a^{(-)}\rangle = \sin \Phi \sin \Theta |u, 0\rangle + \cos \Phi |e, 0\rangle + \sin \Phi \cos \Theta |g, 1\rangle. \quad (5.15)$$

From the simplified functional forms of $|a^{(0),(+),(-)}\rangle$ it is important to note that the state $|a^{(0)}\rangle$ is a so-called “dark state” of the system - of the three eigenvectors of the interaction Hamiltonian, it is the only one that has no component in the state $|e, 0\rangle$.

The STIRAP process relies on this particular dark state [85]. We begin with the system initially in the state $|u, 0\rangle$ (*i.e.*, with the atom pumped in the state $|u\rangle$ and with no photons in the cavity mode). We want to implement a transformation such that the system ends up in the state $|g, 1\rangle$, now with a single photon in the cavity mode. In order for this process to be useful in a quantum networking setting we require that it be coherent - that the off-diagonal terms of the density matrix for the initial state should be preserved in the density matrix of the final state. This precludes allowing any atomic population into state $|e\rangle$ from which (incoherent) spontaneous will quickly dephase the state of the system. From the functional form of $|a^{(0)}\rangle$, it is clear that we can implement this transformation if we can adiabatically sweep the mixing angle Θ from 0 to $\pi/2$. This is where STIRAP derives its name - it is a stimulated Raman process (with the cavity forming one arm of the Λ -pair and the classical field forming the other) which adiabatically follows the dark state $|a^{(0)}\rangle$ to deposit a single photon in the cavity mode.

From the expression for Θ , we see that in the limit $2g \gg \Omega_T$ (or, $2g \ll \Omega_T$) we have $|a^{(0)}\rangle \approx |u, 0\rangle$ (or, $|a^{(0)}\rangle \approx |g, 1\rangle$). Our photon generation protocol will be to initialize the atom in $|u, 0\rangle$, ensuring that at early times, $g \gg \Omega_T(t)$, or that the strength of the classical field is initially very weak. Note that because we will be varying $\Omega_T(t)$, we again emphasize it's time-dependence (the atom-cavity coupling rate g is assumed to be time-independent). We will then increase $\Omega_T(t)$ at a sufficiently slow rate that the coupled atom-cavity state vector will adiabatically (or, reversibly) follow $|a^{(0)}(t)\rangle$ from $|u, 0\rangle$ through a coherent superposition of states to $|g, 1\rangle$. The probability that at time t the system will have evolved to $|g, 1\rangle$ and that there will be a single photon in the cavity mode is given by:

$$P(t) = |\langle g, 1 | a^{(0)}(t) \rangle|^2 = \frac{\Omega_T^2(t)}{\Omega_T^2(t) + 4g^2}. \quad (5.16)$$

In this way, as long as the adiabaticity of the process is maintained, the application of the classical field $\Omega_T(t)$ will “trigger” the generation of one-and-only-one photon. Interestingly, this protocol also allows us to “shape” the temporal wavepacket of the single photon by varying $\Omega_T(t)$ [86].

It remains to discuss how best to restrict the experimental parameters in order to ensure adiabaticity. The concern is that as the state of the system $|\Psi(t)\rangle$ evolves it will acquire some component outside of $|a^{(0)}(t)\rangle$. We can quantify this process by taking note of the quantum adiabatic theorem [6] which dictates that a state vector which evolves according to the Schrödinger equation and has a minimum energy gap $\epsilon = \hbar\omega_{\pm}$ between eigenstates adjacent to that which is being adiabatically followed will evolve adiabatically as long as the following condition is met:

$$|\langle a^{(\pm)} | \partial_t |\Psi(t)\rangle| < |\epsilon/\hbar|. \quad (5.17)$$

Here, $|a^{(\pm)}\rangle$ are the two, adjacent eigenstates and ∂_t is the quantum operator for the partial derivative with respect to time. In other words, as long as the spread in energies associated with the state which is being followed is small compared the energy splitting between its adjacent eigenstates, then the system will adiabatically follow its original state. Adiabatic following can also be thought of in the Bloch vector picture, as described in [87]. In the

context of STIRAP, the adiabatic theorem is equivalent to the statement $|\dot{\Theta}| < |\epsilon/\hbar|$ [85], or in terms of the relevant experimental parameters:

$$|\dot{\Theta}| = \left| \frac{2\dot{\Omega}_T(t)g}{\Omega_T^2(t) + 4g^2} \right| < \left| \Delta + \sqrt{\Delta^2 + 4g^2 + \Omega_T^2(t)} \right| \quad \Rightarrow \quad (5.18)$$

$$|\dot{\Omega}_T(t)| < \left| g^{-1}(\Omega_T^2(t) + 4g^2) \left[\Delta + \sqrt{\Delta^2 + 4g^2 + \Omega_T^2(t)} \right] \right|. \quad (5.19)$$

If we consider only early times then the system is still in the initial limit $2g \gg \Omega_T$ and adiabaticity requires:

$$\Omega_T(t) < 4g \left| \Delta + \sqrt{\Delta^2 + 4g^2} \right| t. \quad (5.20)$$

We have thus far neglected the importance of dissipation in this system. The rate of atomic decay from the excited state, γ , has been adiabatically eliminated from the problem along with any population in $|e\rangle$. Decay from the cavity mode at κ , however, is still relevant to this discussion. If excitation escapes the cavity and is detected or measured before the complete transfer of population from atom-to-field, then the temporal shape of the photon will be governed not by $\Omega_T(t)$ but by the magnitude of κ . However, because we are in the strong coupling regime $g \gg \kappa$, it follows from Equation (5.20) that we are able to adiabatically sweep $\Omega_T(t)$ over its full range in $\tau \gg 1/\kappa$. Operation in the regime of strong coupling guarantees that the STIRAP process is coherent and efficient.

5.2.2 Physical Implementation in Cesium

The generalization of the STIRAP scheme described in the previous Section to cesium is straightforward. In the laboratory we can treat any two appropriately-coupled Zeeman substates $|3, m_F\rangle, |4, m'_F\rangle$ in the $F = 3$ and $F = 4$ hyperfine ground state manifolds as states $|u\rangle$ and $|g\rangle$. Likewise, Zeeman states in any excited state hyperfine manifold which exhibits dipole coupling to both ground states (*i.e.*, $F' = 3$ and $F' = 4$) will function as $|e\rangle$. In particular, we will tune the cavity near resonance with the $(4 \leftrightarrow 3')$ transition and use a classical Ω_T field which is near-resonant with $(3 \leftrightarrow 4)$ to affect the STIRAP process. On this transition, the maximum atom-cavity coupling constant is $g_0 = (2\pi)(14.87 \text{ MHz})$ (see

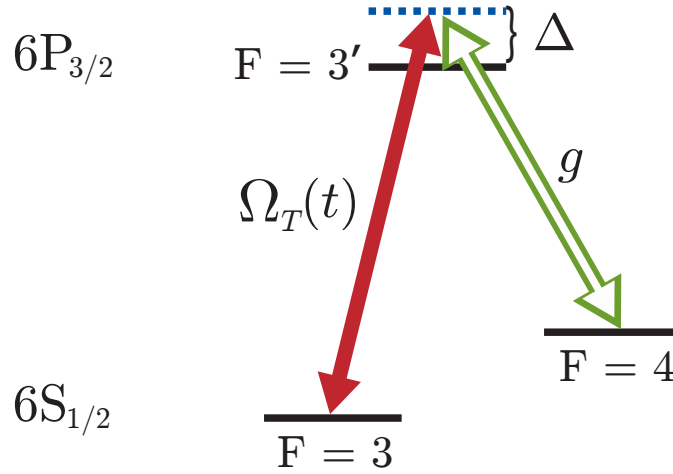


Figure 5.2: Atomic level diagram. Double arrow g indicates the coherent atom-cavity coupling, and $\Omega_T(t)$ is the classical field. The cavity and Ω field are blue-detuned from atomic resonance by Δ .

Chapter 2). The energy level diagram for this system is shown in figure 5.2.

5.3 A Deterministic Source of Single Photons

In this Section, we will very briefly review the work expanded upon in Reference [40]. This project was the first in which I was personally involved in the Kimble group and constitutes our group's first experimental implementation of the STIRAP method described in Section 5.2. The goal of this measurement was to demonstrate that the STIRAP process could be used to efficiently and deterministically generate single photons from the coupled atom-cavity system. Our primary concern was with verifying that the state of light generated in the cavity mode was to high degree one and only one photon. A similar demonstration was carried out by the group of G. Rempe in 2002 using atoms falling through the mode of the cavity [88]. However this implementation allowed for the production of on average much less than one “signal” (as opposed to background) photon per atom passing through the cavity mode. Because of this significant background, the emitted field did not exhibit the sub-Poissonian photon statistics requisite to claim to that a device is a deterministic

source of single photons [89]. Our demonstration, by contrast, allowed for in excess of 1.4×10^5 photons per atom. Although this constitutes “old” work in that it was first carried out in 2004, before we had developed the Raman techniques described in Chapter 4 to characterize and control the atomic system, I view this experiment as one of the most significant and important advances our group has made with respect to cavity QED-based quantum networking. It is therefore worth briefly mentioning here, especially in order to set the stage for Section 5.4.

5.3.1 Overview and Results

This set of measurements was carried out before we were able to independently measure and control the DC magnetic bias fields at the location of the cavity. During the experimental cycle the current directed through the bias coils was that necessary to null the fields at the location of the lower MOT and was likely contributing a static bias of magnitude $|\vec{B}| \sim 0.5$ G. In order to implement the STIRAP process, we load atoms into the FORT using the $(3 \leftrightarrow 3')$ and $(4 \leftrightarrow 4')$ lattice pair. After each loading attempt, atoms present in the cavity are optically pumped into a state within the $F = 3$ ground state manifold and then illuminated by a sequence of laser pulses which we will label by their associated Rabi frequencies $\{\Omega_3(t), \Omega_4(t)\}$. These pulses are derived from and follow the same optical paths as the lattice beams. The first of each pair, $\Omega_3(t)$, functions as the classical field of Rabi frequency $\Omega_T(t)$ necessary to implement STIRAP. As $\Omega_3(t)$ is adiabatically ramped ON, one photon is created in the cavity mode because the atomic transition $F' = 3' \rightarrow F = 4$ is tuned near-resonance with the cavity. The emitted photon leaves the cavity as a freely propagating, spatially Gaussian wavepacket whose temporal profile is determined by the external field $\Omega_3(t)$. The atom is then incoherently repumped back to $F = 3$ by the second laser pulse, $\Omega_4(t)$, and the protocol repeated for subsequent single photon generations.

Within each photon generation trial, the first pulse $\Omega_3(t)$ is 1 μs in duration and contains light tuned 10 MHz blue of $(3 \leftrightarrow 3')$, which initiates the adiabatic transfer $F = 3 \rightarrow 4$ between the ground hyperfine levels, with the emission of a photon into the cavity mode. The second pulse $\Omega_4(t)$ is turned ON 1 μs after $\Omega_3(t)$ is gated OFF and is 5 μs in duration. It is tuned 17 MHz blue of $(4 \leftrightarrow 4')$ and recycles the atom back to the $F = 3$ ground state

through spontaneous decay ($4' \rightarrow 3$). The detuning between the ($4 \leftrightarrow 3'$) transition at ω_{43} and the cavity resonance ω_C is $\Delta_{AC} \equiv (\omega_C - \omega_{43}) = (2\pi)(9 \text{ MHz})$.

The lifetime for a trapped atom in the presence of the driving $\Omega_{3,4}$ fields is $T \simeq 0.14$ s, which should be compared to the repetition period $\Delta t = 10 \mu\text{s}$ for single-photon generation. The presence of an atom in the cavity is discriminated based on the rate at which we register photodetection events. If no photodetection event is registered within the previous 500 windows during which $\Omega_3(t)$ is ON then those previous 500 trials are disregarded and the atom is assumed to have left the trap. The measured overall efficiency for photodetection of emitted light for this set of measurements was $\alpha = (2.4 \pm 0.4)\%$ and we infer that each generation attempt succeeds with probability $\phi_G = 1.15 \pm 0.18$, where this high success probability derives from strong coupling of atom and cavity field. This implies that the probability with which an atom remains coupled to the cavity but fails to produce a photodetection in 500 successive trials is $(1 - \alpha)^{500} \approx 5 \times 10^{-6}$. This also means that on average, we generate (detect) about 1.4×10^4 (350) single photon pulses from each trapped atom.

In order to quantify the quantum (or single photon) character of the emission we measure the quantity:

$$R_0 \equiv \frac{P_1^2}{2P_2}, \quad (5.21)$$

where P_N is the probability for N photodetection events following a single $\Omega_3(t)$ pulse. We use R_0 to distinguish the photon statistics of the state of light which we are producing in the cavity from a weak coherent state of light (*i.e.*, with $P_0 \sim 1$). For an ideal single photon source we have $P_N = 0, N \neq 1$ which implies $R_0 \rightarrow \infty$. For an attenuated (classical) laser field

$$P_2 = \frac{P_1^2}{2P_0} \approx \frac{P_1^2}{2} \quad (5.22)$$

which means $R_0 \approx 1$. Experimentally we measure $R_0 = 20.8 \pm 1.8 \gg 1$ *at the location of the detectors*. We were able to isolate the principal limitation on R_0 to rare events (about 3% of the successful loading attempts) in which two atoms are loaded into the trap (this

work preceded the real-time atom detection-based loading scheme documented in Tracy Northup's thesis [26]). By limiting the data to photodetections registered at later times in the trapping cycle when such two atom events are more likely to have decayed, we find $R_0 \gtrsim 150$. As we will discuss in Subsection 5.3.2, there are some caveats associated with characterizing a photon source in terms of R_0 .

An example of the pulse shape for single photon generation is shown in Figure 5.3a over the detection window $[t_0, t_0 + \delta t]$ within which the control field $\Omega_3(t)$ is ON, where $\delta t = 1 \mu\text{s}$, and t_0 corresponds to the onset time of $\Omega_3(t)$. Plotted is a histogram of the total counts $n(t)$ summed over both single photon counting avalanche photodiode modules and binned according to their delay with respect to t_0 . This histogram is a sum over all repeated trials of the generation process from all atomic trapping events. For the particular choice of $\Omega_3(t)$ employed here, single-photon pulses have duration $\tau \simeq 120 \text{ ns}$ (FWHM).

To quantify the suppression of two-photon events, we present in Figure 5.3b,c the time dependence of the photon statistics over the course of the $\Omega_3(t)$ pulse. Figure 5.3b displays the integrated probabilities for single $P_1(t)$ and joint $P_2(t)$ detection events for times t after the onset t_0 of the control pulse $\Omega_3(t)$. More specifically, $P_1(t)$ is the fraction of trials in which we registered only one photodetection event in the interval $[0, t]$, where for each trial $t = 0$ refers to t_0^j . We calculate $P_1(t)$ and $P_2(t)$ for an effective single detector without dead time or after-pulsing, and define $P_{1,2} \equiv P_{1,2}(\delta t)$. Over the duration of the control pulse $0 \leq t \leq \delta t$, $P_1(t)$ rises to a final value $P_1 = 0.0284$; that is, the probability to register a single photoelectric event in a trial is 2.84%. From Figure 5.3c we see that $P_2(t)$ reaches a limiting value of $P_2 = 2.52 \times 10^{-5}$, or a total probability of 0.00252% to measure a coincidence at the photodetectors.

Figure 5.3d examines the ratio

$$R(t) \equiv \frac{P_1^2(t)}{2P_2(t)}. \quad (5.23)$$

This Figure restates the result that two-photon events are greatly suppressed relative to a coherent state, namely $R \equiv R(\delta t) = 15.9 \pm 1.0$. The background rate during the Ω_3 drive pulses is time-independent, and can be obtained from the record of photoelectric detections

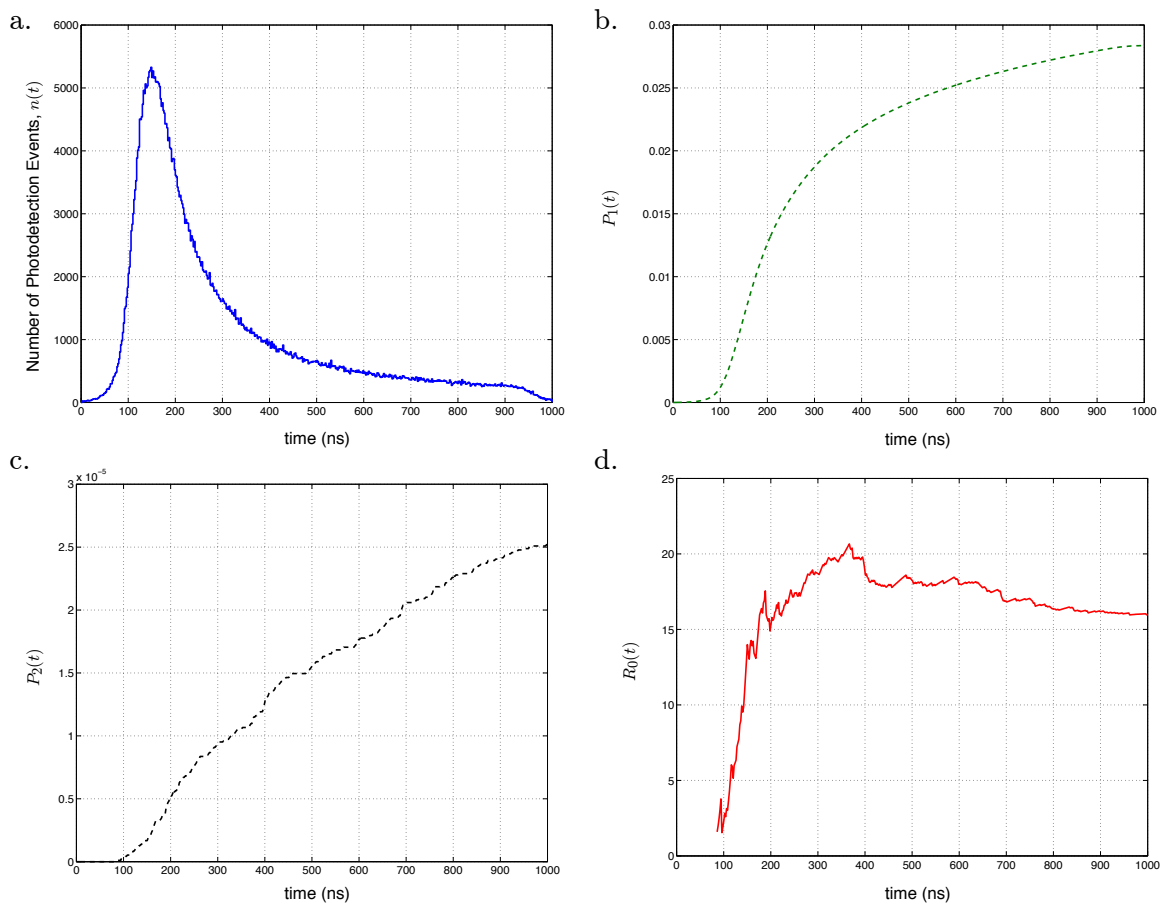


Figure 5.3: a. Histogram of photodetection times, $n(t)$ in the window $\{t_0, t_0 + \delta_t\}$. b. Integrated probability to register one photodetection event as a function of time, $P_1(t)$. b. Integrated probability to register two photodetection events, $P_2(t)$. c. Suppression of two photodetection events relative to a weak coherent state, $R_0(t)$. All four traces exhibit a minimum integration time of $\tau_d = 2$ ns, set by the time resolution of the P7888 event counting interface.

when no atom is trapped. The measured background count probability is $P_B = 2.7 \times 10^{-4}$ for the entire window, of which $P_D = 0.82P_B$ comes from detector dark counts, and the rest from various sources of scattered light. For an ideal single photon source, coincidence events at the two detectors in the same trial would arise only from background counts, since the source never emits two photons in one trial. Using the known values of $P_1(t)$ and P_B , we can easily predict the background-limited value $R_B(t)$ for this idealized scenario. We find that our measured values are lower than this prediction ($R_B \equiv R_B(\delta t) = 52.5$), indicating a significant rate of excess coincidences which are explained by the significant non-zero probability of loading two atoms into the cavity and their subsequent production of two-photon events [40].

5.3.2 Attenuation and R

In this Section, we will briefly examine how the measured photon statistics of an arbitrary intracavity field state $|\chi\rangle$ vary as a function of inefficiencies in the optical path to our detectors. Our goal is to determine what information the quantity R tells us about the system and how that quantity varies as a function of attenuation in the cavity output path for a variety of intracavity field states. In order to model these effects, we will assume that the intracavity field, $|\chi\rangle$ can be expressed as an arbitrary superposition of Fock states:

$$\begin{aligned} |\chi\rangle &= \sum_n |n\rangle \langle n|\chi\rangle \\ &= \sum_n e^{i\phi} \sqrt{P_n} |n\rangle, \end{aligned} \quad (5.24)$$

where P_n is the probability of observing n intracavity photons when measuring $\hat{a}^\dagger \hat{a}$, and where:

$$\sum_n P_n = 1, \quad (5.25)$$

$$\sum_n n P_n = \langle n \rangle. \quad (5.26)$$

We now model our output path as shown in Figure 5.4, beginning with the intracavity

state $|\chi\rangle$ which propagates through some fixed attenuator \mathcal{A} before arriving at an ideal number state-resolving detector. In practice, the Hanbury-Brown-Twiss geometry of our output path allows us to resolve only components of the field up to and including $n = 2$, so we will generally limit our discussion to that basis. The effect of \mathcal{A} is to transmit any photon impinging on it with probability $P_{\mathcal{A}} = (1 - \alpha)$ ($0 \leq \alpha \leq 1$). It is important to note that we treat all incident photons as statistically independent from one another - the effect of attenuator \mathcal{A} depends in no way on correlations between incident photons (as might be the case if it were to contain, for example, any sort of interferometric device). This is a reasonable assumption for our cavity output path.

Propagation of an n -photon input state $|\chi\rangle = |n\rangle_{\text{in}}$ ($P_n = 1$) through the attenuator will yield a state with an n -photon component which will be measured with probability $P'_n = (\alpha)^n$, where the primed probability indicates measurement after \mathcal{A} . Similarly, the $(n - 1)$ -photon component of the transmitted state will be measured with probability:

$$P'_{n-1} = \binom{n}{n-1} (1 - \alpha) \alpha^{n-1},$$

and so on for the $(n - 2)$ -, $(n - 3)$ -, \dots , 1-, and 0-photon components of this state (the first term of this expression is the binomial coefficient, n -choose- $n - 1$). We can generalize this transformation to an arbitrary input state, $|\chi\rangle$:

$$\begin{aligned} P_n &\xrightarrow{\mathcal{A}} P'_n \\ &= \sum_{k=n}^{\infty} \binom{k}{n} (1 - \alpha)^{(k-n)} \alpha^n P_k. \end{aligned} \quad (5.27)$$

In the previous Section we introduced the function the function R :

$$R \equiv \frac{P_1^2}{2P_2}. \quad (5.28)$$

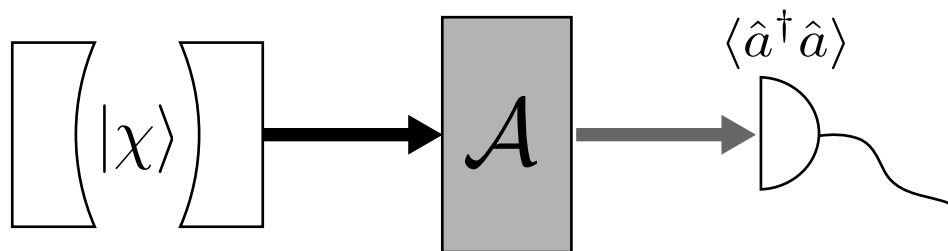


Figure 5.4: Simple model of cavity output path for number state detection of an arbitrary intracavity field state $|\chi\rangle$.

Using Equation 5.27, we see:

$$\begin{aligned}
 R &\xrightarrow{A} R' \\
 &= \frac{(P'_1)^2}{2P'_2} \\
 &= \frac{(\sum_{k=1}^{\infty} k(1-\alpha)^{(k-1)}P_k)^2}{\sum_{k=2}^{\infty} k(k-1)(1-\alpha)^{(k-2)}P_k}.
 \end{aligned} \tag{5.29}$$

Note that R is not invariant under attenuation, but instead varies as a function of α and the initial distribution of detection probabilities associated with state $|\chi\rangle$.

Coherent State

Now suppose that our initial state $|\chi\rangle$ is a coherent state of light [6, 87], *i.e.*,

$$P_n = \frac{e^{-\langle n \rangle} \langle n \rangle^n}{n!}, \tag{5.30}$$

such that:

$$\begin{aligned}
 P_0 &= e^{-\langle n \rangle} \\
 P_1 &= e^{-\langle n \rangle} \langle n \rangle \\
 P_2 &= \frac{1}{2} e^{-\langle n \rangle} \langle n \rangle^2 = \frac{1}{2} \langle n \rangle P_1 \\
 R &= \frac{P_1^2}{2P_2} = \frac{P_1^2}{\langle n \rangle P_1} = e^{-\langle n \rangle} = P_0.
 \end{aligned} \tag{5.31}$$

As expected, a weak coherent state exhibits $R \rightarrow 1$ as $P_0 \rightarrow 1$. The effect of attenuation on a coherent state can be shown using Equation 5.27:

$$\begin{aligned} P'_n &= \sum_{k=n}^{\infty} \binom{k}{n} (1-\alpha)^{(k-n)} \alpha^n \frac{e^{-\langle n \rangle} \langle n \rangle^k}{k!} \\ &= \frac{e^{-\alpha \langle n \rangle} (\alpha \langle n \rangle)^n}{n!}. \end{aligned} \quad (5.32)$$

Comparing this result with Equation 5.30, we see that \mathcal{A} reduces the mean photon number of the coherent state by a factor of α (but the state remains a coherent state). This isn't a surprise, given how we modeled the attenuator and in consideration of how we expect a "real" attenuator to function. Because the output of the attenuator is still a coherent state, we know that R' is given by:

$$\begin{aligned} R' &= P'_0 \\ &= e^{-\alpha \langle n \rangle} = e^{(1-\alpha) \langle n \rangle} R \end{aligned} \quad (5.33)$$

such that, in general, $R' \geq R$ for all values of α . As we attenuate a weak coherent state it only gets weaker as it approaches the limit of the vacuum state and $P_0 = 1$.

One-Photon State

We now consider the trivial case of an ideal single-photon intracavity field, $|\chi\rangle = |1\rangle$ ($P_1 = 1, P_{n \neq 1, n \geq 0} = 0$). After attenuation, we have:

$$\begin{aligned} P'_0 &= (1-\alpha), \\ P'_1 &= \alpha, \\ \text{and } P'_n &= 0 \quad (n > 1). \end{aligned}$$

Therefore, $R = R' = \infty$ because $P_2 = P'_2 = 0$. Again, this is unsurprising in that we expect this state to never exhibit a two-photon component and therefore R remains invariant.

One-Photon State with Two-Photon Defect

A more interesting and applicable exercise is to look at an approximation of the results from the previous Subsection. We assume that a nearly pure single-photon state is generated in the cavity mode with a very small defect in the form of a small two-photon generation probability δ , *i.e.*:

$$\begin{aligned} P_0 &= 0, \\ P_1 &= 1 - \delta, \\ P_2 &= \delta, \quad (\delta \ll 1) \\ P_{n \geq 3} &= 0. \end{aligned}$$

The source of this two photon defect is irrelevant, but could be from multiple atoms, scattering or any equivalent source. For this distribution of probabilities,

$$R = (1 - \delta)^2 / (2\delta). \quad (5.34)$$

After attenuation, the photon statistics for this state are given by:

$$\begin{aligned} P'_0 &= (1 - \alpha)(1 - \delta) + (1 - \alpha)^2 \delta, \\ P'_1 &= \alpha(1 - \delta) + 2(1 - \alpha)\delta\alpha, \\ P'_2 &= \alpha^2 \delta, \\ P'_n &= 0 \quad (n \geq 3). \end{aligned}$$

So,

$$R' = \frac{(1 + 2(1 - \alpha)\delta - \delta)^2}{2\delta} \quad (5.35)$$

$$= \frac{(1 + 2(1 - \alpha)\delta - \delta)^2}{(1 - \delta)^2} R = \left(1 + \frac{4(1 - \alpha)\delta(1 - \alpha\delta)}{(1 - \delta)^2} \right) R \quad (5.36)$$

Note that, in general, $R' \geq R$, and for small δ , $R' \sim R$, as expected. (Also note that there is a singularity at $\alpha = 0$, *i.e.*, complete extinction of all incident light, such that R' is

undefined).

In the previous Section, we measured that $\alpha = 0.024$ and $R'_{\text{avg}} = 15.9$. We also measured a value of P_2 which gives $\delta \simeq 0.0312$. Note that this is in good agreement with the expected probability with which two atoms were inadvertently loaded into the cavity mode. From this we can deduce that the intracavity value of R was $R \simeq 14.1$, such that $R/R' = 0.88$. In summary, R differs significantly from R' only in the regime wherein δ and/or α is close to 0. Because of our small detection efficiency, we are in the lower limit of this regime and it is therefore important that we make the distinction between the value of R measured at the detectors and the value of R for the state of light inside of the cavity if we wish to use R as a means for quantifying the single-photon character of the light.

Two-Photon State

Finally, we look at the effects of an attenuator on a pure two-photon state such as that which we might attempt to generate from two atoms trapped within our cavity. This discussion was originally brought up in the context of attempting to use real-time discrimination of the number of atoms coupled to the cavity mode in order to deterministically load two atoms into the FORT and produce an optical state characterized by a preponderance of coincidence photodetections upon measurement. Assuming that two atoms generate two photons with unit efficiency, this is the special case $\delta = 1$ of the previous example:

$$\begin{aligned} P_0 &= 0, \\ P_1 &= 0, \\ P_2 &= 1, \\ P_{n \geq 3} &= 0. \end{aligned}$$

so that:

$$\begin{aligned}
 P'_0 &= (1 - \alpha)^2, \\
 P'_1 &= 2\alpha(1 - \alpha), \\
 P'_2 &= \alpha^2, \\
 P'_n &= 0 \quad (n \geq 3).
 \end{aligned}$$

We therefore expect $R = 0$ for the unattenuated state and

$$\begin{aligned}
 R' &= \frac{4\alpha^2(1 - \alpha)^2}{2\alpha^2} \\
 &= 2(1 - \alpha)^2.
 \end{aligned} \tag{5.37}$$

For the measured value of α in our experiment this would imply $R' = 1.8$. This is perhaps a counter-intuitive result. With $R > 1$ as a measure of the quality of a single-photon source relative to a weak coherent state, we arrive at the conclusion that an attenuated ideal two-photon state is a reasonably “good” single photon source.

In summary, we have described the effect of a fixed attenuator on the photon statistics of an arbitrary linear superposition of Fock states. In particular, we have demonstrated that R is not an invariant quantity under attenuation, but is instead a function of the attenuation factor α and the pre-attenuation photon statistics of the light. In fact R' is generally larger than R . As a consequence, it is important to make a distinction between the pre-attenuation value R and the post-attenuation R' .

In some sense, R is still an appropriate quantity for us to consider. By way of our measurement apparatus, we have access to only 3 components of the probability distribution for an input state of light - $\{P_0, P_1, P_2\}$ - and, at least for a coherent state, R is a function of all three. It also serves as a quick and easy way of comparing the small moments of the field for a given state to those of a weak coherent state. However, as we have seen, it is also deficient in the sense that it isn't invariant under attenuation and that it makes no consideration of higher moment field terms. It is essential, then, that when we use the quantity R as a parameter for characterization of an unknown field state that we take these

considerations into account and draw only those conclusions which are warranted based on the limitations in how R is defined.

5.4 Demonstration of Reversibility

A distinguishing aspect of the STIRAP protocol is that it is adiabatic and should therefore also be inherently reversible. Through this process, a photon emitted from one atom-cavity system A can be efficiently transferred to another atom-cavity system B . Furthermore, it should be possible to map coherent superpositions reversibly from atom to field

$$(c_0|b\rangle + c_1|a\rangle) \otimes |0\rangle \rightarrow |b\rangle \otimes (c_0|0\rangle + c_1|1\rangle), \quad (5.38)$$

and from field to atom,

$$|b\rangle \otimes (c_0|0\rangle + c_1|1\rangle) \rightarrow (c_0|b\rangle + c_1|a\rangle) \otimes |0\rangle. \quad (5.39)$$

Here $|a\rangle$ and $|b\rangle$ are atomic states and $|0\rangle$ and $|1\rangle$ are Fock states of the cavity field. Over the past decade, single-photons have been generated in diverse physical systems [90]; however, most such sources are not in principle reversible, and for those that are, no experiment prior to this had verified the reversibility of either the emission or the absorption process.

In this Section, we describe an important advance related to the interface of light and matter by explicitly demonstrating the reversible mapping of a coherent optical field to and from the hyperfine ground states of a single, trapped Cesium atom. This mapping could also be demonstrated by absorbing a single-photon state, but we use a coherent state instead because the phase information of this state allows us to verify explicitly the reversibility of the absorption process. Specifically, we map an incident coherent state with $\bar{n} = 1.1$ photons into a coherent superposition of $F = 3$ and $F = 4$ ground states with transfer efficiency $\zeta = 0.057$. Because we use a coherent state rather than a coherent superposition of $n = 0, 1$ Fock states, Equations 5.38, 5.39 only approximately describe our system. For a $\bar{n} = 0.68$ coherent state (corresponding to $\bar{n} = 1.1$ at the face of the input mirror), the

fraction of the population that lies in the $n = 0, 1$ subspace is:

$$|c_0|^2 + |c_1|^2 = (1 + \bar{n}) e^{-\bar{n}} \simeq 0.85. \quad (5.40)$$

After the initial state transfer between field and atom, we then map the stored atomic state back to a field state. The reversibility of the overall process is confirmed by observations of interference between the final field state and a reference field that is phase coherent with the original coherent state, resulting in a fringe visibility $v_a = 0.46 \pm 0.03$ for the adiabatic absorption and emission processes. We thereby provide the first verification of the fundamental primitive upon which the quantum state-transfer protocol in described in Section 5.1 is based.

We again refer to the atomic level diagram shown in Figure 5.2; the states used in the current scheme include ground state manifolds $F = 3$ and $F = 4$ and excited state manifold $F = 3'$, corresponding to the states $|g\rangle, |u\rangle, |e\rangle$ in the discussion of Section 5.2. The cavity is tuned to frequency $\omega_C = \omega_{43} + \Delta$, where ω_{43} is the frequency of the $(4 \leftrightarrow 3')$ transition, and $\Delta = (2\pi)(10 \text{ MHz})$ is the cavity-atom detuning. A linearly polarized probe beam drives the cavity at frequency ω_C with pumping strength $\lambda(t)$ and can be variably oriented along either cavity birefringent axis \hat{l}_\pm . The lattice beams are again used to drive the atom transverse to the cavity axis at frequency $\omega_A = \omega_{33} + \Delta$ to provide a classical field with Rabi frequency $\Omega_T(t)$. For the measurements described in this section, we have implemented the phase-lock between the repumper laser from which the lattice beams are derived and the probe laser (Chapter 3), so their relative detuning $\delta = \omega_A - \omega_C$ is phase-stable and equal to the ground-state hyperfine splitting, Δ_{HF} .

Our experimental procedure is as follows: after loading an atom into the FORT, we subject it to 2,000 trials lasting a total of 360 ms, where each trial consists of eight discrete measurements performed on the atom. These measurements are used to quantify the coherence of the absorption process, as well as for calibrations and background monitoring and are described in Table 5.1. After these trials, we check that the atom has survived in the trap by attempting to generate 10,000 single photons in rapid succession, which are detected by monitoring the cavity output with the two single-photon counting avalanche

Number	F_i	Ω_1	λ_1	λ_2	θ	Measurement
1	4	OFF	ON	OFF	-	incoherent absorption probability
2	4	ON	ON	OFF	-	coherent absorption probability
3	4	ON	ON	ON	θ_0	adiabatic fringe at fixed phase
4	4	ON	ON	ON	θ	adiabatic fringe at variable phase
5	3	OFF	OFF	OFF	-	generate single photon
6	4	OFF	OFF	OFF	-	check background count level
7	4	OFF	ON	ON	θ_0	incoherent fringe at fixed phase
8	4	OFF	ON	ON	θ	incoherent fringe at variable phase

Table 5.1: Table of the eight discrete measurements performed at each of the 2,000 trials carried out per atom. For each of the eight the pulse Ω_2 is ON and used to attempt photon generation at the end of the individual measurement. Each of these eight is described in more detail in the accompanying text.

photodiodes. We keep only the data from atoms that have survived all the trials as indicated by correlation with detection of a fraction of these photons. For most of the data that we keep, only a single atom is present in the trap, but occasionally two or more atoms may be loaded. From measurements performed during the 2,000 trials, we determine that at least 80% of the data presented here involve a single atom.

For each trial, we prepare the atom in $F = 4$ and then drive the system with a series of light pulses, with timing as shown in Fig. 5.5. The classical field $\Omega_T(t)$ generates pulses $\Omega_{1,2}$, and the cavity probe $\lambda(t)$ generates pulses $\lambda_{1,2}$. For any given measurement within a trial, some of these pulses are ON and the others are OFF. Pulse λ_1 is the freely propagating coherent state that is to be mapped into the atom. The strength of this pulse is set so that there are $\bar{n} = 1.1$ mode-matched photons at the face of the input mirror. Because of mirror losses [28], if no atom were present, this would give rise to a pulse inside the cavity with $\bar{n} = 0.68$ photons. The falling edge of pulse Ω_1 is used to perform the adiabatic absorption of λ_1 (as in Eq. 5.39). The intensity of the lattice light is such that when Ω_1 is fully ON, its Rabi frequency is $\sim 8\gamma$, a value found to maximize the adiabatic absorption probability.

When the λ_1 pulse is absorbed, some of the atomic population is transferred from $F = 4$ to $F = 3$. With λ_2 OFF, the pulse Ω_2 allows us to determine the fraction of the population that has been transferred: if the atom is in $F = 4$, then Ω_2 does nothing, while if the atom is in $F = 3$, then the rising edge of Ω_2 transfers it back to $F = 4$ and generates a single photon via the mapping in Eq. 5.38. Finally, with both pulses Ω_2 and λ_2 ON, we verify that λ_1 was absorbed coherently. The Ω_2 and λ_2 pulses act together to generate a field inside the cavity; if λ_1 was absorbed coherently, then the amplitude of this field will depend on the relative phase θ of λ_1 , λ_2 .

This dependence can be understood by considering a simple model in which Ω_2 and λ_2 act independently. With λ_2 OFF and Ω_2 ON, the Ω_2 pulse transfers the atom from a superposition of $F = 3, 4$ into $F = 4$ by generating a field α in the cavity whose phase depends on the phase of the atomic superposition. In turn, the phase of the original atomic superposition is set by the phase of λ_1 . With λ_2 ON and Ω_2 OFF, the λ_2 pulse generates a field β inside the cavity whose phase is set by λ_2 . If Ω_2 and λ_2 acted independently, then when both Ω_2 and λ_2 were ON, the fields α and β would combine to give a total field $\alpha + \beta$, whose amplitude depends on the phase difference θ between λ_1 and λ_2 . Because Ω_2 and λ_2 do not act independently, this model is only approximately correct. Nevertheless, the phase of the final field still depends on θ for the coherent processes associated with $\lambda_{1,2}$, $\Omega_{1,2}$.

We first consider a series of measurements which demonstrate that the λ_1 pulse transfers more population from $F = 4$ to $F = 3$ in the presence of the Ω_1 pulse than in its absence. We start with the atom in $F = 4$ and apply the λ_1 pulse, either with the Ω_1 pulse (Table 5.1, Measurement 2 - adiabatic absorption, which consists of both coherent and incoherent components) or without it (Table 5.1, Measurement 1 - only incoherent absorption ($4 \rightarrow 3'$), with spontaneous decay to $F = 3$). In either case, λ_1 transfers some population from $F = 4$ to $F = 3$. To quantify the population transfer, we apply Ω_2 and measure the probability that a single photon is detected within $1 \mu\text{s}$ of the rising edge of Ω_2 . We thereby infer the fraction of the atomic population that was in $F = 3$. This involves subtracting a background probability of 0.0025, which we determine by pumping the atom to $F = 4$ and applying Ω_2 (Table 5.1, Measurement 6), and dividing by the single photon generation efficiency of 0.036, which we determine by pumping the atom into $F = 3$ and applying Ω_2 (Table 5.1,

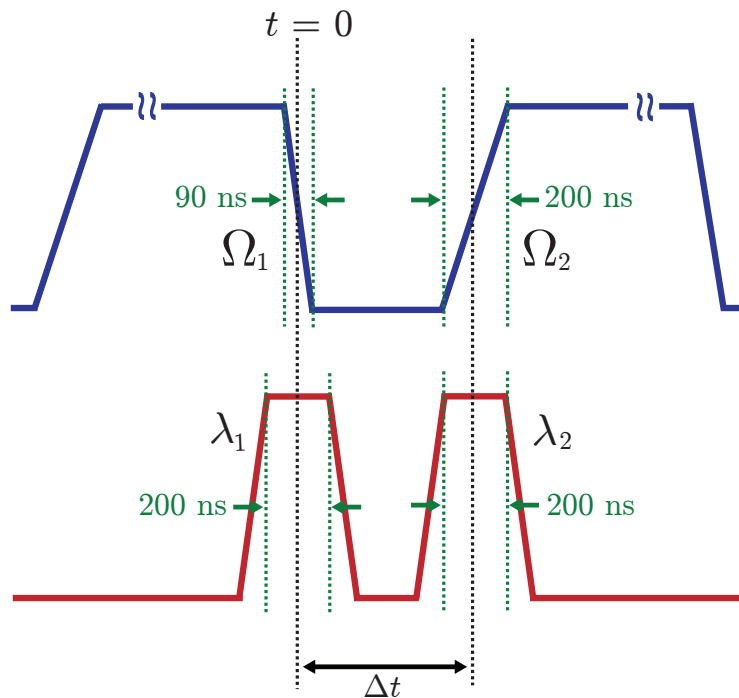


Figure 5.5: Timing diagram: the upper curve shows the Ω_1 and Ω_2 pulses; the lower curve shows the λ_1 and λ_2 pulses. Each of these pulses can be turned ON/OFF independently. Here Δt is the delay between the falling edge of Ω_1 and the rising edge of Ω_2 . By enabling various combinations of these pulses, and/or varying the relative phase θ between λ_1 and λ_2 , we perform different measurements on the atom. Pulses $\Omega_{1,2}$ and $\lambda_{1,2}$ are generated using acousto-optic modulators (AOMs); the relative phase θ between λ_1 and λ_2 is set by the phase difference of the RF pulses driving the probe AOM.

Measurement 5). For these measurements, the separation between the falling edge of Ω_1 and the rising edge of Ω_2 is $\Delta t = 290$ ns. The probe is polarized along \hat{l}_- , so that we only detect photons that are orthogonally polarized to λ_1 (where, again, we detect only light emitted along \hat{l}_+); this is important for later measurements taken with λ_2 ON in order to ensure that the emerging signal is not dominated by the component of λ_2 that is transmitted by the cavity. For adiabatic absorption (Ω_1 ON), we find that the probability p_a for the atom to be transferred from $F = 4$ to $F = 3$ by λ_1 is $p_a = 0.063 \pm 0.002$, whereas for incoherent absorption (Ω_1 OFF), the probability is $p_i = 0.046 \pm 0.001$. The ratio of the adiabatic to the

incoherent absorption probability is $r = p_a/p_i = 1.38 \pm 0.04$.

For the next group of measurements we set $\Delta t = 2 \mu\text{s}$ and polarize the probe along \hat{l}_+ , so we only detect photons which are emitted with the same polarization as λ_1 . As shown in Figure 5.6, we vary the arrival time t_1 of the λ_1 pulse and study the effect on the adiabatic-to-incoherent ratio r . This ratio is maximized when λ_1 is well-aligned with the falling edge of Ω_1 at $t = 0$ (thus enabling STIRAP). If λ_1 arrives too early ($t_1 \ll 0$), then any population that it transfers from $F = 4$ to $F = 3$ is pumped back to $F = 4$ by Ω_1 . If λ_1 arrives too late ($t_1 \gg 0$), then Ω_1 is already OFF, resulting in incoherent transfer with $r = 1$. Figure 5.6 also shows the results of a computer simulation of the absorption process. The simulation predicts values for p_a and p_i and therefore the ratio $r = p_a/p_i$. The correspondence between our simulation and the actual measurements of r vs t_1 in Figure 5.6 is qualitatively reasonable (the only free parameter in the simulation is the atom-cavity coupling g). The simulation can also be used to partition p_a into a coherent component p_a^c and an incoherent component p_a^i . We define the coherent component of r by $r^c = p_a^c/p_i$, the incoherent component of r by $r^i = p_a^i/p_i$, and plot r^c, r^i vs. t_1 in Fig. 5.6. The simulation indicates that the value of t_1 for which the adiabatic absorption process is maximally coherent is roughly the value of t_1 that maximizes the adiabatic transfer probability, and suggests that for this value of t_1 the adiabatic absorption process has appreciable coherence, with $r^c/r^i \simeq 1$.

In Figure 5.7, we present measurements that demonstrate that the adiabatic absorption process is indeed coherent. As before, we prepare the atom in $F = 4$ and apply λ_1 , either with or without Ω_1 , followed by Ω_2 . But now we add the λ_2 pulse, which overlaps with the rising edge of Ω_2 . If the λ_1 pulse is absorbed coherently, then the amplitude of the field generated by the combined action of Ω_2 and λ_2 will depend on the relative phase θ of λ_1 and λ_2 . By recording the cavity output as a function of θ and observing this dependence, we can verify that the λ_1 pulse was absorbed coherently. To accomplish this, we repeat the above sequence for different values of θ , where for each relative phase, we measure the mean number of photons $n(\theta)$ emitted from the cavity within a fixed detection window. Here we again orient the probe along \hat{l}_- and detect along \hat{l}_+ . We take data both with Ω_1 ON (Table 5.1, Measurement 4) and OFF (Table 5.1, Measurement 8), so as to obtain results $n_a(\theta)$ and

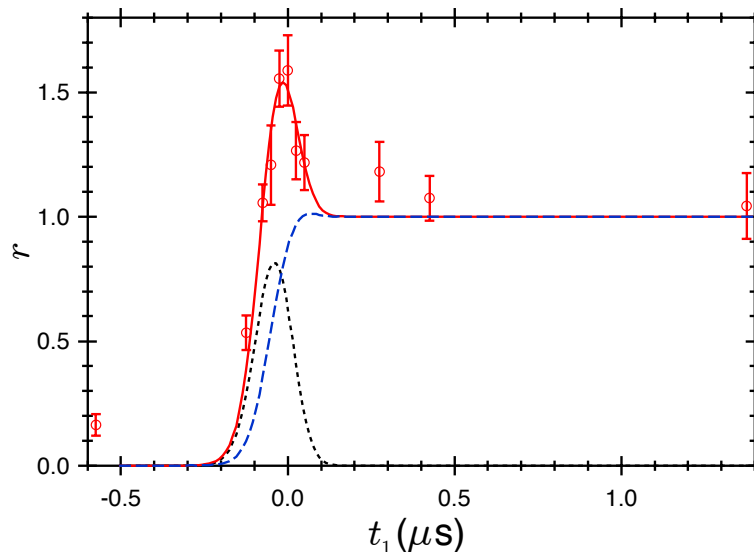


Figure 5.6: Ratio r of adiabatic transfer probability to incoherent transfer probability vs. arrival time t_1 for the incident coherent pulse λ_1 . Red data points (\circ): r versus t_1 (experiment). Red solid curve: r vs. t_1 (computer simulation). Black dotted curve: coherent component r^c vs. t_1 (simulation). Blue dashed curve: incoherent component r^i vs. t_1 (simulation).

$n_i(\theta)$ both for adiabatic and incoherent absorption. Figure 5.7 plots $R_a(\theta) = n_a(\theta)/n_a(\theta_0)$ and $R_i(\theta) = n_i(\theta)/n_i(\theta_0)$, where θ_0 is a fixed phase (Table 5.1, Measurements 3 and 7). Note that these ratios, rather than the photon numbers themselves, are employed in order to cancel small, slow drifts in the intensity of the light beams. Significantly, we observe an appreciable phase-dependence with visibility $v_a = 0.46 \pm 0.03$ for the adiabatic absorption curve $R_a(\theta)$, while no such variation is recorded for the incoherent absorption curve $R_i(\theta)$.

The fringe visibility is limited by the intrinsic incoherent component of the absorption process, as well as by the mismatch in amplitudes and pulse shapes for the α, β fields. For the results shown in Fig. 5.7, a 200 ns detection window is used around the peak of the emission process. If we increase the detection window to 1 μs , thus degrading the pulse shape overlap, the visibility drops to $v_a = 0.18 \pm 0.01$.

In conclusion, we have demonstrated the reversible transfer of a classical pulse of light to and from the internal state of a single trapped atom, which represents a significant

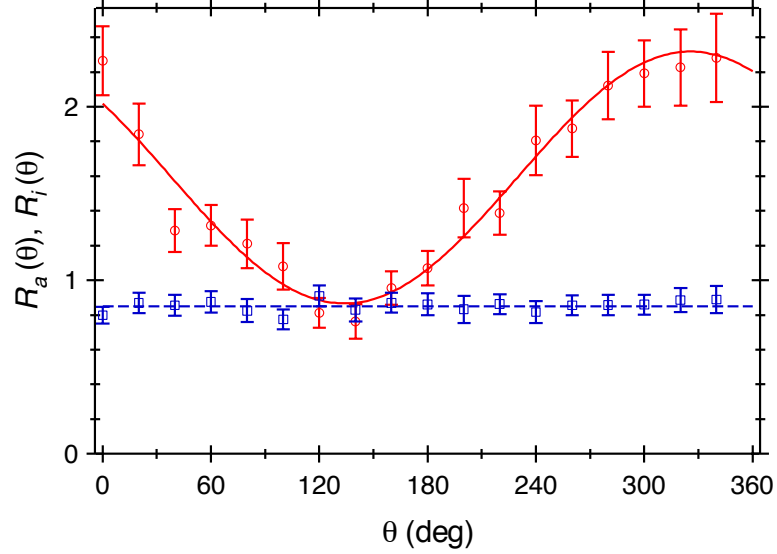


Figure 5.7: Ratios $R_a(\theta), R_i(\theta)$ for photon generation as a function of the relative phase θ between the $\lambda_{1,2}$ fields. Red data points (\circ): $R_a(\theta)$ for adiabatic state transfer with Ω_1 ON. Blue points (\square): $R_i(\theta)$ for the incoherent process with Ω_1 OFF. The full curve is a fit to obtain the fringe visibility $v_a \simeq 0.46 \pm 0.03$. These data are for a 200 ns detection window, where, on average, each point represents about 130 atoms. The error bars represent statistical fluctuations from atom to atom.

step towards the realization of quantum networks based upon interactions in cavity QED. Explicitly, we have presented a detailed investigation of the adiabatic absorption of an incident coherent state with $\bar{n} = 1.1$ photons. A fraction $p_a = 0.063$ of the atomic population has been transferred from $F = 4$ to $F = 3$, with the efficiency of the transfer being $\zeta \equiv p_a/\bar{n} = 0.057$. Here ζ provides an estimate of the efficiency that could be obtained if we adiabatically absorbed a single photon state instead of a coherent state, and should be compared to the much lower efficiencies possible in free space.

The factors that limit the transfer efficiency include the passive mirror losses [28], the fact that our cavity mirrors have equal transmission coefficients $T_1 = T_2$ (as opposed to $T_1 \gg T_2$ for a single-sided cavity), and the coupling of the atom to both polarization modes of the cavity. Even in the ideal case without scatter and absorption losses in the mirrors, for a three-level atom coupled to a two-sided cavity ($T_1 = T_2$) with two modes, the maximum

possible adiabatic transfer probability would be $\zeta = 0.25$. By implementing a single-sided cavity with losses as achieved in Reference [91], we estimate that ζ could be improved to $\zeta \sim 0.9$ for coupling schemes with a single polarization. In the longer term, a more robust method for transferring quantum states in a quantum network would be to encode states in polarization degrees of freedom rather than photon number. Thus, an important next step will be to demonstrate the mapping of polarization states of light onto Zeeman states of the atom [92].

Chapter 6

Experimental Atom-Cavity Dynamics

In Chapter 2 we described the eigenenergy spectra and temporal dynamics of simple, open atom-cavity systems for two-state atoms and one-mode cavities. We also explored how this model can be generalized to the complicated multiplicity of states associated with atomic cesium and cavities which support multiple near-degenerate modes. In this Chapter we will apply this theory to our experiment.

In contrast with the work in Chapter 5, we will begin in Section 6.1 by describing a series of measurements wherein the atom is impulsively (*i.e.*, non-adiabatically) driven. By applying a short pulse (temporal width shorter than $\Delta t_g = \pi/2g(\vec{r})$) of an optical field tuned to free-space resonance with the atom, we can deposit the system in an even superposition of its two eigenstates. This is the quantum mechanical analogue of a hammer striking one of two, coupled classical pendula. The result is an oscillation in time of the excitation imparted to the system between the atom and the cavity field. By monitoring the transmission of the cavity, we can gather an ensemble of photon arrival times which exhibit this characteristic oscillation.

Shifting from time-domain measurements to frequency-domain spectroscopy, in Section 6.2 we will briefly review measurements made in 2004 and 2005 of the characteristic vacuum Rabi spectrum for one-and-the-same atom coupled to our cavity. After this, we will also describe a series of more recent measurements wherein we are able to measure transmission spectra for ensembles of one and two atoms continuously coupled to the cavity mode.

6.1 Time-Domain Measurements

Chapter 5 outlined a series of experiments wherein photons were deterministically generated in the cavity mode by slowly and reversibly varying the Rabi frequency, Ω_T , of a classical optical field coupled directly to the atom. A feature of this STIRAP process is that as Ω_T varies, the system follows a dark state characterized by the absence of population in any atomic excited states. In order to follow this dark state, $\Omega_T(t)$ must vary slowly enough to satisfy the adiabaticity condition:

$$|\dot{\Omega}_T(t)| \lesssim g_0^2, \quad (6.1)$$

where g_0 is the maximal rate of atom-cavity coupling. By taking advantage of the dark state we ensure that the process remains coherent and suffers no dephasing due to spontaneous emission. However, by adiabatically eliminating the atomic excited state we also preclude the system from undergoing evolution as described by the Jaynes-Cummings Hamiltonian. While STIRAP relies explicitly upon strong atom-field coupling, the photon generation mechanism is itself a Raman process and does not exhibit the “hallmark” dynamics of strong coupling cavity QED.

In this section we will explore the complimentary parameter regime, wherein the classical field impulsively (*i.e.*, non-adiabatically) excites the atom. By driving it with a sufficiently short classical pulse, we can populate the excited state of the atom much faster than any other process affecting the system (coherent or incoherent). In the limit of a pulse with a delta function envelope at time t_0 , we can model the effect of a field of the proper strength as instantaneously changing the state of the system:

$$|\psi(t)\rangle = |g, 0\rangle \quad (t < t_0) \quad \longrightarrow \quad |\psi(t_0)\rangle = |e, 0\rangle \quad (6.2)$$

after which the state is left to evolve freely in time. Recall that in Chapter 2 we used the quantum master equation approach to explore this circumstance for a two-state atom and a one-mode cavity which led to Equation (2.58), an expression for the intracavity photon number n at zero atom-cavity detuning as a function of $t' = (t - t_0)$, the amount of time

after the atom was initially excited. We can generalize this formula to the case of arbitrary atom-cavity detuning Δ_{AC} :

$$n(t') = e^{-(\kappa+\gamma)t'} \frac{g^2(\vec{r})}{g_E^2(\vec{r})} \sin^2 [g_E(\vec{r})t'] \quad (6.3)$$

where $g_E(\vec{r})$ is the “effective” vacuum Rabi frequency:

$$g_E(\vec{r}) \equiv \sqrt{\frac{1}{4}(\gamma - \kappa - i\Delta_{AC})^2 + g^2(\vec{r})}. \quad (6.4)$$

In short, because our system is in the regime of strong coupling, we expect the intracavity photon number to undergo vacuum Rabi oscillation which should manifest itself in photodetection of the field emitted from the cavity following the impulse.

For real, experimental pulses, $\Omega_T(t)$, of finite duration we also need to consider how the system evolves during the short period of time during which the impulse is still driving the atom and yet the atom-cavity dynamics are also beginning to manifest themselves. In order to quantify the effect of the finite temporal width of the impulse we can add an interaction term to the system Hamiltonian:

$$\hat{H}_I(t) = \hbar\Omega_T(t)(|e\rangle\langle g| + |g\rangle\langle e|). \quad (6.5)$$

With this term included in the Liouvillian along with the full, time-dependent form of $\Omega_T(t)$, numerical integration of the full master equation allows us to determine the state of the intracavity field as a function of time. In the Subsection 6.1.2 we will use this approach to model the dynamics of the full state space of the cesium $D2$ line coupled to a birefringent cavity and under what circumstances this model agrees with data obtained in the laboratory. First, however, the following Subsection will describe how we generate short pulses $\Omega_T(t)$ in the laboratory and introduce our experimental protocol for measuring this effect.

6.1.1 Resonant Vacuum Rabi Oscillation

In this Subsection we describe the experimental observation of vacuum Rabi oscillation in the time domain for one atom strongly coupled to a cavity at nominal zero atom-cavity

detuning, $\Delta_{AC} = 0$. The oscillation manifests itself in the temporal wave packet of photons generated in the cavity mode from an atom which has been excited by a fast pulses of resonant laser light. The shape of this wave packet is reconstructed by histogramming the detection times of photodetection events in the cavity output mode. By averaging over a physically reasonable distribution of values for $g(\vec{r})$ and numerically integrating the quantum master equation for the system we are able to model the shape of the wave packet.

This work follows the publication of a set of similar measurements made by the group of G. Rempe at MPQ Garching for single rubidium atoms in a cavity with characteristic parameters $(g_0, \kappa, \gamma) = (2\pi)(5.0, 2.7, 3.0)$ MHz [93, 94]. These parameters sit marginally inside of the regime of strong-coupling and therefore prohibit the direct observation of vacuum Rabi oscillation on resonance. However Rempe's group is still able to infer the effective vacuum Rabi frequency near resonance by measuring the characteristic narrowing of the photon wave packet which manifests itself even in when the system is not deep within the strong coupling regime. Also, by introducing a fixed atom-cavity detuning, they are able to increase the *effective* Rabi frequency and thereby recover the oscillatory character of the wave form. In contrast with the work of the Garching group, we are able to clearly resolve Rabi oscillation at zero atom-cavity detuning because our system is deep within the regime of strong coupling.

In order to observe this effect, the length of the physics cavity was tuned into resonance with the free space ($4 \leftrightarrow 5'$) transition. This transition exhibits the largest rate of coherent coupling in the $D2$ manifold (see Table 3.2) and is therefore most likely to exhibit prominent vacuum Rabi oscillation. For this configuration, the parameters of our system are $(g_0, \kappa, \gamma) = (2\pi)(33.7, 3.9, 2.6)$ MHz, where g_0 is given for the ($|4, 4\rangle \leftrightarrow |5', 5\rangle$) transition in the atom. The depth of the FORT is set to $U_0/h \approx 45$ MHz. For the work described in this Section the static magnetic field is nulled to the level of ~ 40 mG at the cavity center. As usual, we have a polarizing beamsplitter cube at the cavity output which is oriented such that we detect only cavity emission from the higher-frequency birefringent mode.

The field corresponding to the classical pulses $\Omega_T(t)$ is derived from the master laser and shifted by acousto-optic modulation into free space resonance with the ($4 \leftrightarrow 5'$) transition. This light is coupled through an EO Space brand fiber-coupled integrated electro-optic

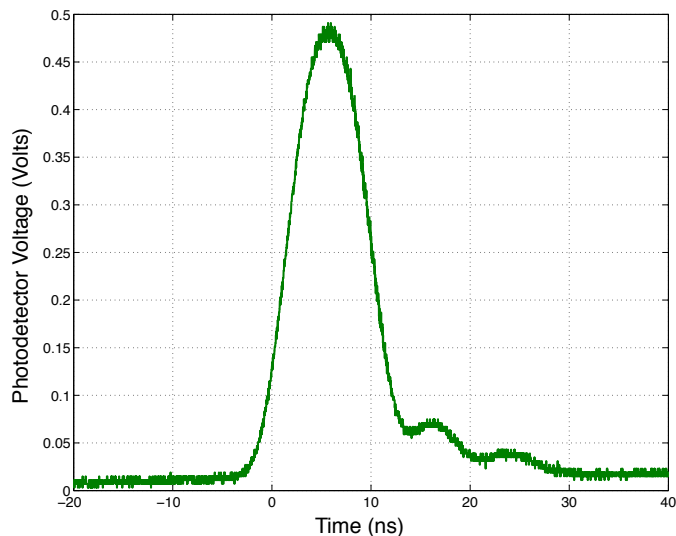


Figure 6.1: Measured photodetector voltage into 50Ω versus time for $\Omega_T(t)$ pulses generated using an EO Space MZIS as described in the text.

Mach-Zehnder interferometric switch (MZIS). This device consists of a fiber-coupled waveguide configured as a two-arm Mach-Zehnder interferometer. A lithium niobate electro-optic element is integrated into one of the two arms such that the phase shift induced by the EO will intensity modulate the transmitted light. The MZIS has two electronic input ports which control the voltage across the crystal: the first is a DC bias connector which allows the user to introduce a static electro-optic phase shift to light passing through the active element and the second is an 50Ω impedance RF-connector which permits broadband phase modulation with a bandwidth exceeding 10 GHz.

A constant reference voltage $V_\pi \approx 2.3 \text{ V}$ is applied to the DC port in order to maximally extinguish transmission in the absence of an RF input signal and the MZIS has been integrated into a temperature-servoed monolithic copper heatsink in order to eliminate slow thermal phase shifts. For a properly polarized input field, the MZIS offers a maximum extinction ratio of 1 : 250 at DC. The optical pulses with which we drive the atom are generated by feeding a nominal square pulse of width $\tau_T = 10 \text{ ns}$ and amplitude $V_T = 4.0 \text{ V}$ into the RF port of the MZIS. The resulting optical waveform was measured on an amplified photodetector with 150 MHz of gain bandwidth; the photocurrent through 50Ω is shown

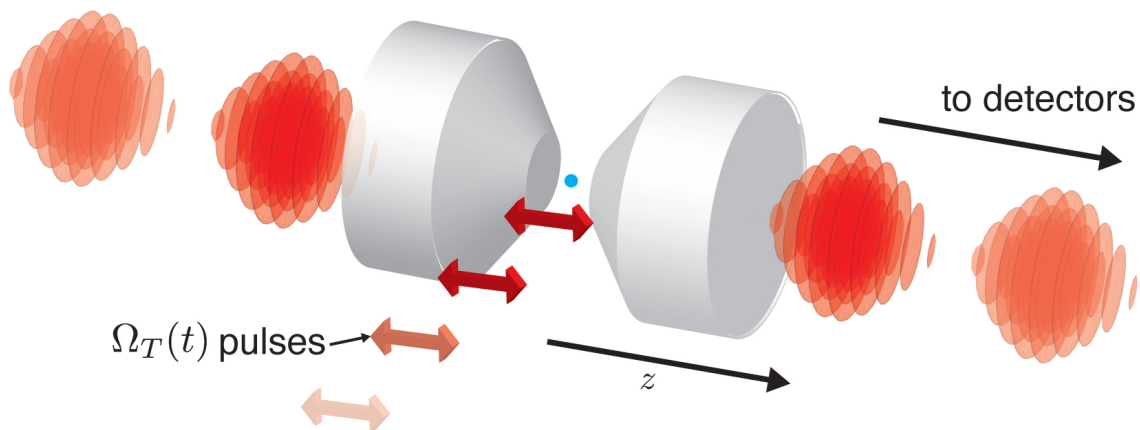


Figure 6.2: Schematic diagram of the experiment. The classical pulses $\Omega_T(t)$ are polarized along the \hat{z} -axis by a polarizing beamsplitter cube and impinge upon trapped atoms at the cavity center. Cavity emission is collected from the output mirror and directed into the detection path.

in Figure 6.1. The small oscillation on the falling edge of the pulse is likely due to a slight electrical impedance mismatch into the RF port of the MZIS. The short electronic pulses which are fed into the EO are derived from an SRS DG535 delay generator which is externally triggered by TTL-level pulses from the ADWin Gold. The same pulse used to trigger the DG535 is also used to trigger acquisition of data by the P7888 counting card in order to reference each pulse with respect to the photodetection events to which it corresponds.

The EO Space MZIS devices we use offer very low switching voltages by integrating the electro-optic crystal into micron-scale optical waveguides. As a result, the optical intensities inside of the waveguide can be large enough to induce photorefractive damage in the crystal at even modest input powers. The manufacturer recommendation is to not exceed 5 mW CW through the device and we have generally abided by that limit. The optical loss associated with propagation through an MZIS which is voltage biased for high-transmission is on the order of 2.5 dB. This means that the peak optical power we can expect in a pulse generated using the these devices is ~ 2.5 mW.

The pulses generated by the MZIS are coupled from fiber to free-space where they are polarized along the \hat{z} -axis (*i.e.*, along the cavity axis) by a polarizing beamsplitter cube

(Figure 6.2). The path which this light follows is that of the “unbalanced” side beam described in Section 3.5.2. For typical input power to the MZIS and the focal properties of the path which steers that beam to the cavity we anticipate that the peak optical intensity of $\Omega_T(t)$ is $\max[I_T(t)] \sim 1500I_{sat}$ which corresponds to $\max[\Omega_T(t)] \sim (2\pi)(35 \text{ MHz})$ for the $(|4, 4\rangle \leftrightarrow |5', 5\rangle)$ transition. During the finite duration of the pulse, the effect of $\Omega_T(t)$ is to induce Rabi oscillation of atomic population between the $F = 4$ ground state and the $F = 5'$ excited state. Ultimately, the probability with which the atom will be deposited in the cavity-coupled excited state is a function of the “area” under the pulse envelope (*i.e.*, the total, integrated energy contained within each pulse). However, as described in Chapter 3, the cavity aperture is sufficiently narrow that beams of this sort suffer significant near-field diffraction. In practice, as we average over many measurements involving atoms which are trapped in spatially distinct FORT wells, each atom will couple to the classical field with a unique Rabi frequency $\Omega_T(\vec{r}, t)$ (now written to emphasize the spatial as well as temporal dependence). In the next Subsection we will model what implications this averaging effect might have on the shape of the wave packet emitted from the cavity mode and on the dynamics of the system as a whole.

Following each attempt to load an atom into the FORT potential, we perform 100 experimental cycles each comprised of a set of trials. The cycles begin by optically pumping the atom into a random initial Zeeman state in the $F = 4$ ground state manifold using the $(3 \leftrightarrow 3')$ lattice beams. After the initial optical pumping phase, we perform 1×10^3 trials, each consisting of a trigger pulse sent to the DG535 which drives the MZIS. These trigger pulses (and the trials) are separated in time by $\Delta t = 4 \mu\text{s}$ (rate-limited by the trigger reset delay of the DG535). At the beginning of each trial, a pulse is sent to trigger both the DG535 and to the “start” channel of the P7888 counting card in order to correlate subsequent photodetections with the rising edge of $\Omega_T(t)$. After the full set of trials is complete, we begin a new cycle and again optically pump the atom into $F = 4$. The reason for these interleaved optical pumping intervals is to prevent the atom from off-resonantly scattering into the decoupled $F = 3$ ground state manifold. Note that for this set of measurements we have elected not to employ the incoherent Raman optical pumping technique of Section 4.5 (or any other Zeeman-selective state preparation protocol) simply because doing so would

reduce the duty cycle per-trial by more than a factor of 1×10^4 . Motivated by our relatively small efficiency for measuring cavity emission we have instead elected to acquire data at a higher rate at the expense of averaging over atom-cavity coupling constants and FORT-induced AC Stark shifts for each transition within the $F = 4$ manifold. In Section 6.1.4 we will describe a similar set of measurements but with a Zeeman-state selective initialization protocol.

Data analysis is carried out by selecting only photodetection events which fall within a small window ($\Delta t_{win} = 60$ ns) following the rising edge of $\Omega(t)_T$ (as gated by events registered on channel C of the P7888). If, following either the beginning of the first cycle or any subsequent photodetection event within the detection window, there are no other properly-windowed photodetection events in the next 2×10^3 trials then there is presumed to be no atom present in the cavity mode. Should it be determined that there is no atom present in the cavity at any point during the first 4×10^3 trials following a loading attempt then all data from that loading attempt is classified as containing no atom. By contrast, if the presence of an atom is verified throughout those first 4×10^3 trials then data taken during that loading attempt (and for which the continued presence of an atom is verified) is classified as corresponding to the presence of an atom in the cavity. We can then time histogram or otherwise analyze the “atom present” photodetection events during the windowed interval in order to extract photon statistics, temporal wave packet shapes or another accessible observable which we might have interest in. The results shown in Subsection 6.1.3 are obtained in this manner.

6.1.2 Numerical Simulation

Before we discuss any experimental results, it is useful to briefly describe the theoretical model which we will use to interpret the data. As mentioned earlier in the Chapter, the approach we will take is to model the time evolution of the density matrix for the full atom-cavity system by numerical integration of the master equation. This model is formulated using the Quantum Optics Toolbox (QOT) package for MATLAB as described in Appendix C. Within the context of the simulation we will write the density matrix in terms of tensor product states in the $|F, m_F, n_a, n_b\rangle$ basis where $F \in \{4, 5'\}$ and with the quantization

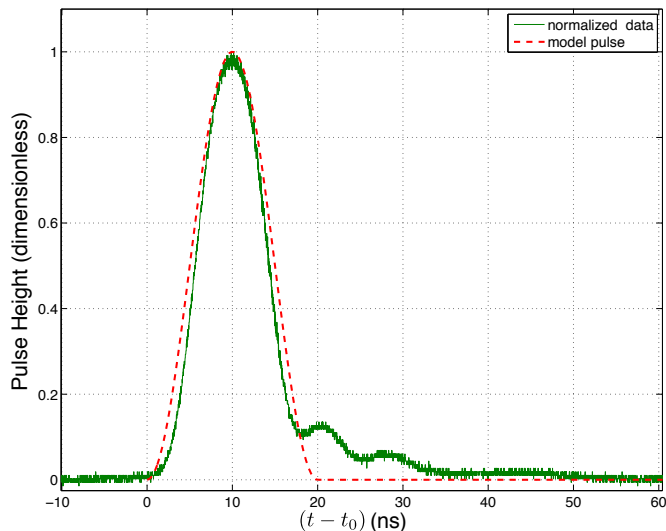


Figure 6.3: Shape of the model impulse function $A(t)$ (dashed) as compared to the normalized photodetector voltage for the physical pulses generated by the MZIS (solid, same as Figure 6.2).

direction specified along the cavity axis. The states $|n_a\rangle$ ($|n_b\rangle$) represent the Fock states of the higher (lower) frequency birefringent cavity mode which is presumed to be oriented along the \hat{x} (\hat{y})-axis. In order to restrict the Hilbert space associated with this calculation to a size compatible with the memory handling capabilities of the laboratory computers, we truncate the basis of cavity Fock states in both modes to $(n_a, n_b) \in \{0, 1, 2\}$. This is a reasonable assumption in the weak-driving limit where the contribution to the total intracavity field from states with $n_{a,b} \geq 3$ is typically less than 0.01%.

Pulse Shape

The model Hamiltonian for the system includes many of the relevant experimental parameters described in Chapters 2 and 3. These include the Zeeman state-dependent FORT-induced AC Stark shifts (and associated atom-cavity detunings), state-dependent rates of atom-cavity coupling and the cavity birefringent frequency splitting. Additionally, the Hamiltonian includes an explicitly time-dependent term corresponding to the classical field $\Omega_T(t)$ where the shape of the impulse is approximated by the QOT pulse function. The

envelope of $\Omega_T(t)$ thereby takes the form:

$$\Omega_T(t) = \Omega_0 A(t) \quad (6.6)$$

where $A(t)$ is given by:

$$A(t) = A_1(t)A_2(t) \quad (6.7)$$

$$A_1(t) = \begin{cases} 0 & (t < [t_1 - \frac{1}{2}\tau_r]) \\ \frac{1}{2} [1 + \sin(\pi[t - t_1]/\tau_r)] & (|t - t_1| \leq \frac{1}{2}\tau_r) \\ 1 & t > [t_1 + \frac{1}{2}\tau_r] \end{cases} \quad (6.8)$$

$$A_2(t) = \begin{cases} 1 & (t < [t_2 - \frac{1}{2}\tau_r]) \\ \frac{1}{2} [1 - \sin(\pi[t - t_2]/\tau_r)] & (|t - t_2| \leq \frac{1}{2}\tau_r) \\ 0 & t > [t_2 + \frac{1}{2}\tau_r] \end{cases} \quad (6.9)$$

This is a pulse with rise and fall times given by τ_r and start (stop) times given by t_1 (t_2). In order to model the pulse shown in Figure 6.1 we use the parameters $\tau_r = 10$ ns, $t_1 = 5$ ns and $t_2 = 15$ ns ($t_0 = 0$ corresponds to the beginning of the simulation). In Figure 6.3 the normalized photocurrent measured for MZIS-generated pulses is plotted in comparison with $A(t)$.

Initial Atomic State

Recall that the polarization of the classical Ω_T field is oriented along the quantization axis specified in our model. As such, this field drives $\Delta m_F = 0$ transitions in this basis. We therefore expect that if we could prepare the atom in a single Zeeman state, $|\psi(t_0)\rangle = |4, m_F\rangle$, that the fraction of the population transferred to $|5', m_F\rangle$ should depend on the integrated energy in the pulse and the dimensionless dipole moment for the ($|4, m_F\rangle \leftrightarrow |5', m_F\rangle$) transition (Appendix A). Likewise, we expect the branching ratio from excited states $|5, m_F\rangle$ via emission into the cavity mode to ground states $|4, m_F \pm 1\rangle$ (as well as the rates of atom-cavity coupling, g , for this process) to also be a function of the dimensionless dipole matrix elements. These expectations are clearly in agreement with our model as borne out in the top

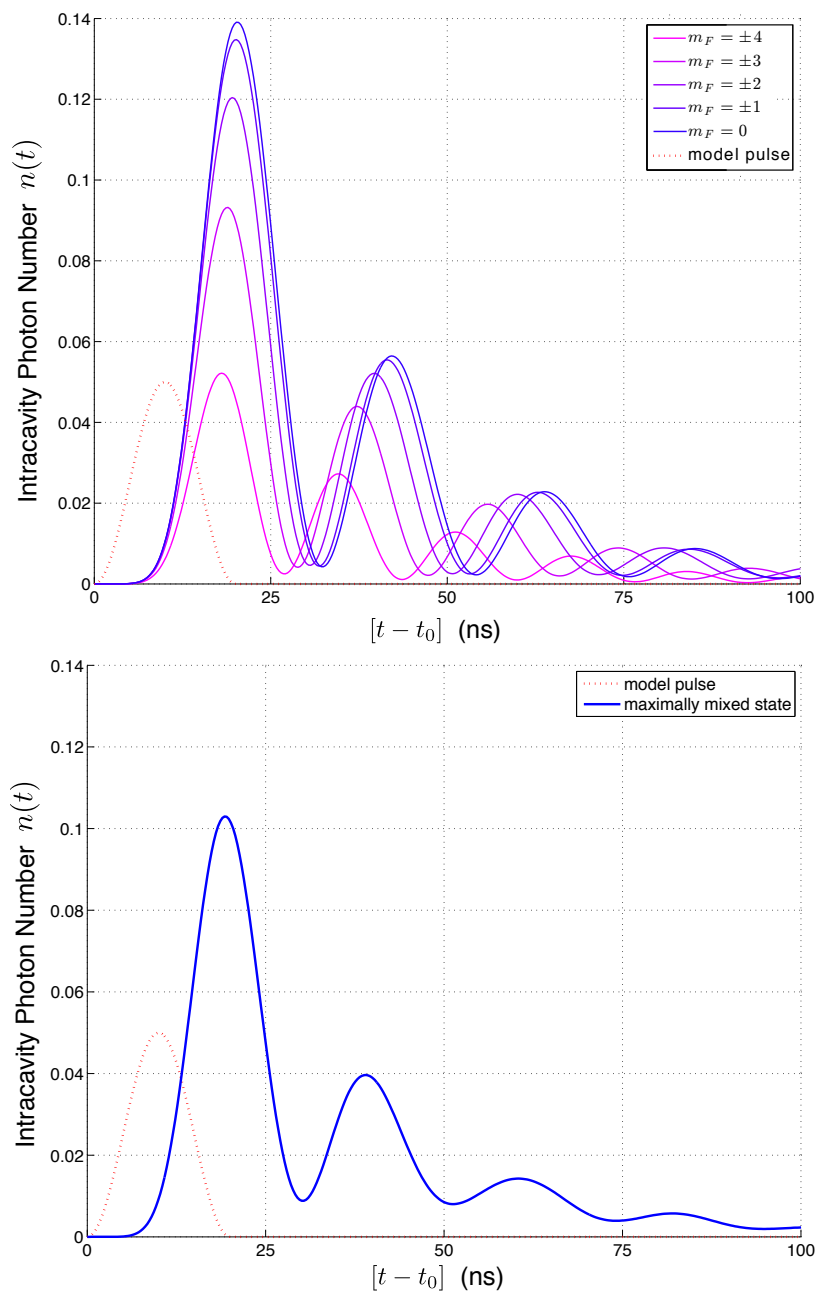


Figure 6.4: Intracavity photon number in the higher-frequency cavity mode as a function of time following an impulse of magnitude $\Omega_0 = (2\pi)(35 \text{ MHz})$ for (top) an atom prepared in a well-defined initial Zeeman state $|F, m_F\rangle$ with respect to the quantization axis and (bottom) an atom prepared in the maximally mixed state. For reference, the model pulse $A(t)$ is plotted as well (with arbitrary amplitude).

panel of Figure 6.4 where we have plotted $n(t) = \langle \hat{a}^\dagger \hat{a} \rangle = \text{Tr}(\hat{a}^\dagger \hat{a} \hat{\rho}(t))$, the time-dependent intracavity photon number in the higher-frequency mode of the cavity as predicted by integration of the master equation. This model includes an impulse of associated Rabi frequency $\Omega_T(t) = (2\pi)(35 \text{ MHz})A(t)$ and assumes maximal atom-cavity coupling such that for the edge state cycling transitions, $g_0 = (2\pi)(33.7 \text{ MHz})$. The five traces in this plot correspond to preparation of the system in the states $|\psi(t_0)\rangle = \{|4, 0\rangle, |4, \pm 1\rangle, |4, \pm 2\rangle, |4, \pm 3\rangle, |4, \pm 4\rangle\}$ (due to the symmetries inherent to the model, we obtain approximately equal results for both states $|\psi(t_0)\rangle = |4, \pm m_F\rangle$).

The first thing to take note of is that regardless of initial state we predict unambiguous vacuum Rabi nutation in $n(t)$. Also, the magnitude of the intracavity field is dependent on the initial state of the system in a way which agrees with the scaling of dimensionless dipole moments for π -polarized light on this transition (starting with $m_F = 0$ the dipole moments grow smaller as we move towards the edge states). Smaller dipole moments mean smaller Rabi frequencies for those transitions to which the classical impulse couples and therefore, in the limit of weak driving, less excitation deposited in the system. Finally, the frequency of the damped oscillation in $n(t)$ is larger towards the atomic edge states where the dipole moments for coupling to σ^\pm -polarized fields (those polarizations which the cavity supports) are largest.

As mentioned earlier, for this set of experiments there is no magnetic bias field applied to the system and therefore no efficient protocol for Zeeman state preparation. Instead we will assume that the initial atomic state is the maximally mixed state comprised of Zeeman substates within the $F = 4$ ground state manifold:

$$\hat{\rho}_A(t_0) = \frac{1}{9} \sum_{m_F=-4}^4 |4, m_F\rangle \langle 4, m_F|. \quad (6.10)$$

In the bottom panel of Figure 6.4 we have plotted $n(t)$ for an atom initially prepared in this state. Although this is essentially the incoherent sum of the traces from the upper panel, vacuum Rabi oscillation is still clearly visible. We do note, however, that after the first full cycle of the oscillation there is significant dephasing and a reduction in contrast. Given the cavity linewidth, $\kappa = (2\pi)(3.8 \text{ MHz})$, and the total detection efficiency for an intracavity

field, $\alpha = 0.086$, we can use this calculation to infer the total probability to experimentally register a single photodetection event in the $\Delta t_{win} = 60$ ns interval following the impulse:

$$P_1 = 2\kappa\alpha\delta t \sum_{t'=t_i}^{t_i+\Delta t_{win}} n(t', \delta t). \quad (6.11)$$

Here δt is the time interval used to carry out the numerical integration and $t_i \equiv t_0 + t_1 + \tau_r$ is the time at which $\Omega_T(t_i) = \max[\Omega_T(t)]$. For the parameters of the bottom trace in Figure 6.4 and experimental parameters presented in Chapter 3 we calculate $P_1 = 0.0070$.

Averaging Effects

In the previous Subsection we alluded to the necessity for ensemble averaging over both the range of accessible classical Rabi frequencies Ω_0 due to diffraction of the side beam by the cavity aperture and the range of accessible atom-cavity coupling rates $g(\vec{r})$ for atoms in different FORT wells and at different temperatures. In a very simple approximation where we do not consider temperature, the positions z_q where atoms might be located are the intensity maxima of the FORT:

$$z_q = \frac{\lambda_F}{2}(2q+1) - \frac{L}{2}, \quad (1 \leq q \leq 90) \quad (6.12)$$

where the cavity mirrors are located at $z = \pm L/2$. Atoms located at z_q will couple to the impulse with maximum Rabi frequency

$$\Omega'_0(z) = \Omega_0 \sqrt{\frac{I(z_q)}{I_0}} \quad (6.13)$$

where $I(z)$ is the distribution of side beam intensities approximated by Equation (3.56) and $I_0 \equiv \max[I(z)]$. From Equation (3.51) we know that atom-cavity coupling rate at z_q is given by:

$$g(0, 0, z_q) = g_0 \left| \cos \left(\pi \frac{(2q+1)}{2} \frac{\lambda_F}{\lambda_{D2}} \right) \right|. \quad (6.14)$$

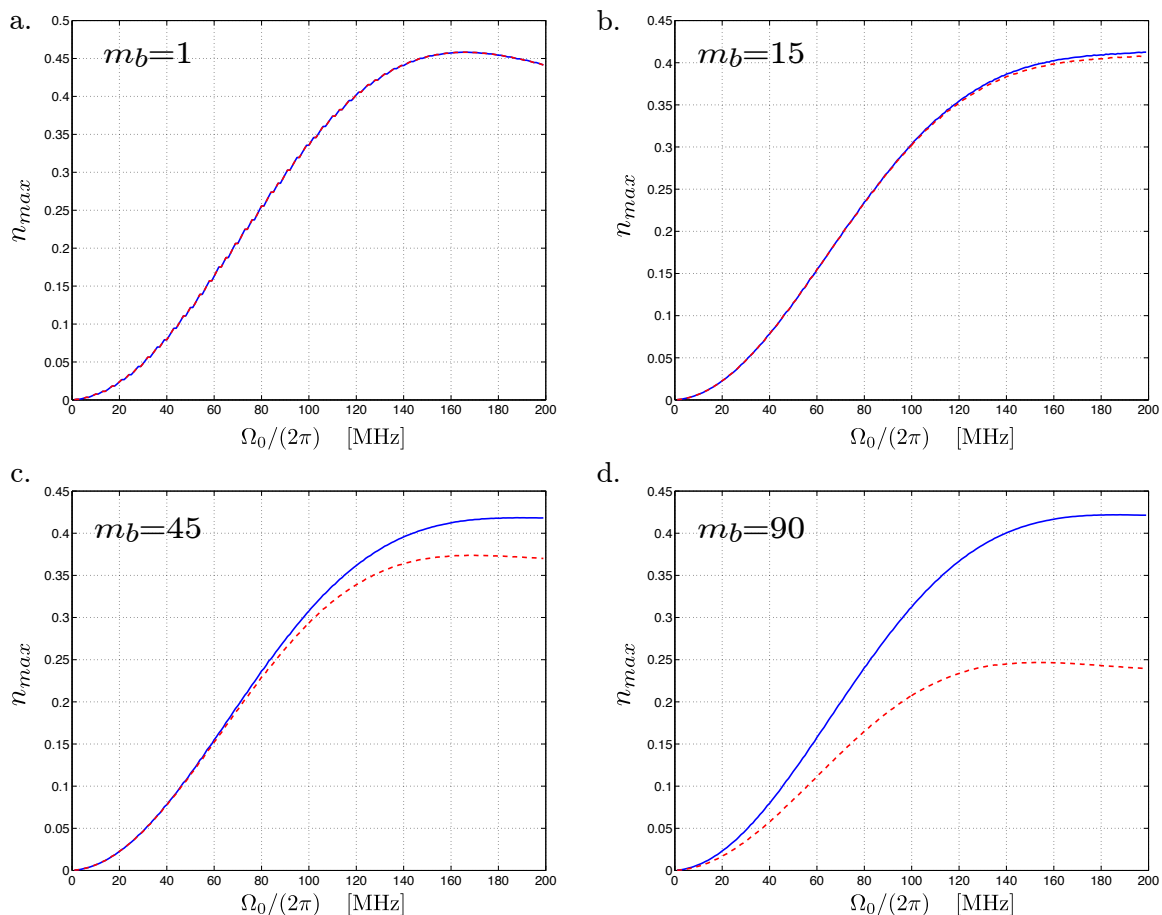


Figure 6.5: Calculated maximum intracavity photon number in the higher-frequency birefringent mode, n_{max} , as a function of maximum classical pulse Rabi frequency, Ω_0 for averaging over the best-coupled a. $m_b = 1$, b. $m_b = 15$, c. $m_b = 45$, and d. $m_b = 90$ FORT wells. The solid blue traces represent an average involving only $\Omega'_0(z_q)$ and uniform, maximal atom-field coupling $g(\vec{r}) = g_0$. The dashed red traces are for averaging over both $\Omega'_0(z_q)$ and $g(\vec{r}) = g(0, 0, z_q)$.

As we will see, the principle effect of ensemble averaging over the accessible Ω_0 is to diminish the probability with which an excitation will be deposited in the cavity mode following the impulse and to average away any coherent dynamics between the impulse and the atom (when the system is in the strong-coupling regime). The dominant effect associated with averaging over the range of accessible $g(\vec{r})$ is to dephase the optical Rabi nutation (when the impulse is weakly driving the atom).

Figure 6.5 shows calculations of the maximum intracavity photon number in the higher-frequency birefringent cavity mode (*i.e.*, $n_{max}(\Omega_0) \equiv \max[n(t, \Omega_0)]$) as a function of the maximum Rabi frequency Ω_0 experienced by the atom during the impulse under different averaging conditions. We choose to consider $n_{max}(\Omega_0)$ because, first, it is proportional to the signal which we will collect in the laboratory and, second, it is a good measure of the probability that the impulse will introduce an excitation to the system and that this excitation will propagate from the atom to the cavity mode via QED. The red (dashed) traces in each of the four panels correspond to averaging over the values of $\{\Omega'_0(z_q), g(0, 0, z_q)\}$ for the $m_b \in \{1, 15, 45, 90\}$ “best-coupled” FORT wells. These are the m_b wells for which $g(0, 0, z_q)$ is largest. These curves were obtained by finding n_{max} at each z_q for atoms coupled to the cavity at rate $g(0, 0, z_q)$ and to the classical impulse at frequency $\Omega'_0(z_q)$. We then simply average the resulting n_{max} assuming the atom can be located in any of the m_b locations with equal probability. The blue (solid) curve in each panel is for comparison and involves averaging over only $\Omega'_0(z_q)$ with the atom-cavity coupling rate held maximal and constant, $g(\vec{r}) = g_0$. This separation is somewhat contrived but allows us to quantify the significance of averaging over atom-cavity coupling rates with respect to the the probability for an excited atom to deposit that excitation in the cavity mode (as opposed to averaging over $\Omega'_0(z_q)$, which primarily affects the probability with which the atom will be excited in the first place).

Despite differences in the amplitudes of these curves, the shapes are relatively uniform. Initially, as Ω_0 is increased from zero, the classical impulse has the effect of exciting the atom with increasing probability. After a brief transient, the system enters a linear regime wherein the Rabi frequency of the impulse is roughly proportional to the probability that a photon will be deposited in the mode of the cavity. In the limit of large Ω_0 , the curve

rolls off and the probability to excite the system becomes roughly constant. To understand this effect, consider the the case where the atom is prepared in one, well-defined Zeeman state and the classical pulses couple to the atom with a single maximum Rabi frequency. Here we would expect that in the “saturation” regime, we will continue to observe coherent dynamics - the atom would undergo Rabi oscillation induced by the impulse at the same time that the QED system is undergoing vacuum Rabi nutation. Indeed, for the trace corresponding to $m_b = 1$ (where we consider only one atom-field coupling rate and one value of $\Omega'_0(z_q)$), we continue to see structure even at large Ω_0 (which is complicated due to the initial mixed state of the atom). As we include more values of $\Omega'_0(z_q)$ in the average, however, the atom-impulse portion of the coupled oscillation begins to dephase. Just as in Chapter 4 where dephasing in our cavity-based Raman scheme lead to the Raman pair depositing the system at random in one coupled state or the other, we see a similar effect here. For an average over a large range of values $\Omega'_0(z_q)$, the impulse excites the system with some uniform probability (and, as we will see later, begins decohering the QED dynamics as well).

We can also compare the red and blue traces in each panel of Figure 6.5 with an eye towards determining the circumstances under which it is necessary to perform averaging over both position-dependent quantities. Recall that in the red curves we are considering both $g(\vec{r})$ and $\Omega'_0(z_q)$ while for the blue we are holding $g(\vec{r}) = g_0$ constant and averaging only the impulse strength. Panel 6.5a corresponds to the single-best coupled FORT well and not surprisingly the two curves overlap. However as we introduce more wells we begin to see the effect which averaging the atom-field coupling rate has on the probability to introduce an excitation into the cavity mode following excitation of the atom. For each m_b we have $g_{max} \geq g(\vec{r}) > g_{min}$ ($m_b = 15$: $[g_{max}, g_{min}] = (2\pi)[33.7, 32.6]$ MHz; $m_b = 45$: $[g_{max}, g_{min}] = (2\pi)[33.7, 24.6]$ MHz; $m_b = 90$: $[g_{max}, g_{min}] = (2\pi)[33.7, 0.2]$ MHz). As long as the full range of values $g(\vec{r})$ which are being included in the sum still satisfy the strong coupling criteria then there is a significantly increased probability that an excited atom will deposit that excitation in the cavity mode as opposed to decaying into free space (as discussed in Chapter 2). This is particularly true in the limit of weak driving (small Ω_0) where we can closely approximate $n_{max}(\Omega_0)$ by its value when $g(\vec{r})$ is held constant at g_0 .

However as we begin averaging over z_q which offer only weak coupling between atom and cavity, the importance of averaging over $g(\vec{r})$ becomes more pronounced.

We can also explore the effect of averaging on the shape (as opposed to the maximum value) of $n(t)$. In order to do this, we will consider values of z_q for $m_b = 45$. In past work, we have empirically observed (*c.f.*, [41]) that atoms tend to survive a significant number of experimental trials in the FORT only at positions z_q which correspond to large atom-cavity coupling (this will also become clear from the data described in the next Subsection). Typically we expect $m_b \sim 45$ will correspond to laboratory data. Over a range of Ω_0 we calculate the intracavity photon number as a function of time, $n(t)$, which is then normalized with respect to its maximum, n_{max} :

$$n'(t, \Omega_0) = \frac{n(t, \Omega_0)}{n_{max}(\Omega_0)}. \quad (6.15)$$

The result, $n'(t)$, allows us to directly compare the shapes of wave packets at different Ω_0 . The upper panel of Figure 6.6 shows a colormap of $n'(t, \Omega_0)$ versus $(t - t_0)$ and Ω_0 for an average over $g(0, 0, z_q)$ and $\Omega'_0(z_q)$. Notice that the shape of $n'(t, \Omega_0)$ changes abruptly near the values of Ω_0 where we predicted saturation phenomena, above. In order to quantify the dependence of n' on the impulse Rabi frequency we can make cuts through the data at times $t_a = 32.7$ ns (dashed red line) and $t_b = 41.8$ ns (dashed green line), which roughly correspond (in the limit of weak driving) to the minimum of the first trough and the maximum of the second peak of the oscillation, respectively. In the bottom panel of Figure 6.6 we plot $n(t_a, \Omega_0)$ and $n(t_b, \Omega_0)$ (omitting data at very small Ω_0 which exhibit artifacts of error in the numerical integration routine). Over the full range of Ω_0 there is nearly a factor of 3 change in $n(t_a, \Omega_0)$ and less than a $\sim 10\%$ change in $n(t_b, \Omega_0)$. However if we confine ourselves to the limit of small Ω_0 , we can expect only small changes to the shape of the pulse emitted from the cavity (and principally at the location of the first trough in the oscillation of the wave packet) as we vary the impulse Rabi frequency. As we will see later in this Subsection, the dominant contribution to dephasing of the vacuum Rabi oscillation in the limit of weak driving is averaging over multiple values of $g(\vec{r})$ and not $\Omega'_0(z)$.

The reason for this lengthy exposition on how we expect ensemble averaging to affect our

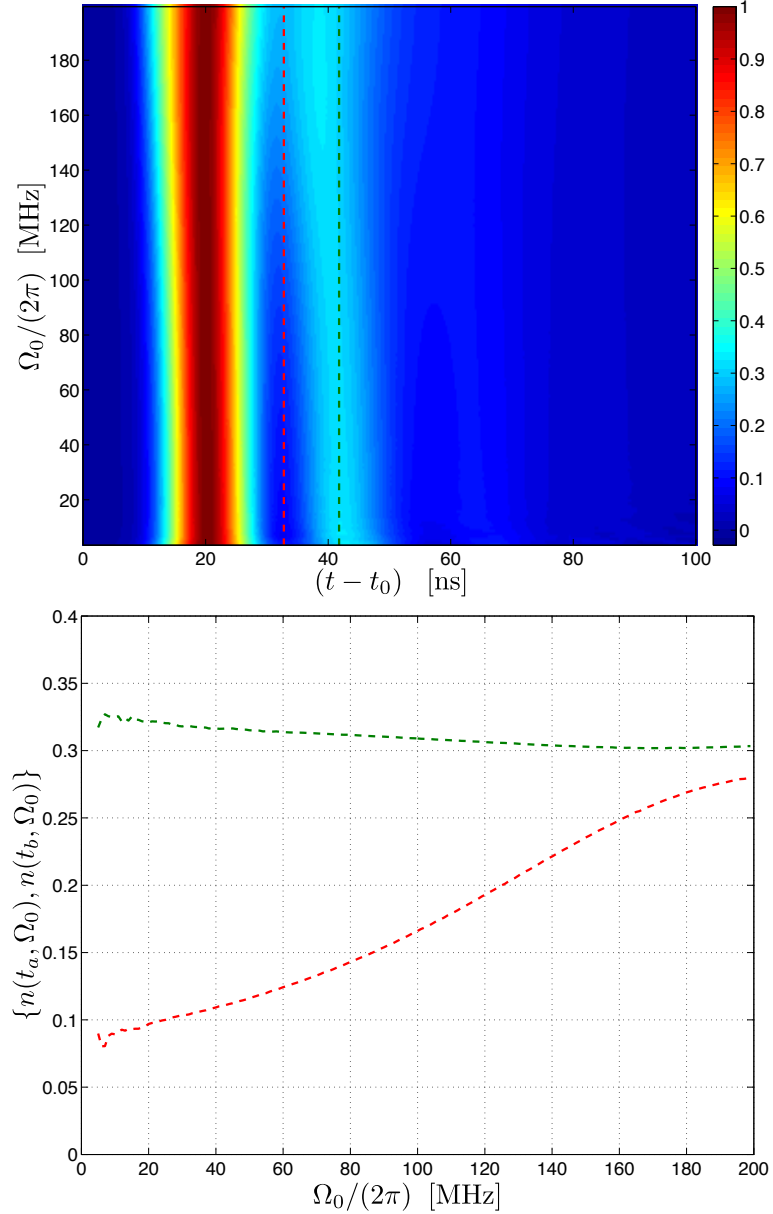


Figure 6.6: Color map of the normalized intracavity photon number, $n'(t)$, versus time and maximum impulse Rabi frequency Ω_0 . Cuts made at $t_a = 32.7$ ns and $t_b = 41.8$ ns quantify dephasing of the optical Rabi nutation due to the strength of the pulse (lower panel shows $n'(t_a, \Omega_0)$ in red and $n'(t_b, \Omega_0)$ in green).

experimental signal is that in the laboratory we have only an order-of-magnitude estimate as to the optical intensity of the impulse at the location of the atom. The expression derived in Chapter 3 for $I(z)$ provides a very rough approximation of the diffraction pattern at the cavity center by modeling the cavity aperture as a two-dimensional slit but ignores complex effects resulting from the non-zero thickness of the mirrors. If the shape of the wave packet emitted from the cavity following the impulse were very sensitive to the distribution of intensities at the center of the cavity then it would be difficult to quantitatively model any signals we see in the lab. However it is clear from this analysis that we can largely decouple the average over $\Omega'_0(z)$ from that over $g(0,0,z)$ as long as we remain in the limit of small Ω_0 . As we will see in the next Section, by varying the intensity of the impulse light in a controlled way and measuring the resulting photodetection probability we can roughly infer the value of Ω_0 for that beam. From this inference we can then perform the necessary ensemble averaging over $g(\vec{r})$ and then compare n' with normalized data from the laboratory to demonstrate agreement between theory and experiment with respect to the shape of the vacuum Rabi oscillation in the cavity output.

Thermal Averaging

Before we describe the data, however, we should generalize our model to include non-zero atomic temperatures (at fixed Ω_0). We will assume that the temperature of the atom is both radially and axially given by:

$$T = \mathcal{T}_0 \frac{U_0}{k_b}. \quad (6.16)$$

Here \mathcal{T}_0 is the ratio between the thermal energy of the atom and the depth of the trapping potential, U_0 (however note that we have no particular evidence that in this configuration of the experiment the atomic motion is thermal so this serves only as an approximation). In order to carry out the average we select the values of q corresponding to the m_b best-coupled wells we wish to consider and then calculate g at all locations $\{x, y, z\} = \{r', z\}$ within that

well:

$$g_q(x, y, z) = g_0 \left| \cos \left(2\pi \frac{z}{\lambda_{D2}} \right) \exp \left(-\frac{(x+y)^2}{w_{D2}} \right) \right|. \quad (6.17)$$

Recall that λ_{D2} and w_{D2} are the wavelength and waist of the cavity QED field. For all possible locations within the q th FORT well, $(z_q - \lambda_F/2) \leq z \leq (z_q + \lambda_F/2)$ and $0 \leq r' \leq 2\sqrt{\mathcal{T}_0}w_F$, we perform a weighted sum of the calculated intracavity photon as function of time for that value $g_q(x, y, z)$ where the weights are given by a thermal distribution.

I have included the `MATLAB` script which I use to perform thermal averaging below. This script relies on a properly-configured version of `cesiumsim.m` (as described in Appendix C) where the pulse shape has been adjusted according to the parameters of our model and the input and output variables have been properly defined.

```
%-----
% thermalavg.m
% March 20, 2009
%-----
% user-defined variables
%-----

Omega0 = 35; % impulse Rabi frequency/(2 pi) [MHz]
g0 = 33.7; % maximum atom-cavity coupling/(2 pi) [MHz]

nbestwells = 35; % the number of "best" wells to consider
T = 0.15; % kbT in units of U0

lp = 852.357e-9; % probe wavelength [m]
lf = 935.586e-9; % FORT wavelength [m]
wp = 23.43e-6; % probe waist [m]
wf = 24.54e-6; % FORT waist [m]
```

```

sigmasqz = T*lf^2/(8*pi^2); % thermal spread in axial position
sigmasqr = T*wf^2/4; % thermal spread in radial position

steps = 100; % coarseness of the average
rstep = 4*sqrt(sigmasqr)/steps;
zstep = lf*0.5/steps;

%-----
% initialize dummy variables
%-----

transmission = zeros(1,500);
denom = 0;
indexg = 0;

%-----
% construct array of n(t) for full range of g's
%-----
for g = 0:.01:g0;
    indexg = indexg+1;
    % call simulation code - na, nb are photon numbers in two cavity modes
    [na nb] = cesiumsim([4],[5],0,[4 5],2*pi*Omega0,2*pi*g);
    glist(indexg,:) = real(na);
end

%-----
% sort wells by g
%-----

for well = 0:89

```

```

%determine value of g for each FORT well
wellg(1,well+1) = cos(pi*(2*well+1)/2*lf/lp);
wellg(2,well+1) = 0.5*(2*well+1);
end
wellg=sortrows(abs(wellg)',-1); % sort list of well g's

%-----
% perform averaging
%-----

for bestwell = 1:nbestwells;
    %value of z at center of well # bestwell
    z0 = 0.5*lf*(wellg(bestwell,2));
    for z = z0:zstep:z0+lf/2;
        for r = 0:rstep:rstep*steps;
            % g at (r,z) with respect to center of # bestwell
            g_rz = abs(cos(2*pi*z/lp)*exp(-r^2/wp^2));
            % find array index in glist corresponding to g_rz
            index_glist = floor(g_rz*g0/.01)+1;
            % transmission is the weighted intracavity photon number
            transmission = transmission+glist(index_glist, :)*...
                exp(-(z-z0)^2/(2*sigmasqz))*r*exp(-r^2/(2*sigmasqr));
            % denom is used to properly weight the average
            denom = denom+exp(-(z-z0)^2/(2*sigmasqz))*r*exp(-r^2/(2*sigmasqr));
        end
    end
end
transmission = transmission/denom;
%-----

```

In Figure 6.7 we explore how averaging over m_b and \mathcal{T}_0 affects the shape of $n(t)$. Un-

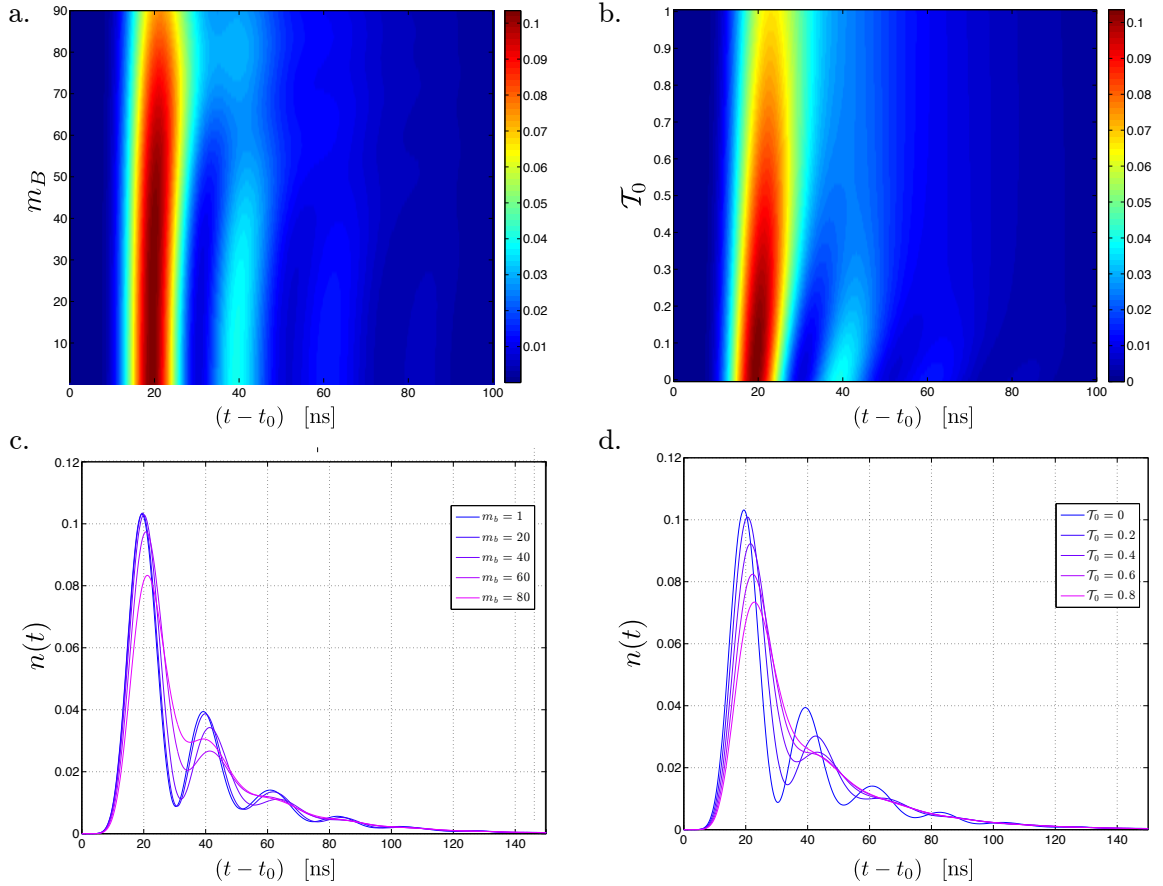


Figure 6.7: Color map plots of $n(t)$ versus t and a. m_b , the number of best-coupled wells and b. \mathcal{T}_0 , the atomic temperature as a fraction of the potential depth. Panels c. and d. illustrate how $n(t)$ changes shape as more well-coupled sites or larger temperatures are considered in the model. These calculations were carried out with $\Omega_0 = (2\pi)(35 \text{ MHz})$. Averages taken over different m_b are calculated with $\mathcal{T}_0 = 0$ and likewise averaging over \mathcal{T}_0 is done with $m_b = 1$.

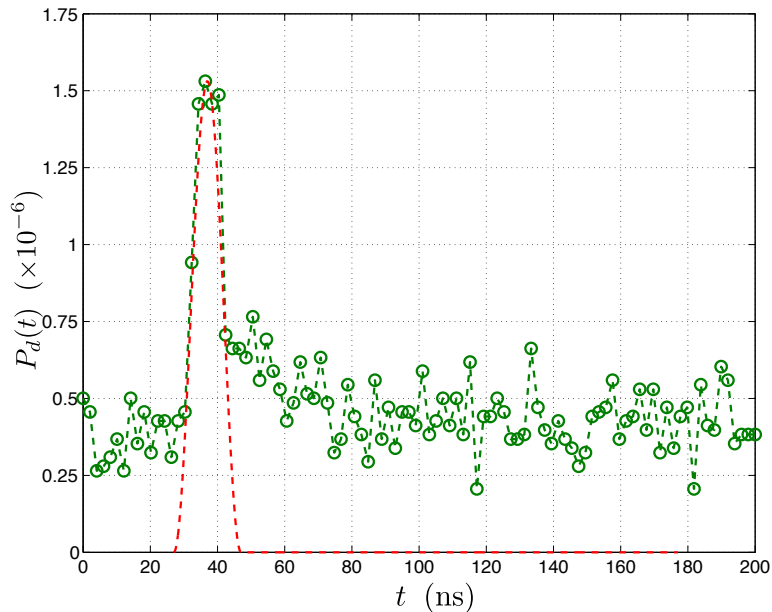


Figure 6.8: Data points correspond to the measured probability, $P_d(t)$ to register a photodetection event in a 2 ns window of time centered at t with no atoms present in the cavity. The red curve represents the location of the model pulse described in the previous Subsection.

surprisingly, as we sum over a larger range of values $g(\vec{r})$, the Rabi oscillation present in the intracavity wave packet begins to dephase. In particular, we note that for values of $m_b \gtrsim 60$ and for $\mathcal{T}_0 \gtrsim 0.3$, the oscillation starts to become indistinct. In practice, it is difficult to predict which range of values $\{m_B, \mathcal{T}_0\}$ will correspond to the data observed in the laboratory. Under very different experimental conditions we have observed in the past that $m_b < 30$ and $\mathcal{T}_0 < 0.1$ [41, 29], but predicting the heating effects and trap survival probabilities associated with the particular interaction we are implementing here is difficult. Instead, in the next Subsection, we will use the temporal shape of the emitted wave packet to make an inference of the temperature and position of the ensemble of atoms which contribute to the measurements.

6.1.3 Results and Correspondence with Theory

In order to analyze the data it is useful to begin with a baseline measurement for which no atoms are present in the cavity (Figure 6.8). To ensure the absence of atoms from the data, we turn off the current supplies which are used to generate the quadrupole fields necessary to form the upper and lower MOTs. The quantity which we will evaluate is the probability as a function of time, $P_d(t)$, to register a photodetection event in the 2 ns time bins centered at times t and defined by the P7888 card. For the data corresponding to no atoms, we see a spike in $P_d(t)$ centered near $t = 38$ ns. This corresponds to scatter of light from the MZIS off the cavity substrates and into the detector. The small amount of scattered light contains two useful pieces of information. First, it allows us to determine the arrival time of the optical pulse at the cavity with respect to the detection trigger event (thereby accounting and correcting for small delays in the electronics and coaxial cables used to trigger the pulse). This in turn determines t_0 , or the location of the model pulse described in the previous Subsection, and registers any theoretical calculations in time with respect to experimental data. Secondly, this measurement allows us to determine the background probability with which light will be scattered from the impulse into the detectors (as opposed to from the atom and subsequently into the cavity mode). We have observed that the amount of light scattered from the cavity mirrors into the detector path is very sensitive to the physical alignment of the impulse beam through the cavity aperture. Significant misalignment can increase the rate of scatter by as much as an order of magnitude. Outside of the window of time near the impulse the background level is otherwise consistent with the cumulative rate of dark counts from our APDs (*i.e.*, a ~ 200 Hz dark count rate translates into a uniform background detection probability $P_B \sim 0.4 \times 10^{-6}$).

Figure 6.9 shows a typical measurement of $P_d(t)$ with the MOTs fully functioning and with the presence of atoms in the cavity verified as described in Subsection 6.1.1. The particular set of data shown in this Figure is an average over 647 successful FORT loading attempts and constitutes 7.76×10^4 photodetection events (with a total probability conditioned on an impulse to register a photodetection event of $P_1 = 0.00598$). Note that the maximum of $P_d(t)$ in the presence of atoms is a factor of 200 larger than the maximum of baseline data from Figure 6.8. Importantly, the maximum of $P_d(t)$ also occurs near $t = 49$

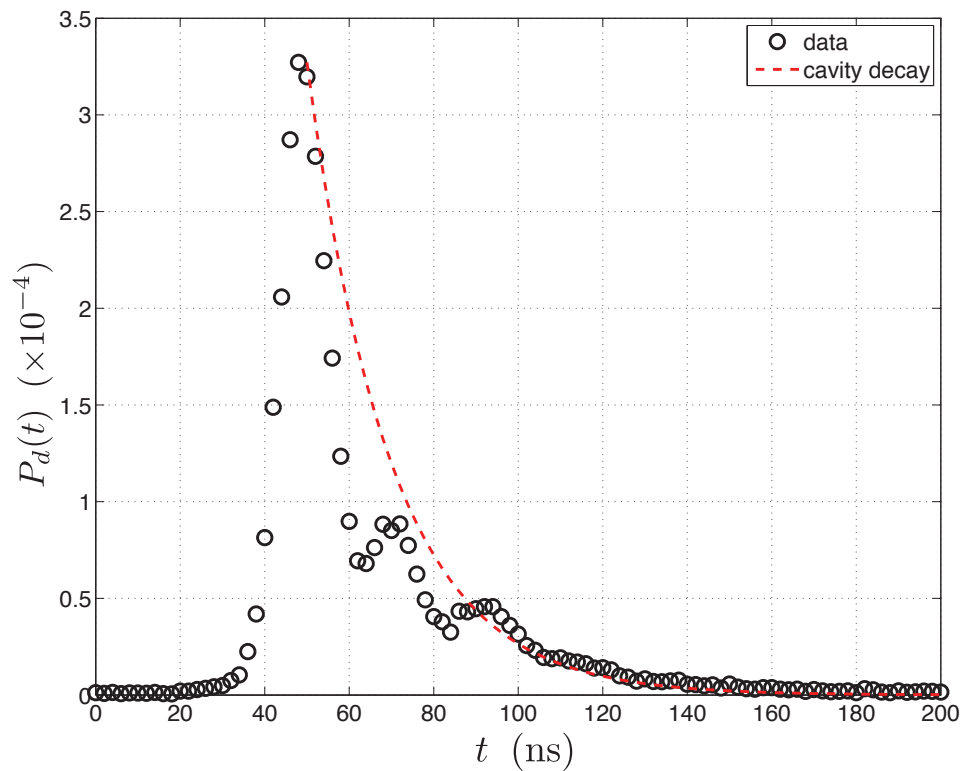


Figure 6.9: Photodetection probability (\circ) corresponding to the presence of an atom in the cavity. Note that the scale is now $\times 10^{-4}$ as opposed to in Figure 6.8 where it was $\times 10^{-6}$. The red (dashed) curve corresponds to the predicted cavity ring down exponential with time constant 2κ for an intracavity field (in the absence of an atom) which exhibits a maximum value of $P_d(t)$ equivalent to that measured in this data.

ns which is offset from the scattered light (and therefore from the arrival of the impulse at the cavity) by 11 ns. This small delay is a strong indication that the light being detected in cavity emission is the result of excitation in the atom gradually coupling to the cavity mode as opposed to scattered impulse light directly reaching the detectors. We can also compare the shape of the measured $P_d(t)$ to the anticipated cavity decay in the absence of a strongly-coupled atom (red, dashed line in Figure 6.9). The data clearly exhibits structure on a timescale faster than the cavity bandwidth which is another indication of atom-cavity dynamics manifest in the wave packet shape.

Before we discuss the correspondence between data and theory, it is useful to attempt to infer the Rabi frequency associated with the optical pulses generated using the MZIS. In order to do this, we measured $P_d(t)$ using four different optical powers coupled through the switch. The photocurrent through 50Ω , V_{max} , of the resulting pulses were measured by detection at the same photodiode used to record Figure 6.2. The optical power associated with these pulses was far below the saturation limit of the photodiode and so we will assume that the response of the detector is linear. The resulting $P_d(t)$ for each of $V_{max} = (30, 65, 250, 540)$ mV are shown in Figure 6.10 and demonstrate the dependence of $P_d(t)$ on V_{max} (as mentioned earlier, we choose not to use higher optical powers so as to prevent potential photorefractive damage of the MZIS). From each of these data sets we can determine the integrated probability P_1 to register a single photodetection event conditioned on the start of a trial. The value of P_1 for each V_{max} are presented in Figure 6.11 with the horizontal (Voltage) axis rescaled:

$$\Omega_0 = \sqrt{V_{max}} \frac{(2\pi)(56.5 \text{ MHz})}{\sqrt{540 \text{ mV}}} \quad (6.18)$$

such that the data point at $V_{max} = 540$ mV coincides with a theoretical curve derived from the averaging techniques described in the previous Subsection. The locations of the three remaining points are not constrained to fall on the theoretical curve but are scaled using the same factor and show reasonable agreement with numerical simulation (red trace). This calculation corresponds to an average taken over $m_b = 45$ wells for atoms at zero temperature, $\mathcal{T}_0 = 0$, and incorporate the measured detection efficiency $\alpha = 0.086$. In

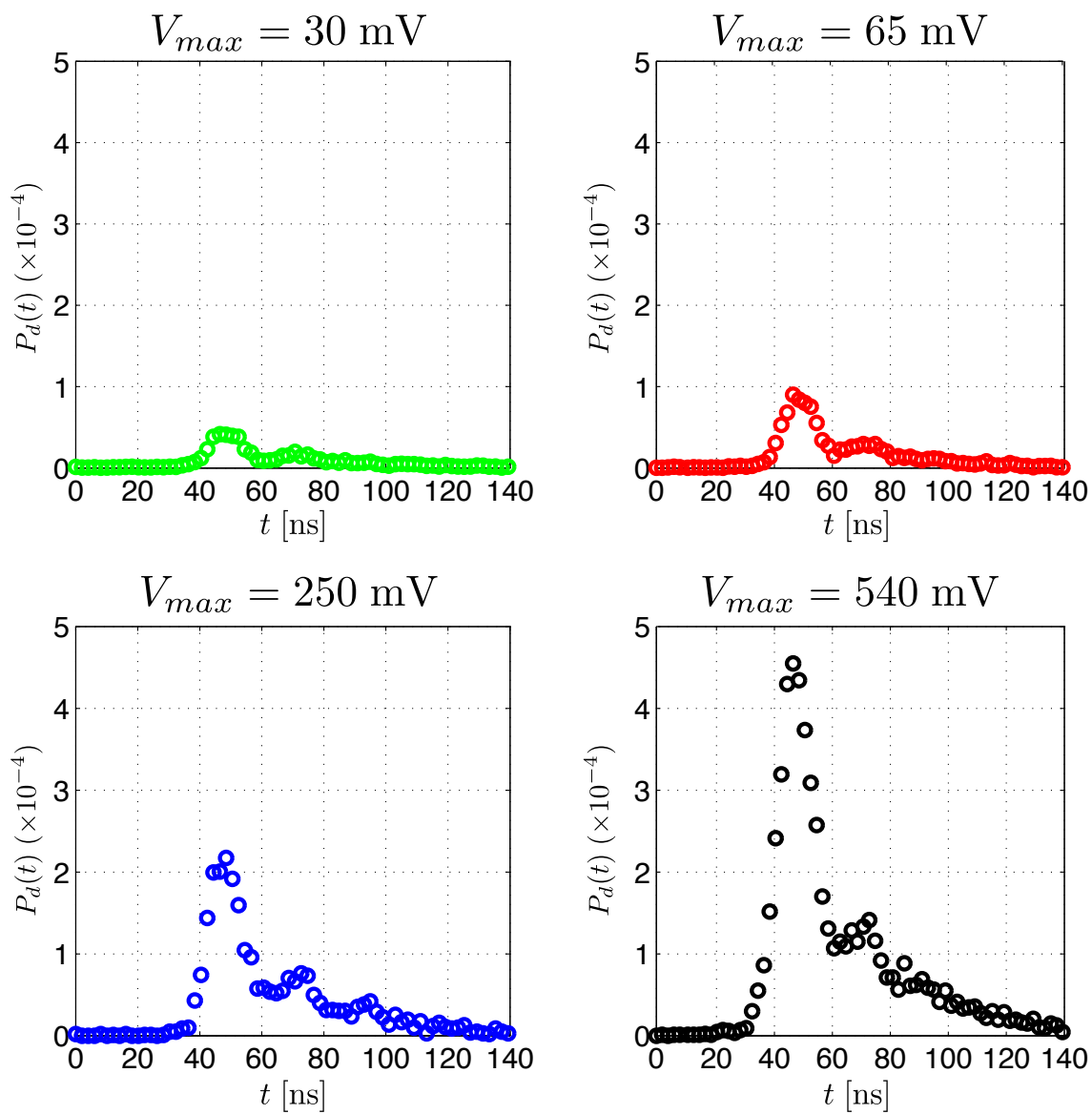


Figure 6.10: Photodetection probability $P_d(t)$ versus time for $V_{max} = (30, 65, 250, 540)$.

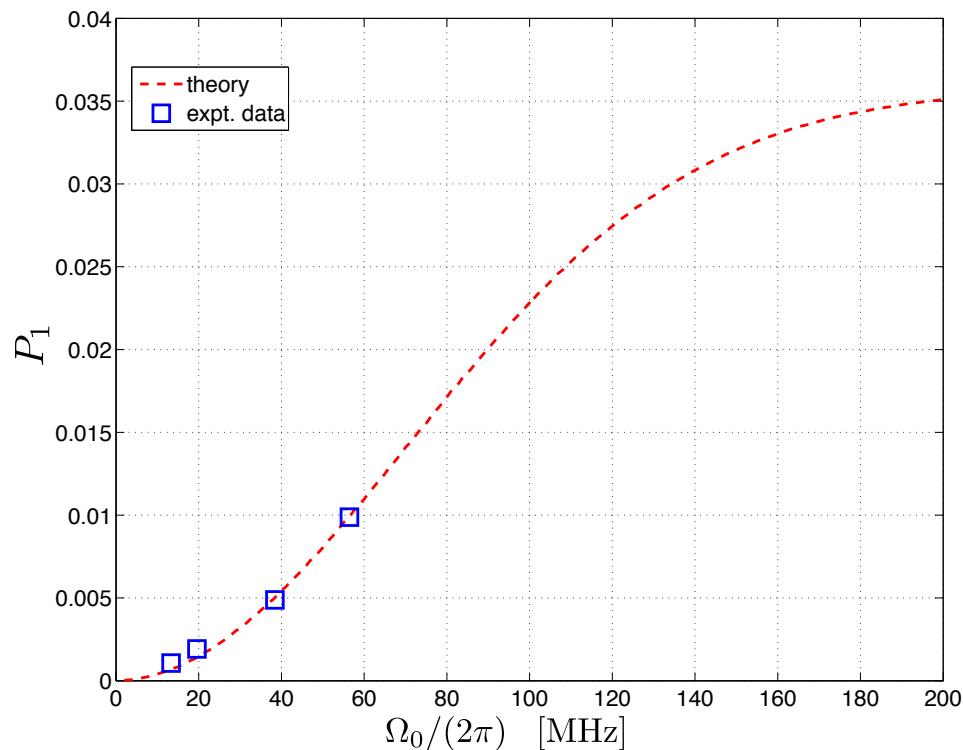


Figure 6.11: Measured integrated photodetection probability P_1 versus pulse Rabi frequency. The horizontal axis of the plot has been rescaled as described in the text such that that point corresponding to $V_{max} = 540$ mV coincides with theory (dashed red curve). The remaining three points are rescaled by the same factor and show reasonable agreement with the theory.

averaging over $\Omega'_0(z_q)$ we have used the simple intensity pattern $I(z_q)$ from Chapter 3 (and should therefore be considered only approximate). Nonetheless, it is clear that we are operating in the limit of weak driving. Based on the analyses of the previous Subsection this suggests that by rescaling the theoretically predicted wave packet shape we should be able to closely model the shape of the measured cavity emission.

In Figure 6.12 we plot $P'_d(t)$ which is the same set of data shown in Figure 6.9 but normalized with respect to the maximum wave packet amplitude. We have also plotted the full averaged and normalized solution to the master equation, $P'_e(t)$, for $m_b = 54$ wells and $\mathcal{T}_0 = 0.025$. We have assumed a maximum impulsive Rabi frequency $\Omega_0 = (2\pi)(40$

MHz). The values of m_b and \mathcal{T}_0 were the only unconstrained parameters in the solution. The master equation results are registered in time with respect to the experimental data by centering the theoretical model pulse at the location of the scattering peak shown in Figure 6.8 (*i.e.*, $t = 38$ ns). We have chosen these particular values of the unconstrained parameters by doing a full search of the parameter space and selecting the pair of values for which the integrated difference between the theoretical prediction and the data was minimized, *i.e.*,

$$\{m_b, \mathcal{T}_0\} : \min \left(\sum_{t=t_d} |P'_d(t) - P'_e(t, m_b, \mathcal{T}_0)| \right) \quad (6.19)$$

where the t_d are those values of t on which the data collection windows of the $P7888$ were centered. The particular set of $\{m_b, \mathcal{T}_0\}$ chosen here best satisfies this criteria, but other combinations can provide very similar results. Generally in a range $45 < m_b < 60$ and $\mathcal{T}_0 < 0.05$ we see favorable agreement between theory and experiment. It can be seen that there is a strong correspondence between the theoretically predicted wave packet shape and that observed in the laboratory. Also, the shape of the emitted wave packet clearly exhibits oscillation due to Jaynes-Cummings-type dynamics. The greatest discrepancy is between the measured and predicted amplitudes of the third maximum in the oscillation, although the location of that maximum is still well-predicted. This discrepancy could be due to any of a number of phenomena such as a non-uniform distribution of FORT wells or non-thermal distributions of atomic temperatures.

In summary, we have experimentally demonstrated Rabi nutation of excitation between atom and field in the setting of strongly-coupled cavity QED. The Rabi oscillation manifests itself on the temporal shape of the field emitted from the cavity mode following fast excitation of the atom by pulse of resonant laser light. Unlike previous similar measurements [93], we are able to observe an oscillatory signal even for the case of zero atom-cavity detuning. The shape of this wave form is in good agreement with a detailed theoretical model involving numerical integration of the master equation for the system and accounting for ensemble averaging effects present in the measurement. As will be described in the next Subsection, this work was carried out in the context of another project focused on demonstration of

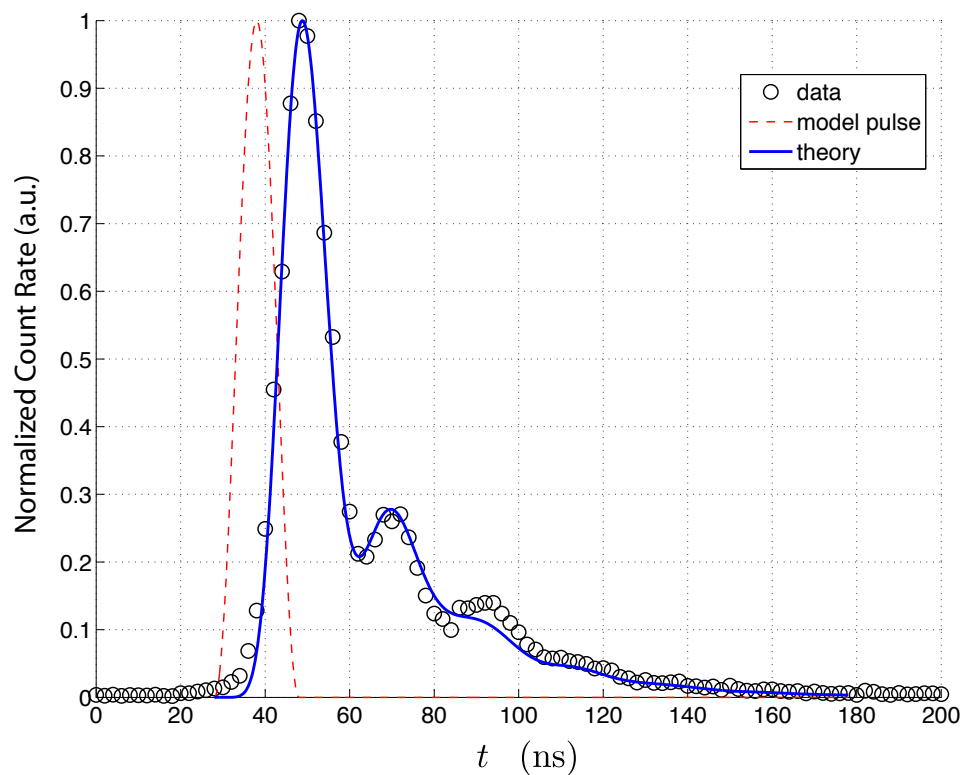


Figure 6.12: Normalized data (\circ) plotted in comparison with the solution to the full master equation (blue line) for the intracavity photon number averaged over the $m_b = 54$ best-coupled wells at a temperature of $\mathcal{T}_0 = 0.025$. The values of m_B and \mathcal{T}_0 were the only unconstrained parameters in the model and the pair of values chosen are chosen to minimize the integrated difference between the experimental data and theory. The arrival time of the model impulse (red dashed line) is that measured in Figure 6.8.

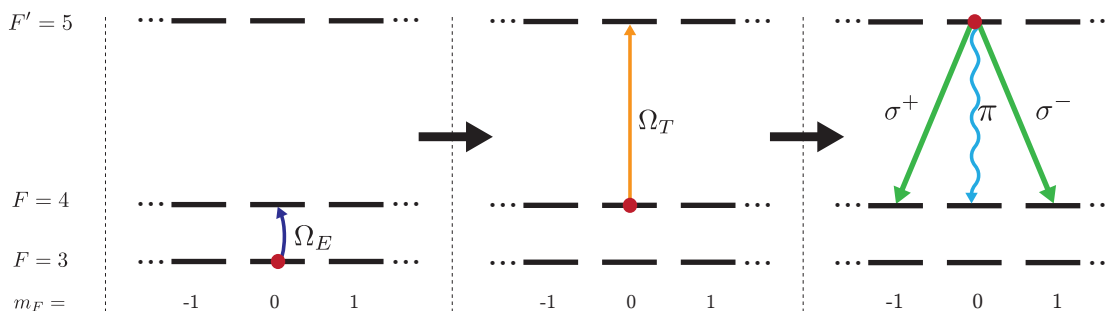


Figure 6.13: Initial state preparation procedure and schematic of decay channels for impulsive excitation of atoms prepared in a well-defined Zeeman state. In the third panel, π -polarized light is unsupported by the cavity mode and therefore decays via spontaneous emission into spatial modes other than the QED mode.

entanglement between photons emitted from the cavity mode and the internal state of the atom. Although we have not yet been able to measure entanglement, we have observed a series of interesting correlations between photodetection and measurement of the atomic Zeeman state.

6.1.4 Atom-Photon Correlation Measurements

In the previous Subsection we performed measurements wherein the static magnetic field at the location of the cavity was nulled and the the atom was optically pumped into a random Zeeman substate within the $F = 4$ hyperfine ground state manifold. This configuration was motivated by the need to accumulate a large number of photodetection events in order to reconstruct the temporal wave packet of the field generated in the cavity mode following an $\Omega_T(t)$ pulse (introducing optical pumping would very significantly reduce the duty cycle for the experiment). In this Subsection we will instead explore the effect of $\Omega_T(t)$ on the state of the atom. In order to do this, we apply a static magnetic bias field, $\vec{B} = (0, 0, 1.2)$ G, oriented along the axis of the cavity in order to break the degeneracy between the $|F, m_F\rangle$ ground states and establish a quantization axis.

A preliminary diagnostic measurement which we undertook was to demonstrate that impulsive excitation of the atom following preparation in a properly-defined initial state

transfers population from that state to adjacent spin states in a well-understood way. The protocol for this measurement is shown in Figure 6.13. Using the incoherent Raman-based optical pumping technique introduced in Chapter 4, we deposit a large fraction of the initial atomic population in the state $|F, m_F\rangle = |3, 0\rangle$ (typically $p_{(3,0)} \equiv p_3(m_F = 0) \approx 0.65$). After the pumping protocol finishes we apply a π -pulse of Raman light (with the Raman pair in the FORT-Raman configuration). Recall that a π -pulse is a Raman pulse of duration $\tau_R = \pi/\Omega_E$, where Ω_E is the effective Rabi frequency of the Raman pair, and ideally affects complete inversion of population between the two coupled states. The Raman pair is tuned into free-space resonance with the ($|3, 0\rangle \leftrightarrow |4, 0\rangle$) transition such that effect of the π -pulse is to transfer a significant fraction of the population in $|3, 0\rangle$ to $|4, 0\rangle$. The efficacy of the Raman pulse is limited by the dephasing of the resultant Rabi oscillation over τ_R and is characterized by a state transfer probability $p_R \approx 0.8$. Following this initial step and averaged over an ensemble of similar measurements, we have prepared an incoherent mixture of atom population:

$$\hat{\rho}_A \approx \frac{(1 - p_{(3,0)})}{6} \sum_{m_F \neq 0} (|3, m_F\rangle \langle 3, m_F|) + p_{(3,0)}(1 - p_R) |3, 0\rangle \langle 3, 0| + p_{(3,0)}p_R |4, 0\rangle \langle 4, 0|. \quad (6.20)$$

Note that we are assuming that the last two terms in the density matrix are incoherent because we are assuming that the defect in the π -pulse is the result of dephasing and not because we improperly specified τ_R . The reason that we have decided to use a Raman pulse to move population into the desired state in the $F = 4$ manifold rather than directly pumping into that state is twofold. First, our technique for incoherent Raman-based state preparation fails in the $F = 4$ manifold when only $\Delta m_F = 0$ Raman transitions are permitted by the orientation of static magnetic fields in the system (the edge states are also “dark” states of the process and population becomes trapped there). The second reason is that by moving population directly from $|3, 0\rangle$ to $|4, 0\rangle$ we have ensured that the small residual populations due to imperfections in the pumping process are present only in states corresponding to $m_F \neq 0$ in the uncoupled $F = 3$ manifold. Because the vast majority of population in the coupled $F = 4$ manifold is driven there by the Raman π -pulse, the

only way in which the Ω_T pulse can change the state of the atom is by interacting with population in $|4, 0\rangle$ (excluding negligibly small off-resonant interactions).

After we have prepared the system in the state described by Equation (6.20), we then apply the classical impulse to the atom. As described in the previous subsections, the effect of this pulse is to excite the atom with some probability p_T . Recall that because we are now applying a static magnetic field along the cavity (\hat{z} -) axis and because the Ω_T pulse is polarized along that direction of that field, the effect of the pulse is to transfer population from $|4, 0\rangle$ to $|5', 0\rangle$. From the excited state $|5', 0\rangle$ there are three possible decay channels. The transition $|5', 0\rangle \rightarrow |4, 0\rangle$ corresponds to emission of a photon with π -polarization relative to \hat{z} . This transition is not strongly-coupled to the cavity because the cavity can only support fields polarized orthogonally to its longitudinal axis and therefore this decay channel corresponds only to spontaneous emission into modes other than the QED mode. The other two decay channels are $|5', 0\rangle \rightarrow |4, \pm 1\rangle$ corresponding to emission of σ^\mp -polarized photons, respectively. Photons of these polarizations are cavity-supported and therefore these transitions exhibit Jaynes-Cummings dynamics and can be emitted from the cavity due to strong coupling (although free space decay on these transitions is also allowed). We can express the fraction of the σ^\pm -polarized decay which is coupled out of the cavity as approximately $p_C = \kappa/(\gamma + \kappa) \approx 0.59$ whereas the fraction that is emitted in a 4π solid angle via spontaneous decay is $(1 - p_C) = \gamma/(\gamma + \kappa)$. Note that p_C is approximate and depends in a limited way on $g(\vec{r})$.

In free space and in the absence of Zeeman state-dependent FORT AC Stark Shifts, the branching fraction for each of the three channels is given simply by the square of the dimensionless dipole moment for the transition in question (Appendix A). For the three transitions described here, the probability with which the atom decays to $|4, 0\rangle$ is given by $p_{\pi, F} = 5/9 \approx 0.55$ whereas the probabilities to decay to $|4, \pm 1\rangle$ are $p_{\pm, F} = 2/9 \approx 0.22$ (the two are equal due to the symmetry requirements). By introducing a cavity with a significant rate of coherent coupling we can also induce emission into $|4, \pm 1\rangle$ with branching fractions $p_{\pm, C}$, which are approximately equal. The ratio of cavity emission to free-space emission is, again, approximately p_C . If we reintroduce the FORT shifts to the problem we must recall that those shifts to the $F = 5'$ excited state manifold (Figure 3.12) were

defined with respect to a quantization axis oriented along the polarization of the FORT (*i.e.*, along the axis of the higher-frequency birefringent mode of the cavity, \hat{l}_+). The state $|5', 0\rangle$ is therefore only approximately a “good” eigenstate of the system with respect to the basis which we have chosen and is generally a superposition of eigenstates in a basis with \hat{z} oriented along \hat{l}_+ . The state-dependent perturbation from the FORT thereby permits decay from $|5', 0\rangle$ to states other than $\{|4, 0\rangle, |4, \pm 1\rangle\}$ and also breaks the symmetry that results in $p_{+,F} = p_{-,F}$ and $p_{+,C} = p_{-,C}$. For the typical FORT depths which we use in the laboratory, calculations suggest this effect is a small one with only $\sim 5\%$ of the population in the atom moving into states with $m_F \neq (0, \pm 1)$ in steady state.

In Chapter 3 we described how we can use Raman spectroscopy to resolve the population in individual Zeeman states (or rather measure, as a function of Raman detuning, the population inversion between hyperfine ground states). In Figure 6.14 we have plotted Raman spectra with the range of the scan narrowed to focus on population in states corresponding to $m_F = (0, \pm 1)$. The blue curve is a spectrum measured immediately following the incoherent Raman optical pumping initialization protocol. As anticipated, the abundance of population initially in $|3, 0\rangle$ manifests itself as a large resonance centered on $\delta = 0$. Likewise we see smaller features centered near $\delta = (2\pi)(\pm 1 \text{ MHz})$ corresponding to residual population able to make the transitions ($|3, \pm 1\rangle \leftrightarrow |4, \pm 1\rangle$). The green trace corresponds to a spectrum measured after the Raman π -pulse has transferred population from $|3, 0\rangle$ to $|4, 0\rangle$ but in the absence of the Ω_T pulse. Here we see a constant background indicative of the fact that a significant fraction of the atomic population now begins the measurement in $F = 4$. Because the signal which we measure in the laboratory is the population in $F = 4$ as a function of detuning, any population initially in a particular Zeeman substate $|4, m_F\rangle$ will manifest itself now as a dip (as opposed to a peak, for population in $F = 3$) in the spectrum at the appropriate detuning. In this spectrum we see a pronounced dip at zero detuning corresponding to the significant fraction of the atomic population which now begins in $|4, 0\rangle$. We also continue to observe peaks near $\delta = (2\pi)(\pm 1 \text{ MHz})$, indicating that there is a larger fraction of the population initially in $|3, \pm 1\rangle$ than in $|4, \pm 1\rangle$. Finally, the red curve is a spectrum taken after the full state initialization procedure and the Ω_T pulse. This spectrum again exhibits a dip near zero detuning, however now of smaller magnitude.

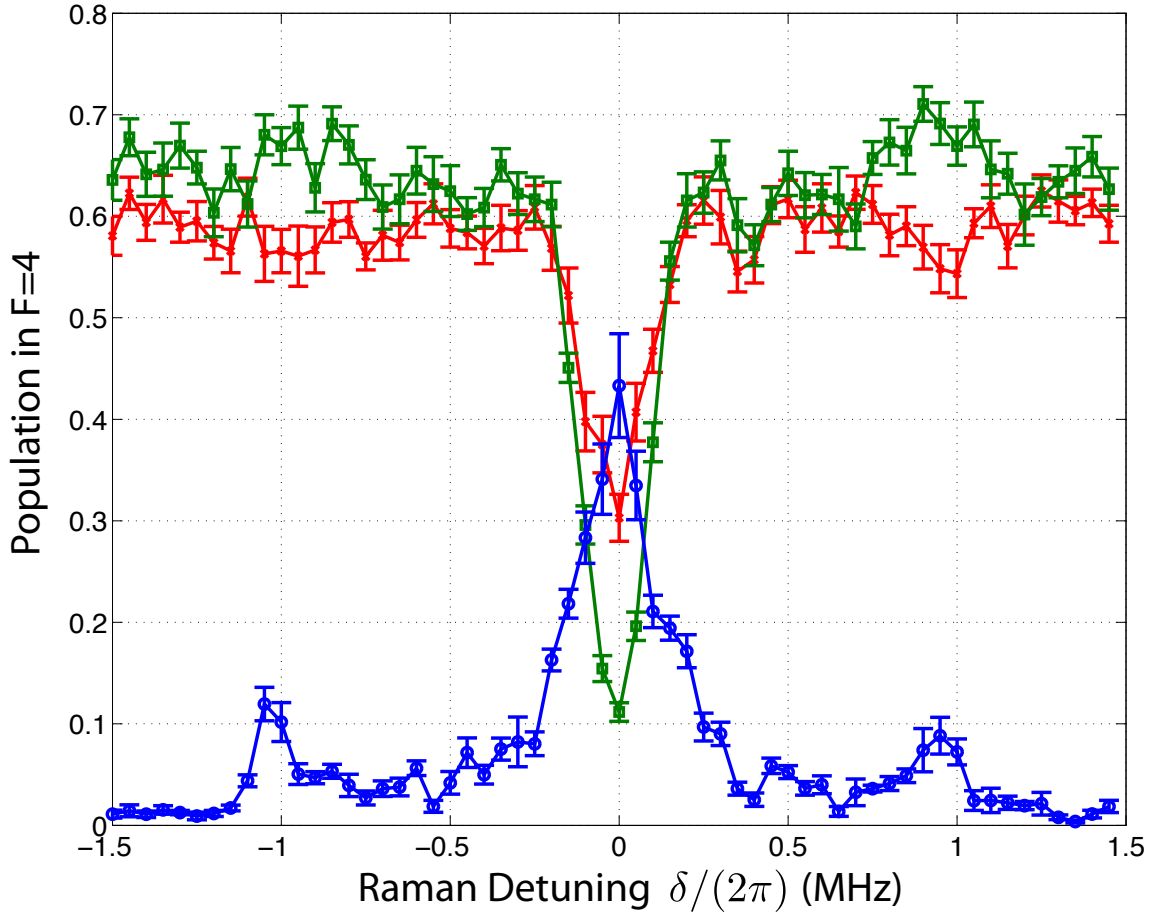


Figure 6.14: Raman spectra taken at three different stages in the state preparation protocol. Blue (\circ) immediately after optical pumping in $|3,0\rangle$, green (\square) after both optical pumping and the Raman π -pulse on $(|3,0\rangle \leftrightarrow |4,0\rangle)$ and red (\times) after pumping, the π -pulse and the Ω_T pulse. Compare the red and green traces near $\delta = (2\pi)(\{0, \pm 1\})$ MHz. These detunings correspond to the transitions $(|3,0\rangle \leftrightarrow |4,0\rangle)$ and $(|3, \pm 1\rangle \leftrightarrow |4, \pm 1\rangle)$ are the spectroscopic features here are indicative of how Ω_T changes the internal state of the atom, moving population from $|4,0\rangle$ to $|4, \pm 1\rangle$.

Because the background level remains approximately unchanged we can thereby infer that, although there is the same amount of population initially in the $F = 4$ manifold, a smaller fraction of that population is in the state $|4, 0\rangle$. We also now see small dips, as opposed to peaks, near the frequencies corresponding to $(|3, \pm 1\rangle \leftrightarrow |4, \pm 1\rangle)$, which indicates that there is now initially more population $|4, \pm 1\rangle$ than in $|3, \pm 1\rangle$. This provides evidence that the Ω_T pulse is affecting the atom as anticipated, redistributing population from $|4, 0\rangle$ into $|4, \pm 1\rangle$.

So far this discussion has focused only on the state of the atom and traced over the field states in the full density matrix for the system. For modes other than the two orthogonally-polarized cavity modes this is a necessity - our experiment is not equipped to gather fluorescence from the atom and photons in these modes are lost to the environment. We can, however, collect emission from the cavity mode and so we can construct a more complete picture of the interaction by considering states in the product basis $|F, m_F, \pm\rangle \equiv |F, m_F\rangle \otimes |\pm\rangle$. The states $|\pm\rangle$ correspond to the presence of a single σ^\pm -polarized photons in the cavity mode. Following the Ω_T pulse, the density matrix in the single-excitation manifold of states is:

$$\hat{\rho}_1 \approx p_{RP(3,0)} p_{TP+,CP} \left(|4, 1, -\rangle + e^{i\phi} |4, -1, +\rangle \right) \left(\langle 4, 1, -| + e^{-i\phi} \langle 4, -1, +| \right) \quad (6.21)$$

where we have assumed that $p_{+,C} = p_{-,C}$, which is approximately correct, and that the process of decay into the cavity imparts a small differential phase ϕ between the two states. Note that this product state exhibits *a priori* bipartite entanglement between the internal state of the atom and the polarization state of the excitation in the cavity mode.

This type of entanglement - between the internal state of a single atomic system and the polarization of a photon emitted from that atom - results whenever there exist multiple decay channels from a single atomic excited state and has been experimentally observed and verified in the context of both single atom cavity QED and with atoms in free space. The Rempe group in Garching, using a similar apparatus and trapped rubidium atoms, has demonstrated the ability to generate entangled photon pairs by mapping the initial atom-photon entanglement to a second photon thereafter deposited in the cavity mode [94, 52]. The group of Chris Monroe at the University of Maryland has successfully verified

entanglement (and even the application of this entanglement to teleportation schemes [68]) between both atom-photon pairs [66] and atom-atom pairs [67] using a similar technique. Analogous measurements could be made for cesium in principle. However in actual practice these other experiments benefit from the use of atoms with relatively small nuclear spins ($I = 3/2$ for ^{87}Rb , $I = 1/2$ for $^{113,111}\text{Cd}^+$ and for $^{111}\text{Yb}^+$). For cesium we have to contend with a veritable “jungle” of Zeeman ground states in which small amounts of population can reside thereby leading to technical problems associated with high-efficiency optical pumping, state readout, and the mapping of entanglement from atomic to optical states. During my tenure at Caltech we devoted a good deal of time and effort to attempting to verify the entanglement between atom and photon generated in this way (including novel uses of the FORT-Raman pair to coherently mix population in the states $|4, \pm 1\rangle$ by way of an intermediary state $|3, 0\rangle$). The discouraging results of these efforts are well-detailed in Chapter 5 of Tracy Northup’s dissertation and I won’t describe them in any detail here.

Although we have been unable to read out entanglement between atom and photon, we did perform a series of measurements which positively correlated photodetection events in the cavity output mode with the presence of population in $|4, \pm 1\rangle$. The technique we used was similar to that used to obtain the Raman spectrum in Figure 6.14, but rather than unconditionally performing Raman spectroscopy following the Ω_T pulse we conditioned subsequent Raman-based state readout on the detection of a photon. The initial state of the system was prepared as before, with incoherent Raman-based optical pumping and a π -pulse on ($|3, 0\rangle \leftrightarrow |4, 0\rangle$). Following the Ω_T pulse, we then perform another π -pulse, on either ($|3, 0\rangle \leftrightarrow |4, 0\rangle$) or one of ($|3, \pm 1\rangle \leftrightarrow |4, \pm 1\rangle$).

Before we explore the results, we can make simple predictions for the probabilities to detect atomic population in $F = 4$ following each of these three types of π -pulse, both conditioned on photodetection and unconditionally. We expect the atomic populations in

each of the coupled states following the pulse to be:

$$\langle 4, 0 | \hat{\rho}_A | 4, 0 \rangle = p_R p_{(3,0)} [(1 - p_T) + (1 - p_C) p_T p_{\pi,F}] \quad (6.22)$$

$$\langle 4, \pm 1 | \hat{\rho}_A | 4, \pm 1 \rangle = p_R p_{(3,0)} p_T [(1 - p_C) p_{\pm,F} + p_C p_{\pm,C}] \quad (6.23)$$

$$\langle 3, 0 | \hat{\rho}_A | 3, 0 \rangle = p_{(3,0)} (1 - p_R) \quad (6.24)$$

$$\langle 3, \pm 1 | \hat{\rho}_A | 3, \pm 1 \rangle = \frac{(1 - p_{(3,0)})}{6} \quad (6.25)$$

unconditionally and

$$\langle 4, 0 | \hat{\rho} | 4, 0 \rangle = 0 \quad (6.26)$$

$$\langle 4, \pm 1 | \hat{\rho} | 4, \pm 1 \rangle = \frac{p_{\pm,C}}{p_{+,C} + p_{-,C}} \quad (6.27)$$

$$\langle 3, 0 | \hat{\rho} | 3, 0 \rangle = 0 \quad (6.28)$$

$$\langle 3, \pm 1 | \hat{\rho} | 3, \pm 1 \rangle = 0 \quad (6.29)$$

conditionally. The populations in $F = 4$ following each of the π -pulses should be:

$$P_4(m_F) = p_R \langle 3, m_F | \hat{\rho} | 3, m_F \rangle - (1 - p_R) \langle 4, m_F | \hat{\rho} | 4, m_F \rangle + \sum_{n \neq m_F} \langle 4, n | \hat{\rho} | 4, n \rangle. \quad (6.30)$$

In terms of quantities in the laboratory, $p_R \approx 0.8$, $p_{(3,0)} \approx 0.7$, $p_T \approx 0.5$, $p_C \approx 0.6$, $p_{\pi,F} \approx 0.6$, $p_{\pm,F} \approx 0.2$, and $p_{\pm,C} = 0.5$. Here, in approximating the various p_π and p_\pm , we have ignored the effect of the cavity birefringence and FORT-induced shifts which is a reasonable assumption at this level of approximation. We have also estimated the value of p_T based on numerical calculations and the intensity of the Ω_T beam used for these measurements.

Table 6.1 displays the predicted and measured probabilities, P_4 , to detect the presence of an atom coupled to the cavity after the a Raman π -pulse of the type listed and conditioned or unconditioned on the detection of a photon in the cavity output mode. Overall we see reasonably good agreement between our predictions and the observed values, particularly given the level of approximation we had incorporated into those predictions. The deviations from the predicted value $P_4 = 1$ for conditional measurement following no π -pulses

	P_4 , Unconditional		P_4 , Conditional	
Raman Configuration	Predicted	Measured	Predicted	Measured
no π -pulse	0.6	0.62	1	0.92
$(3, 0\rangle \leftrightarrow 4, 0\rangle)$	0.3	0.33	1	0.84
$(3, 1\rangle \leftrightarrow 4, 1\rangle)$	0.5	0.57	0.6	0.70
$(3, -1\rangle \leftrightarrow 4, -1\rangle)$	0.5	0.56	0.6	0.62

Table 6.1: Probabilities to detect the presence of atom in $F = 4$ following a Raman π -pulse of the type listed and conditioned or unconditioned on the detection of a photon in the cavity output mode. The predicted values shown are as calculated in the text.

and pulses on $(|3, 0\rangle \leftrightarrow |4, 0\rangle)$ are likely due to spurious photodetection events, decay into the cavity supporting $\Delta m_F \neq \pm 1$ permitted by the FORT Stark shifts and the cavity birefringence or the small probability of multiple atoms simultaneously coupled to the cavity mode. Notice also that there seems to be an asymmetry in the measurements following Raman pulses coupling $(|3, \pm 1\rangle \leftrightarrow |4, \pm 1\rangle)$. Possible explanations for this effect include cavity birefringence ellipticizing the emitted field (recall that we are projecting the polarization of cavity emission along a linear axis specified by a polarizer at the cavity output) or the FORT AC Stark shifts adding asymmetry to the problem.

Of the four π -pulse configurations described here, the most striking evidence that Ω_T has moved population as anticipated is in the difference between conditional and unconditional P_4 following a π -pulse on $(|3, 0\rangle \leftrightarrow |4, 0\rangle)$. It is clear that the emission of a photon into the mode of the cavity following Ω_T is strongly correlated with the depopulation of $|4, 0\rangle$. We have therefore observed distinct correlation between photodetection in cavity emission and measurement of the internal state of the atom. This work constitutes a preliminary step towards being able to verify the entanglement between the polarization of those photons being detected and the internal state of the atom.

6.2 Frequency-Domain Measurements

The ability to study optical cavity QED in the time domain, for example as discussed in the previous section Section, is relatively novel. This type of measurement benefits from and relies upon advances in photodetection electronics, the ease and availability of devices for generating very short optical pulses but, most of all, from the long-lived interactions that integration of atomic confinement protocols and high finesse optical cavities can only recently provide. By contrast, measurement of the signature frequency-domain features of the system (for example the two-peaked vacuum Rabi spectrum described in Chapter 2) has long been a standard technique for characterizing atom-cavity systems. As the tools available for studying cavity QED have grown more advanced, so too have these measurements. There is a sizable literature devoted to the evolution of atom-cavity spectroscopy - from early measurements taken with atomic beams to measurements carried out (by our group in 2004) in which we were able to extract a full transmission spectrum from exactly one atom. In this Section I will review the advancements made by our group at Caltech during my tenure here with regard to measurement of vacuum Rabi spectra and present a new set of measurements which demonstrate the nonlinear scaling in the shape of these spectra as a function of the discrete number of atoms coupled to the cavity mode.

6.2.1 Review of Early Work

Our group has long relied on key spectroscopic features of the atom-cavity system for performing atomic state measurements (*i.e.*, up-goers and down-goers, as described in Chapter 3). However these measurements generally return a binary answer - “yes” or “no”, the transmission at a particular detuning is above or below a particular threshold, indicating whether the atom is coupled or uncoupled to the cavity. In general, the full transmission spectrum obtained by probing the system the cavity with a field at variable detuning from atom-cavity resonance can contain a considerable amount of information about the nature of the coupling. In fact, within the cavity QED research community there has been a long history of measuring the vacuum Rabi spectrum because observation of a well-defined splitting is a definite hallmark of strong coupling. This work goes back to the early 1990’s

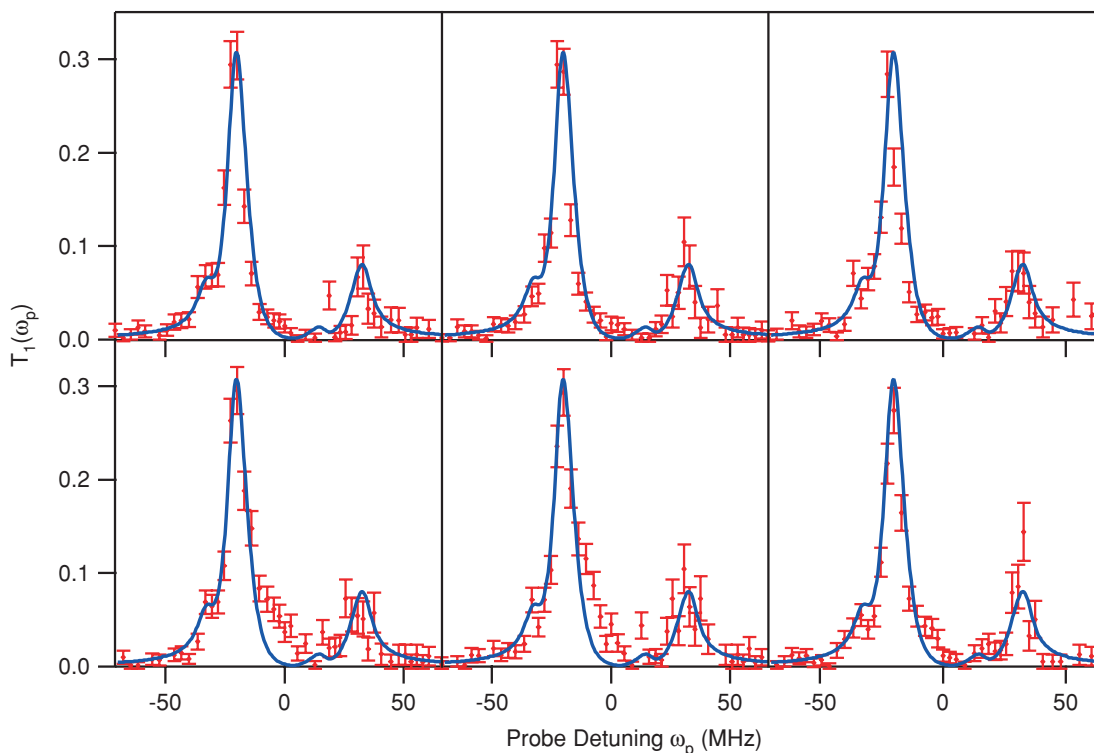


Figure 6.15: Red points represent measured vacuum Rabi spectra $T_1(\omega_p)$ for six individual atoms trapped within our cavity. These six spectra were drawn randomly for a pool of 28 similar spectra and were measured as described in Reference [41]. Each set of data is drawn from one-and-only-one atom. The solid blue trace represents the solution to the master equation for the system [29].

when ultra-high finesse “super” mirrors first became available. The earliest measurements were carried out with atomic beams of varying flux (but typically a mean intracavity atom number $\bar{N} \sim 1$) [95, 96, 97], and which later developed into experiments involving cold atoms falling freely via gravity through the mode of the cavity [98]. Even with the advent of techniques for confinement within the cavity mode, many early measurements involving single, trapped atoms required averaging over $> 10^3$ atoms to reconstruct a full spectrum [99].

In contrast to this earlier work, our group demonstrated in 2004 the ability to map out

an entire vacuum Rabi spectrum for one-and-the-same atom. Upon loading an atom into the intracavity FORT, we proceeded to sweep the frequency of a probe laser eight times over a range of 140 MHz centered on empty cavity resonance. The intensity of the probe laser is such that it only weakly drives system thereby restricting our measurement to the basis of 0 and 1 excitations. At each of a series of discrete detuning values we integrated the number of photodetection events registered in the cavity output mode. For those atoms which were still present in the cavity mode following each of the eight sweeps we then compiled the resultant transmission as a function of probe frequency $T_1(\omega_p)$, and this data is plotted in Figure 6.15. Notice that for each atom we see a clear and well-defined splitting. Also plotted is the steady-state solution to the full master equation to the system which shows excellent agreement with the data. The asymmetries present between the two vacuum Rabi peaks in this data is the result of the myriad experimental complications which have been described throughout this thesis (cavity birefringence, FORT-induced AC Stark shifts, optical pumping effects, etc.). For more details of these measurements please see the theses of Andreea Boca [23] and Kevin Birnbaum [29]. It should be noted however that this is the first true demonstration of atom-cavity spectroscopy in optical cavity QED for precisely one atom and is demonstrative of the type of experiment that our technique for intracavity dipole trapping can realize.

While the ability to resolve a complete vacuum Rabi spectrum for one-and-the-same atom in the weak driving limit is arguably the “gold standard” for spectroscopic characterization of strong atom-cavity coupling, this is by no means the only type of interesting spectroscopic phenomena which can present itself in these measurements. In particular, the Jaynes-Cummings model (and as we will see in the next Subsection, the Tavis-Cummings model for multiple atoms) exhibit interesting nonlinearities as a function of the number of excitations (and atoms) present in the system. Recall, for instance, that as we climb the so-called Jaynes-Cummings “ladder” of states that the energy splitting between the eigenstates of the system scales as \sqrt{n} , where n is the number of excitations present. These nonlinearities are evidence of manifestly quantum phenomena and have lead to a series of interesting results. For instance, in 2005 our group observed what is known as the photon blockade effect (in analogy with the Coloumb blockade effect in solid state physics [100]). In

a simple picture treating a two-state atom and one-mode cavity, the absorption of a single excitation from a probe laser of frequency $\omega_L = \omega_C + g$ resonantly populates one of the two energy eigenstates of the system in the one-excitation manifold of states. Because of the nonlinearity in the Jaynes-Cummings ladder, in order to resonantly excite population from this manifold to the two-excitation manifold of states, the probe laser would need to instead be tuned to $\omega_L = \omega_C + \sqrt{2}g$. Therefore we expect that upon absorption of a photon into the system, the probability that any further absorption of photons from the probe field will be off-resonantly suppressed until the system has again relaxed to the ground state. Effectively, the absorption of one photon blocks subsequent absorption and the atom-cavity system thereby acts as a quantum optical filter, transforming a classical, coherent input field into a field which exhibits sub-Poissonian and antibunched photon statistics. Indeed, we were able to observe these characteristic photon statistics in the laboratory [101] and found them to be in good agreement with a detailed numerical model of the system [102]. While this measurement served as indirect confirmation of the nonlinearity inherent to the eigenenergy spectrum of the Jaynes-Cummings Hamiltonian, the Rempe group has since observed direct spectroscopic evidence of this structure [103].

6.2.2 Vacuum Rabi Spectra for One and Two Atoms

Motivated by the need for a fast and efficient method for discriminating between one or two atoms in a cavity-coupled state, we recently measured the nonlinearity as a function of atom number in the scaling of the vacuum Rabi spectrum. With multiple atoms present in the cavity the simple, two-state atom picture which lead to the Jaynes-Cummings Hamiltonian in Chapter 2 must be replaced by what is known as the Tavis-Cummings interaction Hamiltonian [19] for a number N of two-state atomic systems each coupled with energy $\hbar g_0$ to a single mode of the electromagnetic field. The Hamiltonian takes the form

$$\hat{H}_I = \hbar g_0 \sum_{j=1}^N \left(\hat{a}^\dagger \hat{\sigma}_j^- + \hat{a} \hat{\sigma}_j^+ \right), \quad (6.31)$$

where $(\hat{a}^\dagger, \hat{a})$ and $(\hat{\sigma}_j^+, \hat{\sigma}_j^-)$ are the raising and lowering operators for the field and the j -th atom, respectively. In the limit of weak driving, we truncate our cavity Fock state basis

to $\{|0\rangle_C, |1\rangle_C\}$ and our atomic state basis to $\{|0\rangle_A, |1\rangle_A\}$ where $|0\rangle_A = (|0\rangle_1 |0\rangle_2 \dots |0\rangle_N)$, $|1\rangle_A = \frac{1}{\sqrt{N}} \sum_{k=1}^N (|0\rangle_1 \dots |1\rangle_k \dots |0\rangle_N)$ and $(|0\rangle_k, |1\rangle_k)$ correspond to the ground and excited states of the k -th atom, respectively. In the coupled basis, $\{|1\rangle_C |0\rangle_A, |0\rangle_C |1\rangle_A\}$, the two dressed states of \widehat{H}_I for a single excitation in the system exhibit normal-mode splitting with corresponding energy eigenvalues $E_{\pm} = \pm \hbar g_0 \sqrt{N}$.

In the work described earlier in this Section, this splitting has been measured experimentally for $N = 1$ (where the Tavis-Cummings model reduces to the Jaynes-Cummings model) and for N fluctuating over the duration of the measurement with Poissonian statistics, but never for $N > 1$ and stationary. Here we report the first observation of the normal-mode splitting for two atoms strongly coupled to an optical cavity and verify the nonlinear scaling of the normal-mode splitting as a function of N . This result relies on a new technique for the real-time discrimination of intracavity atom number (see Chapter 4 of Tracy Northup's dissertation [26]) and represents a first step towards the implementation of more complex protocols involving controlled interactions between a small number of atoms sharing a common coupling to a single cavity mode.

In order to measure the spectrum, the cavity is tuned such that the resonant frequency of the high-frequency birefringent mode coincides with the $(4 \leftrightarrow 5')$ transition in cesium (for spectroscopy we rely on this transition because it is closed and therefore requires minimal repumping during the course of a measurement). A laser drives the cavity with a probe field σ^+ -polarized with variable detuning Δ_p from the shared atom-cavity resonance such that the average intracavity photon number for an empty cavity is $\bar{n} = 0.2$. The transmission of the higher-frequency mode-polarized component of this field is monitored and recorded downstream. Immediately following the release of a MOT and subsequent PG cooling, there are typically $N_{\text{load}} \sim 10$ atoms trapped in the FORT using the Raman-repumped loading technique described in Chapter 4. In order to perform atom number discrimination and selection [26], we simultaneously apply the probe field, tuned to resonance with the empty cavity and atom ($\Delta_p = 0$), and the Raman field tuned to resonance with the field-insensitive $(|3, 0\rangle \leftrightarrow |4, 0\rangle)$ hyperfine ground state transition ($\delta = 0$). Because we are in the strong coupling regime, just one atom in the cavity-coupled $F = 4$ manifold of ground states is sufficient to significantly suppress transmission of probe. Atoms in the $F = 3$ manifold

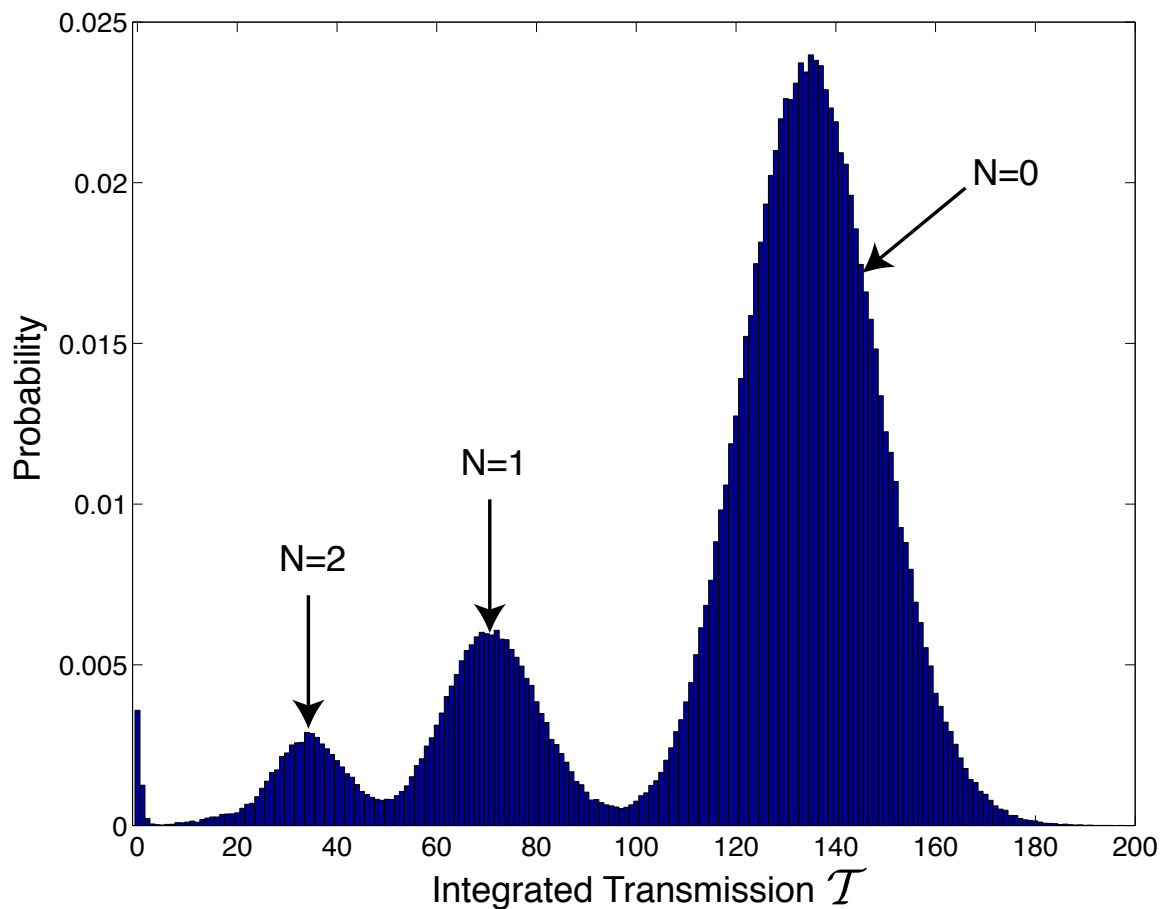


Figure 6.16: Histogram of the integrated photodetection events in transmission \mathcal{T} during a $\tau_{\text{int}} = 500 \mu\text{s}$ interval versus the probability to measure that number of photocounts. This histogram was measured after initial atom number discrimination such that the probability of detecting $N > 2$ atoms in the cavity is greatly reduced. Note that there are three clearly distinct features corresponding to the empty cavity transmission ($N = 0$), as well as $N = 1$ and $N = 2$ atoms.

are uncoupled and do not affect the cavity field. We integrate photocounts from probe for $\tau_{\text{int}} = 1$ ms with the Raman pair effective Rabi frequency set such that $\Omega_E \gg (2\pi)(\tau_{\text{int}}^{-1})$. The effect of the Raman pair is to induce the atomic state of each atom in the trap to oscillate rapidly between coupled and uncoupled ground states. As a result, the average integrated photocounts will vary as the atom number,

$$\bar{\mathcal{T}}(\tau_{\text{int}}, N, \bar{n}, \alpha) \simeq 1/2^N \bar{n} \tau_{\text{int}} \alpha \quad (6.32)$$

where $\alpha = 0.04$ is the measured detection efficiency for this set of data. A histogram of repeated measurements of \mathcal{T} is shown in Figure 6.16 and demonstrates features corresponding to the presence of $N \in \{0, 1, 2, \dots\}$ atom and exhibiting widths consistent with counting statistics. This technique allows us to discriminate the presence of $(0, 1, 2)$ atoms and to condition the start of any subsequent experiment on the presence of the desired number of atoms in the cavity.

To acquire an average atom-cavity transmission spectra for N atoms, $\bar{T}_N(\omega_p)$, we begin each of a series of trials by preparing $N_{\text{load}} > 2$ atoms in the FORT followed by repetition of the atom number discrimination technique described above until we have determined that $N \leq 2$. We then repeat the following protocol a total of 200 times over $\tau_{\text{total}} = 540$ ms. First, we cool the motion of atoms within the trap by applying first order Raman sideband cooling for a duration $\tau_{\text{cool}} = 2$ ms with $\Omega_E \sim (2\pi)(200 \text{ kHz})$ (Chapter 4). Empirically this was found to significant extend the effective lifetime of atoms within the FORT for this type of measurement. Following each cooling interval, we drive the cavity with probe at a fixed atom-cavity detuning Δ_p , which is iterated from trial-to-trial over a range of 160 MHz in steps of 3 MHz. The transmission of the \hat{l}_+ -polarized component of the probe in photocounts is integrated for $\tau_{\text{probe}} = 100 \mu\text{s}$ and recorded. Finally, we perform atom number detection for a duration $\tau_{\text{int}} = 500 \mu\text{s}$. Based on the integrated photocounts for this interval, we are able to discriminate the intracavity atom number on a measurement-by-measurement basis.

In order to ensure that each spectrum corresponds to exactly N atoms, those trials for which each of the 200 cooling and measurement intervals corresponded to the detection of $N = (1, 2)$ atoms are kept, while those for which the measured atom number varied during

the trial are discarded. The total, average transmission spectra $T_{1,2}(\omega_p)$ are constructed by averaging the integrated photocounts obtained during probe intervals for every valid trial corresponding to detuning Δ_p . These spectra are then divided by a normalization spectrum taken at each fixed value of the detuning, however with the cavity manually tuned into resonance with the probe field at that detuning. This allows us to account and correct for effects associated with beam pointing and intensity variations as a function of the frequency at which the AOM used to provide the probe shifts is driven. In Figure 6.17, we present transmission spectra $T_1(\omega_p)$, obtained by averaging over 1567 single-atom trials (21 mean trials per data point), and $T_2(\omega_p)$, averaged over 785 two-atom trials (10 mean trials per data point).

Both spectra exhibit a well-resolved normal-mode splitting consistent with operation in the regime of strong coupling. Due to the extremely large size of the Hilbert space for the full, two-atom, two-mode cavity master equation we are unable to carry out a complete numerical simulation of this result as was done for previous measurements in this dissertation. In fact, the requirements needed to simply generate the Liouvillian for this system far exceed the memory handling capabilities of both `MATLAB` as well as the Windows operating system. Truncation of the state space to a limited number of Zeeman states is impossible given that our probe interval is much shorter than that necessary for the system to enter steady state. Instead we can make some qualitative observations about the two spectra. First, it is clear that the shapes of the spectra are similar and that the scaling is nonlinear. By selecting clearly-resolved local maxima $T_2(\omega_{max})$ in the two atom spectrum and the analogous maxima on $T_1(\omega'_{max})$ we can calculate $\omega_{max}/\omega'_{max} \approx 0.93\sqrt{2}$, where $\omega_{max}/\omega'_{max} = \sqrt{2}$ is the scaling anticipated by the simple Tavis-Cummings model. Another important feature to note with regard to the two spectra is that near $\Delta_p = (2\pi)(-43 \text{ MHz})$ there is a large, well-resolved spectroscopic difference between T_1 and T_2 which suggests that in an integration time of only $100 \mu\text{s}$ we are able to resolve the number of cavity-coupled atoms. Using the scaling in the vacuum Rabi spectrum as a signal for fast resolution of the intracavity atom number could a potentially useful technique for performing experiments wherein, for instance, simultaneous projective measurements on two cavity-coupled and mutually-entangled atoms are necessary.

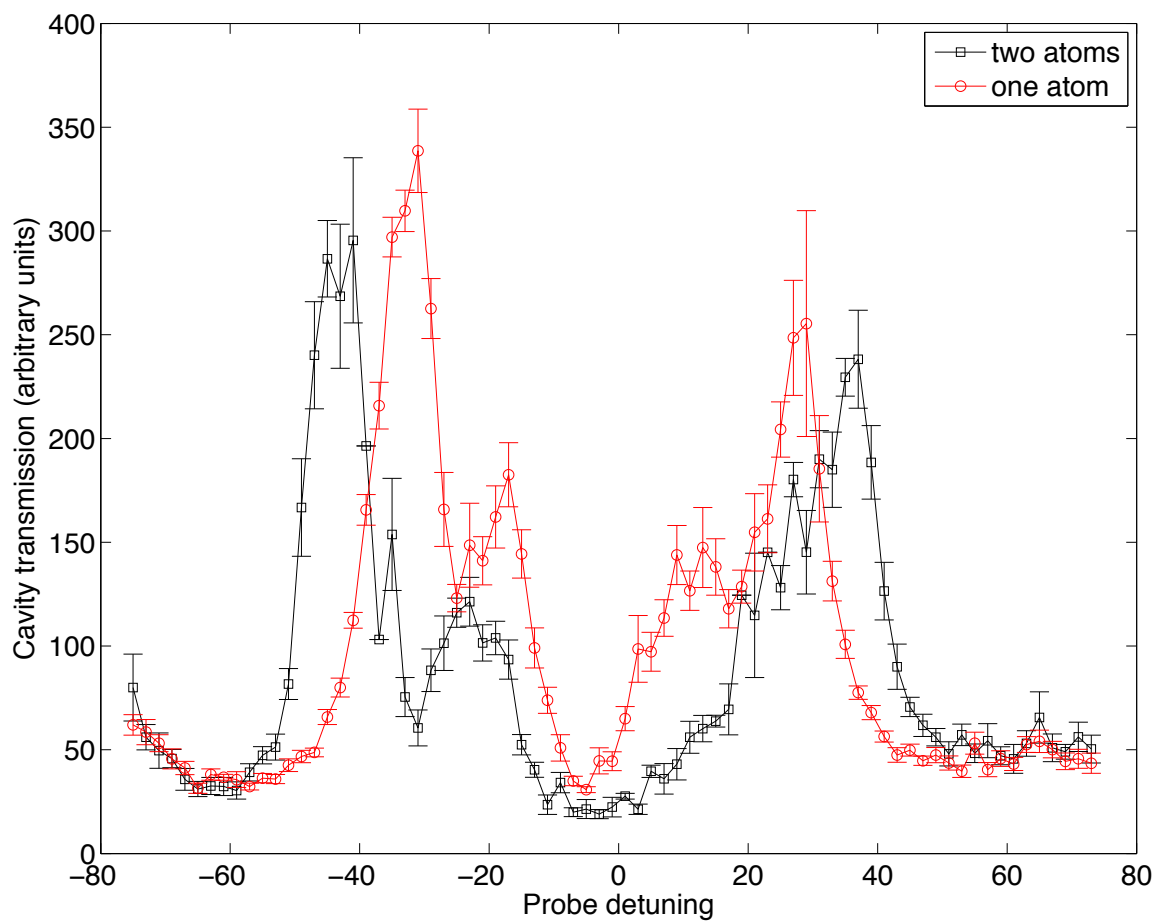


Figure 6.17: Vacuum Rabi spectra for one and two atoms, $T_1(\omega_p)$ and $T_2(\omega_p)$. Data corresponds to 1567 trials with one atom present in the cavity and 785 trials with two atoms present. Both spectra are divided by a normalization spectrum which corrects for beam pointing and intensity fluctuations as a function of detuning, Δ_p .

Appendix A

Cesium D2 Dipole Matrix Elements

$ 3, m_F\rangle \leftrightarrow F', m_F\rangle$ (π -polarization)							
$m_F =$	-3	-2	-1	0	1	2	3
$F' = 2$		$-\sqrt{\frac{5}{21}}$	$-\sqrt{\frac{8}{21}}$	$-\sqrt{\frac{3}{7}}$	$-\sqrt{\frac{8}{21}}$	$-\sqrt{\frac{5}{21}}$	
$F' = 3$	$\frac{3}{4}$	$\frac{1}{2}$	$\frac{1}{4}$	0	$-\frac{1}{4}$	$-\frac{1}{2}$	$-\frac{3}{4}$
$F' = 4$	$\sqrt{\frac{5}{48}}$	$\sqrt{\frac{5}{28}}$	$\sqrt{\frac{25}{112}}$	$\sqrt{\frac{5}{21}}$	$\sqrt{\frac{25}{112}}$	$\sqrt{\frac{5}{28}}$	$\sqrt{\frac{5}{48}}$

Table A.1: Dipole matrix elements $\langle F', m'_F | e\hat{r} | 3, m_F \rangle$ in units of $\langle J' || e\hat{r} || J \rangle$ for transitions from the $6S_{1/2}, F = 3$ ground state which satisfy $(m'_F - m_F) = 0$.

$ 3, m_F\rangle \leftrightarrow F', m_F + 1\rangle$ (σ^+ -polarization)							
$m_F =$	-3	-2	-1	0	1	2	3
$F' = 2$	$\sqrt{\frac{5}{7}}$	$\sqrt{\frac{10}{21}}$	$\sqrt{\frac{2}{7}}$	$\sqrt{\frac{1}{7}}$	$\sqrt{\frac{1}{21}}$		
$F' = 3$	$\sqrt{\frac{3}{16}}$	$\sqrt{\frac{5}{16}}$	$\sqrt{\frac{3}{8}}$	$\sqrt{\frac{3}{8}}$	$\sqrt{\frac{5}{16}}$	$\sqrt{\frac{3}{16}}$	
$F' = 4$	$\sqrt{\frac{5}{336}}$	$\sqrt{\frac{5}{112}}$	$\sqrt{\frac{5}{56}}$	$\sqrt{\frac{25}{168}}$	$\sqrt{\frac{25}{112}}$	$\sqrt{\frac{5}{16}}$	$\sqrt{\frac{5}{12}}$

Table A.2: Dipole matrix elements $\langle F', m'_F | e\hat{r} | 3, m_F \rangle$ in units of $\langle J' || e\hat{r} || J \rangle$ for transitions from the $6S_{1/2}, F = 3$ ground state which satisfy $(m'_F - m_F) = +1$.

$ 3, m_F\rangle \leftrightarrow F', m_F - 1\rangle$ (σ^- -polarization)							
$m_F =$	-3	-2	-1	0	1	2	3
$F' = 2$			$\sqrt{\frac{1}{21}}$	$\sqrt{\frac{1}{7}}$	$\sqrt{\frac{2}{7}}$	$\sqrt{\frac{10}{21}}$	$\sqrt{\frac{5}{7}}$
$F' = 3$		$-\sqrt{\frac{3}{16}}$	$-\sqrt{\frac{5}{16}}$	$-\sqrt{\frac{3}{8}}$	$-\sqrt{\frac{3}{8}}$	$-\sqrt{\frac{5}{16}}$	$-\sqrt{\frac{3}{16}}$
$F' = 4$	$\sqrt{\frac{5}{12}}$	$\sqrt{\frac{5}{16}}$	$\sqrt{\frac{25}{112}}$	$\sqrt{\frac{25}{168}}$	$\sqrt{\frac{5}{56}}$	$\sqrt{\frac{5}{112}}$	$\sqrt{\frac{5}{336}}$

Table A.3: Dipole matrix elements $\langle F', m'_F | e\hat{r} | 3, m_F \rangle$ in units of $\langle J' || e\hat{r} || J \rangle$ for transitions from the $6S_{1/2}, F = 3$ ground state which satisfy $(m'_F - m_F) = -1$.

$ 4, m_F\rangle \leftrightarrow F', m_F\rangle$ (π -polarization)									
$m_F =$	-4	-3	-2	-1	0	1	2	3	4
$F' = 3$		$-\sqrt{\frac{7}{144}}$	$-\sqrt{\frac{1}{12}}$	$-\sqrt{\frac{5}{48}}$	$-\frac{1}{3}$	$-\sqrt{\frac{5}{48}}$	$-\sqrt{\frac{1}{12}}$	$-\sqrt{\frac{7}{144}}$	
$F' = 4$	$\sqrt{\frac{7}{15}}$	$\sqrt{\frac{21}{80}}$	$\sqrt{\frac{7}{60}}$	$\sqrt{\frac{7}{240}}$	0	$-\sqrt{\frac{7}{240}}$	$-\sqrt{\frac{7}{60}}$	$-\sqrt{\frac{21}{80}}$	$-\sqrt{\frac{7}{15}}$
$F' = 5$	$\sqrt{\frac{1}{5}}$	$\sqrt{\frac{16}{45}}$	$\sqrt{\frac{7}{15}}$	$\sqrt{\frac{8}{15}}$	$\sqrt{\frac{5}{9}}$	$\sqrt{\frac{8}{15}}$	$\sqrt{\frac{7}{112}}$	$\sqrt{\frac{16}{45}}$	$\sqrt{\frac{1}{5}}$

Table A.4: Dipole matrix elements $\langle F', m'_F | e\hat{r} | 4, m_F \rangle$ in units of $\langle J' || e\hat{r} || J \rangle$ for transitions from the $6S_{1/2}, F = 4$ ground state which satisfy $(m'_F - m_F) = 0$.

$ 4, m_F\rangle \leftrightarrow F', m_F + 1\rangle$ (σ^+ -polarization)									
$m_F =$	-4	-3	-2	-1	0	1	2	3	4
$F' = 3$	$\sqrt{\frac{7}{36}}$	$\sqrt{\frac{7}{48}}$	$\sqrt{\frac{5}{48}}$	$\sqrt{\frac{5}{72}}$	$\sqrt{\frac{1}{24}}$	$\sqrt{\frac{1}{48}}$	$\frac{1}{12}$		
$F' = 4$	$\sqrt{\frac{7}{60}}$	$\sqrt{\frac{49}{240}}$	$\sqrt{\frac{21}{80}}$	$\sqrt{\frac{7}{24}}$	$\sqrt{\frac{7}{24}}$	$\sqrt{\frac{21}{80}}$	$\sqrt{\frac{49}{240}}$	$\sqrt{\frac{7}{60}}$	
$F' = 5$	$\sqrt{\frac{1}{45}}$	$\sqrt{\frac{1}{15}}$	$\sqrt{\frac{2}{15}}$	$\sqrt{\frac{2}{9}}$	$\sqrt{\frac{1}{3}}$	$\sqrt{\frac{7}{15}}$	$\sqrt{\frac{28}{45}}$	$\sqrt{\frac{4}{5}}$	1

Table A.5: Dipole matrix elements $\langle F', m'_F | e\hat{r} | 4, m_F \rangle$ in units of $\langle J' || e\hat{r} || J \rangle$ for transitions from the $6S_{1/2}, F = 4$ ground state which satisfy $(m'_F - m_F) = +1$.

$ 4, m_F\rangle \leftrightarrow F', m_F - 1\rangle$ (σ^- -polarization)									
$m_F =$	-4	-3	-2	-1	0	1	2	3	4
$F' = 3$			$\frac{1}{12}$	$\sqrt{\frac{1}{48}}$	$\sqrt{\frac{1}{24}}$	$\sqrt{\frac{5}{72}}$	$\sqrt{\frac{5}{48}}$	$\sqrt{\frac{7}{48}}$	$\sqrt{\frac{7}{36}}$
$F' = 4$		$-\sqrt{\frac{7}{60}}$	$-\sqrt{\frac{49}{240}}$	$-\sqrt{\frac{21}{80}}$	$-\sqrt{\frac{7}{24}}$	$-\sqrt{\frac{7}{24}}$	$-\sqrt{\frac{21}{80}}$	$-\sqrt{\frac{49}{240}}$	$-\sqrt{\frac{7}{60}}$
$F' = 5$	1	$\sqrt{\frac{4}{5}}$	$\sqrt{\frac{28}{45}}$	$\sqrt{\frac{7}{15}}$	$\sqrt{\frac{1}{3}}$	$\sqrt{\frac{2}{9}}$	$\sqrt{\frac{2}{15}}$	$\sqrt{\frac{1}{15}}$	$\sqrt{\frac{1}{45}}$

Table A.6: Dipole matrix elements $\langle F', m'_F | e\hat{r} | 4, m_F \rangle$ in units of $\langle J' || e\hat{r} || J \rangle$ for transitions from the $6S_{1/2}$, $F = 4$ ground state which satisfy $(m'_F - m_F) = -1$.

Appendix B

ADWIN Gold Timing Code

In this Appendix, I will briefly layout the syntax and structure of the code which we use to control the timing for our experiment. As mentioned in Chapter 3, the overall timing is controlled by an ADWin-brand ADWin Gold pulse generation system using TTL-level logic. The ADWin comes pre-packaged with control software called ADBasic which offers very basic programming functions but is not conducive to generating large or complex pulse sequences. In order to accommodate the types of timing sequences which we typically perform in the laboratory, David Boozer has coded a versatile and user-friendly pulse compiler program in c ('pulse.c'). This compiler program has its own metalanguage which is completely independent of the ADBasic system and which compiles timing input files ('timing.in') into a form which ADBasic can conveniently read ('foo.txt').

I very strongly emphasize that the original design and coding for this system were carried out entirely by David Boozer. I will omit the ADBasic script and compiler code necessary to translate this section into a form which can communicate with the ADWin, and refer the reader directly to David in order to obtain this information if interested. With that said, however, the metalanguage in which the timing code is written is very simple to interpret, conveys all the information about the timing of the system necessary to understand, at an operational-level, what we are doing and has not yet been formally documented anywhere.

B.1 Syntax

The syntax for the pulse.c metalanguage is as follows:

```

<cmd> --> p<name> : <cmd>
    --> invert <digital channel>
    --> define t<name> <time>
    --> define c<name> <int>
    --> define a<name> <int>
    --> begin_comment <cmds> end_comment
    --> [<time>, <time>] <digital channel>
    --> <time> aout <analog channel> > <float>
    --> <time> inline ' <string> '
    --> <time> loop <int> { <cmds> }

<time> --> <time> + <time>
    --> <time> - <time>
    --> ( <time> )
    --> start( p<name> )
    --> stop( p<name> )
    --> t<name>
    --> <float>

<digital channel> --> c<name>
    --> <int>

<analog channel> --> a<name>
    --> <int>

```

Line comments are denoted by ; and block comments (*i.e.*, omission of blocks of code from the script) are done by inserting `begin_comment` and `end_comment` around the block of code. These code block are generally then reinserted into the script by line-commenting the block comment headers.

B.2 Header and Preamble

```

;-----
; timing.in
; David Boozer
; 03 May 2006
;-----
; to load these pulses into ADwin box:
;   type "C:\ADwin\ADbasic3\Inc>pulse-new timing.in" in DOS
;   run ADbasic, open "C:\ADwin\ADbasic3\Programs\pulses.bas",
;   press B to reboot then C to compile
;
; all time are in units of ms
;-----
; define channels
;-----

define c_umot_bfield 0      ; H/L --> field on/off
define c_lmot_bfield 4      ; H/L --> field on/off

define c_45_mot 3          ; H/L --> 4-5' mot light on/off
define c_mot_frequency 1    ; H/L --> 4-5' mot light pgc/doppler frequency
define c_mot_intensity 2    ; H/L --> 4-5' mot light pgc/doppler intensity

define c_probe 5           ; H/L --> cavity probe on/off

define c_44_load 6         ; H/L --> 4-4' load light on/off
define c_44_pump 7         ; H/L --> 4-4' pump light on/off

define c_33_pump 29        ; H/L --> 3-3' pumping light on/off

```

```

define c_33_load 9      ; H/L --> 3-3' loading light on/off
define c_33_mot 10     ; H/L --> 3-3' mot light on/off

define c_44_side 13    ; H/L --> 4-4' side light on/off
define c_45_side 21

define c_olddraman_a 14 ; H/L --> load Raman frequency on/off
define c_olddraman_b 17 ; H/L --> noise Raman frequency on/off
define c_olddraman_c 20 ; H/L --> misc. Raman frequency on/off
define c_olddraman_d 22 ; H/L --> misc. Raman frequency on/off
define c_olddraman_e 30 ; H/L --> misc. Raman frequency on/off

define c_probe_freq 8  ; frequency switch for probe upshift

define c_card_trig 12  ; downgoing edge triggers APD card

define c_channel_c 15  ; rising edge goes to channel C of counting card

define c_tag 27        ; falling edge goes to channel D of counting card

define c_dummy 31     ; dummy channel

;-----
; invert channels
;-----

invert c_45_mot
invert c_umot_bfield
invert c_mot_frequency

```

```
invert c_33_pump
```

```
invert c_33_load
```

```
invert c_33_mot
```

```
invert c_44_load
```

```
invert c_44_pump
```

```
invert c_44_side
```

```
invert c_nearres_raman
```

```
invert c_probe_freq
```

```
invert c_tag
```

```
-----  
; define times  
-----
```

```
define t_umot_pgc_start    150.0
```

```
define t_umot_pgc_stop    t_umot_pgc_start + 10.0
```

```
define t_lmot_catch       t_umot_pgc_stop + 180.0
```

```
define t_lmot_pgc_start   t_lmot_catch + 150.0
```

```
define t_lmot_pgc_stop    t_lmot_pgc_start + 10.0
```

```
define t_load_start       t_lmot_pgc_stop + 30.0
```

```
define t_load_end         t_load_start + 5.0
```

B.3 External Device Programming

```

;-----
; pulse sequence
;-----

begin_comment

; c_olddraman_c
0.0 inline 'text = "cfrq:value 82.700 MHz"'
0.0 inline 'serial_out (10)'
0.0 inline 'text = "cfrq:inc 50.0 kHz"'
0.0 inline 'serial_out (10)'

end_comment

```

B.4 MOT and FORT Loading

```

; set number of times to loop, as for scans, etc.
1.0 loop 1 {

; set bias coil currents for lower mot loading
0.0 aout 1 > -1.66 ; z axial (0.5 A/V)
0.0 aout 2 > -5.68 ; x fed-from-above (0.5 A/V)
0.0 aout 3 > -6.16 ; y fed-from-below (1 A/V)

; load upper mot
[0.0, t_umot_pgc_start] c_umot_bfield
[0.0, t_umot_pgc_stop] c_45_mot
[0.0, t_umot_pgc_stop] c_33_mot

```

```

; pg cool atoms in upper mot
[t_umot_pgc_start, t_umot_pgc_stop] c_mot_intensity
[t_umot_pgc_start, t_umot_pgc_stop] c_mot_frequency

; catch atoms in lower mot
[t_lmot_catch, t_lmot_pgc_start-5.0] c_lmot_bfield
[t_lmot_catch, t_lmot_pgc_start-5.0] c_45_mot
[t_lmot_catch, t_lmot_pgc_start-5.0] c_33_mot

; pg cool atoms in lower mot
[t_lmot_pgc_start, t_lmot_pgc_stop] c_45_mot
[t_lmot_pgc_start, t_lmot_pgc_stop] c_33_mot
[t_lmot_pgc_start, t_lmot_pgc_stop] c_mot_intensity
[t_lmot_pgc_start, t_lmot_pgc_stop] c_mot_frequency

; load an atom into the FORT using a combination of Raman and Lattice
[t_load_start, t_load_end] c_44_load
;[t_load_start, t_load_end] c_33_load
;[t_load_start, t_load_end] c_probe
[t_load_start, t_load_end] c_oldraman_a

; set bias coil currents for Raman transitions
t_load_end+5.0 aout 1 > -1.625 ; z axial (null is at -1.625) (.5 A/V)
t_load_end+5.0 aout 2 > -2.00 ; x fed-from-above (null is at -2.00) (0.5 A/V)
t_load_end+5.0 aout 3 > -5.00 ; y fed-from-below (null is at -5.00) (1 A/V)

; trigger photon counting card with downgoing edge
p_trigger_card:
[t_load_end+14.0, t_load_end+15.0] c_card_trig

```

```

; see if we have an atom by downgoer detection
[t_load_end+15.0, t_load_end+15.1] c_probe
[t_load_end+15.0, t_load_end+15.1] c_33_load
;[t_load_end+14.0, t_load_end+14.1] c_43_probe
;[t_load_end+16.0, t_load_end+16.5] c_44_pump

; tag atom at the P7888
t_load_end+15.2 inline 'n_pulses(i,11)'

```

B.5 Individual Experiment Code Blocks

I have included some sample blocks of code for individual experiments which we have performed in the laboratory.

B.5.1 STIRAP-Based Single Photon Generation

```

;-----
; Single Photon Generation
;-----

begin_comment

t_load_end+20 loop 50000 {

[0.000,0.001] c_channel_c

[0.000,0.001] c_33_pump
[0.002,0.006] c_44_pump
}

```

```
end_comment
```

B.5.2 Reversible State Transfer Measurements

```
;------
; Fringe Measurement
;------
```

```
begin_comment
```

```
define t_start t_load_end+20.0
```

```
p_cycle:
```

```
t_start loop 2000 {
```

```
[0.000,0.001] c_channel_c
```

```
;;; Measurement #1: (incoherent absorbtion)
```

```
define t_1 0.020
```

```
; pump atom to F=4
```

```
[t_1+0.000, t_1+0.008] c_33_load
```

```
[t_1+0.001, t_1+0.009] c_33_side
```

```
; second 3-3' on, first 4-3' on
```

```
[t_1+0.0100, t_1+0.0127] c_43_veto_on
```

```
[t_1+0.0100, t_1+0.0170] c_srs_trig
```

```
[t_1+0.0124, t_1+0.0170] c_33_pump
```

```
;;;;; Measurement #2: (coherent absorbtion)
```

```
define t_2 0.040
```

```
; pump atom to F=4
```

```
[t_2+0.000, t_2+0.008] c_33_load
```

```
[t_2+0.001, t_2+0.009] c_33_side
```

```
; first & second 3-3' on, first 4-3' on
```

```
[t_2+0.0100, t_2+0.0127] c_43_veto_on
```

```
[t_2+0.0100, t_2+0.0170] c_srs_trig
```

```
[t_2+0.0100, t_2+0.0170] c_33_pump
```

```
;;;;; Measurement #3: (fringe, fixed phase)
```

```
define t_3 0.060
```

```
; pump atom to F=4
```

```
[t_3+0.000, t_3+0.008] c_33_load
```

```
[t_3+0.001, t_3+0.009] c_33_side
```

```
; first & second 3-3' on, first & second 4-3' on
```

```
[t_3+0.0100, t_3+0.0170] c_43_veto_on
```

```
[t_3+0.0100, t_3+0.0170] c_srs_trig
```

```
[t_3+0.0100, t_3+0.0170] c_33_pump
```

```
;;;;; Measurement #4: (fringe, vary phase)

define t_4 0.080

; pump atom to F=4

[t_4+0.000, t_4+0.008] c_33_load
[t_4+0.001, t_4+0.009] c_33_side

; first & second 3-3' on, first & second 4-3' on

[t_4+0.0100, t_4+0.0170] c_43_veto_on
[t_4+0.0100, t_4+0.0170] c_srs_trig
[t_4+0.0100, t_4+0.0170] c_33_pump
[t_4+0.0100, t_4+0.0127] c_which_phase

;;;;; Measurement #5: (efficiency) pump atom to F=3, second 3-3' on

define t_5 0.100

; pump atom to F=3

[t_5+0.000, t_5+0.008] c_44_load
[t_5+0.001, t_5+0.009] c_44_side

; second 3-3' on

[t_5+0.0100, t_5+0.0170] c_srs_trig
[t_5+0.0124, t_5+0.0170] c_33_pump
```

```
;;;;; Measurement #6: (background) pump atom to F=4, both 3-3' on
```

```
define t_6 0.120
```

```
; pump atom to F=4
```

```
[t_6+0.000, t_6+0.008] c_33_load
```

```
[t_6+0.001, t_6+0.009] c_33_side
```

```
; first & second 3-3' on
```

```
[t_6+0.0100, t_6+0.0170] c_srs_trig
```

```
[t_6+0.0100, t_6+0.0170] c_33_pump
```

```
;;;;; Measurement #7: (no fringe, fixed phase)
```

```
define t_7 0.140
```

```
; pump atom to F=4
```

```
[t_7+0.000, t_7+0.008] c_33_load
```

```
[t_7+0.001, t_7+0.009] c_33_side
```

```
; second 3-3' on, first & second 4-3' on
```

```
[t_7+0.0100, t_7+0.0170] c_43_veto_on
```

```
[t_7+0.0100, t_7+0.0170] c_srs_trig
```

```
[t_7+0.0124, t_7+0.0170] c_33_pump
```

```
;;;; Measurement #8: (no fringe, vary phase)

define t_8 0.160

; pump atom to F=4

[t_8+0.000, t_8+0.008] c_33_load
[t_8+0.001, t_8+0.009] c_33_side

; second 3-3' on, first & second 4-3' on

[t_8+0.0100, t_8+0.0170] c_43_veto_on
[t_8+0.0100, t_8+0.0170] c_srs_trig
[t_8+0.0124, t_8+0.0170] c_33_pump
[t_8+0.0100, t_8+0.0127] c_which_phase

}

define t_atom_detect stop(p_cycle);

[t_atom_detect, t_atom_detect+0.001] c_channel_c;

p_atom_detect:
t_atom_detect+0.001 loop 10000 {
[0.000,0.001] c_33_load
[0.001,0.002] c_44_pump
}

define t_delay stop(p_atom_detect);
```

```
[t_delay+1.0, t_delay+11.0] c_33_load;
```

```
end_comment
```

B.5.3 Raman Spectroscopy

```
;-----  
; raman scan, FORT+Raman configuration  
;-----
```

```
begin_comment
```

```
p_main_loop:
```

```
t_load_end+20.0 loop 500 {
```

```
define t_raman_pump 0.000
```

```
p_pump_r:
```

```
; Incoherent Raman Optical Pumping
```

```
0.001 loop 40 {
```

```
[t_raman_pump+0.00000, t_raman_pump+0.00030] c_44_side ; 1
```

```
[t_raman_pump+0.00030, t_raman_pump+0.00060] c_44_pump
```

```
[t_raman_pump+0.00060, t_raman_pump+0.00090] c_44_side ; 2
```

```
[t_raman_pump+0.00090, t_raman_pump+0.00120] c_44_pump
```

```
[t_raman_pump+0.00120, t_raman_pump+0.00150] c_44_side ; 3
```

```
[t_raman_pump+0.00150, t_raman_pump+0.00180] c_44_pump
```

```
[t_raman_pump+0.00180, t_raman_pump+0.00210] c_44_side ; 4
```

```
[t_raman_pump+0.00210, t_raman_pump+0.00240] c_44_pump
```

```
[t_raman_pump+0.00240, t_raman_pump+0.00270] c_44_side ; 5
```

```
[t_raman_pump+0.00270, t_raman_pump+0.00300] c_44_pump
```

```
[t_raman_pump+0.00300, t_raman_pump+0.00330] c_44_side ; 6
```

```

[t_raman_pump+0.00330, t_raman_pump+0.00360] c_44_pump
[t_raman_pump+0.00360, t_raman_pump+0.00390] c_44_side ; 7
[t_raman_pump+0.00390, t_raman_pump+0.00420] c_44_pump
[0.00500, 0.01500] c_oldraman_b
}

```

```

define t_raman_start_r stop(p_pump_r)+0.001
define t_probe_atom_r t_raman_start_r+0.025

```

```

[t_raman_start_r, t_probe_atom_r] c_oldraman_c

```

```

[t_probe_atom_r+0.000, t_probe_atom_r+0.001] c_channel_c
[t_probe_atom_r+0.002, t_probe_atom_r+0.200] c_probe
[t_probe_atom_r+0.100, t_probe_atom_r+0.200] c_33_load

```

```

[t_probe_atom_r+0.200, t_probe_atom_r+0.205] c_dummy
}

```

```

; Step detuning remotely
stop(p_main_loop)+1.0 inline 'text = "cfrq:up"'
stop(p_main_loop)+1.0 inline 'serial_out (10)'

```

```

end_comment

```

B.5.4 Fast Atomic Excitation

```

;-----
; cavity on 4-5', fast pulses of 4-5' from the side
;-----

```

```
begin_comment

define t_start t_load_end+20.0

p_cycle:
t_start loop 5000 {

[0.000,0.001] c_channel_c

[0.005,0.006] c_45_side

; pump the atom to F=4
[0.010,0.020] c_33_load
[0.010,0.020] c_33_side

}

define t_atom_detect stop(p_cycle)+20.0;

[t_atom_detect, t_atom_detect+0.001] c_channel_c
[t_atom_detect, t_atom_detect+0.100] c_probe
[t_atom_detect, t_atom_detect+0.100] c_33_load

[t_atom_detect+50.0, t_atom_detect+65.0] c_probe
[t_atom_detect+50.0, t_atom_detect+75.0] c_33_load

end_comment

}
```

Appendix C

Quantum Optics Toolbox Simulation

C.1 Introduction

Throughout my years at Caltech, a number of people have contributed to an effort to build a numerical model of the complete cesium energy level spectrum as it undergoes strong coupling with two, orthogonal non-degenerate cavity modes. One implementation was described by Kevin Birnbaum in his thesis in the context of modeling the vacuum Rabi spectrum measurements described in Chapter 6. Kevin's code relies on the underpinnings of Sze Tan's `MATLAB` Quantum Optics Toolbox (QOT) suite to carry out numerical integration of the master equation for the full system. After Kevin's departure, Tracy Northup contributed to this set of simulation code over the interceding years.

Independently of Kevin, David Boozer also developed a similar piece of simulation code for use with QOT. Using David's code, which is otherwise undocumented, as a starting point, I made a series of modifications and generalizations. The resulting m-files, which are described in this Appendix, provide the tools necessary to model a broad array of phenomena in our system. This code was used to obtain a variety of numerical results in this thesis, particularly in Chapter 6.

In the following sections I present the code with comments where appropriate in order to describe how the master equation is formulated and integrated and how the code can be used to predict particular observables. I neglect any discussion of the QOT syntax, which is well described in the documentation which accompanies the package.

As a word of warning, the size of the Hilbert space necessary to include every possible Zeeman state of the atom in the simulation will far exceed the memory handling capabilities of most MATLAB installations. For sufficiently large Hilbert spaces, it is necessary to run this code on a machine running MATLAB natively in a 64-bit Linux environment with > 8 GB of available system memory.

C.2 Preamble and User-Specified Parameters

```

%-----
% cesiumsim.m
% March 9, 2009
%-----
% Simulate atom-cavity effects on any transition within
% the D2 manifold of transitions
%-----
% User-specified input parameters are:
%-----
% g_states: vector list of hyperfine ground states to include in
%           simulation (i.e., [3 4])
% e_states: vector list of hyperfine excited states to include in
%           simulation (i.e., [3 4 5])
% z_states: vector list of specific Zeeman states in which to
%           initialize atom (i.e., [3,0;4,0] prepares a mixture of
%           |3,0> and |4,0>
% coupled_states: specifies which transition is resonant with the
%                 cavity (i.e, [4 5])
% Omega: specifies the strength of whatever probe or drive
%         field is used in the simulation, in MHz
% delay: passes a small, user controlled time delay for impulse
%         or timed events in the code, in us

```

```

% probe_freq: specifies the detuning of a probe or driving field
%               from the cavity resonance, in MHz
%-----
% Common user-specified output parameters are:
%-----
% na: time-dependent (or steady state) photon number in mode a
% nb: time-dependent (or steady state) photon number in mode b
% other: any variable called within the script can be introduced
% here as an output variable if needed
%-----
function [na, nb, other] = rabi_sim(g_states, e_states, z_states,
coupled_states, Omega, delay, probe_freq)
%-----
% specify constant parameters for simulation
%-----
gamma = 2*pi*5.2;
% atomic decay rate, fullwidth [MHz]
g = 2*pi*32.0;
% atom-cavity coupling rate [MHz]
kappa=2*pi*8.4;
% cavity linewidth, fullwidth [MHz]

splitting = 2*pi*2.1;
% ((frequency of x-mode)-(frequency of y-mode))/2, the birefringent splitting
cavity_freq = 0;
% cavity frequency relative to the user-specified transition

Delta_g = sparse(2*pi*[0 0 -9192 0]);
% ground state hyperfine splitting [MHz]
Delta_e = sparse(2*pi*[0 603.45 452.24 251.00 0]);

```

```

% excited state hyperfine splittings [MHz]

B = 2*pi*[0.0,0.0,0.0]; % magnetic field [Bx,By,Bz] [MHz]

Le4 = 4/15; % Lande g-factor for e4
Lg4 = 1/4; % Lande g-factor for g4
Lg3 = -1/4; % Lande g-factor for g3
Le2 = -2/3; % Lande g-factor for e2
Le5 = 1; % Lande g-factor for e5

t = 0.1+delay; % duration of simulation [us]
N = 1e3; % number of points
delta = t/(N-1); % timestep [us]

tlist = linspace(0,t,N); % initialize the list of simulation

%-----
% check user inputs for null values and duplicates
%-----

if isempty(g_states)==1||isempty(e_states)==1
    error('Invalid atomic state spaces.')
end

% sort and find unique elements of input state variables
e_states = unique(e_states);
g_states = unique(g_states);

%-----

```

```

% if Zeeman states are user-specified, count them
%-----
if max(ismember(g_states,3))==1; Ng3 = 2*3 + 1; else Ng3 = 0; end
% enumerate the number of states in g3 manifold
if max(ismember(g_states,4))==1; Ng4 = 2*4 + 1; else Ng4 = 0; end
% enumerate the number of states in g4 manifold
if max(ismember(e_states,3))==1; Ne3 = 2*3 + 1; else Ne3 = 0; end
% enumerate the number of states in e3 manifold
if max(ismember(e_states,4))==1; Ne4 = 2*4 + 1; else Ne4 = 0; end
% enumerate the number of states in e4 manifold
if max(ismember(e_states,2))==1; Ne2 = 2*2 + 1; else Ne2 = 0; end
% enumerate the number of states in e2 manifold
if max(ismember(e_states,5))==1; Ne5 = 2*5 + 1; else Ne5 = 0; end
% enumerate the number of states in e5 manifold

Natomic = Ng3 + Ng4 + Ne3 + Ne4 + Ne2 + Ne5; % total number of atomic states

Na = 2; % number of Fock states (mode a)
Nb = 2; % number of Fock states (mode b)

```

C.3 Generate System Operators

C.3.1 Atomic Operators

```

%-----
% generate full basis of atomic state vectors
%-----

for k=1:Natomic
    psi{k} = tensor(basis(Natomic,k),basis(Na,1),basis(Nb,1));
end

```

```
%-----  
% prepare atomic dipole operators  
%-----  
  
% define Clebsch-Gordan operators  
% murelj is the QOT built-in function for finding dimensionless  
% atomic dipole moments  
  
[cg_4m4,cg_404,cg_4p4] = murelj(4,4);  
[cg_3m4,cg_304,cg_3p4] = murelj(3,4);  
[cg_4m3,cg_403,cg_4p3] = murelj(4,3);  
[cg_3m3,cg_303,cg_3p3] = murelj(3,3);  
[cg_3m2,cg_302,cg_3p2] = murelj(3,2);  
[cg_4m5,cg_405,cg_4p5] = murelj(4,5);  
  
% define dipole moment operators  
  
d_4m4 = sqrt(7/12)*cg_4m4;  
d_404 = sqrt(7/12)*cg_404;  
d_4p4 = sqrt(7/12)*cg_4p4;  
  
d_3m4 = sqrt(5/12)*cg_3m4;  
d_304 = sqrt(5/12)*cg_304;  
d_3p4 = sqrt(5/12)*cg_3p4;  
  
d_4m3 = sqrt(1/4)*cg_4m3;  
d_403 = sqrt(1/4)*cg_403;  
d_4p3 = sqrt(1/4)*cg_4p3;
```

```

d_3m3 = sqrt(3/4)*cg_3m3;
d_303 = sqrt(3/4)*cg_303;
d_3p3 = sqrt(3/4)*cg_3p3;

d_3m2 = cg_3m2;
d_302 = cg_302;
d_3p2 = cg_3p2;

d_4m5 = cg_4m5;
d_405 = cg_405;
d_4p5 = cg_4p5;

%-----
% construct atomic lowering operators for specified states
%-----

% lowering operators for 4 <-- 4'

if (max(ismember(g_states,4))==1)&&(max(ismember(e_states,4))==1))
g4_m_e4 = sparse(Natomic, Natomic);
g4_0_e4 = sparse(Natomic, Natomic);
g4_p_e4 = sparse(Natomic, Natomic);

g4_m_e4(index_g(4,-4):index_g(4,4),index_e(4,-4):index_e(4,4)) = d_4m4;
g4_0_e4(index_g(4,-4):index_g(4,4),index_e(4,-4):index_e(4,4)) = d_404;
g4_p_e4(index_g(4,-4):index_g(4,4),index_e(4,-4):index_e(4,4)) = d_4p4;

g4_m_e4 = tensor(qo(g4_m_e4),identity(Na),identity(Nb));
g4_0_e4 = tensor(qo(g4_0_e4),identity(Na),identity(Nb));
g4_p_e4 = tensor(qo(g4_p_e4),identity(Na),identity(Nb));

```

```

g4_x_e4 = -sqrt(1/2)*(g4_p_e4 - g4_m_e4);
g4_y_e4 = i*sqrt(1/2)*(g4_p_e4 + g4_m_e4);
g4_z_e4 = g4_0_e4;
end

% lowering operators for 3 <-- 4'

if (max(ismember(g_states,3))==1)&&(max(ismember(e_states,4))==1)
g3_m_e4 = sparse(Natomic, Natomic);
g3_0_e4 = sparse(Natomic, Natomic);
g3_p_e4 = sparse(Natomic, Natomic);

g3_m_e4(index_g(3,-3):index_g(3,3),index_e(4,-4):index_e(4,4)) = d_3m4;
g3_0_e4(index_g(3,-3):index_g(3,3),index_e(4,-4):index_e(4,4)) = d_304;
g3_p_e4(index_g(3,-3):index_g(3,3),index_e(4,-4):index_e(4,4)) = d_3p4;

g3_m_e4 = tensor(qo(g3_m_e4),identity(Na),identity(Nb));
g3_0_e4 = tensor(qo(g3_0_e4),identity(Na),identity(Nb));
g3_p_e4 = tensor(qo(g3_p_e4),identity(Na),identity(Nb));

g3_x_e4 = -sqrt(1/2)*(g3_p_e4 - g3_m_e4);
g3_y_e4 = i*sqrt(1/2)*(g3_p_e4 + g3_m_e4);
g3_z_e4 = g3_0_e4;
end

% lowering operators for 4 <-- 3'

if (max(ismember(g_states,4))==1)&&(max(ismember(e_states,3))==1)
g4_m_e3 = sparse(Natomic, Natomic);

```

```

g4_0_e3 = sparse(Natomic, Natomic);
g4_p_e3 = sparse(Natomic, Natomic);

g4_m_e3(index_g(4,-4):index_g(4,4),index_e(3,-3):index_e(3,3)) = d_4m3;
g4_0_e3(index_g(4,-4):index_g(4,4),index_e(3,-3):index_e(3,3)) = d_403;
g4_p_e3(index_g(4,-4):index_g(4,4),index_e(3,-3):index_e(3,3)) = d_4p3;

g4_m_e3 = tensor(qo(g4_m_e3),identity(Na),identity(Nb));
g4_0_e3 = tensor(qo(g4_0_e3),identity(Na),identity(Nb));
g4_p_e3 = tensor(qo(g4_p_e3),identity(Na),identity(Nb));

g4_x_e3 = -sqrt(1/2)*(g4_p_e3 - g4_m_e3);
g4_y_e3 = i*sqrt(1/2)*(g4_p_e3 + g4_m_e3);
g4_z_e3 = g4_0_e3;
end

% lowering operators for 3 <-- 3'

if (max(ismember(g_states,3))==1)&&(max(ismember(e_states,3))==1)
g3_m_e3 = sparse(Natomic, Natomic);
g3_0_e3 = sparse(Natomic, Natomic);
g3_p_e3 = sparse(Natomic, Natomic);

g3_m_e3(index_g(3,-3):index_g(3,3),index_e(3,-3):index_e(3,3)) = d_3m3;
g3_0_e3(index_g(3,-3):index_g(3,3),index_e(3,-3):index_e(3,3)) = d_303;
g3_p_e3(index_g(3,-3):index_g(3,3),index_e(3,-3):index_e(3,3)) = d_3p3;

g3_m_e3 = tensor(qo(g3_m_e3),identity(Na),identity(Nb));
g3_0_e3 = tensor(qo(g3_0_e3),identity(Na),identity(Nb));
g3_p_e3 = tensor(qo(g3_p_e3),identity(Na),identity(Nb));

```

```

g3_x_e3 = -sqrt(1/2)*(g3_p_e3 - g3_m_e3);
g3_y_e3 = i*sqrt(1/2)*(g3_p_e3 + g3_m_e3);
g3_z_e3 = g3_0_e3;
end

% lowering operators for 3 <-- 2'

if (max(ismember(g_states,3))==1)&&(max(ismember(e_states,2))==1)
g3_m_e2 = sparse(Natomic, Natomic);
g3_0_e2 = sparse(Natomic, Natomic);
g3_p_e2 = sparse(Natomic, Natomic);

g3_m_e2(index_g(3,-3):index_g(3,3),index_e(2,-2):index_e(2,2)) = d_3m2;
g3_0_e2(index_g(3,-3):index_g(3,3),index_e(2,-2):index_e(2,2)) = d_302;
g3_p_e2(index_g(3,-3):index_g(3,3),index_e(2,-2):index_e(2,2)) = d_3p2;

g3_m_e2 = tensor(qo(g3_m_e2),identity(Na),identity(Nb));
g3_0_e2 = tensor(qo(g3_0_e2),identity(Na),identity(Nb));
g3_p_e2 = tensor(qo(g3_p_e2),identity(Na),identity(Nb));

g3_x_e2 = -sqrt(1/2)*(g3_p_e2 - g3_m_e2);
g3_y_e2 = i*sqrt(1/2)*(g3_p_e2 + g3_m_e2);
g3_z_e2 = g3_0_e2;
end

% lowering operators for 4 <-- 5'

if (max(ismember(g_states,4))==1)&&(max(ismember(e_states,5))==1)
g4_m_e5 = sparse(Natomic, Natomic);

```

```

g4_0_e5 = sparse(Natomic, Natomic);
g4_p_e5 = sparse(Natomic, Natomic);

g4_m_e5(index_g(4,-4):index_g(4,4),index_e(5,-5):index_e(5,5)) = d_4m5;
g4_0_e5(index_g(4,-4):index_g(4,4),index_e(5,-5):index_e(5,5)) = d_405;
g4_p_e5(index_g(4,-4):index_g(4,4),index_e(5,-5):index_e(5,5)) = d_4p5;

g4_m_e5 = tensor(qo(g4_m_e5),identity(Na),identity(Nb));
g4_0_e5 = tensor(qo(g4_0_e5),identity(Na),identity(Nb));
g4_p_e5 = tensor(qo(g4_p_e5),identity(Na),identity(Nb));

g4_x_e5 = -sqrt(1/2)*(g4_p_e5 - g4_m_e5);
g4_y_e5 = i*sqrt(1/2)*(g4_p_e5 + g4_m_e5);
g4_z_e5 = g4_0_e5;
end

%-----
% construct atomic projection operators
%-----

% projection operator onto g4 manifold

if (max(ismember(g_states,4))==1)
g4_g4 = sparse(Natomic, Natomic);
g4_g4(index_g(4,-4):index_g(4,4),index_g(4,-4):index_g(4,4)) = eye(2*4+1);
g4_g4 = tensor(qo(g4_g4),identity(Na),identity(Nb));
end

% projection operator onto g3 manifold

```

```

if (max(ismember(g_states,3))==1)
g3_g3 = sparse(Natomic, Natomic);
g3_g3(index_g(3,-3):index_g(3,3),index_g(3,-3):index_g(3,3)) = eye(2*3+1);
g3_g3 = tensor(qo(g3_g3),identity(Na),identity(Nb));
end

% projection operator onto e4 manifold

if (max(ismember(e_states,4))==1)
e4_e4 = sparse(Natomic, Natomic);
e4_e4(index_e(4,-4):index_e(4,4),index_e(4,-4):index_e(4,4)) = eye(2*4+1);
e4_e4 = tensor(qo(e4_e4),identity(Na),identity(Nb));
end

% projection operator onto e3 manifold

if (max(ismember(e_states,3))==1)
e3_e3 = sparse(Natomic, Natomic);
e3_e3(index_e(3,-3):index_e(3,3),index_e(3,-3):index_e(3,3)) = eye(2*3+1);
e3_e3 = tensor(qo(e3_e3),identity(Na),identity(Nb));
end

% projection operator onto e2 manifold

if (max(ismember(e_states,2))==1)
e2_e2 = sparse(Natomic, Natomic);
e2_e2(index_e(2,-2):index_e(2,2),index_e(2,-2):index_e(2,2)) = eye(2*2+1);
e2_e2 = tensor(qo(e2_e2),identity(Na),identity(Nb));
end

```

```

% projection operator onto e5 manifold

if (max(ismember(e_states,5))==1)
e5_e5 = sparse(Natomic, Natomic);
e5_e5(index_e(5,-5):index_e(5,5),index_e(5,-5):index_e(5,5)) = eye(2*5+1);
e5_e5 = tensor(qo(e5_e5),identity(Na),identity(Nb));
end

```

C.3.2 Cavity Operators

```

%-----
% photon destruction operators
%-----

a = tensor(identity(Natomic),destroy(Na),identity(Nb));
b = tensor(identity(Natomic),identity(Na),destroy(Nb));

c_p = -sqrt(0.5)*(a + i*b);
c_m = sqrt(0.5)*(a - i*b);

```

C.4 Generate Decay Superoperators

```

%-----
% construct atom and cavity decay superoperators
%-----

% atomic decay e4 --> g4

if (max(ismember(g_states,4))==1)&&(max(ismember(e_states,4))==1)
L1 = 0.5*gamma*(2*spre(g4_x_e4)*spost(g4_x_e4') + ...
2*spre(g4_y_e4)*spost(g4_y_e4') + ...

```

```

2*spre(g4_z_e4)*spost(g4_z_e4') - ...
spre(g4_x_e4'*g4_x_e4) - spost(g4_x_e4'*g4_x_e4) - ...
spre(g4_y_e4'*g4_y_e4) - spost(g4_y_e4'*g4_y_e4) - ...
spre(g4_z_e4'*g4_z_e4) - spost(g4_z_e4'*g4_z_e4));
else L1=0;end;

% atomic decay e4 --> g3

if (max(ismember(g_states,3))==1)&&(max(ismember(e_states,4))==1)
L2 = 0.5*gamma*(2*spre(g3_x_e4)*spost(g3_x_e4') + ...
2*spre(g3_y_e4)*spost(g3_y_e4') + ...
2*spre(g3_z_e4)*spost(g3_z_e4') - ...
spre(g3_x_e4'*g3_x_e4) - spost(g3_x_e4'*g3_x_e4) - ...
spre(g3_y_e4'*g3_y_e4) - spost(g3_y_e4'*g3_y_e4) - ...
spre(g3_z_e4'*g3_z_e4) - spost(g3_z_e4'*g3_z_e4));
else L2=0;end;

% atomic decay e3 --> g4

if (max(ismember(g_states,4))==1)&&(max(ismember(e_states,3))==1)
L3 = 0.5*gamma*(2*spre(g4_x_e3)*spost(g4_x_e3') + ...
2*spre(g4_y_e3)*spost(g4_y_e3') + ...
2*spre(g4_z_e3)*spost(g4_z_e3') - ...
spre(g4_x_e3'*g4_x_e3) - spost(g4_x_e3'*g4_x_e3) - ...
spre(g4_y_e3'*g4_y_e3) - spost(g4_y_e3'*g4_y_e3) - ...
spre(g4_z_e3'*g4_z_e3) - spost(g4_z_e3'*g4_z_e3));
else L3=0;end;

% atomic decay e3 --> g3

```

```

if (max(ismember(g_states,3))==1)&&(max(ismember(e_states,3))==1)
L4 = 0.5*gamma*(2*spre(g3_x_e3)*spost(g3_x_e3') + ...
2*spre(g3_y_e3)*spost(g3_y_e3') + ...
2*spre(g3_z_e3)*spost(g3_z_e3') - ...
spre(g3_x_e3'*g3_x_e3) - spost(g3_x_e3'*g3_x_e3) - ...
spre(g3_y_e3'*g3_y_e3) - spost(g3_y_e3'*g3_y_e3) - ...
spre(g3_z_e3'*g3_z_e3) - spost(g3_z_e3'*g3_z_e3));
else L4=0;end;

```

```

% atomic decay e2 --> g3

```

```

if (max(ismember(g_states,3))==1)&&(max(ismember(e_states,2))==1)
L5 = 0.5*gamma*(2*spre(g3_x_e2)*spost(g3_x_e2') + ...
2*spre(g3_y_e2)*spost(g3_y_e2') + ...
2*spre(g3_z_e2)*spost(g3_z_e2') - ...
spre(g3_x_e2'*g3_x_e2) - spost(g3_x_e2'*g3_x_e2) - ...
spre(g3_y_e2'*g3_y_e2) - spost(g3_y_e2'*g3_y_e2) - ...
spre(g3_z_e2'*g3_z_e2) - spost(g3_z_e2'*g3_z_e2));
else L5=0;end;

```

```

% atomic decay e5 --> g4

```

```

if (max(ismember(g_states,4))==1)&&(max(ismember(e_states,5))==1)
L6 = 0.5*gamma*(2*spre(g4_x_e5)*spost(g4_x_e5') + ...
2*spre(g4_y_e5)*spost(g4_y_e5') + ...
2*spre(g4_z_e5)*spost(g4_z_e5') - ...
spre(g4_x_e5'*g4_x_e5) - spost(g4_x_e5'*g4_x_e5) - ...
spre(g4_y_e5'*g4_y_e5) - spost(g4_y_e5'*g4_y_e5) - ...
spre(g4_z_e5'*g4_z_e5) - spost(g4_z_e5'*g4_z_e5));
else L6=0;end;

```

```
% cavity decay
```

```
L7 = 0.5*kappa*(2*spre(a)*spost(a') - spre(a'*a) - spost(a'*a));
```

```
L8 = 0.5*kappa*(2*spre(b)*spost(b') - spre(b'*b) - spost(b'*b));
```

C.5 Prepare Initial Density Matrix

```
%-----  
% reference unpolarized density matrices  
%-----
```

```
% uniform distribution in F=4
```

```
rho_unpolarized_4 = 0;
```

```
if max(ismember(g_states,4))==1
```

```
for m=-4:4
```

```
    psi0 = psi{index_g(4,m)};
```

```
    rho_unpolarized_4 = rho_unpolarized_4 + psi0*psi0';
```

```
end
```

```
rho_unpolarized_4 = rho_unpolarized_4/trace(rho_unpolarized_4);
```

```
end
```

```
% uniform distribution in F=3
```

```
rho_unpolarized_3 = 0;
```

```
if max(ismember(g_states,3))==1
```

```
for m=-3:3
```

```
    psi0 = psi{index_g(3,m)};
```

```
    rho_unpolarized_3 = rho_unpolarized_3 + psi0*psi0';
```

```

end
rho_unpolarized_3 = rho_unpolarized_3/trace(rho_unpolarized_3);
end

%-----
% customize initial state based on user input (z_states)
%-----

rho_custom = 0;

if isscalar(z_states)==0;
    num_states=size(z_states);
    for m=1:1:num_states(1)
        psi0 = psi{index_g(z_states(m,1),z_states(m,2))};
        rho_custom = rho_custom + psi0*psi0';
    end
    rho_custom = rho_custom/trace(rho_custom);
else
    if z_states == 3
        rho_custom = rho_unpolarized_3;
    elseif z_states == 1
        psi0 = 1/sqrt(2)*(psi{index_g(4,1)} + psi{index_g(4,-1)});
        rho_custom = psi0*psi0';
    else rho_custom = rho_unpolarized_4;
    end
end
end

```

C.6 State-Dependent Detuning Effects

C.6.1 Magnetic Fields

```

%-----
% magnetic field Hamiltonians
%-----

% note:  $L_{e3} = 0$ , so  $e_3$  does not couple to magnetic fields
b2 = double(jmat(2,'x')*B(1) + jmat(2,'y')*B(2) + jmat(2,'z')*B(3));
b3 = double(jmat(3,'x')*B(1) + jmat(3,'y')*B(2) + jmat(3,'z')*B(3));
b4 = double(jmat(4,'x')*B(1) + jmat(4,'y')*B(2) + jmat(4,'z')*B(3));
b5 = double(jmat(5,'x')*B(1) + jmat(5,'y')*B(2) + jmat(5,'z')*B(3));

%generate Hamiltonians for splittings in user-specified states

Hg3 = sparse(Natomic,Natomic);
if max(ismember(g_states,3))==1
Hg3(index_g(3,-3):index_g(3,3),index_g(3,-3):index_g(3,3)) = Lg3*b3;
end

Hg4 = sparse(Natomic,Natomic);
if max(ismember(g_states,4))==1
Hg4(index_g(4,-4):index_g(4,4),index_g(4,-4):index_g(4,4)) = Lg4*b4;
end

He2 = sparse(Natomic,Natomic);
if max(ismember(e_states,2))==1
He2(index_e(2,-2):index_e(2,2),index_e(2,-2):index_e(2,2)) = Le2*b2;
end

```

```

He4 = sparse(Natomic,Natomic);
if max(ismember(e_states,4))==1
He4(index_e(4,-4):index_e(4,4),index_e(4,-4):index_e(4,4)) = Le4*b4;
end

He5 = sparse(Natomic,Natomic);
if max(ismember(e_states,5))==1
He5(index_e(5,-5):index_e(5,5),index_e(5,-5):index_e(5,5)) = Le5*b5;
end

Hg3 = tensor(qo(Hg3),identity(Na),identity(Nb));
Hg4 = tensor(qo(Hg4),identity(Na),identity(Nb));
He2 = tensor(qo(He2),identity(Na),identity(Nb));
He4 = tensor(qo(He4),identity(Na),identity(Nb));
He5 = tensor(qo(He5),identity(Na),identity(Nb));

% the total magnetic field Hamiltonian
H_mag = Hg3 + Hg4 + He2 + He4 + He5;

```

C.6.2 FORT Shifts

```

%-----
% FORT shifts
%-----
% construct FORT Hamiltonian in a basis with quantization axis set along the
% axis of the (linear) polarization of the FORT

E_fort = 2 * pi * 40; % 6S1/2, F = 4 FORT shift in MHz

% a note on the convention used here: in general, the Stark shifts on the
% 6P3/2 Zeeman states take the form:

```

```

%                               E_shift/E_fort = x + y * m^2
% where coefficients x, y depend upon which hyperfine state we are working
% with and must be calculated independently. For the details of these
% calculations see Chapter 3 of this thesis.

x = [0 0.9269 1.1117 1.0377 0.8530];
y = [0 0.0277 -0.0323 -0.0083 0.0129];

H_fort = 0;
for state = 1:length(e_states)
    f = e_states(state);
    for m=-f:f
        psi0 = psi{index_e(f,m)};
        H_fort = H_fort + E_fort * ((x(f) - 1) + y(f) * m^2) *psi0*psi0';
    end
end

%-----
% rotation matrices (for moving FORT shift Hamiltonian into proper basis)
%-----

R = sparse(Natomic,Natomic);

if max(ismember(g_states,3))==1
R(index_g(3,-3):index_g(3,3),index_g(3,-3):index_g(3,3)) = ...
    double(expm(jmat(3,'y')*i*pi/2));
end

if max(ismember(g_states,4))==1
R(index_g(4,-4):index_g(4,4),index_g(4,-4):index_g(4,4)) = ...

```

```

    double(expm(jmat(4,'y')*i*pi/2));
end

if max(ismember(e_states,2))==1
R(index_e(2,-2):index_e(2,2),index_e(2,-2):index_e(2,2)) = ...
    double(expm(jmat(2,'y')*i*pi/2));
end

if max(ismember(e_states,3))==1
R(index_e(3,-3):index_e(3,3),index_e(3,-3):index_e(3,3)) = ...
    double(expm(jmat(3,'y')*i*pi/2));
end

if max(ismember(e_states,4))==1
R(index_e(4,-4):index_e(4,4),index_e(4,-4):index_e(4,4)) = ...
    double(expm(jmat(4,'y')*i*pi/2));
end

if max(ismember(e_states,5))==1
    R(index_e(5,-5):index_e(5,5),index_e(5,-5):index_e(5,5)) = ...
    double(expm(jmat(5,'y')*i*pi/2));
end

R = tensor(qo(R),identity(Na),identity(Nb));

% total FORT Hamiltonian
H_fort = R' * H_fort * R; % rotate FORT Hamiltonian into our basis

```

C.6.3 Cavity Effects

```

%-----

```

```

% Birefringent Splitting
%-----

H_biref = splitting*a'*a - splitting*b'*b;

%-----

% Probe Detuning Effects
%-----

H_probe = 0;
for state = 1:length(e_states)
    f = e_states(state);
    detuning = Delta_e(max(coupled_states));
H_probe = H_probe + (Delta_e(f) - detuning - probe_freq)*...
eval(['e' num2str(f) '_e' num2str(f)]);
end

H_probe = H_probe + (cavity_freq - probe_freq) * (a' * a + b' * b);

```

C.7 Interaction Hamiltonians

C.7.1 Jaynes-Cummings Hamiltonian

```

%-----

% Jaynes-Cummings Hamiltonian H0
%-----

% select the appropriate x-, y-, and z-coupled atomic raising and lowering
% operators for composing the Jaynes Cummings Hamiltonian based on the
% user-input 'coupled_states' vector

c_op_x = eval(['g' num2str(coupled_states(1)) '_x_e' num2str(coupled_states(2))]);

```

```

c_op_y = eval(['g' num2str(coupled_states(1)) '_y_e' num2str(coupled_states(2))]);
c_op_z = eval(['g' num2str(coupled_states(1)) '_z_e' num2str(coupled_states(2))]);

% Jaynes Cummings Hamiltonian

H0 = g*(a'*c_op_x + a*c_op_x') + g*(b'*c_op_y + b*c_op_y');

```

C.7.2 User-Controlled Interactions

Some combination of the following sample Hamiltonians can be added to the simulation to model relevant effects:

```

%-----
% user-defined Hamiltonians
%-----

trise = 0.006;
tfall = trise;
tstart = 0.010 - 0.5*trise;
tend = 0.010 + 0.5*trise;

%Hamiltonians for impulsive excitation from the side
H1 = 0.5*Omega*(c_op_z + c_op_z')*fn('pulse',0,tstart,trise,tend,tfall);
H2 = 0.5*Omega*(c_op_z + c_op_z')*fn('pulse',0,tstart + delay,trise,tend + ...
    delay,tfall);

% generate impulse shapes using QOT pulse function
for k=1:length(tlist)
    impulse1(k) = pulse(tlist(k),tstart,trise,tend + delay,tfall);
    impulse2(k) = pulse(tlist(k),tstart + delay,trise,tend + delay,tfall);
end

```

```
% Hamiltonian for driving the atom continuously from the side
```

```
H1 = 0.5 * Omega * (c_op_z + c_op_z');
```

```
% Hamiltonians for driving the cavity
```

```
% time-dependent driving field, linear polarization
```

```
H1 = 0.5 * sqrt(Omega) * kappa * (a + a') *...  
fn('pulse',0,tstart,trise,tend+delay,tfall);
```

```
% continuous-driving, linear polarization
```

```
H1 = 0.5 * sqrt(Omega) * kappa * (a + a');
```

```
% continuous-driving, circular polarization
```

```
H1 = 0.5 * sqrt(Omega) * kappa * (c_p + c_p');
```

C.8 Construct Integrate Liouvillian

```
%-----  
% Total Hamiltonian  
%-----
```

```
% compose the total Hamiltonian (HSS is steady-state Hamiltonian, if desired)
```

```
H = H0 + H1 + H_mag + H_biref + H_fort + H_probe;
```

```
HSS = H0 + H1 + H_mag + H_biref;
```

```
%-----  
% Construct Liouvillian
```

```

%-----

L = -i*(spre(H) - spost(H));
LSS = -i*(spre(HSS) - spost(HSS));
for L_index=1:1:8;
    L_temp=eval(['L' num2str(L_index)]);
    if isa(L_temp,'qo')==1;
        L=L+L_temp;
        LSS = LSS+L_temp;
    end
end

%-----
% Time Evolve System (or find steady-state)
%-----

rho = integrate(L,tlist,rho_custom);
% for information about integrate() see the subroutine description, below
rho0 = rho[length(rho)];
rhoss = steady(LSS);

```

C.9 Calculate Observables

```

%-----

% Evaluate Output State and Return Results
%-----

na = zeros(N,1);
% number of photons in mode a of the cavity
nb = zeros(N,1);
% number of photons in mode b of the cavity

```

```

na = expect(rho, a'*a);
nb = expect(rho, b'*b);

% probabilities for the atom to be in any of a number of hyperfine manifolds
pg3 = expect(rho, g3_g3);
pg4 = expect(rho, g4_g4);
pe4 = expect(rho, e4_e4);
pe3 = expect(rho, e3_e3);

% total intracavity photon number
n_tot = (sum(na)+sum(nb))*kappa*delta;

% probabilities for the atom to be in a Zeeman state in F=4
pz4 = zeros(9,N);
if max(ismember(g_states,4)) == 1
for m=-4:4
    psi0=psi{index_g(4,m)};
    temp = psi0'*rho0*psi0;
    pz4(m+5,:) = expect(rho,psi0*psi0');
    disp(sprintf ('%2d, %7.4f\n', m, double(temp)));
end
end

% probabilities for the atom to be in a Zeeman state in F=3
pz3 = zeros(7,N);
if max(ismember(g_states,3)) == 1
for m=-3:3
    psi0=psi{index_g(3,m)};
    temp = psi0'*rho0*psi0;

```

```

pz3(m+4,:) = expect(rho,psi0*psi0');
disp(sprintf ('%2d, %7.4f\n', m, double(temp)));
end
end

% probability for the atom to be in a particular arbitrary state
psi0 = 1/sqrt(2)*(psi{index_g(4,1)} + psi{index_g(4,-1)});
p_super = expect(rho,psi0*psi0');

```

C.10 Subroutines

C.10.1 Integrating the Master Equation

```

%-----
% integrate the master equation
%-----
function rho_new = integrate (L,tlist,rho_old);

options.lmm = 'ADAMS';
options.iter = 'FUNCTIONAL';
options.reltol = 1e-6;
options.abstol = 1e-6;
options.mxstep = 500;

ode2file ('file1.dat', L, rho_old, tlist);
odesolve ('file1.dat', 'file2.dat');

fid = fopen ('file2.dat', 'rb');
rho_new = qread (fid, dims(rho_old), size(tlist));
fclose (fid);

```

end

C.10.2 Calculating Indices for Atomic States

```

%-----
% subroutines to calculate index into atomic state vector array
%-----
% The following routines represent "smart" indexing systems for
% assigning tensorial indices to atomic states based on arbitrary
% combinations of cesium hyperfine states specified by the user.

% index_g begins indexing the user-specified ground state manifolds

function n = index_g(F,m)
n=0; % zero index
    if (max(ismember(F, g_states)) == 1)
        % verify that the requested index is part of the user-specified state space
        for loop_n = 1:length(g_states);
            % loops through all user-specified hyperfine manifolds,
            % from smallest F-value to largest
            if g_states(loop_n)<F
                % for all specified manifolds with F-value (= F')
                % smaller than input variable F
                n = n + 2*g_states(loop_n)+1; % add (2F + 1) to the present index
            else
                if g_states(loop_n) == F
                    n = n + m + F +1;
                end
            end
        end
    end
end
end

```

```

    else error('Error: Indexing state not specified in user input.')
    end
end

```

```
function n = index_e(F,m)
```

```
n=0;
```

```
    if (max(ismember(F, e_states)) == 1)
```

```
        for loop_n = 1:length(g_states);
```

```
            n = n + (2*g_states(loop_n) + 1);
```

```
        end
```

```
        for loop_n = 1:length(e_states);
```

```
            if e_states(loop_n)<F
```

```
                n = n + 2*e_states(loop_n)+1;
```

```
            else
```

```
                if e_states(loop_n) == F
```

```
                    n = n + m + F +1;
```

```
                end
```

```
            end
```

```
        end
```

```
    else error('Error: Indexing state not specified in user input.')
    end
end

```

```
end
```

```
function y = pulse (t, tstart, trise, tend, tfall)
```

```
if (t <= tstart - 0.5*trise)
```

```
    y = 0.0;
```

```
elseif (t > tstart - 0.5*trise && t < tstart + 0.5*trise)
    y = 0.5*(1 + sin(pi*(t - tstart)/trise));
elseif (t >= tstart + 0.5*trise && t <= tend - 0.5*tfall)
    y = 1.0;
elseif (t > tend - 0.5*tfall && t < tend + 0.5*tfall)
    y = 0.5*(1 - sin(pi*(t - tend)/tfall));
else
    y = 0.0;
end
end
end
```

Bibliography

- [1] D. W. Vernooy. *Cold atoms in cavity QED for quantum information processing*. PhD thesis, California Institute of Technology, 2000.
- [2] J. McKeever, J. R. Buck, A. D. Boozer, A. Kuzmich, H.-C. Nägerl, D. M. Stamper-Kurn, and H. J. Kimble. State-Insensitive Cooling and Trapping of Single Atoms in an Optical Cavity. *Phys. Rev. Lett.*, 90:133602, 2003.
- [3] E. T. Jaynes and F. W. Cummings. Comparison of quantum and semiclassical radiation theories with application to the beam maser. *Proc. IEEE*, 51:89, 1963.
- [4] W. P. Schleich. *Quantum Optics in Phase Space*. Wiley-VCH, Berlin, 2001.
- [5] H. Giessen, J. D. Berger, G. Mohs, P. Meystre, and S. F. Yelin. Cavity-modified spontaneous emission: From Rabi oscillations to exponential decay. *Phys. Rev. A*, 53(4):2816–2821, Apr 1996.
- [6] E. Merzbacher. *Quantum Mechanics*. John Wiley & Sons, Inc., New York, 1998.
- [7] H. J. Carmichael. *Statistical Methods in Quantum Optics*, volume 2. Springer, Berlin, 2008.
- [8] D. Press, S. Goetzinger, S. Reitzenstein, C. Hofmann, A. Loeffler, M. Kamp, A. Forchel, and Y. Yamamoto. Photon antibunching from a single quantum-dot-microcavity system in the strong coupling regime. *Phys. Rev. Lett.*, 98:117402, 2007.
- [9] A. Wallraff, D. I. Schuster, A. Blais, L. Frunzio, R. S. Huang, J. Majer, S. Kumar, S. M. Girvin, and R. J. Schoelkopf. Strong coupling of a single photon to a super-

- conducting qubit using circuit quantum electrodynamics. *Nature*, 431(7005):162–167, 2004.
- [10] I. Chiorescu, P. Bertet, K. Semba, Y. Nakamura, C. J.P.M. Harmans, and J. E. Mooij. Coherent dynamics of a flux qubit coupled to a harmonic oscillator. *Nature*, 431(7005):159–162, 2004.
- [11] D. Steck. Cesium D Line Data. <http://steck.us/alkalidata/cesiumnumbers.pdf>, September 2008.
- [12] P. Violino E. Arimondo, M. Inguscio. Experimental determinations of the hyperfine structure in the alkali atoms. *Rev. Mod. Phys.*, 49(1):33–77, 1977.
- [13] National Institute of Standards and Technology. The NIST Reference on Constants, Units and Uncertainty. <http://physics.nist.gov/>, January 2009.
- [14] G. Arfken. *Mathematical Methods for Physicists*. Harcourt, San Diego, 2001.
- [15] A. D. Boozer. *Raman transitions in cavity QED*. PhD thesis, California Institute of Technology, 2005.
- [16] R. Loudon. *The Quantum Theory of Light*. Oxford University Press, Oxford, 2nd edition, 1983.
- [17] A.E. Siegman. *Lasers*. University Science Books, Sausalito, CA, 1986.
- [18] P. Horak, H. Ritsch, T. Fischer, P. Maunz, T. Puppe, P. W. H. Pinkse, and G. Rempe. Optical Kaleidoscope Using a Single Atom. *Phys. Rev. Lett.*, 88:043601, Jan 2002.
- [19] M. Tavis and F. W. Cummings. Exact solution for an n -molecule-radiation-field hamiltonian. *Phys. Rev.*, 170:379–384, 1968.
- [20] H J Kimble. Strong interactions of single atoms and photons in cavity qed. *Physica Scripta*, T76:127–137, 1998.
- [21] J. R. Buck. *Cavity QED in microsphere and Fabry-Perot cavities*. PhD thesis, California Institute of Technology, 2003.

- [22] J. McKeever. *Trapped atoms in cavity QED for quantum optics and quantum information*. PhD thesis, California Institute of Technology, 2004.
- [23] A. Boca. *Experiments in cavity QED: Exploring the interaction of quantized light with a single trapped atom*. PhD thesis, California Institute of Technology, 2005.
- [24] C. J. Hood. *Real-time measurement and trapping of single atoms by single photons*. PhD thesis, California Institute of Technology, 2000.
- [25] T. W. Lynn. *Measurement and control of individual quanta in cavity QED*. PhD thesis, California Institute of Technology, 2003.
- [26] T. E. Northup. *Coherent control in cavity QED*. PhD thesis, California Institute of Technology, 2008.
- [27] R. G. DeVoe, C. Fabre, K. Jungmann, J. Hoffnagle, and R. G. Brewer. Precision optical-frequency-difference measurements. *Phys. Rev. A*, 37:1802–1805, Mar 1988.
- [28] C. J. Hood, H. J. Kimble, and J. Ye. Characterization of high-finesse mirrors: Loss, phase shifts, and mode structure in an optical cavity. *Phys. Rev. A*, 64:033804, Aug 2001.
- [29] K. M. Birnbaum. *Cavity QED with multilevel atoms*. PhD thesis, California Institute of Technology, 2005.
- [30] C. Wieman, G. Flowers, and S. Gilbert. Inexpensive laser cooling and trapping experiment for undergraduate laboratories. *Am. J. Phys.*, 63(4):317–330, 1995.
- [31] H. J. Metcalf and P. Vander Straten. *Laser Cooling and Trapping*. Springer, New York, 1999.
- [32] R. Miller, T. E. Northup, K. M. Birnbaum, A. Boca, A. D. Boozer, and H. J. Kimble. Trapped atoms in cavity QED: coupling quantized light and matter. *J. Phys. B.: At. Mol. Opt. Phys.*, 38(9):S551–S565, 2005.

- [33] C. J. Hood, T. W. Lynn, A. C. Doherty, A. S. Parkins, and H. J. Kimble. The Atom-Cavity Microscope: Single Atoms Bound in Orbit by Single Photons. *Science*, 287(5457):1447–1453, 2 2000.
- [34] *CRC Handbook of Chemistry and Physics*. CRC Press, Inc., Boca Raton, 78th edition, 1997.
- [35] A. Ashkin. *Optical Trapping and Manipulation of Neutral Particles Using Lasers*. World Scientific, Mountain View, CA, 2007.
- [36] M. Abramowitz and I. A. Stegun. *Handbook of Mathematical Functions with Formulas, Graphics and Mathematical Tables*. Dover, New York, 1964.
- [37] D. Boiron, A. Michaud, P. Lemonde, Y. Castin, C. Salomon, S. Weyers, K. Szymaniec, L. Cогnet, and A. Clairon. Laser cooling of cesium atoms in gray optical molasses down to 1.1 μK . *Phys. Rev. A*, 53(6):R3734–R3737, Jun 1996.
- [38] E. D. Black. An introduction to pound–drever–hall laser frequency stabilization. *Am. J. Phys.*, 69(1):79–87, 2001.
- [39] Wolfgang Demtröder. *Laser Spectroscopy*. Springer, Berlin, November 2002.
- [40] J. McKeever, A. Boca, A. D. Boozer, R. Miller, J. R. Buck, A. Kuzmich, and H. J. Kimble. Deterministic Generation of Single Photons from One Atom Traped in a Cavity. *Science*, 303:1992–1994, 2004.
- [41] A. Boca, R. Miller, K. M. Birnbaum, A. D. Boozer, J. McKeever, and H. J. Kimble. Observation of the Vacuum Rabi Spectrum for One Trapped Atom. *Phys. Rev. Lett.*, 93:233603, 2004.
- [42] P. Maunz, T. Puppe, I. Schuster, N. Syassen, P. W. H. Pinkse, and G. Rempe. Cavity cooling of a single atom. *Nature*, 428:50, 2004.
- [43] A. D. Boozer. Theory of Raman transitions in cavity QED. *Phys. Rev. A*, 78:425202, 2008.

- [44] J. Dupont-Roc C. Cohen-Tannoudji and G. Grynberg. *Atom-Photon Interactions: Basic Processes and Applications*. Wiley-Interscience, New York, 1998.
- [45] M. A. Nielsen and I. L. Chuang. *Quantum Computation and Quantum Information*. Cambridge University Press, October 2000.
- [46] A. D. Boozer, R. Miller, T. E. Northup, A. Boca, and H. J. Kimble. Optical pumping via incoherent raman transitions. *Phys. Rev. A*, 76(6), 2007.
- [47] A. Kastler. Nobel prize lecture. 1966.
- [48] W. Happer. Optical pumping. *Rev. Mod. Phys.*, 44:169, 1972.
- [49] L. S. Cutler. United States Patent 4,425,653, 1980.
- [50] C. Audoin. *Metrologia*, 29:113, 1992.
- [51] J. Xiao X. Yang C. Zhang H. Wang M. Xiao B. Wang, Y. Han and K. Peng. Preparation and determination of spin-polarized states in multi-zeeman-sublevel atoms. *Phys. Rev. A.*, 75:051801(R), 2007.
- [52] A. Kuhn G. Rempe T. Wilk, S. C. Webster. Single-atom single-photon quantum interface. *Science*, 317:488, 2007.
- [53] M. H. Anderson, R. D. Jones, J. Cooper, S. J. Smith, D. S. Elliott, H. Ritsch, and P. Zoller. Observation of population fluctuations in two-level atoms driven by a phase diffusing field. *Phys. Rev. Lett.*, 64(12):1346–1349, Mar 1990.
- [54] K. P. Dinse, M. P. Winters, and J. L. Hall. Doppler-free optical multiplex spectroscopy with stochastic excitation. *J. Opt. Soc. Am. B*, 5(9):1825–1831, 1988.
- [55] S. Lathi, S. Kasapi, and Y. Yamamoto. Phase-sensitive frequency-modulation noise spectroscopy with a diode laser. *Opt. Lett.*, 21(19):1600–1602, 1996.
- [56] T. Yabuzaki, T. Mitsui, and U. Tanaka. New type of high-resolution spectroscopy with a diode laser. *Phys. Rev. Lett.*, 67(18):2453–2456, Oct 1991.

- [57] A. D. Boozer, A. Boca, R. Miller, T. E. Northup, and H. J. Kimble. Cooling to the Ground State of Axial Motion for One Atom Strongly Coupled to an Optical Cavity. *Phys. Rev. Lett.*, 97:083602, 2006.
- [58] D. Leibfried, R. Blatt, C. Monroe, and D. Wineland. Quantum dynamics of single trapped ions. *Rev. Mod. Phys.*, 75(1):281–324, Mar 2003.
- [59] W. Alt, D. Schrader, S. Kuhr, M. Müller, V. Gomer, and D. Meschede. Single atoms in a standing-wave dipole trap. *Phys. Rev. A*, 67(3):033403, Mar 2003.
- [60] A. S. Parkins and H. J. Kimble. *J. Opt. B: Quantum Semiclass. Opt.*, 1:496, 1999.
- [61] D. Bouwmeester and A. Zeilinger. *The physics of quantum information: basic concepts*. Springer-Verlag, London, UK, 2000.
- [62] C. Monroe, D. M. Meekhof, B. E. King, W. M. Itano, and D. J. Wineland. Demonstration of a fundamental quantum logic gate. *Phys. Rev. Lett.*, 75(25):4714–4717, Dec 1995.
- [63] M. D. Barrett, J. Chiaverini, T. Schaetz, J. Britton, W. M. Itano, J. D. Jost, E. Knill, C. Langer, D. Leibfried, R. Ozeri, and D. J. Wineland. Deterministic quantum teleportation of atomic qubits. *Nature*, 429(6993):737–739, 06 2004.
- [64] M. Riebe, H. Haffner, C. F. Roos, W. Hansel, J. Benhelm, G. P. T. Lancaster, T. W. Korber, C. Becher, F. Schmidt-Kaler, D. F. V. James, and R. Blatt. Deterministic quantum teleportation with atoms. *Nature*, 429(6993):734–737, 06 2004.
- [65] D. Kielpinski, C. Monroe, and D. J. Wineland. Architecture for a large-scale ion-trap quantum computer. *Nature*, 417(6890):709–711, 06 2002.
- [66] B. B. Blinov, D. L. Moehring, L. M. Duan, and C. Monroe. Observation of entanglement between a single trapped atom and a single photon. *Nature*, 428(6979):153–157, 03 2004.
- [67] D. L. Moehring, P. Maunz, S. Olmschenk, K. C. Younge, D. N. Matsukevich, L. M.

- Duan, and C. Monroe. Entanglement of single-atom quantum bits at a distance. *Nature*, 449(7158):68–71, 09 2007.
- [68] S. Olmschenk, D. N. Matsukevich, P. Maunz, D. Hayes, L.-M. Duan, and C. Monroe. Quantum Teleportation Between Distant Matter Qubits. *Science*, 323(5913):486–489, 2009.
- [69] D. Felinto, C. W. Chou, J. Laurat, E. W. Schomburg, H. de Riedmatt, and H. J. Kimble. Conditional control of the quantum states of remote atomic memories for quantum networking. *Nature Physics*, 2:841, 2006.
- [70] J. Laurat, K. S. Choi, H. Deng, C. W. Chou, and H. J. Kimble. Heralded Entanglement between Atomic Ensembles: Preparation, Decoherence, and Scaling. *Phys. Rev. Lett.*, 99:180504, 2007.
- [71] Q. A. Turchette, C. J. Hood, W. Lange, H. Mabuchi, and H. J. Kimble. Measurement of conditional phase shifts for quantum logic. *Phys. Rev. Lett.*, 75(25):4710–4713, Dec 1995.
- [72] A. D. Boozer, A. Boca, R. Miller, T. E. Northup, and H. J. Kimble. Reversible state transfer between light and a single trapped atom. *Phys. Rev. Lett.*, 98(19):193601, 2007.
- [73] P. Zoller, Th. Beth, D. Binosi, R. Blatt, H. Briegel, D. Bruss, T. Calarco, J.I. Cirac, D. Deutsch, J. Eisert, A. Ekert, C. Fabre, N. Gisin, P. Grangiere, M. Grassl, S. Haroche, A. Imamoglu, A. Karlson, J. Kempe, L. Kouwenhoven, S. Kröll, G. Leuchs, M. Lewenstein, D. Loss, N. Lütkenhaus, S. Massar, J.E. Mooij, M.B. Plenio, E. Polzik, S. Popescu, G. Rempe, A. Sergienko, D. Suter, J. Twamley, G. Wendin, R. Werner, A. Winter, J. Wrachtrup, and A. Zeilinger. Quantum information processing and communication. *Euro. Phys. J. D*, 36(2):203–228, 2005.
- [74] H. J. Kimble. The quantum internet. *Nature*, 453(7198):1023–1030, 06 2008.
- [75] L.-M. Duan and H. J. Kimble. Scalable photonic quantum computation through cavity-assisted interactions. *Phys. Rev. Lett.*, 92(12):127902, Mar 2004.

- [76] C. H. Bennett. Quantum and classical information: Transmission and computation. *Physics Today*, 48(10):24–30, 1995.
- [77] A. K. Ekert. Quantum cryptography based on bell’s theorem. *Phys. Rev. Lett.*, 67(6):661–663, Aug 1991.
- [78] Vittorio Giovannetti, Seth Lloyd, and Lorenzo Maccone. Quantum-Enhanced Measurements: Beating the Standard Quantum Limit. *Science*, 306(5700):1330–1336, 2004.
- [79] J. I. Cirac, P. Zoller, H. J. Kimble, and H. Mabuchi. Quantum state transfer and entanglement distribution among distant nodes in a quantum network. *Phys. Rev. Lett.*, 78:3221–3224, 1997.
- [80] H.-J. Briegel, W. Dür, J. I. Cirac, and P. Zoller. Quantum repeaters: The role of imperfect local operations in quantum communication. *Phys. Rev. Lett.*, 81(26):5932–5935, Dec 1998.
- [81] J. Oreg, F. T. Hioe, and J. H. Eberly. Adiabatic following in multilevel systems. *Phys. Rev. A*, 29(2):690–697, Feb 1984.
- [82] J. R. Kuklinski, U. Gaubatz, F. T. Hioe, and K. Bergmann. Adiabatic population transfer in a three-level system driven by delayed laser pulses. *Phys. Rev. A*, 40(11):6741–6744, Dec 1989.
- [83] P. Zoller A. S. Parkins, P. Marte and H. J. Kimble. Synthesis of arbitrary quantum states via adiabatic transfer of zeeman coherence. *Phys. Rev. Lett.*, 71:3095, 1993.
- [84] B.W. Shore N.V. Vitanov, M. Fleischhauer and K. Bergmann. Coherent Manipulation of Atoms and Molecules by Sequential Pulses. *Adv. in At. Mol. and Opt. Phys.*, 46:55–190, 2001.
- [85] U. Gaubatz, P. Rudecki, S. Schiemann, and K. Bergmann. Population transfer between molecular vibrational levels by stimulated raman scattering with partially overlapping laser fields. a new concept and experimental results. *J. Chem. Phys.*, 92(9):5363–5376, 1990.

- [86] Matthias Keller, Birgit Lange, Kazuhiro Hayasaka, Wolfgang Lange, and Herbert Walther. Continuous generation of single photons with controlled waveform in an ion-trap cavity system. *Nature*, 431(7012):1075–1078, 10 2004.
- [87] L. Mandel and E. Wolf. *Optical Coherence and Quantum Optics*. Cambridge University Press, Cambridge, 1995.
- [88] Axel Kuhn, Markus Hennrich, and Gerhard Rempe. Deterministic single-photon source for distributed quantum networking. *Phys. Rev. Lett.*, 89(6):067901, Jul 2002.
- [89] H. J. Kimble. Comment on deterministic single-photon source for distributed quantum networking. *Phys. Rev. Lett.*, 90(24):249801, Jun 2003.
- [90] B. Sanders P. Grangier and J. Vuckovic, editors. *Focus on Single Photons on Demand*, volume 6. 2004.
- [91] G. Rempe, R. J. Thompson, H. J. Kimble, and R. Lalezari. Measurement of ultralow losses in an optical interferometer. *Opt. Lett.*, 17(5):363–365, 1992.
- [92] W. Lange and H. J. Kimble. Dynamic generation of maximally entangled photon multiplets by adiabatic passage. *Phys. Rev. A*, 61(6):063817, May 2000.
- [93] J. Bochmann, M. Mücke, G. Langfahl-Klabes, C. Erbel, B. Weber, H. P. Specht, D. L. Moehring, and G. Rempe. Fast excitation and photon emission of a single-atom-cavity system. *Phys. Rev. Lett.*, 101(22):223601, 2008.
- [94] B. Weber, H. P. Specht, T. Müller, J. Bochmann, M. Mücke, D. L. Moehring, and G. Rempe. Photon-photon entanglement with a single trapped atom. *Phys. Rev. Lett.*, 102(3):030501, 2009.
- [95] R. J. Thompson, G. Rempe, and H. J. Kimble. Observation of normal-mode splitting for an atom in an optical cavity. *Phys. Rev. Lett.*, 68(8):1132–1135, Feb 1992.
- [96] R. J. Thompson, Q. A. Turchette, O. Carnal, and H. J. Kimble. Nonlinear spectroscopy in the strong-coupling regime of cavity qed. *Phys. Rev. A*, 57(4):3084–3104, Apr 1998.

- [97] J. J. Childs, K. An, M. S. Otteson, R. R. Dasari, and M. S. Feld. Normal-mode line shapes for atoms in standing-wave optical resonators. *Phys. Rev. Lett.*, 77(14):2901–2904, Sep 1996.
- [98] C. J. Hood, M. S. Chapman, T. W. Lynn, and H. J. Kimble. Real-time cavity qed with single atoms. *Phys. Rev. Lett.*, 80(19):4157–4160, May 1998.
- [99] P. Maunz, T. Puppe, I. Schuster, N. Syassen, P. W. H. Pinkse, and G. Rempe. Normal-mode spectroscopy of a single-bound-atom cavity system. *Phys. Rev. Lett.*, 94(3):033002, Jan 2005.
- [100] K.K. Likharev. Single-electron devices and their applications. *Proceedings of the IEEE*, 87(4):606–632, Apr 1999.
- [101] K. M. Birnbaum, A. Boca, R. Miller, A. D. Boozer, T. E. Northup, and H. J. Kimble. Photon blockade in an optical cavity with one trapped atom. *Nature*, 436:87–90, 2005.
- [102] K. M. Birnbaum, A. Boca, R. Miller, A. D. Boozer, T. E. Northup, and H. J. Kimble. Theory of photon blockade by an optical cavity with one trapped atom (<http://www.arxiv.org/quant-ph/0507065>), 2005.
- [103] I. Schuster, A. Kubanek, A. Fuhrmanek, T. Puppe, P. W. H. Pinkse, K. Murr, and G. Rempe. Nonlinear spectroscopy of photons bound to one atom. *Nat Phys*, 4:382–385, 2008.